Universidade Federal de Minas Gerais
Instituto de Ciências Exatas - Departamento de Química
Programa de Pós-Graduação em Química

Structural, membrane interaction and biological studies of PS-O1 and LyeTx I-b peptide derivatives

Estudos estruturais, de interação com membranas e biológicos de derivados peptídicos da PS-O1 e LyeTx I-b

Lucas Raposo Carvalho
Belo Horizonte
2022

Lucas Raposo Carvalho

Structural, membrane interaction and biological studies of PS-O1 and LyeTx I-b peptide derivatives

Estudos estruturais, de interação com membranas e biológicos de derivados peptídicos da PS-O1 e LyeTx I-b

Tese apresentada ao Departamento de Química do Instituto de Ciências Exatas da Universidade Federal de Minas Gerais como requisito parcial para a obtenção do grau de Doutor em Ciências - Química.

Orientador : Prof. Dr. Jarbas Magalhães Resende

Belo Horizonte
2022

Ficha Catalográfica

Carvalho, Lucas Raposo.
Structural, membrane interaction and biological studies of PS-O1 and LyeTx I-b peptide derivatives [manuscrito] / Lucas Raposo Carvalho. 2022.
180 f. : il., gráfs., tabs.

Orientador: Jarbas Magalhães Resende.

Tese (doutorado) – Universidade Federal de Minas Gerais – Departamento de Química.
Bibliografia: f. 150-169.
Apêndice: f. 170-180.

1. Química orgânica – Teses. 2. Peptídios – Síntese – Teses. 3. Produtos de ação antimicrobiana – Teses. 4. Ressonância magnética nuclear – Teses. 5. Arginina – Teses. 6. Formação de anéis (Química) – Teses. 7. Cromatografia liquida de alta eficiência – Teses. 8. Testes biológicos – Teses. 9. Atividade antifúngica – Teses. 10. Citotoxidade de mediação celular – Teses. 11. Agentes antibacterianos - Teses. I. Resende, Jarbas Magalhães, Orientador. II. Título.

CDU 043

Elaborada por Sérgio Ferreira da Silva – CRB6-2719.

UNIVERSIDADE FEDERAL DE MINAS GERAIS

"Structural, Membrane Interaction, and Biological Studies of PS-O1 and LyeTx I-b Peptide Derivatives"

Lucas Raposo Carvalho

Tese aprovada pela banca examinadora constituída pelos Professores:

Prof. Jarbas Magalhães Resende - Orientador
UFMG

Prof. Adolfo Henrique de Moraes Silva
UFMG

Prof. Tiago Antônio da Silva Brandão
UFMG

Prof. Fábio Ceneviva Lacerda de Almeida
UFRJ

Prof. Cláudio Francisco Tormena
UNICAMP

Belo Horizonte, 26 de outubro de 2022.

Documento assinado eletronicamente por **Adolfo Henrique de Moraes Silva**, **Professor do Magistério Superior**, em 26/10/2022, às 18:18, conforme horário oficial de Brasília, com fundamento no art. 5º do Decreto nº 10.543, de 13 de novembro de 2020.

Documento assinado eletronicamente por **Tiago Antonio da Silva Brandao**, **Professor do Magistério Superior**, em 26/10/2022, às 18:20, conforme horário oficial de Brasília, com fundamento no art. 5º do Decreto nº 10.543, de 13 de novembro de 2020.

Documento assinado eletronicamente por **Jarbas Magalhaes Resende**, **Professor do Magistério Superior**, em 26/10/2022, às 18:25, conforme horário oficial de Brasília, com fundamento no art. 5º do Decreto nº 10.543, de 13 de novembro de 2020.

Documento assinado eletronicamente por **Claudio Francisco Tormena**, **Usuário Externo**, em 27/10/2022, às 10:01, conforme horário oficial de Brasília, com fundamento no art. 5º do Decreto nº 10.543, de 13 de novembro de 2020.

Documento assinado eletronicamente por **Fabio Ceneviva Lacerda de Almeida**, **Usuário Externo**, em 01/11/2022, às 15:13, conforme horário oficial de Brasília, com fundamento no art. 5º do Decreto nº 10.543, de 13 de novembro de 2020.

A autenticidade deste documento pode ser conferida no site https://sei.ufmg.br/sei/controlador_externo.php?acao=documento_conferir&id_orgao_acesso_externo=0, informando o código verificador **1849182** e o código CRC **EBCCDA9D**.

Agradecimentos

Durante o período do doutorado, conheci muitas pessoas, tive muitos aprendizados e passei por muitas experiências que me ajudaram a passar por momentos difíceis ou aumentaram a felicidade de momentos agradáveis.

Mãe e pai, meu agradecimento ao que vocês fizeram e fazem por mim, para que eu me torne uma pessoa melhor e feliz comigo mesmo nunca será o suficiente dado o tamanho da influência que vocês e o caminho que vocês trilharam têm sobre mim. Grande parte do que sou hoje é devido aos ensinamentos verbais e exemplares que vocês me passaram, e não poderia ser mais orgulhoso em ser filho de vocês dois como sou.

Jarbas, te agradeço imensamente pelos anos de companheirismo e aprendizado. Sem você, esse trabalho não teria tomado a forma que tomou e muito do que sei hoje, não saberia. Também gostaria de agradeçer outros professores muito importantes para a minha formação profissional e pessoal, em especial Adolfo, Willian, Rosemeire e Tiago; as lições, risadas e os pensamentos profundos que tive com vocês estarão fixos no meu consciente e serão levados por muitos e muitos anos.

Aos meus amigos que fiz em Belo Horizonte durante essa trajetória, em especial, Glaucimar, Diego, Orclévio, Breno, Gabi, Samara, Ruth e Júlio, meu muitíssimo obrigado. Estar perto de vocês, dividir momentos de alegria, tristeza, raiva e euforia foram mais do que essenciais para me manter no meu caminho durante esse período.

Também não poderia deixar de citar os amigos já de longa data, como o Dani, Lincom, Darienny, Gabriel, Zé Orelha, Barban, Adan, Léo, Selma, que sempre me apoiaram e fazem parte da minha vida e tudo que construí e eu serei eternamente grato por tudo isso. Aos antigos mestres, também extendo meus agradecimentos abundantes e insuficientes; Eder, Maurício, Juliana Fedoce, Frederico, Regiane e Sávio, vocês sempre serão exemplos a serem seguidos e levarei um pedaço de vocês na minha vida profissional.

Aos entes queridos que já se foram, a marca que deixaram no meu coração e na minha vida ficará sempre na memória, com um gosto de amor que só a saudade traz.

À Aline, *partner in crime*, metade do nosso infinito e *life-long goddess*, muito obrigado.

Por fim, agradeço aos órgãos de fomento, Fundação de Amparo à Pesquisa do Estado de Minas Gerais (FAPEMIG), Conselho Nacional de Desenvolvimento Científico e Tecnológico (CNPq), Coordenação de Aperfeiçoamento de Pessoal de Pessoal de Nível

Superior (CAPES), e Financiadora de Estudos e Projeto (FINEP) pelo apoio financeiro, e à FAPEMIG e CAPES pela bolsa concedida durante o doutorado. Agradeço também ao Centro de Laboratório Multiusuários (CELAM, UFMG), Laboratório de Ressonância Magnética Nuclear de Alta Resolução (LAREMAR, LIPq, UFMG), Laboratório de Espectroscopia no UV-Vis (Departamento de Química, UFMG) e Fundação Ezequiel Dias (FUNED) pelo apoio de infraestrutura.

"The greatest teacher, failure is.
Luke, we are what they grow beyond;
that is the true burden of all masters."

- Yoda

Resumo

Peptídeos antimicrobianos (PAMs) são promissores candidatos a fármacos para combater a resistência bacteriana, sendo moléculas com mecanismos de ação diversos. Além disso, a secreção cutânea de anuros e venenos de aranhas são fontes abundantes de PAMs e a filloseptina PS-O1, assim como a LyeTx I-b, são peptídeos de interesse do nosso grupo de pesquisa. Estratégias de alterações de peptídeos, como modificações pós-translacionais e inserção de resíduos visam melhorar propriedades farmacológicas desses potenciais fármacos. Sendo assim, neste trabalho, foram sintetizados seis compostos, dois peptídeos (**PS-O1** e **R1G2-PS-O1**) e dois derivados propargílicos (**[Pra^1]PS-O1** e **R[Pra]PS-O1**) por Fmoc-SPFS e dois glicotriazol-peptídeos (**PS-O1 GtP e R1A2-PS-O1 GtP**) por CuAAC. Os derivados **LyeTx I-b$_{\mathbf{cys}}$** e **LyeTx I-bPEG** foram sintetizados pelo colaborador Júlio César Moreira Brito. A síntese dos derivados da **PS-O1** tiveram rendimentos de síntese entre 8,7 e 26,5% e, de purificação, entre 73,4 e 91,5%, com graus de pureza entre 91 e 98%, verificados por CLAE-FR. Todos os derivados sintetizados foram caracterizados por MALDI-TOF-MS e tiveram suas preferências conformacionais analisadas por dicroísmo circular na presença de misturas TFE:H_2O, micelas de SDS e DPC e vesículas de POPC e POPC:POPG 3:1, indicando a formação de estruturas α-helicoidais a partir de determinados valores de concentração para todos os meios exceto LUVs de POPC. A estrutura tridimensional dos peptídeos **PS-O1**, **PS-O1 GtP**, **R1G2-PS-O1**, **R1A2-PS-O1 GtP**, **LyeTx I-b$_{\mathbf{cys}}$** e **LyeTx I-bPEG** foram determinadas por experimentos de RMN, revelando diferentes porcentages e localizações de estruturas α-helicoidais. Observou-se que, enquanto a introdução da unidade glicosídica aumentou a estruturação para a **PS-O1**, um efeito contrário foi observado para a **R1G2-PS-O1**, sendo potencialmente atribuído à diferentes interações estabilizantes de hélice próximas à porção N-terminal. Um alto grau de similaridade estrutural entre os peptídeos **LyeTx I-b$_{\mathbf{cys}}$** e **LyeTx I-bPEG** foi observado. Por fim, estudos de atividade anti-fúngica para os derivados da **PS-O1** mostram que a **R1G2-PS-O1** apresentou atividade pronunciadamente superior aos outros, corroborando dados estruturais observados por RMN.

PALAVRAS-CHAVE: **Peptídeos antimicrobianos, filloseptinas, LyeTx I-b, espectroscopia de RMN, interações peptídeo-membrana, glicotriazol-peptídeos, peptídeos pegilados, arginina**.

Abstract

Antimicrobial peptides (AMPs) are promising drug candidates when fighting bacterial resistance, being molecules with many mechanisms of action. Furthermore, the skin secretion of anurans and spider poisons are rich sources of AMPs, and phylloseptine PS-O1, alongside LyeTx I-b, are peptides of interest to our research group. Peptide alteration strategies, such as post-translational modifications and residue insertion, aim to improve the biological properties of these drug candidates. As such, in this work, six compounds were synthesized, being two peptides (**PS-O1** and **R1G2-PS-O1**) and two propargylic derivatives (**[Pra^1]PS-O1** and **R[Pra]PS-O1**) by Fmoc-SPPS and two glucotriazole-peptides (**PS-O1 GtP** and **R1A2-PS-O1 GtP**) using the CuAAC reaction. Two peptides, **LyeTx I-b$_{\mathbf{cys}}$** and **LyeTx I-bPEG**, were synthesized by collaborator Júlio César Moreira Brito. PS-O1 derivatives were synthesized (8.7 to 26.5% yield), purified by RP-HPLC (73.4 to 91.5% yield), with purities ranging from 92% to 98%, and analyzed by MALDI-TOF-MS. Circular dichroism was used to analyze their conformational preferences in the presence of TFE/H_2O mixtures, SDS and DPC micelles, and POPC and POPC/POPG 3:1 vesicles, indicating α-helical structural motifs starting from specific concentrations for all media except POPC LUVs. The three-dimensional structure of **PS-O1**, **PS-O1 GtP**, **R1G2-PS-O1**, **R1A2-PS-O1 GtP**, **LyeTx I-b$_{\mathbf{cys}}$**, and **LyeTx I-bPEG** was determined by 2D NMR experiments, revealing various α-helical percentages and positions. While the introduction of a glucose unit increased structure formation for **PS-O1**, an opposite effect was observed for **R1G2-PS-O1**, being potentially attributed to different helix stabilizing interactions at the *N*-terminus. A high degree of structural similarity between **LyeTx I-b$_{\mathbf{cys}}$** and **LyeTx I-bPEG** was observed. Finally, antifungal biological studies for **PS-O1** derivatives show that **R1G2-PS-O1** is considerably more active than the other three, supporting structural data obtained by NMR analyses.

KEYWORDS: **Antimicrobial peptides, phylloseptins, LyeTx I-b, NMR spectroscopy, peptide-membrane interactions, glucotriazole-peptides, PEGylated peptides, arginine**.

List of Figures

List of Tables

Acronyms

^{1}H–^{13}C-HSQC ^{1}H–^{13}C Heteronuclear Single Quantum Correlation. 82, 88, 89, 94, 95, 100, 101, 110, 112, 138, 139

^{1}H–^{15}N-HSQC ^{1}H–^{15}N Heteronuclear Single Quantum Correlation. 82, 88, 89, 94, 95, 102, 138, 139, 141, 149

Ala Alanine. 84, 97, 98, 112, 139, 141, 146, 147

AMP Antimicrobial peptide. 33–37, 50, 51, 72, 74, 77, 79, 80, 114, 122, 125, 134–136, 144, 147, 148

Arg Arginine. 36, 69, 74, 79, 80, 99, 108, 125, 131, 133

Asn Asparagine. 52, 102, 115

CD Circular Dichroism Spectroscopy. 64–68, 76, 77, 80, 96, 110, 148

CL Cardiolipin. 63, 122

CuAAC Copper(I)-catalyzed Azide Alkyne Cycloaddition. 47, 49, 50, 53, 54, 148

Cys Cysteine. 46, 136, 139, 146, 149

DCM Dichloromethane. 52–54, 70

DIC *N*,*N*-diisopropylcarbodiimide. 41, 42, 52

DMF *N*,*N*-dimethylformamide. 40, 43, 52, 54

DPC Dodecylphosphocholine. 63, 68, 70, 74, 76, 77, 148

DSS Sodium 3-(trimethylsilyl)propane-1-sulfonate. 94, 138

FID Free-Induction Decay. 95

Fmoc 9-Fluorenylmethyloxycarbonyl. 37, 39, 43, 45, 52, 53, 137, 148

Gln Glutamine. 139, 141, 146

Gly Glycine. 73, 74, 99, 113, 116, 121

Gt Glucotriazole. 72, 73, 142, 148, 149

GtP Glucotriazole-peptide. 79, 80, 112, 118, 133, 148, 149

His Histidine. 34, 35, 69, 74, 100, 101, 110, 112, 113, 115, 136

HOBt 1-Hydroxybenzotriazole. 42, 52

HSQC Heteronuclear Single Quantum Correlation. 89, 91, 138, 176, 179

Ile Isoleucine. 56, 112

INEPT Insensitive Nuclei Enhancement by Polarization Transfer. 89, 178, 179

IPA Isopropanol. 52, 54

Leu Leucine. 57, 58, 99, 104, 112, 116, 146–148

LUV Large Unilamellar Vesicle. 70, 77, 79, 80, 148

Lys Lysine. 34–36, 125, 139, 141, 142, 147

MALDI-ToF-MS Matrix-Assisted Laser Desorption/Ionization - Time-of-Flight Mass Spectrometry. 54, 57, 58, 139, 148

MD Molecular Dynamics. 91–94

MFC Minimum Fungicidal Concentration. 126, 131

MIC Minimum Inhibitory Concentration. 126–128, 130, 131, 136

mPEG-MAL Methoxy polyethyleneGlycol-maleimide. 136, 137, 139, 144

NaAsc Sodium ascorbate. 53, 54, 57

NMR Nuclear Magnetic Resonance. 63, 64, 82, 86, 88, 89, 91, 94–96, 110, 136–139, 148, 149, 178

NOE Nuclear Overhauser Effect. 84, 86–88, 92, 96, 104, 106, 107, 141, 142, 149

NOESY Nuclear Overhauser Effect SpectroscopY. 82, 84, 86–88, 91, 94–96, 100, 102–104, 106, 114, 117, 138, 141–143, 149

PC Phosphatidylcholine. 63, 124

PE Phosphatidylethanolamine. 121, 122, 125

PG Phosphatidylglycerol. 63, 122, 123

Phe Phenylalanine. 73, 74, 100, 107, 148

POPC 1-Palmitoyl-2-oleoyl-*sn*-glycero-3-phosphocholine. 68, 70, 77, 79, 80, 147, 148

POPG 1-Palmitoyl-2-oleoyl-*sn*-glycero-3-(phospho-rac-(1-glycerol)). 68, 70, 77, 79, 80, 147, 148

Pro Proline. 56, 74, 100, 107

PS Phosphatidylserine. 63, 122–124

RP-HPLC Reverse-Phase High Performance Liquid Chromatography. 55, 58, 60, 139, 148

SDS Sodium dodecylsufate. 68, 70, 74, 76, 77, 148

Ser Serine. 73, 97, 111, 112, 116

SPPS Solid Phase Peptide Synthesis. 37, 39–41, 43, 45, 54, 137, 148

TFA Trifluoroacetic acid. 40, 45, 53–56, 69

TFE Trifluoroethanol. 68, 70–73, 94, 96, 110, 138, 148, 149

TOCSY TOtal Correlation SpectroscopY. 82–84, 88, 94, 95, 97, 98, 100–102, 104, 110, 138, 139, 149

Trp Tryptophan. 36, 142, 147

Val Valine. 84, 112, 115

Contents

Chapter 1 | Introduction

1.1 Bacterial and fungal infections and resistance

One of the most concerning health-related problems is the rapid rise of antimicrobial resistance — *i.e.*, the advent of superbugs. According to the Center for Disease Control and Prevention (CDC), more than 2.8 million antibiotic-resistant infections occur yearly in the United States of America, resulting in more than 35,000 deaths (CDC, 2019; MARSTON et al., 2016). This trend does not show signs of slowing down since the World Health Organization (WHO) has declared antimicrobial resistance as one of the top 10 global public health threats (WHO, 2018).

The recent rise of resistant pathogens like *Staphylococcus aureus* — one of the leading causes of hospital and community infections — is responsible for diseases such as soft tissue infections, osteomyelitis, and fatal pneumonia (GUO et al., 2020). The prevalence of those diseases and many others represents a symptom of an administration problem. Currently, misuse of antimicrobial drugs in medical and agricultural settings is the most important issue regarding resistance (NATHAN, 2020; VENTOLA, 2015).

Recently, COVID-19 has impacted negatively most of the world population, with over 29 million cases and more than 680 thousand deaths in Brazil[1]. Besides, millions of people worldwide were affected by quarantine and social distancing regimes. The issue of bacterial and fungal secondary infections in SARS-CoV-2 patients, known in influenza infections (SHAFRAN et al., 2021), has attracted attention, especially in the early stages of the pandemic (2020).

The primary cause of concomitant infections is the facilitation of bacterial respiratory complications upon viral infections of this tract. Since viruses can hinder the mucociliary clearance configuration, they may hamper the natural mechanism of pathogen excretion, increasing the attachment of bacteria to mucins. Furthermore, the resulting compressed mucus can block the infiltration of immune cells and antimicrobial agents (HENDAUS; JOMHA, 2020; LANGFORD et al., 2020).

Fungal infections, particularly those that induce invasive diseases, are a significant

---

[1] Data obtained in `https://covid.saude.gov.br/`, accessed in 11/2022.

health problem worldwide. For instance, the mortality rate of infected patients is around 40% in Europe (SAM et al., 2018). Also, these diseases are particularly dangerous to immunocompromised patients due to diabetes, organ transplants, and other comorbidities. COVID-19 has worsened the fungal infection problem due to the sensibilization of patients, especially those in Intensive Care Units (ICUs), making them more prone to this type of infection. Specifically, *Candida sp.* infections and mucormycosis in South Asian countries were more prevalent during the SARS-CoV-2 pandemic (RAHMAN, 2021; STONE et al., 2021; HEARD et al., 2020).

Although the fungal resistance problem is not as critical as the bacterial, it is an important issue, mainly due to the similarities between fungal and mammalian cells. This leads to a considerable challenge in drug design since antifungal agents may provoke side effects due to the lack of selectivity (SAM et al., 2018). For example, amphotericin B is one of the most employed antifungal active pharmaceutical ingredients and displays noticeable nephrotoxicity (FAUSTINO; PINHEIRO, 2020).

Finally, widespread conscious use of antibiotics is not an easily achievable short-term goal, and the intrinsic biological characteristics of fungal cells provide hurdles to drug design. Therefore, the discovery of novel antimicrobial agents that bypass or negate resistance mechanisms altogether while having a good spectrum of activity is of great interest, such as Antimicrobial peptides (AMPs).

1.2 Antimicrobial peptides

Pathogenic invasions can trigger two lines of defense, the first involves innate immunity mechanisms, comprised of immune responses of T and B cells against specific antigens. The second defense pathway relates to host defense peptides, or AMPs, present in a wide range of eukaryotic organisms and responsible for providing fast and effective responses (REDDY et al., 2004).

The relevance of AMPs has increased due to the rapid emergence of multidrug-resistant bacteria (NGUYEN et al., 2011). In this context, the Antimicrobial Peptide Database (APD), established in 2004 and currently in its third version — APD3 — contains over 3400 compounds with many distinct therapeutic properties (WANG et al., 2016). Typical attributes of AMPs are relatively small size, being less than ten kDa; pronounced hydrophobicity, and positive net charge (LEI et al., 2019), even though some negatively-charged AMPs are reported (GOMES et al., 2018). Furthermore, many of these peptides exhibit antimicrobial, fungicidal, virucidal, and antineoplasic properties (FELÍCIO et al., 2016). Likewise, changes in their primary structures can modulate specific activity parameters like conformation and charge.

Most AMPs possess a positive net charge, ranging from +2 to +9 (HANCOCK; SAHL, 2006). Also, they may have highly cationic domains, with accumulations of Histidine (His) and Lysine (Lys) residues (WANG et al., 2017). Compared to common antibiotics, this positive net charge may represent a crucial advantage of AMPs. As prokaryotic cell membranes are negatively charged, whereas eukaryotic membranes are zwitterionic, the positive net charge of AMPs usually results in selectivity.

Another kernel characteristic is amphipathicity, *i.e.*, a partition between hydrophobic and hydrophilic residues (WANG et al., 2017). Amphipathicity allows AMPs to penetrate biological membranes and, although many structural motifs can achieve this feature, α-helices are most commonly observed. Hydrophobicity, *i.e.*, the quotient between residues with apolar and polar side-chains, relates to biological activity in the sense that larger values indicate more pronounced cell membrane partition capabilities. Nevertheless, too high values can induce cytotoxicity to mammalian cells and most AMPs present hydrophobicities around 50% (YEAMAN; YOUNT, 2003).

Finally, among the many different possible conformations, α-helices and β-conformations are the most common observed arrangements for AMPs (BAHAR; REN, 2013), with the first being the most abundant[2] (**Figure 1.1**).

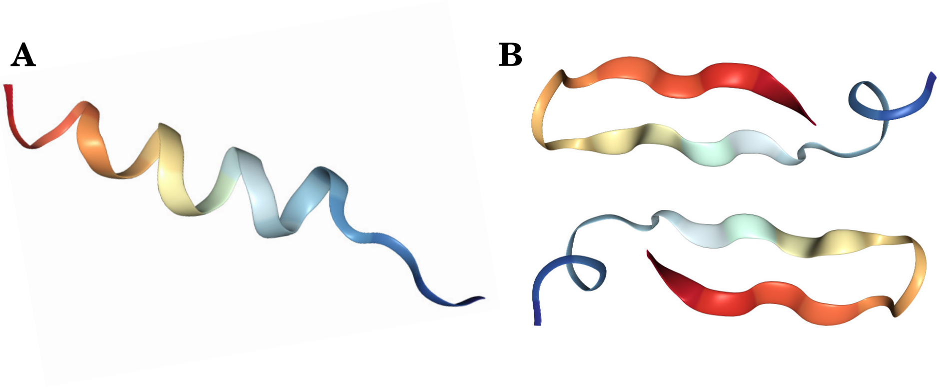

Figure 1.1: Three-dimensional structures of (**A**) the α-helical peptide phylloseptin-3 (PS-3) and (**B**) the β-hairpin peptide thanatin (PDB ID codes 2JQ1 and 5XO9, respectively (RESENDE et al., 2008; SINHA et al., 2017)).

α-Helical peptides are the main motifs in many eukaryotic systems and represent the majority of AMPs of anuran skin secretions, one of the richest sources of these compounds. Finally, the structural length of AMPs usually matches the thickness of membrane bilayers, and mismatches influence the behavior of peptides in membrane environments, like the pore formation step involved in some proposed mechanisms of action for these compounds, which are better discussed in **Chapter 5, Section 5.1** (HOLT; KILLIAN, 2010).

---

[2] A research in the APD-3 yields 501 entries of α-helical peptides (14.44%) and 90 of β-type motifs (2.59%). Research done in 11/2022.

1.2.1 Anuran-derived antimicrobial peptides

Some of the best-studied linear AMPs are found in the skin secretion of anurans (RESENDE et al., 2008) — a rich source of these compounds. The prevalence of AMPs in these animals stems from their moist skin, which makes them dependent on humid environments. Therefore, they are exposed to many microbial pathogens that thrive in these conditions and innate immune defenses, such as AMPs, are produced by their granular skin glands to combat possible infections (LIBÉRIO et al., 2014). Although these animals have prospered in several locations, most anuran species are present in South America, especially in Brazil, Colombia and Ecuador.

Particularly, phylloseptins (CALDERON et al., 2011), found in the skin secretion of *Phyllomedusa* frogs, are of interest, as they have been studied previously by our research group (GUIMARÃES, 2017), and some related molecules are subject of this thesis. They are Lys/His-rich AMPs, containing 19-20 residues on average with 1-3 His residues, and tend to adopt amphipathic α-helices in membrane-mimetic environments, with their charged residues well exposed to water in the presence of vesicles (RESENDE et al., 2014). Furthermore, their primary structures show high homology, particularly at the N-terminus, as evidenced by some examples presented in **Table 1.1** (XU X. LAI, 2015; LEITE et al., 2005).

Table 1.1: Primary structures and number of residues of phylloseptin-1, -2, -3, and -O1.

Peptide	Primary structure	Number of Residues
Phylloseptin-1	FLSLI PHAIN AVSAI AKHN-NH_2	19
Phylloseptin-2	FLSLI PHAIN AVSTL VHHF-NH_2	19
Phylloseptin-3	FLSLI PHAIN AVSAL ANHG-NH_2	19
Phylloseptin-O1	FLSLI PHAIN AVSTL VHHSG-NH_2	20

Phylloseptins are AMPs that have received considerable attention, and some studies have been made to verify their biological potential. Our research group studied Phylloseptins PS-1, PS-2, and PS-3 (**Table 1.1**), and their activity was evaluated against *S. aureus*, *E. coli*, *K. pneumoniae*, *P. aeruginosa*, and *C. albicans* (RESENDE et al., 2008). Phylloseptin-PT, present in the skin secretion of *Phyllomedusa tarsius*, and some synthetic derivatives, is active against *S. aureus* and *C. albicans* (GAO et al., 2016). Phylloseptin-PV1 (*Phyllomedusa vailantii*) is active against *C. albicans* and *S. aureus*, displaying clear membrane permeabilization (LIU et al., 2020). Phylloseptin-PHa, isolated from the skin secretion of *Phyllomedusa hypochondrialis*, displayed activity against *S. aureus*, *C. albicans*, and methicillin-resistant *S. aureus* (MRSA) (LIU et al., 2019). Finally, some phylloseptins were evaluated as antiprotozoal (BRAND et al., 2013; LEITE et al., 2005) and antineoplasic (ZANDSALIMI et al., 2020) agents, evidencing the significant biological potential of these AMPs.

1.2.2 Arginine-containing and glucosylated peptides

Arginine (Arg) residues are responsible for the increase in activity of many AMPs. Also, studies show that it improves membrane translocation of cell-penetrating peptides (CUTRONA et al., 2015). Although the mechanism for this superior activity is not fully described, many theories exist. Some of them relate to:

- Increased cationic content (YANG et al., 2018a);
- Enhanced membrane binding (RICE; WERESZCZYNSKI, 2017; CUTRONA et al., 2015);
- Improved specificity when compared to Lys residues (YANG et al., 2018b);
- The formation of hydrogen bonds with external water molecules and cation-π-like interactions with other residues, further stabilizing secondary structures (CHAN et al., 2006; CLARK et al., 2021); and
- The formation of Arg-Arg like-charge ion pairs in cell-penetrating peptides, stabilizing dimeric structures when accompanied by negatively-charged residues like glutamate or aspartate in aqueous media (VAZDAR et al., 2018; FUTAKI et al., 2001; ALLOLIO et al., 2018).

Other characteristics are the enhanced antimicrobial activity and biofilm disrupting effect of 2% Arg-incorporated NaF toothpaste, and its maintenance of ecological homeostasis (BILJE et al., 2019). Additionally, Arg incorporation in the S1 peptide — found in horseshoe crab hemocytes — furnished smaller cytotoxicity and increased antimicrobial activity against Gram-positive and -negative bacteria (YANG et al., 2018a). An interesting study performed with peptides composed exclusively of Arg and Tryptophan (Trp) residues indicated that the biological activity of Arg is increased when near the aromatic ring of Trp, suggesting the establishment of π-delocalization when their side chains are aligned (CLARK et al., 2021). Finally, the electrostatic interaction between the positive guanidinium moiety with phosphate polar heads of cell membranes, subsequent membrane distortion, and resulting proton gradient were confirmed by analysis of Arg-terminated 15-30 nm nanoparticles that can translocate directly into cells (GHOSH et al., 2019).

Alternatively, glucosylation is one of the most prominent peptide chemical modifications. Saccharide incorporation in peptides results in positive results like increased absorption, resistance against enzymatic degradation (RODRÍGUEZ et al., 2021; REZENDE et al., 2021), increased activity and stability (GRIMSEY et al., 2020; LI et al., 2021), and helicity and polarity modulation according to the saccharide (WU et al., 2020).

In terms of synthesis, although modified 9-Fluorenylmethyloxycarbonyl (Fmoc)-glucoamino acids usually have to be prepared in advance to be used in Fmoc-Solid Phase Peptide Synthesis (SPPS) — a significant hurdle to derivatization — glucopeptides furnish good therapeutic agents since saccharides are often present in biological membranes and corporal fluids, lowering the chances of resistance (RODRÍGUEZ et al., 2021). Additionally, studies show that glucopeptide antibiotics inhibit bacterial cell wall biosynthesis by binding to the ^{D}Ala-^{D}Ala unit of the peptidoglycan stem, blocking transpeptidase action and imposing a steric hindrance to transglucosylase action, lowering cell wall integrity (ACHARYA et al., 2022). An example of biological activity modulation stemming from saccharide insertion is the modification of the AMP HYL-14, a derivative of the peptide HYL, present in the venom of the solitary bee *Hylaeus signatus*. Incorporation of different saccharide units at distinct positions led to the modification of polarity and helical content, while improving stability and activity (WU et al., 2020).

In light of the numerous positive aspects that arginine and saccharide incorporation present and the published evidence of the benefits that stem from their insertion, the respective modifications of AMP sequences are of considerable interest and encompass part of the topics explored in this thesis.

1.2.3 Prevalence of antimicrobial peptide drugs

The Food and Drug Administration (FDA) has approved 239 peptide and protein therapeutics before 2020, 27 of which are small peptides with various applications and only nine are used to treat bacterial infections (CHEN; LU, 2020; DIJKSTEEL et al., 2021), namely Gramicidin D, Daptomycin, Teicoplanin, Colistin, Vancomycin, Oritavancin, Dalbavancin, Telavancin and Nisin (USMANI et al., 2017). Furthermore, FDA-approved antifungic peptides include Anidulafungin and Caspofungin, members of the echinocandin class (ULLIVARRI et al., 2020), and P-113, a histidine-rich peptide derived from the human salivary protein histatin 5 (CHENG et al., 2020). Analysis of the structures of these compounds reveals an apparent lack of small linear peptides, and the prime example of this class of therapeutics is Gramicidin D, composed of a mixture of ionophoric antibiotic peptides Gramicidin A, B, and C, containing a variety of D- and L-amino acid residues, and forming parallel, antiparallel or head-to-head dimeric helices.

Additionally, post-translational modifications such as glucosylation and lipidation are ubiquitous in the structure of these drugs, indicating their importance regarding the enhancement of biological properties. Therefore, considering that linear peptides comprised exclusively of proteinogenic amino acid residues and that display significant biological potential are underrepresented in the pharmaceutical industry, the modification of their structure by transformations such as glucosylation or PEGylation can provide important opportunities to place them in the spotlight.

Finally, the FDA approved eight peptide derivatives as new drugs in 2021 (SHAER et al., 2022) and none of them were for antimicrobial applications, even though it was the highest approval rate between 2016-2021. Also, analyzing the structure of these compounds, no linear peptides, wholly proteogenic or otherwise, were approved, suggesting the continuing need for research and development of this field of pharmaceutics.

Chapter 2 | Synthesis of Peptides and Peptide Derivatives

2.1 Introduction

2.1.1 Fmoc-SPPS

Merrifield gave the first report on SPPS in 1963 (MITCHELL, 2008; MERRIFIELD, 1963). The uniqueness of Merrifield's approach brought solutions to a conundrum of peptide synthesis in solution regarding laborious isolation, purification, and characterization procedures after each step. Since SPPS uses an insoluble polymer support, no recrystallization is required for reaction steps and solvent washings are sufficient.

Although polymer supports furnished speed and simplicity to SPPS, some negative aspects, like the difficulty in synthesizing long chains, were apparent. Long peptide chains are cumbersome since their solvation becomes difficult during their synthesis. Nevertheless, after the synthesis of bradykinin (MERRIFIELD, 1964), SPPS became ubiquitous, being the primary approach to current peptide synthesis. The main modification options of its conditions include different protecting groups, polymer supports, linkers, coupling reagents, removal conditions of the protecting groups, and cleavage conditions.

Protecting groups, polymers supports and linkers

The proper selection of protecting groups and polymer supports for SPPS is crucial for high reaction yields. Currently, the Fmoc protecting group (CARPINO; HAN, 1970; CARPINO; HAN, 1972), removable in alkaline solvents like piperidine and 4-methylpiperidine, is widely used, avoiding low yields that stemmed from acidic-mediated deprotection and cleavage. Another advantage of using Fmoc relates to orthogonal syntheses, or the sequential base-mediated removal of temporary protecting groups during the synthesis followed by a final acid-mediated cleavage of the permanent groups and of the peptide itself from the resin (**Figure 2.1**).

Polymer supports have two distinct characteristics: granulometry (measured in mesh)

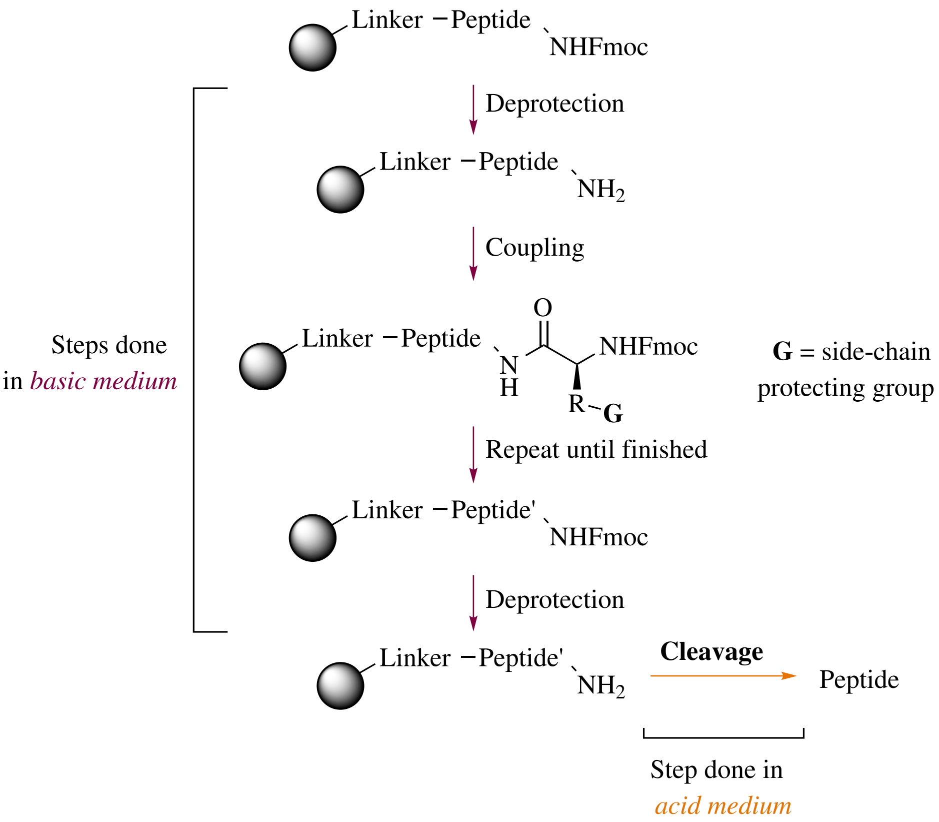

Figure 2.1: Fmoc-SPPS orthogonal synthesis representation, in which steps prior to cleavage are done in basic medium, followed by a final step of acid-mediated cleavage.

and resin loading capacity (measured in mmol.g^{-1}), the latter being the most important. Resin expansion, using solvents like CH_2Cl_2 or *N*,*N*-dimethylformamide (DMF), is crucial during SPPS. Furthermore, DMF, *N*-methylpyrrolidone (NMP), or *N*,*N*-dimethylacetamide (DMA) are commonly used for coupling steps as they provide optimal solvation. Additionally, alcohols (*i.e.*, isopropanol or methanol) can be used in washing steps, shrinking the resin beads and expelling unreacted substances (AMBLARD et al., 2006).

Finally, linkers connect the resin to the peptide and can be modified according to reaction and cleavage conditions. Most common linkers — Rink, Sieber, and Peptide Amide Linker (PAL) for peptide amides (**Figure 2.2, Page 41**) — are commercially available and already attached to resins with some amino protecting group, and most of them release the peptide upon Trifluoroacetic acid (TFA) treatment (SHELTON; JENSEN, 2013).

Coupling reagents

Amide/peptide bonds form the backbone of proteins and peptides, and their formation is the foremost synthetic step in SPPS. Direct condensation between a carboxylic acid and

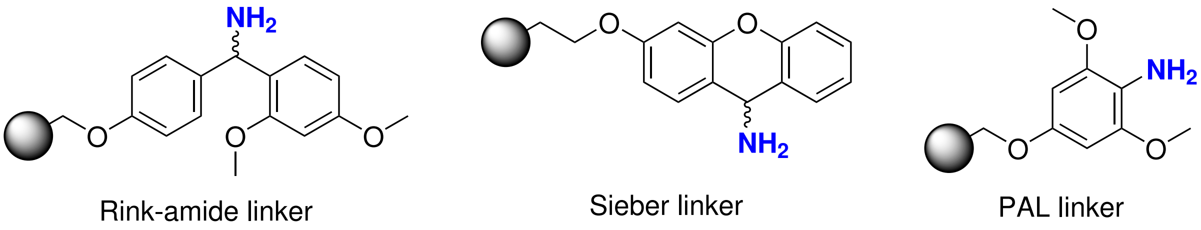

Rink-amide linker

Sieber linker

PAL linker

Figure 2.2: Representations of Rink-amide, Sieber and PAL linkers for peptide amides.

an amine to form an amide is difficult since the −COOH moiety swiftly protonates the amine, furnishing an ammonium ion prior to nucleophilic substitution. Coupling reagents are used in SPPS to form amide bonds and they are divided into four main types: carbodiimides, activated esters, phosphonium salts, and uronium/iminium salts, and further detail will be given regarding the first two.

Considering that each coupling must furnish high amounts of peptides and low amounts of side products, using efficient coupling agents is paramount to avoid alternate, yield-reducing reaction pathways. Examples of those include base-catalyzed isomerization or through the formation of 5(4*H*)-oxazolones (CARPINO, 1988; ANTONOVICS; YOUNG, 1967; GOODMAN; STUEBEN, 1962), of oxazolidine-2,5-diones (EL-FAHAM; ALBERICIO, 2011), diketopiperazines (WARD et al., 1997), and aspartimides (MERGLER et al., 2003a; MERGLER et al., 2003b; MERGLER; DICK, 2005).

The first widely used coupling reagents were carbodiimides, like *N*,*N*'-cyclohexylcarbodiimide (DCC), molecules with an *sp* carbon bound to two sp^2 nitrogens, being weakly basic and reacting with free carboxylic acids to form the *O*-acylisourea (**Figure 2.3**).

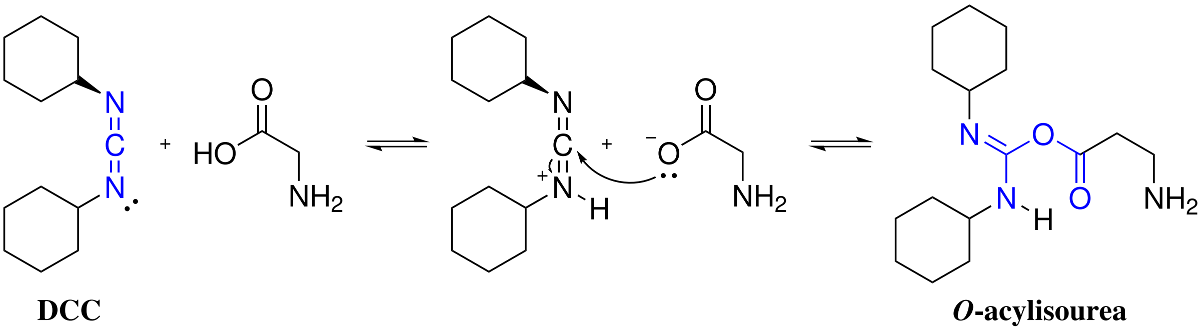

Figure 2.3: Reaction between DCC and glycine to form the corresponding *O*-acylisourea.

Even though DCC was the first carbodiimide reported in SPPS (SHEEHAN; HESS, 1955), it was gradually replaced by reagents like *N*,*N*-diisopropylcarbodiimide (DIC), *N*-ethyl-*N*'-(3-dimethylaminopropyl)carbodiimide (EDC) (SHEEHAN et al., 1961) and *N*-cyclohexyl-*N*'-isopropylcarbodiimide (CIC) (IZDEBSKI et al., 1999) (**Figure 2.4**).

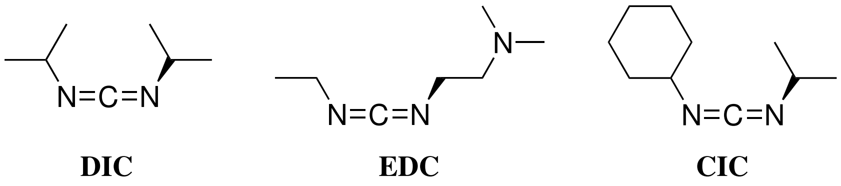

Figure 2.4: Structure representations of common carbodiimides.

Reaction pathways starting from *O*-acylisourea formation are numerous and, while most lead to the desired peptide, some generate undesired byproducts (**Figure 2.5**).

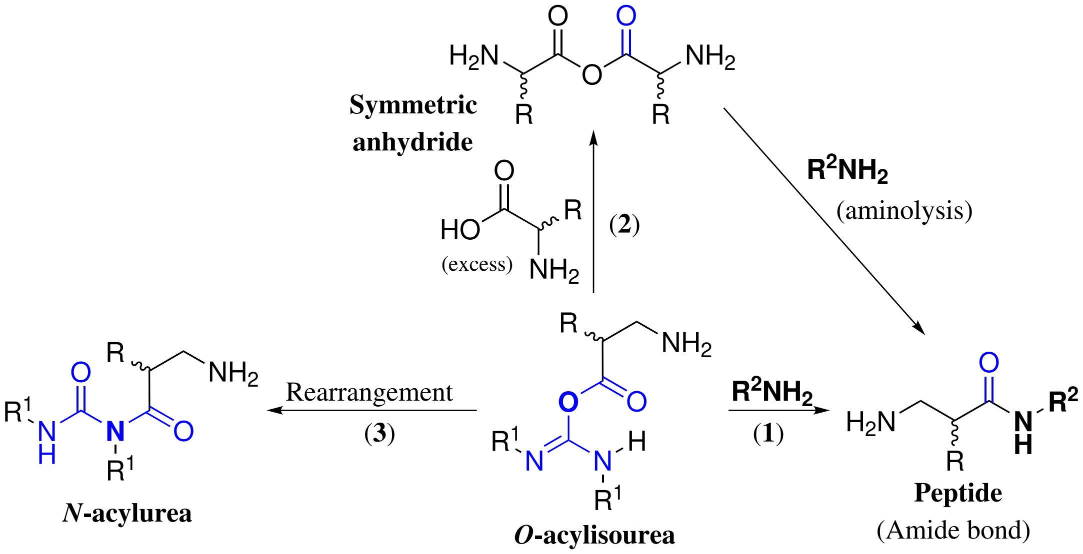

Figure 2.5: Reactions pathways from *O*-acylisourea.

From *O*-acylisourea, aminolysis yields the desired peptide (**Figure 2.5**, **1**). However, under amino acid excess, nucleophilic attack by a second acid molecule provides a symmetrical anhydride (**Figure 2.5**, **2**) prone to aminolysis (MONTALBETTI; FALQUE, 2005; RUBEK; FEITLER, 1973). An irreversible rearrangement can furnish the stable and inert *N*-acylurea (**Figure 2.5**, **3**), consuming the amino acid without forming any peptide (EL-FAHAM; ALBERICIO, 2011). The parallel use of phenol or *N*-hydroxyltriazole-based compounds (**Figure 2.6, Page 43**) as additives can overcome this problem (MONTALBETTI; FALQUE, 2005).

1-Hydroxybenzotriazole (HOBt) + DIC-mediated couplings are ubiquitous and similar to carbodiimide-only reactions. First, DIC undergoes nucleophilic addition by the amino acid, furnishing an amidine ester (**Figure 2.7**, **A**). Protonation and subsequent proton transfer generate an *O*-protonated amidine ester (**Figure 2.7**, **B**), which yields an *O*-(triazol-1-yl)-ester (**Figure 2.7**, **C**) and *N*,*N*'-diisopropylurea (DIU) after substitution with the alkoxide form of HOBt.

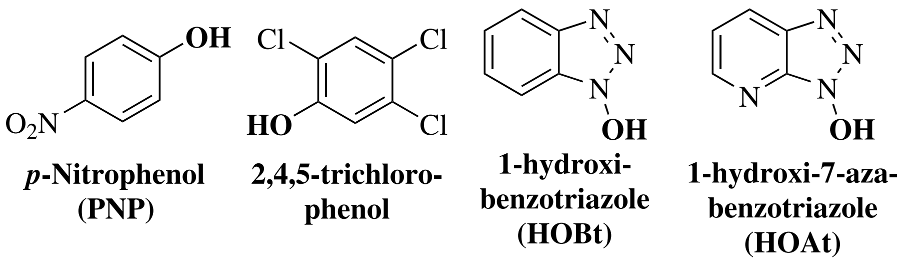

Figure 2.6: Structure of some phenol and N-hydroxyltriazole derivatives commonly used in SPPS in conjunction with carbodiimide to form activated esters.

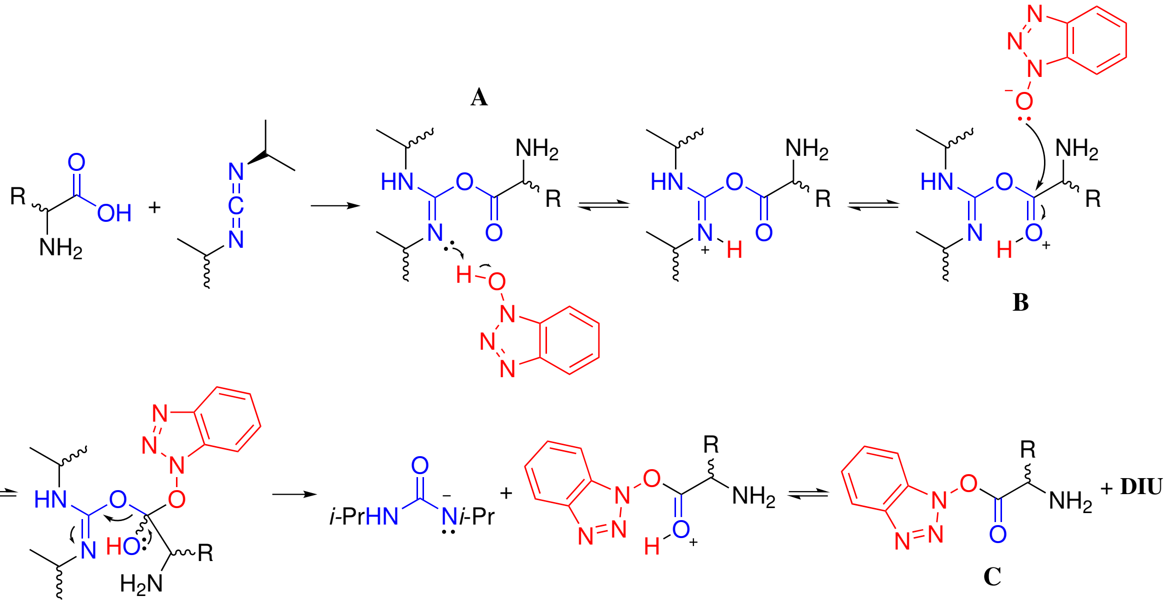

Figure 2.7: Activated ester formation mechanism with an amino acid, HOBt, and DIC.

Deprotection: Removal of the Fmoc group

One of the main steps of SPPS is the removal of the protecting groups. Additionally, Fmoc stability has been studied in the presence of different bases; and primary and some secondary amines, like piperidine and piperazine (FIELDS, 1995), are efficient in the removal of this group. Also, removal is faster in polar solvents — like DMF. A plausible explanation lies in the $E_{1c}B$ reaction mechanism (**Figure 2.8, Page 44**) (FIELDS; NOBLE, 1990).

The most acidic hydrogen of the Fmoc-protected amino acid (**Figure 2.8**, **A**) is abstracted by the piperidine-like molecule[1], furnishing an aromatic fluoren-9-ide (**Figure 2.8**, **B**) (PIRES et al., 2014). The free amino acid (**Figure 2.8**, **C**) and dibenzofulvene (DBV) (**Figure 2.8**, **D**) are then formed with evolution of CO_2. DBV is trapped by the

---

[1] Common pK_a values for these are 11.1 for piperidine, 10.78 for 4-methylpiperidine, and 9.73 for piperazine (LUNA et al., 2016).

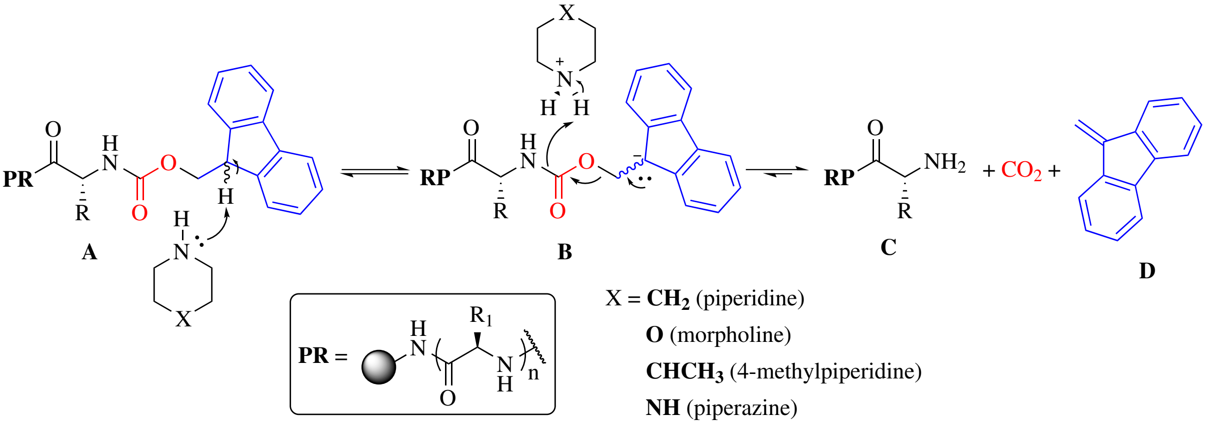

Figure 2.8: Proposed Fmoc removal reaction mechanism.

base, yielding a fulvene-piperidine adduct (**Figure 2.9**, **E**) (FIELDS; NOBLE, 1990).

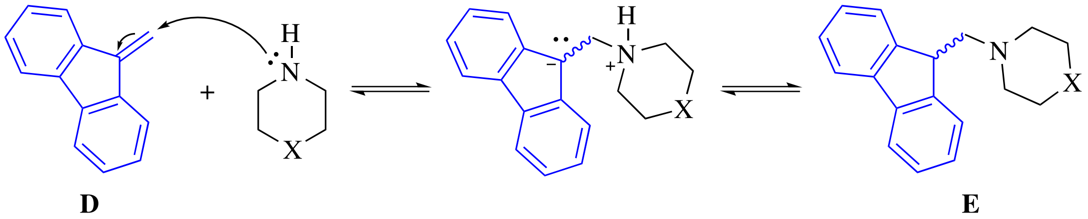

Figure 2.9: Proposed mechanism of the fulvene-piperidine adduct formation.

Reaction Monitoring: The Kaiser Test

The Kaiser test is a well-established method of amino acid identification during peptide synthesis (FRIEDMAN, 2004; MCCALDIN, 1960), using ninhydrin to produce Ruhemann's Purple (RP) in the presence of an amine (**Figure 2.10**).

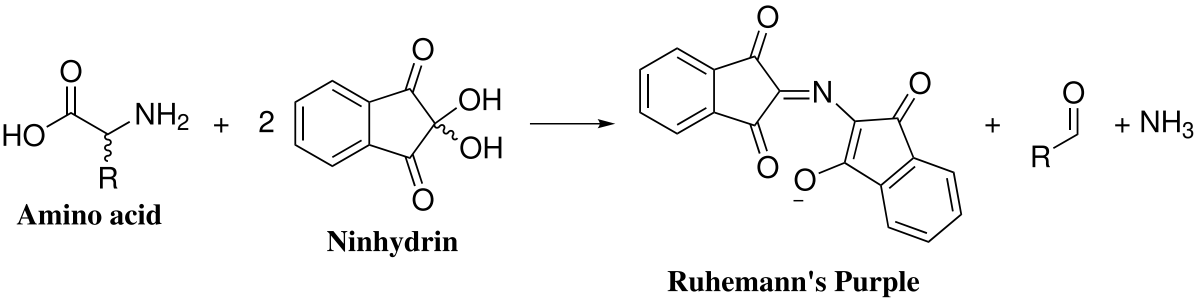

Figure 2.10: General scheme for the reaction of an amino acid and ninhydrin yielding RP, ammonia and the corresponding aldehyde.

The properties of ninhydrin in this reaction were reported by Ruhemann (RUHEMANN, 1910; WEST, 1965) when a mixture of ninhydrin and aqueous solutions of various amines was warmed and a blue hue was observed. Since then, many studies have been performed to enhance reaction yields, kinetics, and conditions.

Moore and Stein (MOORE; STEIN, 1948) developed a photometric determination method of amino acids. Troll and Cannan (TROLL; CANNAN, 1952) then devised an identification protocol using phenol and KCN. Finally, Kaiser (KAISER et al., 1970) applied those tests to SPPS and introduced a qualitative assay, using an apparatus and reagents similar to those shown in **Figure 2.11** (AMBLARD et al., 2006).

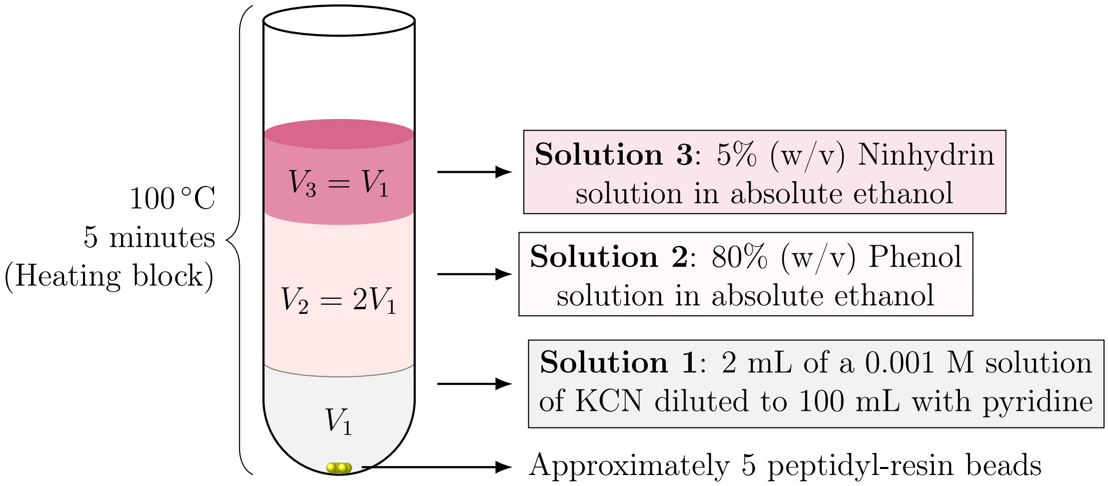

Figure 2.11: General apparatus and chemicals used in the Kaiser test.

Although the results of this test are reliable, some situations do not furnish predictable results. For example, some amino acids do not exhibit the typical deep blue color, such as cysteine (PROTA; PONSIGLIONE, 1973; WHITAKER, 1961), asparagine (SHENG et al., 1993), and proline (FRIEDMAN, 2004). Also, some degrees of peptide aggregation can hinder the efficiency of the assay.

Much work has been done on the reaction mechanism and how it unfolds. Nevertheless, a full discussion of it would be beyond the scope of this text and many papers (MACFAYDEN, 1950; MACFAYDEN; FOWLER, 1950; LAMOTHE; MCCORMICK, 1973; BOTTOM et al., 1978; ZIARIANI et al., 2015; SARIN et al., 1981), and reviews (MCCALDIN, 1960; FRIEDMAN, 2004) approach the subject in great detail.

Cleavage

The final step of SPPS consists of removing the peptide from the resin and linker. For Fmoc-based synthesis, cleavage is done in acidic conditions, *i.e.*, concentrated TFA (AMBLARD et al., 2006; LUNDT et al., 1978). Since TFA removes the residue, linker, and side-chain protecting groups altogether, their careful selection is paramount. **Figure 2.12** shows examples of side-chain protecting groups and some of them furnish cationic intermediates upon treatment with acid, which are susceptible to nucleophilic addition in the presence of amino groups (FIELDS; NOBLE, 1990). Scavengers, like ethanedithiol (EDT), *tris*isopropylsilane (TIS) and water (**Figure 2.13**) (PEARSON et al., 1989; KING et al., 1990) can be used in cleavage cocktails to counteract this high reactivity.

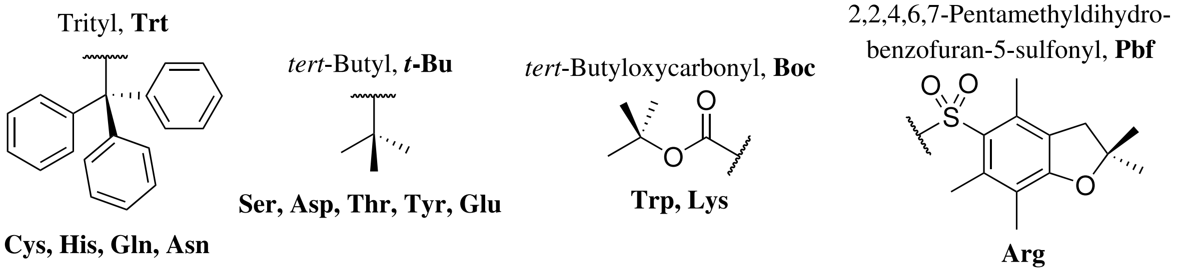

Figure 2.12: Some usual side chain protecting groups employed in SPPS presented along with the corresponding amino acids below each structure.

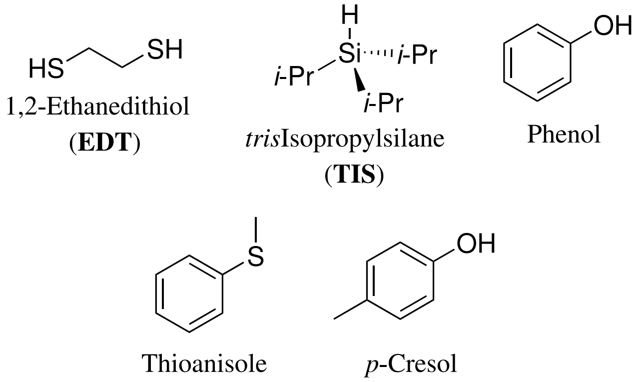

Figure 2.13: Structures of some organic carbocation scavengers used in SPPS.

Specifically, EDT is used when removing Methionine (Met) and Cysteine (Cys) due to the exacerbated nucleophilicity of their side-chains, containing $-SCH3$ and $-SH$, respectively. Specific groups and alternative cleavage solutions are discussed in further detail in the literature (PALLADINO; STETSENKO, 2012; BEHRENDT et al., 2016; LI et al., 2006; CARPINO et al., 1993; ISIDRO-LLOBET et al., 2009; RAMAGE et al., 1991).

2.1.2 The copper(I)-catalyzed azide-alkyne cycloaddition

Reaction discovery and developments

The formation of a triazole ring by reacting an azide with an alkyne is known since 1893, when Arthur Michael first reported the synthesis of 1-phenyl-4,5-dicarbometoxi-1*H*-1,2,3-triazole from phenyl azide and dimethyl acetylenedicarboxilate (**Figure 2.14, Page 47**) (MICHAEL, 1893).

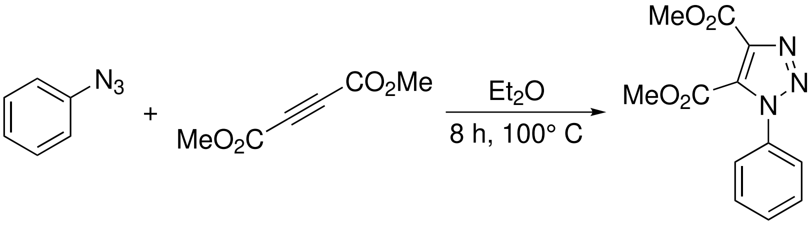

Figure 2.14: Reaction between phenyl azide and dimethyl acetylenedicarboxilate.

Huisgen was the first to investigate the large reaction scope in the 1960s in an extensive study, outlining many reaction conditions (HUISGEN, 1963). The need for high reaction temperatures and the lack of regioselectivity, yielding mixtures of 1,4 and 1,5-disubstituted triazoles (LIANG; ASTRUC, 2011), were the main disadvantages. Both were circumvented when the use of copper as a catalyst in a reaction between propargyl alcohols and azides was reported by L'Abbé (L'ABBÉ, 1984) but, afterward, the reaction received low notoriety. The groups of Meldal (TORNØE et al., 2002) and Sharpless/Fokin (ROSTOVTSEV et al., 2002) then reported, independently, the regioselective copper(I) catalytic reaction between terminal alkyne and azide functional groups, yielding 1,4-disubstituted-1,2,3-triazole as the sole product. This reaction was then known as the Copper(I)-catalyzed Azide Alkyne Cycloaddition (CuAAC) and viewed as one of the prime examples of "click" chemistry (AMBLARD et al., 2009).

Mechanistic aspects

The mechanism has been a point of contention for some time, with the possibility of a concerted $[4 + 2]$ addition being discarded since the beginning, based on computational calculations (HIMO et al., 2005). A stepwise mechanism was proposed instead, which was accurate and a good starting point for the following hypotheses (EL AYOUCHIA et al., 2018) (**Figure 2.15 Page 48**).

The cycle begins with the formation of a copper(I) acetylide[2] (**Figure 2.15, Page 48**, Step **A**) that undergoes ligand exchange with the azide (**Figure 2.15**, Step **B**). The crucial step is the formation of a six-membered metallacycle (**Figure 2.15**, Step **C**), formed by nucleophilic attack of the distal nitrogen atom onto the inner acetylenic carbon (HIMO et al., 2005; RODIONOV et al., 2005). A ring contraction (**Figure 2.15**, Step **D**) yields a copper-triazole intermediate, which is protonated (**Figure 2.15**, Step **E**) and furnishes the triazole.

Although the cycle shows a copper(I) species, copper(II) species in the presence of a

---

[2] The formation of a acetylene-Cu complex lowers the pK_a of the acetylenic proton by 9.8 units. In this context, when using propyne (pK_a *ca.* 25), the feasibility of an aqueous CuAAC reaction in the absence of bases is trivial (HIMO et al., 2005).

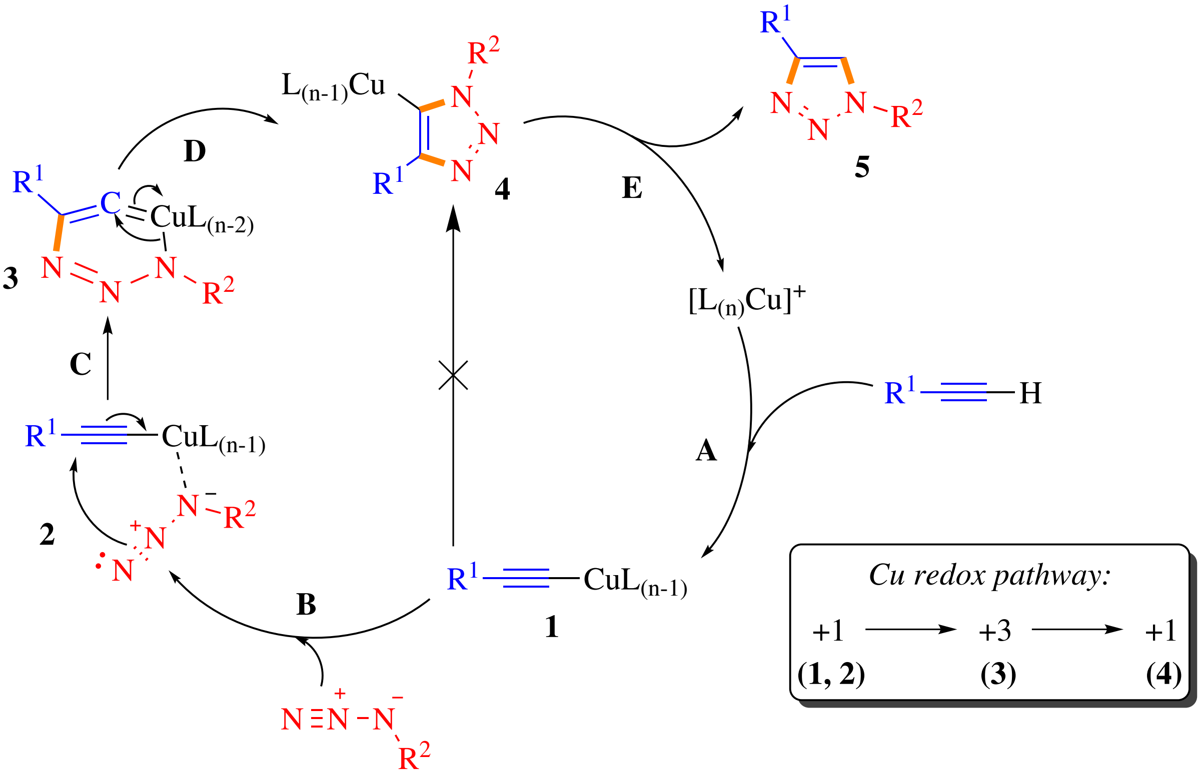

Figure 2.15: CuAAC mechanism as proposed by Rostovtsev and colaborators, with relevant functions colored. The copper oxidation states and their changes are indicated in the box (lower right corner).

reducing agent like sodium ascorbate are commonly used, providing optimal concentrations of Cu(I) in the reaction medium, since a large ion concentration favors acetylide aggregation, slowing down the reaction (HEIN; FOKIN, 2010). However, other systems like organometallic complexes and nanocatalysts have been developed (HALDÓN et al., 2015; LIANG; ASTRUC, 2011), and ruthenium-based catalysts are used to favor 1,5-substitution (RAMASAMY et al., 2018). Although outdated, this mechanism defined important concepts, such as how the copper(I) interacts with the alkyne and the azide — σ-bond with the former and coordination through the alkylated nitrogen with the latter. Also, the theory accounts for and explains the 1,4-substitution pattern (ZHU et al., 2016).

Following computational and kinetic studies (ZHU et al., 2016) indicated that an additional copper ion would aid in the formation and stabilization of the 6-membered metallacycle by alleviating ring strain. Soon after, *bis*(copper) intermediates were detected (JIN et al., 2015; WORELL et al., 2013; IACOBUCCI et al., 2015), and the dinuclear intermediate was inferred to be kinetically favored. Hence, the most recent catalytic cycle is depicted in **Figure 2.16**. Initially, a σ,π-dinuclear copper acetylide is formed (Step **A**) (JIN et al., 2015). The intermediate is then trapped by the azide to form a ternary complex (Step **B**) (IACOBUCCI et al., 2015; ÖZKILIÇ; TÜZÜN, 2016), undergoing rearrangement to form the six-membered metallacycle (Step **C**) with concomitant oxidation of copper(I) to copper(III). The metallacycle is considerably less strained by the presence of a second copper atom (ZHU et al., 2016). A reductive ring contraction (Step **D**) yields a cupric triazolide, which is protonated by the alkyne (Step **E**), releasing the 1,2,3-triazole product and regenerating the cycle.

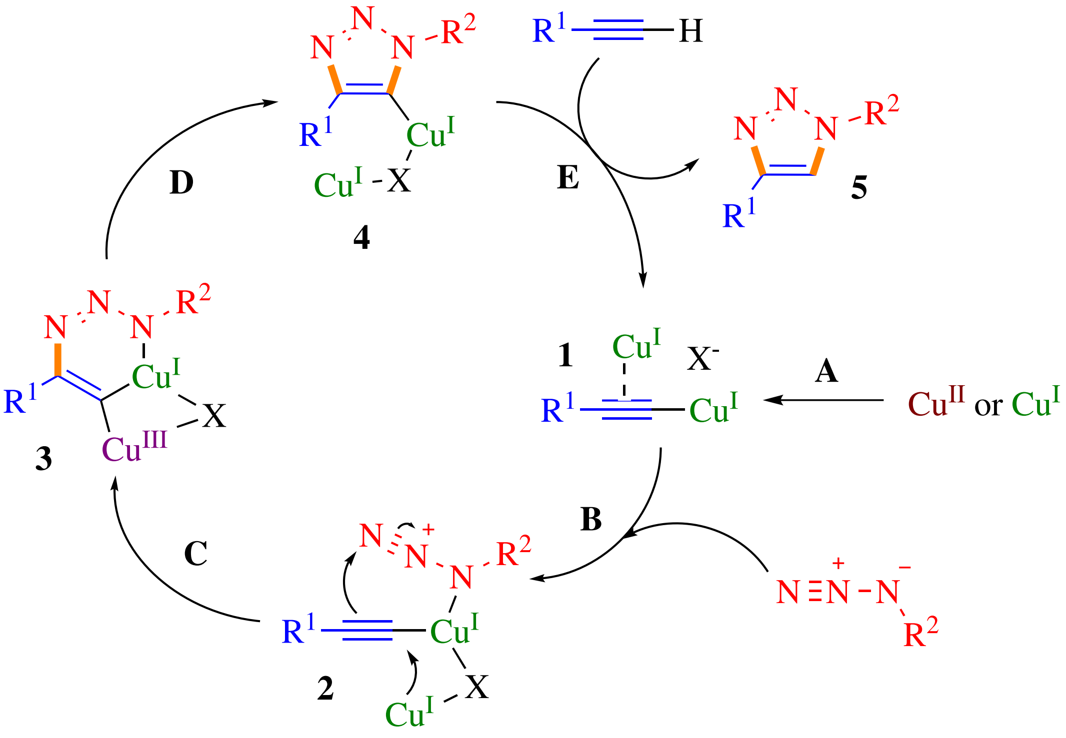

Figure 2.16: Current mechanistic representation of the CuAAC reaction via formation a dinuclear copper acetylide (adapted from (ZHU et al., 2016)).

Differences in this proposed pathway comprise the stabilization of the dinuclear acetylide by the counterion X^-, which happens throughout the cycle. It also contributes to the formation of a more stable metallacycle. Furthermore, it combines the majority of current experimental evidence, even though some intermediates are difficult to detect, such as the ternary complex and the six-membered metallacycle (ZHU et al., 2016).

Glucosylation: Applications in peptide chemistry

The CuAAC has been used in peptide chemistry and organic synthesis for many applications, such as isotopic labeling for medicinal purposes (LIANG; ASTRUC, 2011), synthesis of dendrimers (LIANG; ASTRUC, 2011), nucleoside chemistry (AMBLARD et al., 2009), and peptide dimerization/cyclization (HEDHLI et al., 2017; LIU et al., 2017; CHOW et al., 2019). Nevertheless, post-translational modifications, *i.e.*, changes made to the primary structure after it is synthesized, are the main focus of this work. In particular, emphasis is given to glucosylation, its advantages related to carbohydrates, and the contributions of the CuAAC for it.

Glucosylation is known for increasing the biological activity of AMPs and, currently, vancomycin and telavancin are examples of some glucopeptide antibiotics (GPAs) that are available as commercial drugs (**Figure 2.17**) (BUTLER et al., 2014).

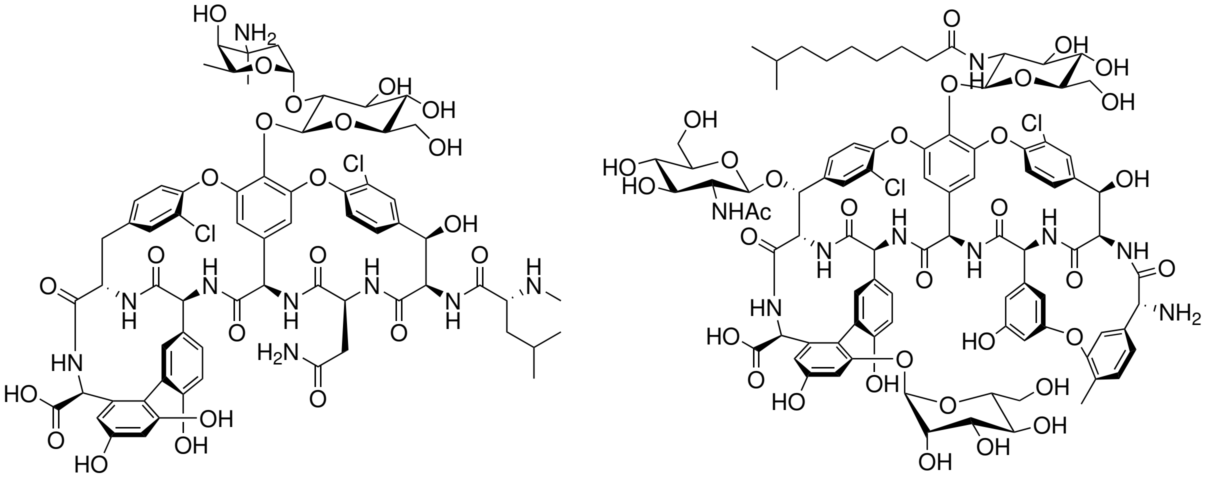

Vancomycin Telavancin

Figure 2.17: Structures of glucopeptide antibiotics vancomycin and telavancin.

Most commercial GPAs have unique tricyclic or tetracyclic heptapeptide cores and are modified by glucosylation, halogenation, oxygenation, and other strategies like lipid chain insertion (BINDA et al., 2014). The insertion of a saccharide into a polypeptide chain can enhance biological properties of peptides and circumvent known hurdles, like poor oral bioavailability due to variable pH conditions throughout the body and the presence of proteases and physical barriers. Also, by improving membrane penetration, increasing metabolic stability, and protecting side-chains from oxidation, carbohydrates represent promising moieties to be incorporated in AMPs (MORADY et al., 2016; BEDNARSKA et al., 2017).

The *O*-, *N*-, *C*, and *S*-linked glucosylations are ubiquitous strategies (ZHANG; KNAPP, 2018) and, in this thesis, carbohydrates were linked to the peptides by *N*-linked glucosylations, done by CuAAC. Although the synthesis of triazolepeptides is well known (TORNØE et al., 2002), the tandem glucotriazole variant was first reported in 2007 (WANG et al., 2007). Furthermore, only one result is shown when searching for "glycotriazole peptide" in the search engine `webofknowledge.com` (Web of Science), whereas no results are shown by searching "glucotriazole peptide".

In the past few years, our group has been working on this subject with the intent of improving the biological activity of certain antimicrobial peptides. For instance, the AMP HSP1 (Hylaseptin-1) was submitted to a "click" reaction with 1-azido-glucose and

1-azido-per-*O*-Ac-*N*-acetylglucosamine (JUNIOR et al., 2017). This strategy was also recently used to obtain alumina nanoparticles decorated with peptides (TORRES et al., 2019). This thesis intends to expand the use of this strategy by investigating the synthesis and membrane interactions of glucotriazole-peptides derived from the AMP **PS-O1**.

2.2 Methodology

2.2.1 Peptide Synthesis by Fmoc-SPPS

Peptides phylloseptin-O1 (**PS-O1**), R1G2-phylloseptin-O1 (**R1G2-PS-O1**), and their respective propargylic derivatives **[Pra^1]PS-O1** and **R1Pra2-PS-O1** were synthesized using the Fmoc-SPPS approach, following a modified procedure (AMBLARD et al., 2006; CHAN; WHITE, 2000). The respective primary structures and number of amino acid residues are shown in **Table 2.1**.

Table 2.1: Primary structures and number of residues of the peptides synthesized in this work.

Peptide	Primary structure	Number of Residues
PS-O1	FLSLI PHAIN AVSTL VHHSG–NH_2	20
R1G2-PS-O1	RGFLS LIPHA INAVS TLVHH SG–NH_2	22
[Pra^1]PS-O1	**Pra**FLSL IPHAI NAVST LVHHS G–NH_2	21
R1Pra2-PS-O1	R**Pra**FLS LIPHA INAVS TLVHH SG–NH_2	22

Considering **PS-O1** for mass and molar amounts, a final mass of 0.2 g ($0.947.10^{-4}$ mol, 2112.47 g.mol^{-1}) was planned. Accordingly, 0.237 g of a 0.40 mmol.g^{-1}, 100-200 mesh Fmoc-Rink Amide resin (Iris Biotech GmbH®) was transferred to a 10 mL polypropylene oral syringe coupled to a polyurethane filter (**Figure 2.18, Page 51**).

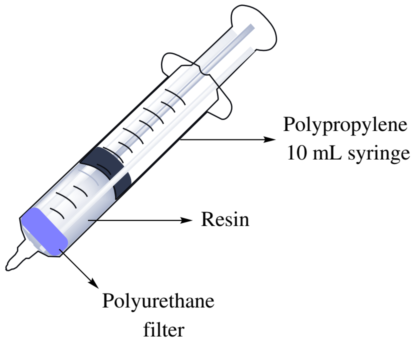

Figure 2.18: Representation of the syringe system used for Fmoc-SPPS in this work.

Resin expansion was then performed for one hour using 3 mL of Dichloromethane (DCM), followed by Fmoc deprotection, using 2 mL of a 20% (v/v) 4-methylpiperidine in DMF solution during two 12-minute-cycles[3]. Stirring was done using a Vortex-type shaker at 450 rpm. Afterwards, an eight-step washing was performed, alternating between 3 mL of DMF and Isopropanol (IPA), three times each, followed by a double 3 mL DCM wash.

Reaction completion was verified by the Kaiser test. About five resin beads were transferred from the syringe to an assay tube, followed by the application of one drop of a 2% (v/v) 0.001 M solution of KCN in pyridine, followed by two drops of an 80% (w/v) phenol solution in absolute ethanol and, finally, one drop of a 5% (w/v) ninhydrin solution in absolute ethanol. The tube was then heated to 100 °C in a heating block for five minutes. When three or more negative Kaiser test results were observed for a single amino acid coupling, chaotropic agents like Triton-X100™ were used (SALVI et al., 2005; MOELBERT et al., 2004). Also, co-solvents such as dimethylsulfoxide (DMSO) were occasionally used (PARADÍS-BAS et al., 2016).

Notably, Kaiser tests during deprotections yielded different colors for different amino acid residues. The test's macroscopic evidence is color, and colored resin beads correlate to the presence of free amino groups, whereas transparent ones indicate their absence. The general adopted guidelines are summarized in **Table 2.2**.

Table 2.2: Possible results for the Kaiser test after deprotection and coupling steps, bead colors and recommended actions.

Synthetic step	Expected bead color	Next action
Effective deprotection	Dark (variable color)	Coupling
Effective coupling	Transparent	Deprotection
Ineffective deprotection	20% or more transparent beads	Repeat deprotection
Ineffective coupling	20% or more dark beads	Repeat coupling

After deprotection, the system was submitted to a coupling reaction with appropriate amounts of DIC (Sigma-Aldrich®), HOBt (Iris Biotech GmbH®), and the respective amino acid (all at a 4:1 molar ratio respective to the peptide) in a DMF (dry):DCM 2:1 solution for three hours. In the synthesis of propargylic derivatives, Fmoc-propargylglycine was used at a 1:1 molar ratio. The syringe content was then washed, alternating between 3 mL of DMF and IPA, three times each, followed by a double 3 mL DCM wash, and another Kaiser test was performed, yielding transparent resin beads (**Table 2.2**).

---

[3] A 0.1 mol.L^{-1} solution of HOBt in 20% (v/v) 4-methylpiperidine/DMF was used instead after an Asparagine (Asn) or aspartate (Asp) residue was coupled to the sequence.

The [deprotection → wash → Kaiser test → coupling → wash → Kaiser test] cycle was performed for every amino acid until the primary structure was completed. For glucotriazole peptides, the CuAAC reaction was done after the last amino acid was coupled.

The standard peptide cleavage procedure was followed (CHAN; WHITE, 2000; AMBLARD et al., 2006). First, Fmoc deprotection was performed, followed by the addition of a TFA:H_2O:TIS 95:2.5:2.5 (v:v:v) solution (both solvents were purchased from Sigma-Aldrich®). A 10 mL liquid:1 g of peptidyl-resin relation was adopted. The reaction mixture was stirred for three hours in a Vortex shaker (450 rpm), and its contents were then transferred to a Falcon®-type centrifuge tube. A light N_2 flow removed TFA excess, and cold diisopropyl ether ($(i\text{-Pr})_2O$) (Vetec®) addition enforced further precipitation. Then, centrifugation was done in an eppendorf® Centrifuge 5430 after each $(i\text{-Pr})_2O$ addition, which was then discarded. The cycles of ether addition, centrifugation, and liquid phase removal were performed four times, using 4-minute-cycles at 5000 rpm for each. Ultrapure water was then added and the crude peptide was lyophilized in a 5 L Thermo ModulyoD® freeze dryer coupled to a Vacuubrand® RZ 9 vacuum pump for 48 hours.

2.2.2 CuAAC Reaction

A general scheme of the CuAAC reaction is depicted in **Figure 2.19**.

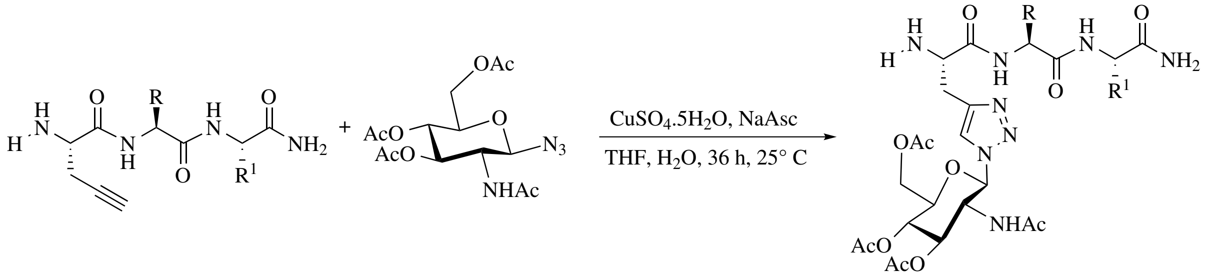

Figure 2.19: General scheme of the CuAAC reaction employed in this work.

[p*O*AcGlcNAc-trz-A^1]PS-O1 (**PS-O1 GtP**) and R1[p*O*AcGlcNAc-trz-A^2]PS-O1 (**R1-A2-PS-O1 GtP**) were synthesized using the respective alkyne-decorated peptidyl-resin precursors via a CuAAC reaction prior to cleavage using 1-azido-per-*O*-Ac-*N*-acetylglucosamine as a reactant, provided by Prof. Ricardo José Alves (Faculdade de Farmácia - UFMG) and synthesized according to Franco (FRANCO, 2015).

For the "click" reaction (JUNIOR et al., 2017), 5 mL of DCM were pulled into the syringe, and it was stirred for 30 minutes using a Vortex shaker. Then, considering 0.15 g ($0.6795.10^{-5}$ mol, 2207.57 g.mol^{-1}) of **PS-O1 GtP**, 0.0608 g ($1.6308.10^{-5}$ mol, 2.4 eq.) of 1-azido-per-*O*-Ac-*N*-acetylglucosamine, 0.00848 g ($0.3398.10^{-5}$ mol, 0.5 eq.) of copper(II) sulfate pentahydrate, and 0.0081 g ($0.4077.10^{-5}$ mol, 0.6 eq.) of Sodium ascorbate

(NaAsc) were weighted in separate flasks. Each solid was then dissolved with minimal amounts of the appropriate solvent (water for both salts and tetrahydrofuran (THF) for the saccharide). Finally, the sugar, copper(II) sulfate, and NaAsc were suctioned, in this order. The system was then stirred for 36 h in a Vortex shaker (450 rpm). Reaction conditions are summarized in **Table 2.3**.

Table 2.3: Summarized conditions used in all CuAAC reactions of this work.

Reagent	**Proportion (molar equivalent)**	**Solvent**	**Reaction time (h)**
1-N3-per-*O*-Ac-NHAcGlu (**A**)	2.4	THF	36
$CuSO_4 \cdot 5\,H_2O$ (**B**)	0.5	H_2O	
NaAsc (**C**)	0.6	H_2O	

After the reaction was completed, the glucotriazole-peptidyl-resin was washed twice with a 10% ethylenediamine tetraacetic acid (EDTA), 25% NaOH (w/v) solution in ultrapure water — a 5% EDTA solution in NH_4OH was a viable substitute — and then alternating between 3 mL of DMF and IPA, three times each, followed by a double 3 mL DCM wash. After workup, the glucotriazole-peptidyl-resin beads acquired a characteristic dark blue color that was observed for every reaction.

Although typical CuAAC procedures in solution consume less reagents and furnish better results, the preferred approach in this thesis was to perform this reaction during SPPS prior to cleavage since the employed TFA could hydrate the unprotected acetylenic moiety of the propargyl-glycine residue, potentially furnishing enolic derivatives which do not react in a pericyclic fashion with azides.

2.2.3 MALDI-ToF-MS Analyses

Products were primarily analyzed by Matrix-Assisted Laser Desorption/Ionization - Time-of-Flight Mass Spectrometry (MALDI-ToF-MS), using a Bruker Daltonics® Autoflex III smartbeam spectrometer (Hamburg, Germany) of Centro de Laboratórios Multiusuários (CELAM), at the Instituto de Ciências Biológicas (ICB) of Universidade Federal de Minas Gerais (UFMG). Samples were placed in a Bruker Daltonics® MTP Anchorchip 384 BC (Hamburg, Germany), mixed with a saturated 2,5-diHydroxibenzoic acid (DHB) or α-cyano-4-hydroxycinnamic acid (CHCA) solution for peptides or arginine-peptides, respectively, and dried at room temperature. Samples were then analyzed in the spectrometer using the Pepmix method. Mass spectra were susbequently acquired in positive mode following calibration, and ultimately analyzed using the mMass Data Miner software (STROHALM et al., 2008).

2.2.4 RP-HPLC Purification

Purification was done by Reverse-Phase High Performance Liquid Chromatography (RP-HPLC) in a Shimadzu® CBM-20A, using an Agilent® ZORBAX Pursuit C18 column (250 × 10 mm, 5 µm) for semi-preparative runs and a Macherey-Nagel® Nucleodur (250 × 4 mm, 5 µm) for analytical runs, both equilibrated with 7.8 parts of a 0.1% aqueous TFA solution (phase A) and 2.2 parts of a 0.08% (v/v) TFA/Acetonitrile (ACN) solution (phase B). Flow was set to 1.0 $mL.min^{-1}$ for analytical runs and 2.0 $mL.min^{-1}$ for semi-preparative runs. Detection was done using a Shimadzu® Photodiode Array SPD-M30A at 220 nm.

Analytical runs of the peptides were done using stock solutions at 1 $mg.mL^{-1}$, an elution gradient of 17 minutes, 20 µL injection volume, an eluent flow of 1.0 $mL.min^{-1}$ and the solvent gradient shown in **Figure 2.20**.

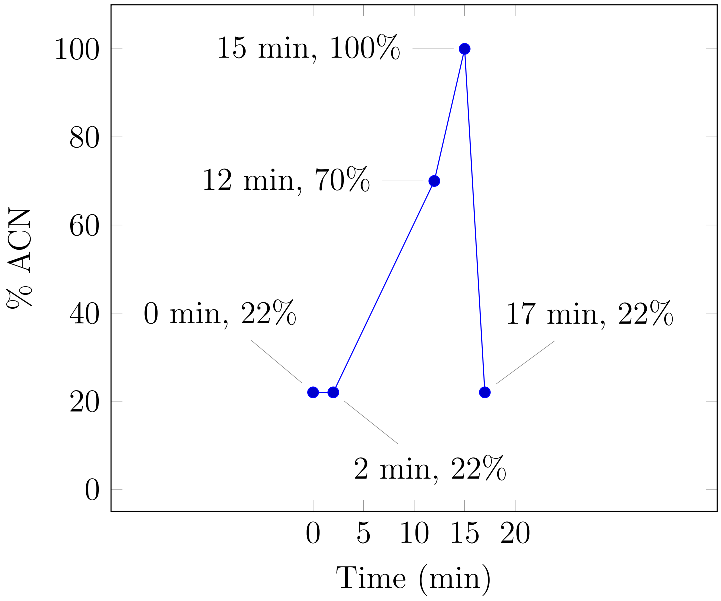

Figure 2.20: Optimized gradient conditions used in the RP-HPLC analytical runs.

Semi-preparative runs were done using stock solutions at 2 $mg.mL^{-1}$, an elution gradient of 36 minutes, 1.3 mL injection volume, an eluent flow of 2.0 $mL.min^{-1}$ and the solvent gradient shown in **Figure 2.21, Page 56**. Samples were automatically collected.

2.3 Results and Discussion

2.3.1 Peptide Synthesis by Fmoc-SPPS

The peptides synthesized by Fmoc-SPPS (**Table 2.1, Page 51**) generaylly did not show unusual events during coupling steps. Specifically, one coupling reaction needed to

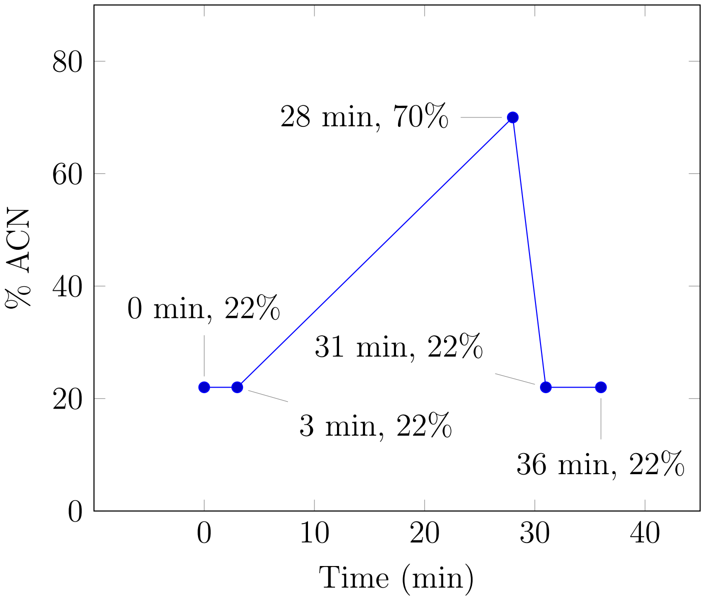

Figure 2.21: Optimized gradient conditions used in the RP-HPLC purification of the synthesized peptides.

occasionally be redone, which was for the Proline (Pro)-adjacent Isoleucine (Ile) residue (Ile-5 for **PS-O1**). This hindrance was not surprising since sterically demanding residues like Ile can hinder coupling, especially at later stages of Fmoc-SPPS. Nevertheless, the addition of Triton-X100™ was enough to circumvent this issue.

As mentioned in **Section 2.2.1, Page 51**, the Kaiser test was the chosen avenue of reaction verification. It was also mentioned that the presence of free amino groups yields colored resin beads and that transparent ones indicate their absence (**Figure 2.22**).

Figure 2.22: Kaiser-test-submitted resin beads color patterns, indicating presence (left) or absence (right) of free amino groups.

Finally, all synthesized peptides precipitated during N_2-promoted TFA evaporation in the form of small, light-reflective particles with a crystalline aspect, even though the peptides were obtained, ultimately, as pale solids.

2.3.2 CuAAC Reaction

Upon the stepwise addition of each reagent specified in **Table 2.3, Page 54**, a particular visual response was noticed. A pale yellow coloration was noticed after saccharide addition. The suction of the copper salt changed the solution color to a slight blue hue, and the subsequent addition of NaAsc immediately furnished a brown tone, which was slowly transformed to a dark blue hue as the reagents mixed. After 24 hours, the reaction showed no color change, which persisted up to the 36-hour mark.

This pattern has been described in the literature (BERG; STRAUB, 2013; HEIN; FOKIN, 2010; SEMENOV et al., 2018; BAE et al., 2005; OWSLEY; CASTRO, 1972) and is correlated to the catalytic cycle steps shown in **Figure 2.16, Page 49**. The pale yellow color is attributed to a transient copper(I) acetylide complex formed in the first catalytic step, which is gradually consumed; additionally, the formation of Cu(II) triazole complexes is attributed to the dark blue tone seen during the reaction.

2.3.3 MALDI-ToF-MS Analyses

The peptide and glucotriazole-peptide derivatives were obtained successfully without major problems. The expected m/z of each compound, their experimental m/z values, and the respective relative errors (*r.e.*) are summarized in **Table 2.4**.

Table 2.4: Theoretical and experimental m/z values of each product with respective relative errors (*r.e.*).

Peptide	**Theoretical m/z**	**Experimental m/z**	**Relative error (*r.e.*)**
PS-O1	2112.17 (100%)	2113.04 (100%)	0.0411%
R1G2-PS-O1	2325.29 (100%)	2325.51 (100%)	0.0001%
PS-O1 GtP	2579.33 (100%)	2578.84 (100%)	0.0002%
R1A2-PS-O1 GtP	2735.43 (100%)	2736.42 (100%)	0.0362%

The small relative errors shown in **Table 2.4** between theoretical and experimental m/z values indicate that all peptides were synthesized appropriatelly.

The MALDI-ToF-MS spectra of all synthesized peptides are shown in **Figure 2.23** and two major peaks can be seen in the spectra of **R1A2-PS-O1 GtP** (**Figure 2.23, D**), one corresponding to the theoretical m/z of **R1A2-PS-O1 GtP** (2736.42) while the other has a $\Delta(m/z) = 113.11$. This difference probably corresponds to a Leucine (Leu) residue, which has a molar mass of 113.19 g.mol^{-1} when considering elimination of a water molecule after coupling. In fact, Leu-19 needed to be recoupled, and an erroneous prior deprotection step could have introduced an additional residue.

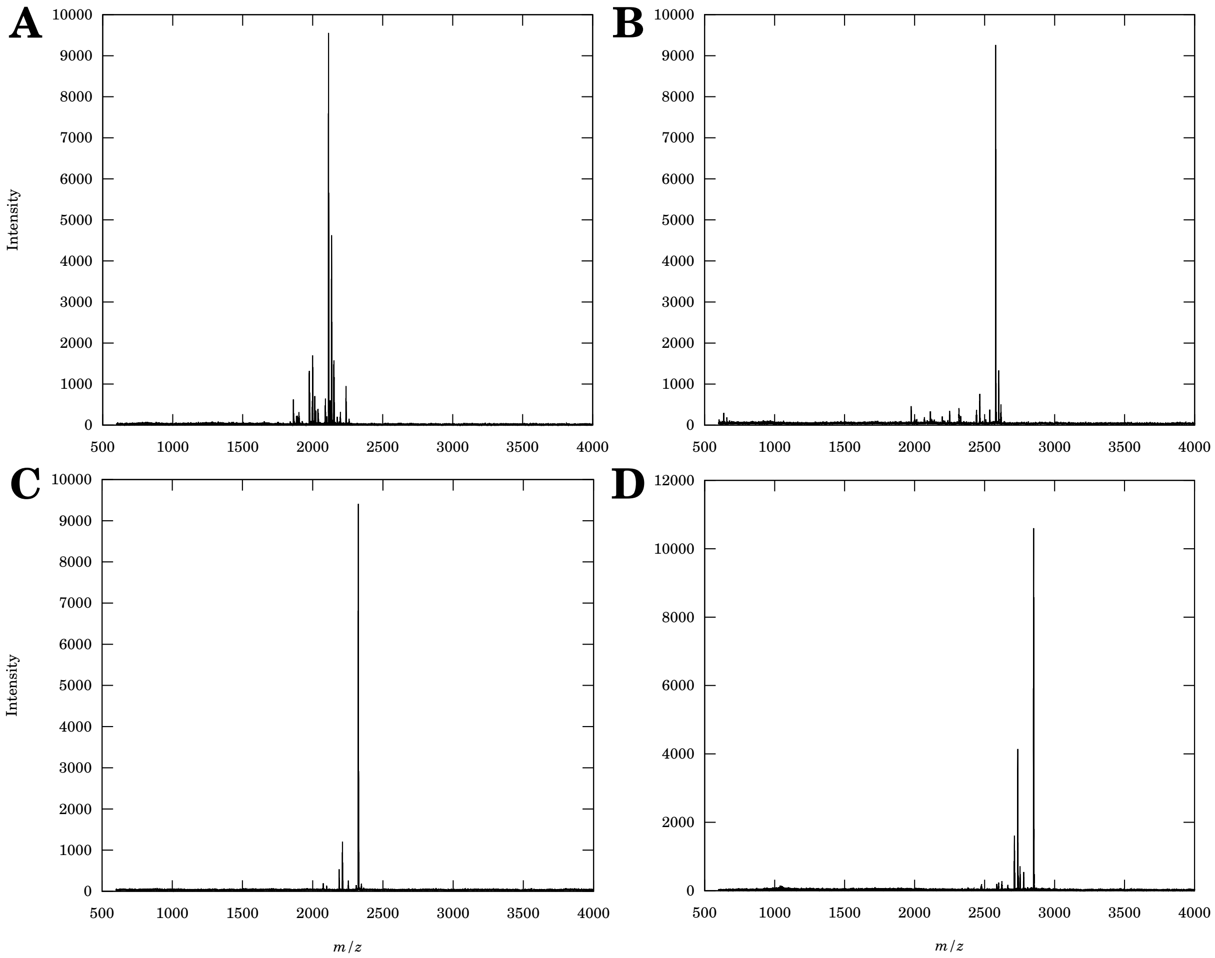

Figure 2.23: Mass spectra of (**A**) **PS-O1**, in DHB, (**B**) **PS-O1 GtP**, in DHB, (**C**) **R1G2-PS-O1**, in CHCA, and (**D**) **R1A2-PS-O1 GtP**, in CHCA. The $[M+H]^+$ molecular ions were detected at, 2113.04, 2325.51, 2578.84, and 2736.42, respectively (the corresponding theoretical m/z values are 2112.17, 2325.29, 2579.33, 2735.43).

2.3.4 RP-HPLC Purification

All semi-preparative RP-HPLC chromatograms were similar, since there was a prominent band corresponding to the desired product with a larger area and height compared to other bands (**Figure 2.24**). The crude peptides had similar retention times to other compounds that were not of interest, which did not hinder the purification collection was automatic. Another contribution to the reproducibility of the purification was the column oven that maintained the temperature at 25 °C. The purification of **R1A2-PS-O1 GtP** was unique since, as alluded to in **Section 2.3.3, Page 57**, there were two major bands in the chromatogram (**Figure 2.24, D**) with retention times equal to 23.95 and 28.43 min, respectively. MALDI-ToF-MS analyses showed that the first band was related to **PS-O1 ΔRA GtP** while the second corresponded to the peptide derivative with an extra Leu residue.

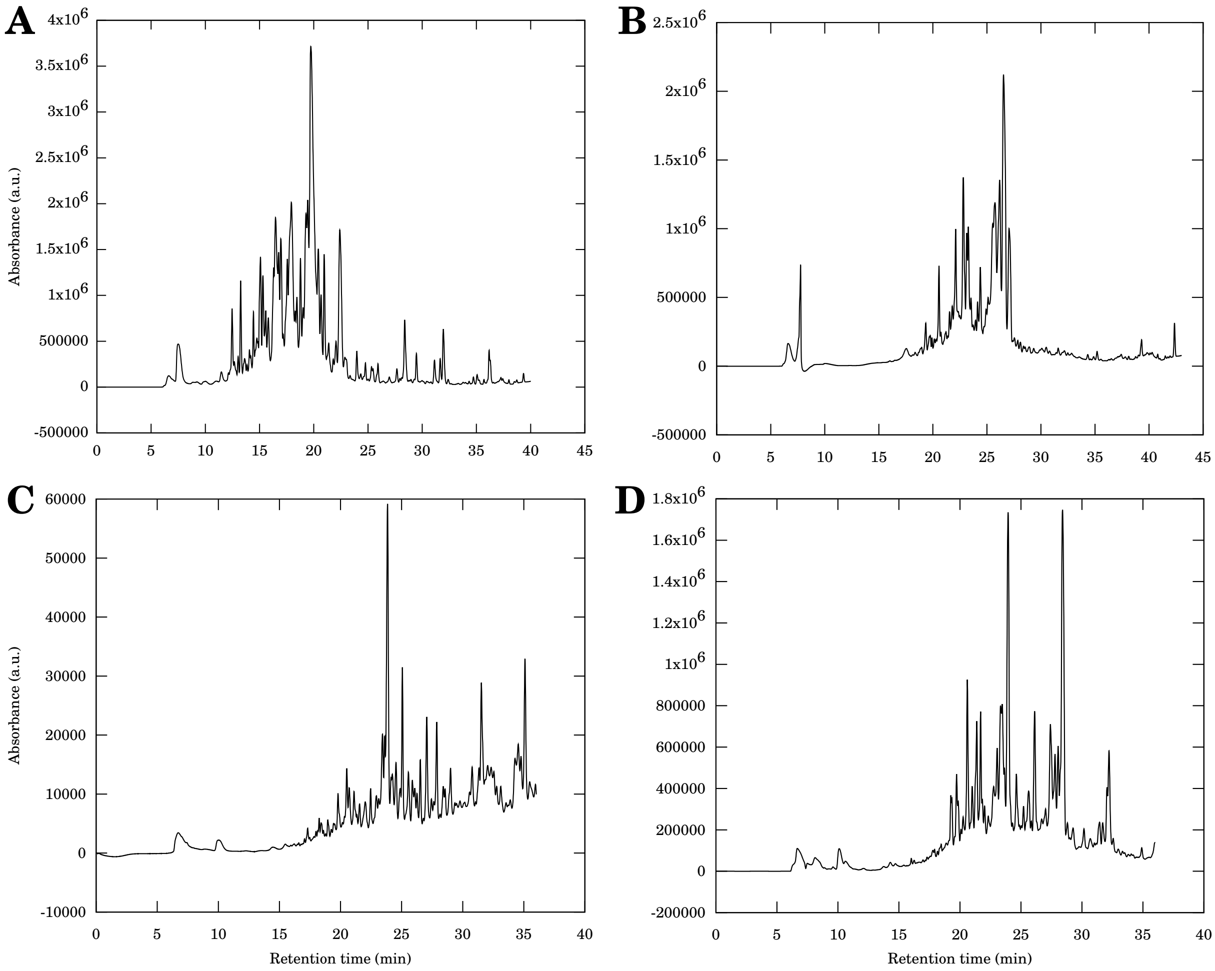

Figure 2.24: Reverse-phase HPLC chromatograms obtained from semi-preparative purifications of (**A**) **PS-O1**, (**B**) **PS-O1 GtP**, (**C**) **R1G2-PS-O1**, and (**D**) **R1A2-PS-O1 GtP**. Respective purification yields are: 73.4% (**PS-O1**), 84.1% (**PS-O1 GtP**), 90.7% (**R1G2-PS-O1**), and 91.5 (**R1A2-PS-O1 GtP**). Purification was performed using an Agilent® ZORBAX Pursuit semi-preparative C18 column (250 × 10 mm, 5 µm). Purifications were conducted using a flow of 2.0 mL.min^{-1}. Elution was performed by a gradient of acetonitrile containing TFA at 0.08% and water containing TFA at 0.1%.

Table 2.5 shows the compiled purification data related to the synthesized products **PS-O1**, **PS-O1 GtP**, **R1G2-PS-O1**, and **R1A2-PS-O1 GtP**.

Table 2.5: Purification data of the synthesized peptides **PS-O1**, **PS-O1 GtP**, **R1G2-PS-O1**, and **R1A2-PS-O1 GtP**.

Peptide	Retention Time (min)	Reaction Yield (%)	Average Coupling Yield (%)	Purification Yield (%)	Purity (%)
PS-O1	19.7	16.5	91	73.4	98.4
PS-O1 GtP	26.5	12.8	90	84.1	92.2
R1G2-PS-O1	23.8	10.5	89	90.7	97.6
R1A2-PS-O1 GtP	24.0	8.7	89	91.5	91.6

While "**Retention Time (min)**" values can be obtained directly, the others require further analysis. Reaction yields are equal to the quotient between the synthesized compound's band area and the sum of all areas; these values can be correlated to the average coupling yield of each step in the SPPS by using

$$\bar{\eta}_C = \eta^{(1/N_b)}, \tag{2.1}$$

where $\bar{\eta}_C$ is the average coupling yield, η is the total reaction yield, and N_b is the number of peptide bonds — *i.e.*, the number of residues minus one. $\bar{\eta}_C$ is a useful quantity to verify if the SPPS reaction steps were done suitably, as was the case for all four peptide derivatives, and also to demonstrate how small overall yields, such as 8.7%, can be equivalent to high individual coupling yields, like 89%, respectively.

Reaction yields and purity values obtained from the semi-preparative and analytical chromatograms, respectively, were calculated considering bands after a certain time, since both columns have a retention time $R_{0.7}$ up to which the elution of relevant compounds is improbable. This value corresponds to the time it takes for the sample to go through 70% of the column volume and is calculated by

$$R_{0.7} = \frac{0.7\pi r^2 h}{F}, \tag{2.2}$$

where r and h are the column radius (cm^2) and length (cm), respectively, and F is the eluent flow (mL.min^{-1}). As such, $R_{0.7}$ is equal to 6.9 min for the semi-preparative runs and equal to 2.2 min for the analytical. Finally, products were obtained with high purity, as can be seen in the RP-HPLC chromatograms in **Figure 2.25**.

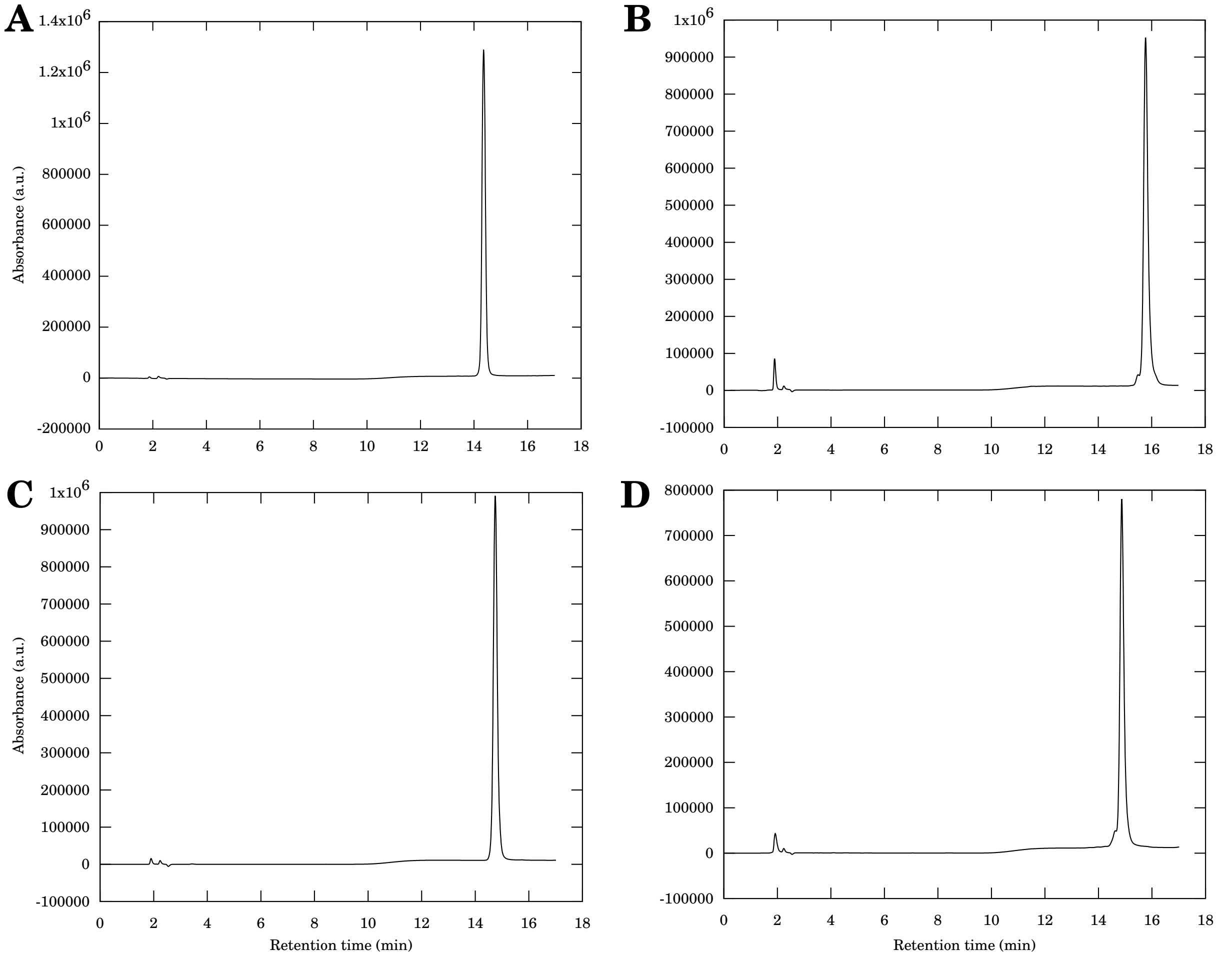

Figure 2.25: Reverse-phase HPLC chromatograms obtained from post-purification analytical runs of (**A**) **PS-O1**, (**B**) **PS-O1 GtP**, (**C**) **R1G2-PS-O1**, and (**D**) **R1A2-PS-O1 GtP**. Respective purities are: 98.35% (**PS-O1**), 92.21% (**PS-O1 GtP**), 97.62% (**R1G2-PS-O1**), and 91.64% (**R1A2-PS-O1 GtP**). Chromatographic characterization of the pure peptides was performed in analytical scale using an Macherey-Nagel® Nucleodur analytical C18 column (250 × 4 mm, 5 μm). Analyses were conducted using a flow of 1.0 mL.min^{-1}. Elution was performed by a gradient of acetonitrile containing TFA at 0.08% and water containing TFA at 0.1%.

Chapter 3 | Biophysic Assays

3.1 Introduction

3.1.1 Membrane mimetic models

Cell membranes are complex biological structures comprised of many elements and have two main purposes: (a) being a biological barrier to the extracellular environment and (b) compartmentalizing specialized and, sometimes, toxic reactions that occur in the intracellular medium. To this end, a protein-containing lipid bilayer is the main motif of a selectively permeable membrane that is also responsible for transcellular transportation and signaling. Although many different models have been used to describe the basic structure of a plasma membrane, Singer and Nicolson's "fluid mosaic model" (**Figure 3.1**) and Simons' "lipid raft" model (STILLWELL, 2016) are commonly used.

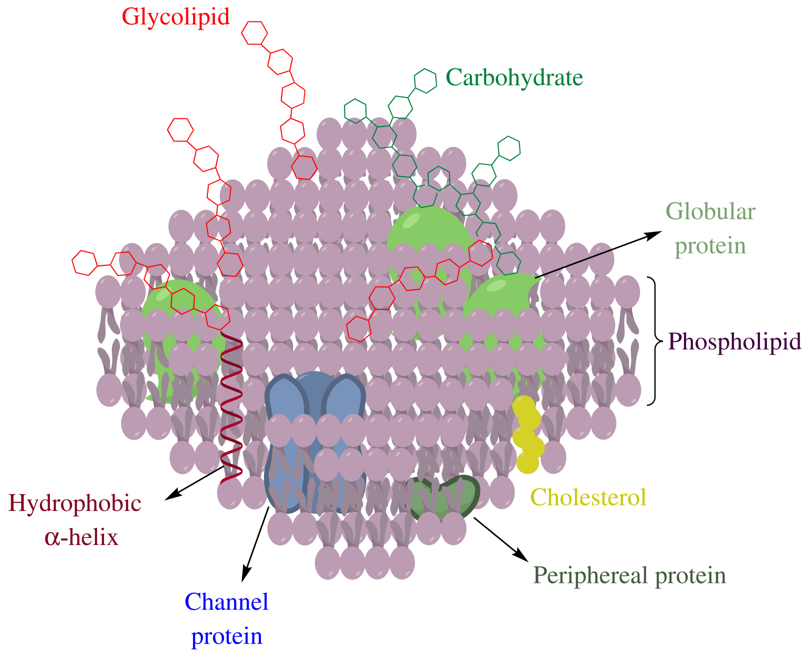

Figure 3.1: Singer and Nicolson's "fluid mosaic model" representation for animal eukaryotic cell membranes.

To understand and rationalize membrane biomimicry, it is important to know which phospholipids are the main bilayer components in each type of organism (either pro or eukaryotic), and the overall charge in each membrane type. Eukaryotic cell membranes are zwitterionic, being composed primarily of Phosphatidylcholine (PC) (**Figure 3.2**), while prokaryotics are mainly anionic and constituted by Phosphatidylglycerol (PG), Phosphatidylserine (PS) and Cardiolipin (CL) (YEAMAN; YOUNT, 2003).

Phosphatidylcholine (PC) Phosphatidylglycerol (PG)

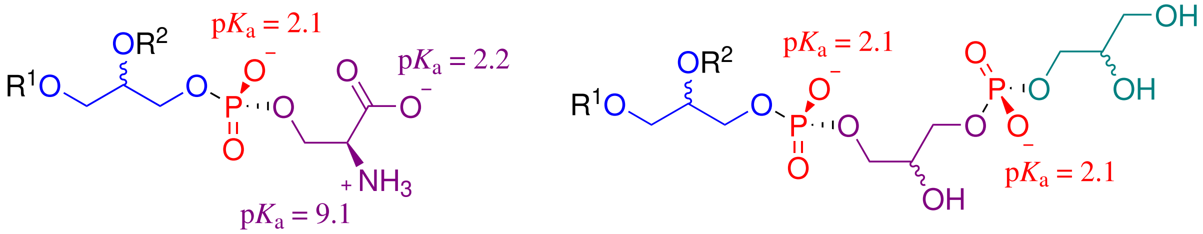

Phosphatidylserine (PS) Cardiolipin (CL)

Figure 3.2: Structure of phosphatidylcholine, phosphatidylglycerol, phosphatidylserine and cardiolipin with relevant pK_a values shown.

The most common biomimetic membrane media used in biophysic assays are micelles, vesicles, and bicelles (**Figure 3.3**) (CATOIRE et al., 2014). The simplest model is represented by detergent micelles (**Figure 3.3, a**), widely employed in the study of peptides in solution—like Nuclear Magnetic Resonance (NMR) structure elucidation. Molecules used to assemble these structure are amphipathic in nature (SEDDON et al., 2004), possessing a hydrophilic "head" and a hydrophobic "tail". When certain conditions are achieved in solution — *i.e.*, the critical micelle concentration (CMC) and Krafft temperature (K_T)[1] — detergent monomers aggregate spontaneously. Even though micellar structures are usually represented as spheres, their form depends on the type of detergent used, since Dodecylphosphocholine (DPC) yields spheres, whereas dodecyl-β-maltoside (β-DDM) (**Figure 3.4**), produces large oblate structures (TIELEMAN et al., 2000; CATOIRE et al., 2014).

---

[1] The CMC is defined as the concentration above which surfactants assemble into miclles and all additional surfactants added will form micelles, and the parameter that described it is the approximatelly constant surface tension. K_T is the temperature at which the solubility of a detergent is equal to its CMC; it is also defined as the triple point of the monomer solubility curve, the CMC temperature curve and the phase transition line of hydrated solids to micelles.

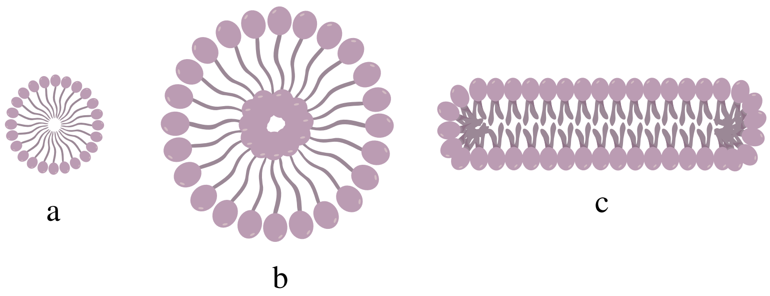

Figure 3.3: Schematic representation of (a) detergent micelles, (b) phospholipid vesicles and (c) bicelles.

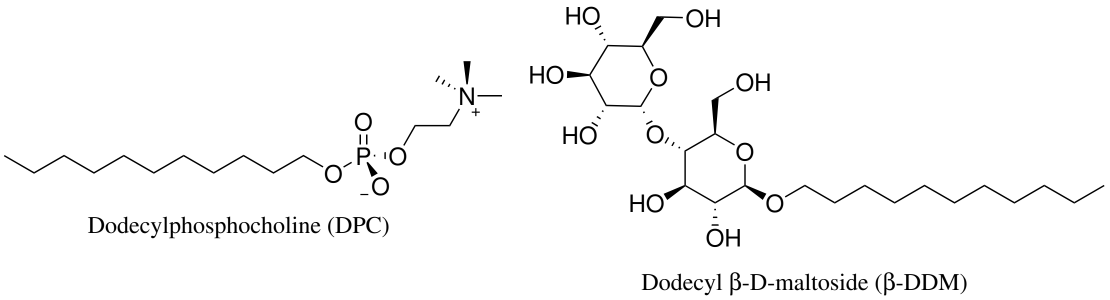

Dodecylphosphocholine (DPC)

Dodecyl β-D-maltoside (β-DDM)

Figure 3.4: Molecular representations of DPC and β-DDM.

Vesicles (**Figure 3.3, b**) are formed spontaneously by mixing up lipids in water and using reconstitution methods — like freeze-thaw followed by extrusion (KNOBLOCH et al., 2015) — yielding macromolecular bilayers. While micelles can be used for solution NMR, vesicles are more often employed in Solid-State NMR. This preference stems from the size difference, since micelles usually have a diameter of *ca.* 1.75 nm, while vesicles range from 20 nm up to a 100 µm, increasing correlation time τ_c values and, consequently, resonance line widths (CRUCIANI et al., 2006; DUPLÂTRE et al., 1996). However, vesicles are extensively employed in biophysical assays such as Isothermal Titration Calorimetry (ITC), Circular Dichroism Spectroscopy (CD), and Surface Plasmon Resonance (SPR).

Lastly, bicelles (**Figure 3.3, c**) are made by mixing two molecules of different sizes, in which a planar bilayer of phospholipids is stabilized by a swimming belt of short-chain lipids. Generally, applications of bicelles originate from a q factor—the molar ratio of phospholipds versus detergents—generating either large anisotropic ($q > 0.5$) bicelles, suitable for solid-state NMR analyses, or small isotropic ($q \leq 0.5$) ones, recommended for solution-state experiments (WARCHAWSKI et al., 2011).

3.1.2 Biophysics Assays

Circular Dichroism Spectroscopy

CD is a spectroscopic technique widely used in peptide and protein analysis, providing important information regarding secondary and tertiary structures, conformational assessments, folding/unfolding thermodynamic and kinetic parameters, and interaction parameters (RANJBAR; GILL, 2009; JOHNSON, 1988).

Polarized light can be considered as a chiral pair of right- and left-polarized components and, to differentiate between them, chiral compounds can be used, like peptides. Therefore, the circular dichroism phenomenon consists of different absorptions of circularly polarized light by asymmetrical molecules (WOODY, 1995). Regular absorption spectroscopy obeys two rules on how the absorbance A varies according to different parameters, described by

$$A = \log\left(\frac{I_0}{I}\right), \text{ and} \tag{3.1}$$

$$A = \varepsilon \cdot c \cdot l, \tag{3.2}$$

where I_0 is the intensity of the incident light; I, the intensity after the light has traveled a distance l through the sample (cm); ε is the molar extinction coefficient (L.mol^{-1}.cm^{-1}), and c is the concentration (mol.L^{-1}) (WOODY, 1995; JOHNSON, 1988; RANJBAR; GILL, 2009). **Equation 3.2** can be rewritten by considering ε as $\Delta\varepsilon = \varepsilon_{lcp} - \varepsilon_{rcp}$, where ε_{lcp} and ε_{rcp} are the extinction coefficients for left and right circularly polarized light, respectively. Therefore, the following relation applies:

$$\Delta A = A_{lcp} - A_{rcp} = (\varepsilon_{lcp} - \varepsilon_{rcp}) \cdot c \cdot l. \tag{3.3}$$

The extinctions coefficients ε can be also be understood to be the amount of each electric field component — $\vec{E}_{\text{rcp}}$ and $\vec{E}_{\text{lcp}}$, effectively responsible for charge redistribution and electronic transitions — that the molecule absorbs. Therefore, CD bands can be either positive or negative, depending on which circularly polarized component is more absorbed (KELLY et al., 2005). When the components are absorbed differently, the radiation becomes elliptically polarized (**Figure 3.5**).

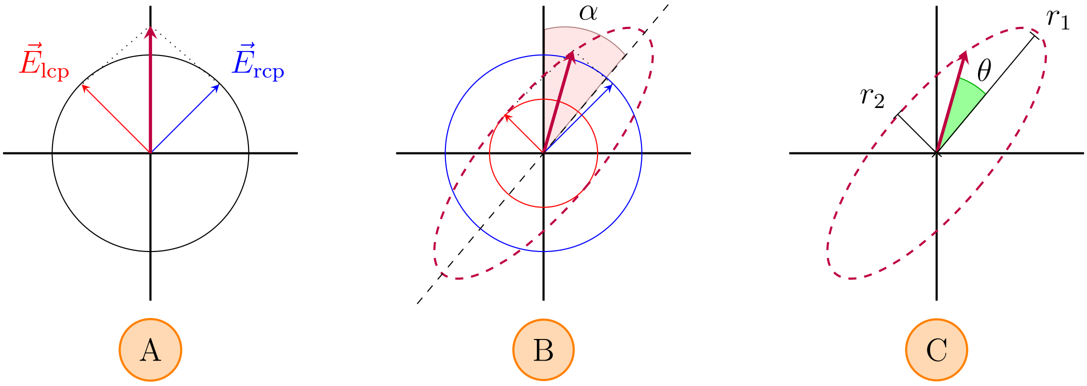

Figure 3.5: Representation of the formation of an elliptically polarized radiation. In (A), both $\vec{E}_{\mathrm{rcp}}$ and $\vec{E}_{\mathrm{lcp}}$ components are absorbed in equal amounts, producing no ΔA. In (B), $\vec{E}_{\mathrm{lcp}}$ is absorbed more strongly, tilting the resulting radiation by α and impairing an elliptical trajectory upon it. (C) depicts the relationship between the ellipticity θ and the ellipse radii r_1 and r_2.

The ellipse radii r_1 and r_2 are related to extinction coefficients ε_{lcp} and ε_{rcp} by

$$\tan\theta = \frac{r_2}{r_1} = \frac{\varepsilon_{lcp} - \varepsilon_{rcp}}{\varepsilon_{lcp} + \varepsilon_{rcp}}, \tag{3.4}$$

where θ is the ellipticity of the system. Therefore, different molar extinction coefficients — *i.e.*, different absorptions — will produce positive or negative angles. Also, although the quantity measured is ΔA, the most common is θ (JOHNSON, 1988; KELLY et al., 2005). The relation between them can be described as

$$\theta = 32.98 \cdot \Delta A. \tag{3.5}$$

Furthermore, results are published as a function of molar ellipticity $[\theta]$ (deg.cm^2.dmol^{-1}) (WOODY, 1995; BAKSHI et al., 2014), given by

$$[\theta] = \frac{100 \cdot \theta}{l \cdot c} = 3298 \cdot \Delta\varepsilon. \tag{3.6}$$

When analyzing the secondary structure of peptides and proteins, CD bands stem from the absorption of radiation in the far ultraviolet region, between $\sim$ 240 and 190 nm, due to the amide chromophores, and in the region between $\sim$ 320 and 260 nm, due to aromatic side chains and disulphide bonds. Furthermore, the electronic transitions of the amide bond are a $n \to \pi^*$ transition at $\sim$ 222 nm and $\pi \to \pi^*$ transitions at $\sim$ 208 and $\sim$ 190 nm (**Table 3.1**) (MILES; WALLACE, 2016). Regarding amide bonds, the $\pi \to \pi^*$ transition has a higher energy compared to $n \to \pi^*$ (RANJBAR; GILL, 2009) and furnishes two bands since, when chromophores are aligned in arrays like in an α-helix, their transitions are split into two due to exciton interactions (GREENFIELD, 2006)[2]. Furthermore, since the transitions of the carbonyl π-electrons are the most significant, the dihedral amide bond angles ϕ and ψ (**Figure 3.6**) are of great importance (RICHARDSON, 1981; RAMACHANDRAN et al., 1963).

Table 3.1: Chromophores/transitions and respective wavelengths related to circular dichroism spectroscopy.

Chromophore/Transition	**Wavelength (nm)**
Aromatic side chain	320 to 260
Disulphide bonds	260
Amide bond ($n \rightarrow \pi^*$)	$\sim$ 222
Amide bond ($\pi \rightarrow \pi^*$)	$\sim$ 208 and 190

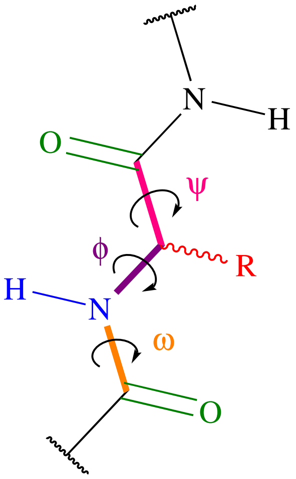

Figure 3.6: Peptide torsion angles ϕ, ψ and ω with related bonds. As shown, ω is related to the carbonyl and NH bonds, ϕ to the NH and C_α−side chain, and ψ to the C_α−side chain and carbonyl group.

Finally, the secondary structure of peptides can be analyzed by following patterns in CD spectra (RANJBAR; GILL, 2009), which are correlated to their folding and are separated as follows:

1. For random coil structures, a positive band at $\sim$ 212 nm ($n \rightarrow \pi^*$) and a negative one at $\sim$ 195 nm ($\pi \rightarrow \pi^*$) are commonly observed;
2. β-Sheet structures present a negative band at $\sim$ 218 nm ($\pi \rightarrow \pi^*$) and a positive one at $\sim$ 196 nm ($n \rightarrow \pi^*$);

---

[2] Although the complete description of exciton splittings in molecular spectroscopy is beyond the scope of this text (KASHA et al., 1965), the coupling of electric dipole allowed $\pi \rightarrow \pi^*$ transitions in a helix leads to resultant transitions with net polarizations parallel and perpendicular to the helix axis (MOFFITT, 1956; BULHELLER et al., 2007), furnishing two bands in the spectrum.

3. Finally, α-helical structures are characterized by a positive band at $\sim$ 192 nm ($\pi \rightarrow \pi^*$, perpendicular) and two negative bands at $\sim$ 208 nm ($\pi \rightarrow \pi^*$, parallel) and $\sim$ 222 nm ($n \rightarrow \pi^*$).

The analysis of the peptide secondary structures comes down to the relative percentage of each conformation in the overall moiety, calculated by deconvolution algorithms based on the theoretical values discussed previously.

3.2 Circular Dichroism Spectroscopy

CD analyses for peptides **PS-O1**, **PS-O1 GtP**, **R1G2-PS-O1** and **R1A2-PS-O1 GtP** were performed in the presence of Trifluoroethanol (TFE):H_2O mixtures, Sodium dodecylsufate (SDS) and DPC micelles, and 1-Palmitoyl-2-oleoyl-*sn*-glycero-3-phosphocholine (POPC) and POPC:1-Palmitoyl-2-oleoyl-*sn*-glycero-3-(phospho-rac-(1-glycerol)) (POPG) 3:1 vesicles (**Figure 3.7**). The adopted procedure was derived from the ones described by Greenfield (GREENFIELD, 2006) and Gusmão (GUSMÃO et al., 2017).

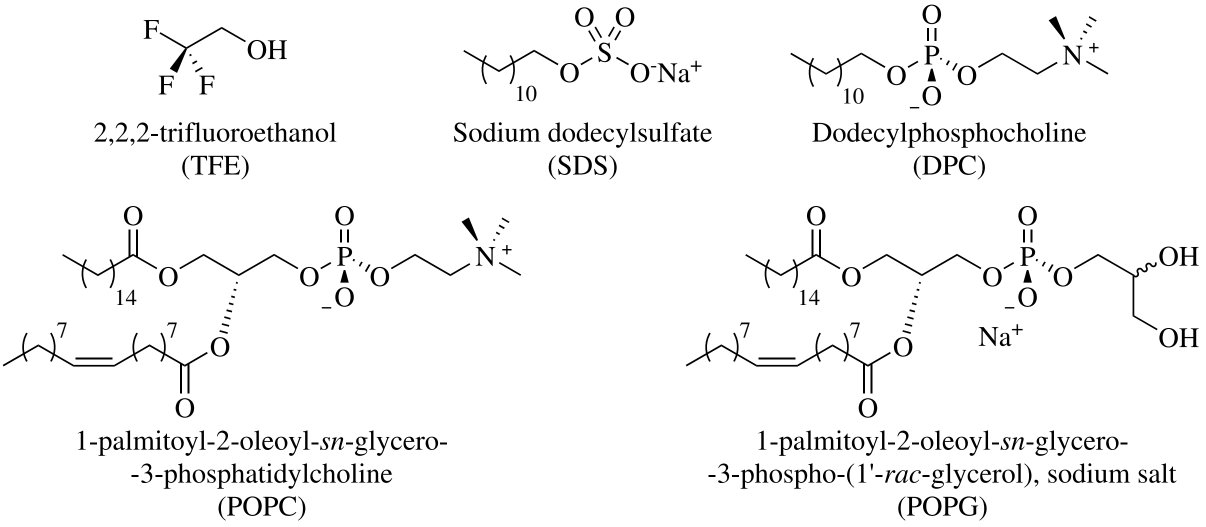

Figure 3.7: Structural representations of TFE, SDS, DPC, POPC and POPG.

All synthesized products were analyzed in the presence of TFE:H_2O solutions (solvent ratios ranging from 0:100 to 60:40, v:v), SDS and DPC micelles (detergent concentrations ranging from 0.5 to 20 mmol.L^{-1}), and POPC and POPC:POPG 3:1 vesicles (liposome concentrations ranging from 0.1 to 2 mmol.L^{-1}). POPC and POPC:POPG 3:1 vesicles were assembled according to the methodology described in **Section 3.2.1, Page 70** and 3 mmol.L^{-1} solutions in ultrapure water were used for dilutions.

Peptide concentrations used in the experiments and relative peptide bond concentrations are displayed in **Table 3.2**.

Table 3.2: Peptide concentrations used in circular dichroism experiments in g.L^{-1} (C_{pep}) and mol.L^{-1}, and respective peptide bond concentrations (C_b), in mol.L^{-1}.

Peptide	C_{pep} **(g.L^{-1})**	**Concentration (mol.L^{-1})**	C_b **(mol.L^{-1})**
PS-O1	0.2	$9.5.10^{-5}$	$1.6.10^{-3}$
PS-O1 GtP	0.2	$7.8.10^{-5}$	$1.3.10^{-3}$
R1G2-PS-O1	0.15	$6.4.10^{-5}$	$1.1.10^{-3}$
R1A2-PS-O1 GtP	0.15	$5.5.10^{-5}$	$1.0.10^{-3}$

Peptide bond concentrations, C_b (mol.L^{-1}), are calculated by

$$C_b = \frac{C_{\text{pep}}}{M_b}, \tag{3.7}$$

where C_{pep} is the peptide concentration, in g.L^{-1}, and M_b is the peptide bond molar mass, in g.mol^{-1}, calculated by

$$M_b = \frac{M_{\text{pep}} + (A_+ \cdot M_{\text{TFA}})}{N_b}, \tag{3.8}$$

where M_{pep} is the peptide molar mass, in g.mol^{-1}, A_+ is the number of positively charged residues, considering that purification was done using TFA at $\sim 0.1\%$ (pH $= 1.9$, p$K_{\text{a}} = 0.52$), which results in the protonation of all His and Arg residues, in the present case. Furthermore, M_{TFA} is the molar mass of TFA and N_b is the number of peptide bonds, or the number of amino acids residues minus one.

A 1.0 mm optical path length rectangular quartz cuvette was used in all analyses. Experiments were performed at 25 °C in a Jasco J-815® spectropolarimeter coupled to a Peltier Jasco PTC-423L® temperature control system. All spectra were recorded with 8 accumulations from 260 to 190 nm, using a 10 nm.min^{-1} scan speed, 1.0 nm spectral bandwidth, 1 s response time, and 0.2 nm step resolution.

Experiments were also performed in a similar way using blank solutions. Baseline correction, smoothing and data conversion from ellipticity to molar ellipticity using peptide bond concentrations values were then performed using Jasco Spectra Manager®. Spectra deconvolution, in order to obtain helicity H values, was done using the CDPro® program suite containing the `SELCON3`, `CDSSTR` and `CONTINLL` algorithms (SREERAMA; WOODY, 2000).

3.2.1 Vesicle preparation

POPC and POPC:POPG 3:1 (mol:mol) vesicles were prepared following an adapted protocol (MAYER et al., 1986; SZOKA; PAPAHADJOPOULOS, 1980; LADKHIN et al., 2010; GUSMÃO et al., 2017). First, 0.00456 g (0.006 mol) of POPC (Avanti® Polar Lipids) was weighed in a 50 mL round-bottom flask and subsequently dissolved in DCM. The solvent was then evaporated under reduced pressure until a thin, homogeneous film was produced at the walls of the flask. The film was then rehydrated using 2 mL of ultrapure water, in order to obtain a turbid white 3.0 mmol.L^{-1} multilamellar vesicle (MLV) solution.

The MLV solution was then submitted to three freeze/thaw cycles to homogenize particle size and increase water encapsulation. Finally, Large Unilamellar Vesicles (LUVs) were obtained by extrusion using an Avanti® Polar Lipids mini-extruder (ALVES et al., 2013), passing the solution a total of 11 times through a 100 nm polycarbonate membrane (Whatman®) until the solution was clearer than the initial suspension. The procedure for POPC:POPG 3:1 vesicles was similar, using 0.00342 g (0.0045 mol) of POPC and 0.00116 g (0.0015 mol) of POPG in 2 mL of ultrapure water, yielding a 3.0 mmol.L^{-1} solution.

3.2.2 Results

The conformational preferences of **PS-O1**, **PS-O1 GtP**, **R1G2-PS-O1**, and **R1A2-PS-O1 GtP** were studied in the presence of TFE:H_2O mixtures (0:100 to 60:40, v:v), SDS and DPC micelles (concentrations between 0.5 and 20 mmol^{-1}) and POPC and POPC:POPG (3:1 mol:mol) vesicles (concentrations ranging from 0.1 to 2.0 mmol^{-1}). The primary structure of each peptide is shown in **Table 3.3** and the results obtained in the presence of TFE:H_2O are shown in **Figure 3.8, Page 71**.

Table 3.3: Primary structures of the peptide sequences analyzed by circular dichroism.

Peptide	**Primary structure**
PS-O1	FLSLI PHAIN AVSTL VHHSG–NH_2
PS-O1 GtP	**GtP**FLSLI PHAIN AVSTL VHHSG–NH_2
R1G2-PS-O1	RGFLS LIPHA INAVS TLVHH SG–NH_2
R1A2-PS-O1 GtP	R**GtP**FLS LIPHA INAVS TLVHH SG–NH_2

In the presence of 0:100 and 10:90 TFE:H_2O, random coil conformations are preponderant, characterized by the molar ellipticity (θ) minimum at $\sim$ 198 nm (blue and red curves, **Figure 3.8**). Although a slight bathochromic shift was observed for θ_{198} from 0:100 to 10:90, the overall pattern persists for all peptides. Interestingly, in the respective spectra of **PS-O1 GtP** (**Figure 3.8, B**), θ values closer to zero are observed for

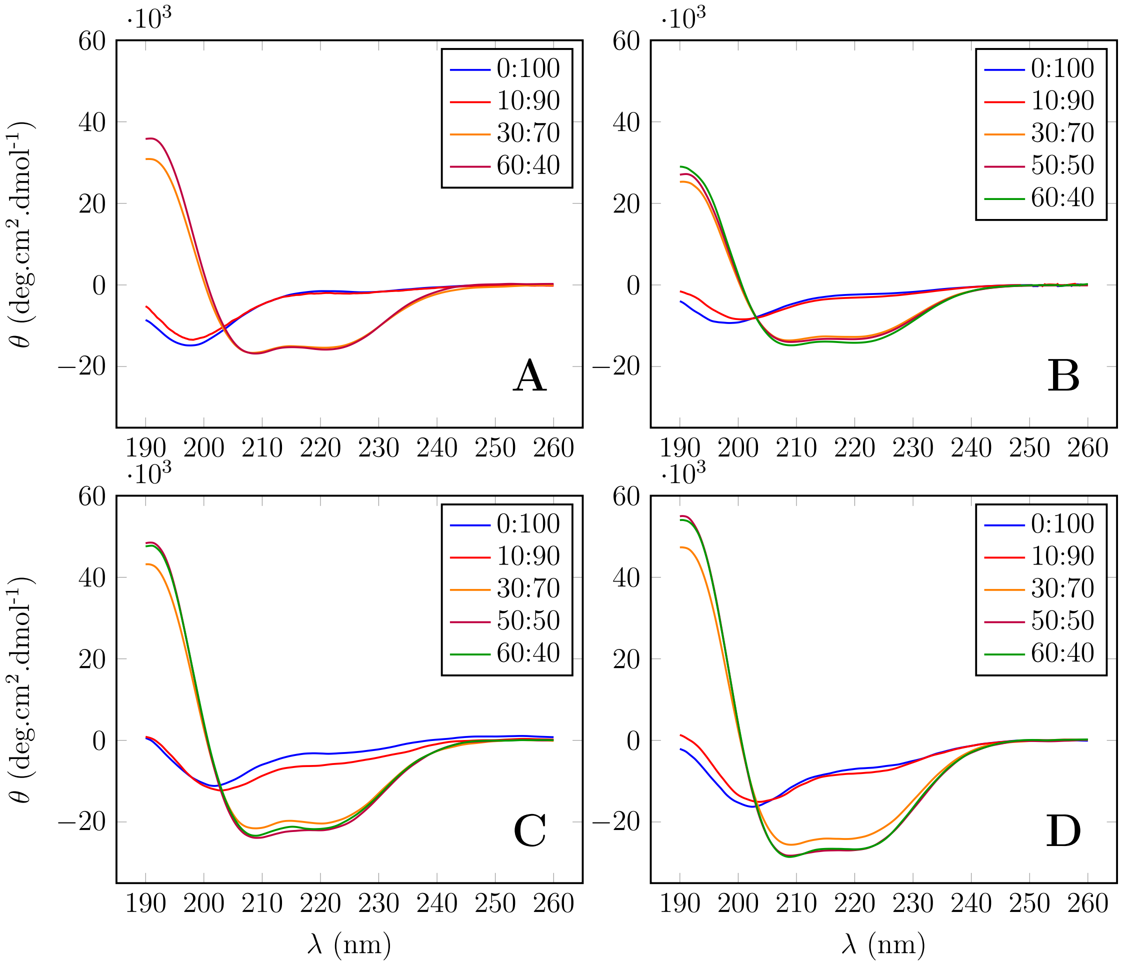

Figure 3.8: CD spectra of (**A**) **PS-O1**, (**B**) **PS-O1 GtP**, (**C**) **R1G2-PS-O1**, and (**D**) **R1A2-PS-O1 GtP** in different proportions of TFE:H_2O.

the two aforementioned curves (0:100 and 10:90) when compared to the other peptides, indicating partial transition profiles from random coil to helical conformations. Although being close to the baseline is a poor indicator of a defined structural motif, the observed pattern clearly points to a random coil conformation. Therefore, some percentage of other non-defined conformational arrangements can make up part of the structural ensemble in these cases, as previously reported in the literature (RESENDE et al., 2008).

However, a significant change was observed for TFE:H_2O 30:70, since one θ maximum at *ca.* 195 nm (θ_{195}) and two minima at *ca.* 208 and 222 nm (θ_{208} and θ_{222}, respectively) were visible for all peptides. Additionally, the curve patterns changed completely, being characteristic of α-helical conformations (RANJBAR; GILL, 2009). Although no significant changes in λ values for these minima and maxima between 30:70 and 60:40 TFE:H_2O were observed, the latter presented higher molar ellipticity at the maximum and more negative θ values at the minima, indicating a higher helicity. Also, these results suggest that the helices are right-handed, as is the case for most peptide and protein structures with L-amino acids, since a left-handed counterpart is associated with a minimum at *ca.* 195 nm and two maxima at *ca.* 208 and 222 nm (MORTISHIRE-SMITH et al., 1991).

The aforementioned results are explained by the fact that, in the absence of TFE, AMPs tend to adopt a random coil conformations due to ion-dipole interactions between charged residues and external water molecules, while also establishing hydrogen bonds between amide protons and water oxygen atoms. As such, internal cohesion by means of interresidue interactions — like hydrogen bonds between carbonyl oxygen atoms and amide protons — does not effectively occur. Alternatively, as TFE concentration increases, external attractions weaken and $[i, i+4]$ CO···HN interactions[3] in the peptide backbone get stronger, increasing helical stabilization. This transition occurs mainly due to the smaller polarity of TFE compared to H_2O, indicated by their dielectric constants, ε — $\varepsilon_{\mathrm{TFE}} = 26.69$ at 298.15 K, and $\varepsilon_{\mathrm{H_2O}} = 79.98$ at 293.15 K (WOHLFARTH, 2015a; WOHLFARTH, 2015b).

To verify this structural behavior for the four peptides, the obtained data was analyzed by CDPro®, yielding the helicity (H) values presented in **Figure 3.9**[4].

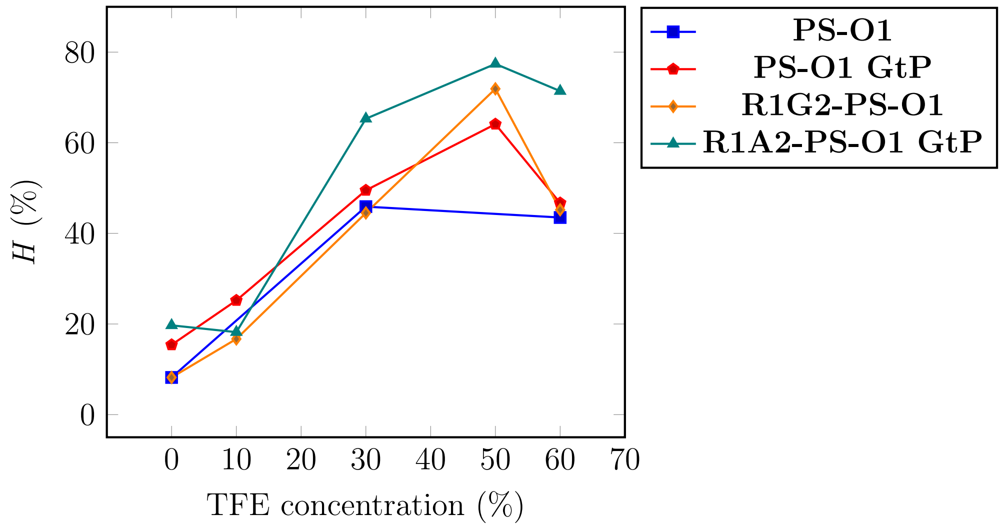

Figure 3.9: Helicity H values for **PS-O1**, **PS-O1 GtP**, **R1G2-PS-O1** and **R1A2-PS-O1 GtP** in the presence of 0:100, 10:90, 30:70, 50:50 and 60:40 (v:v) TFE:H_2O solutions.

Helicity values do not show an exact correspondence to the expected trend since smaller helical content values were obtained for 60:40 TFE:H_2O when compared to 50:50 which displayed, overall, the highest H values. It is worth noticing that the introduction of the Glucotriazole (Gt) moiety increases the maximum helicity of each glucotriazole-peptide when compared to its respective peptide chain counterpart. As the insertion of the Gt

---

[3] The carbonyl oxygen of the i-th residue interacts with the amide hydrogen of the $i+4$-th residue.

[4] **Table A.1, Page 170** contains the numerical values obtained for each peptide.

moiety occurs in a neighbouring position to a Phenylalanine (Phe) residue, it is likely that π-π-type interactions between the triazole and the phenyl group stabilize α-helical conformations locally (BUTTERFIELD et al., 2002), since the heterocycle is an example of a π-deficient cycle (MALIK et al., 2020), similar to pyridine, due to the presence of two pyridine-type nitrogens and one pyrrole-type nitrogen. Therefore, it has π molecular orbitals with a lower overall energy when compared to benzene and the interaction between the two aromatic cycles likely lowers the energy the system.

The establishment of a cation-π-type interaction between the two rings could take place if one of the two pyridine-type nitrogens of the triazole was sufficiently protonated, which would provide helix stabilization (TSOU et al., 2002; SHI et al., 2002). The literature shows a $\mathrm{p}K_{\mathrm{aH}}$ value for 1,2,3-triazoles equal to 1.17 (RUMBLE, 2021) and, as stated previously, the purification conditions established a protonation environment similar to a pH of 1.9. Therefore, since the virtual pH and $\mathrm{p}K_{\mathrm{aH}}$ values are similar, a negligible amount of protonated triazole moieties are likely present in solution and, hence, cation-π-type interactions involving the azole of the Gt unit can be considered absent.

Comparing the obtained H values to the ones reported for analogues **PS-1**, **-2**, and **-3** yields considerably different results, summarized in **Table 3.4** (RESENDE et al., 2008). As can be seen, all synthesized analogues have smaller helicities than **PS-1** and **-2** except for **R1A2-PS-O1 GtP**, which shows a higher helicity than the other synthesized analogues and smaller helicities only when compared to **PS-2**. At 30:70, the four products have higher H than **PS-3**. Although there are no reported H values for **PS-1**, **-2** and **-3** at 50:50 TFE:H_2O, a similar trend would likely be displayed for them as for the synthesized analogues — *i.e.*, maximum H at 50:50.

Table 3.4: Helicity H values for **PS-1**, **-2**, **-3**, **PS-O1**, **PS-O1 GtP**, **R1G2-PS-O1**, and **R1A2-PS-O1 GtP** in the presence of 30:70 and 60:40 TFE:H_2O solutions.

	Helicity *H* (%)			**Helicity *H* (%)**	
Peptide	**TFE:H_2O 30:70**	**TFE:H_2O 60:40**	**Peptide**	**TFE:H_2O 30:70**	**TFE:H_2O 60:40**
PS-1	53	70	**PS-O1**	45.9	43.5
PS-2	75	78	**PS-O1 GtP**	49.5	46.7
PS-3	41	53	**R1G2-PS-O1**	44.5	45.2
			R1A2-PS-O1 GtP	65.3	71.4

Comparing the sequences of **PS-O1** and **PS-2** (**Table 1.1, Page 35** and **Table 3.3, Page 70**), similar helical percentages would be expected, since they are 90% homologous. However, significantly different H values were observed for them. One characteristic that could be attributed to this is the Serine (Ser)-Glycine (Gly) segment at the N-terminus of **PS-O1**, instead of a Phe (**PS-2**). Since Gly is a residue that disturbs α-helical conformations due to a greater rotational freedom, it imposes an unfavorable entropy change when the peptide adopts this motif (ZHOU et al., 1994). The α-helical propensity of individual residues has been studied (ZHOU et al., 1994; PACE; SCHOLTZ, 1998; BLABER et al., 1993) and while some residues facilitate helix formation, others are indifferent, destabilizers or strong destabilizers—most notably Pro and Gly (**Figure 3.10**).

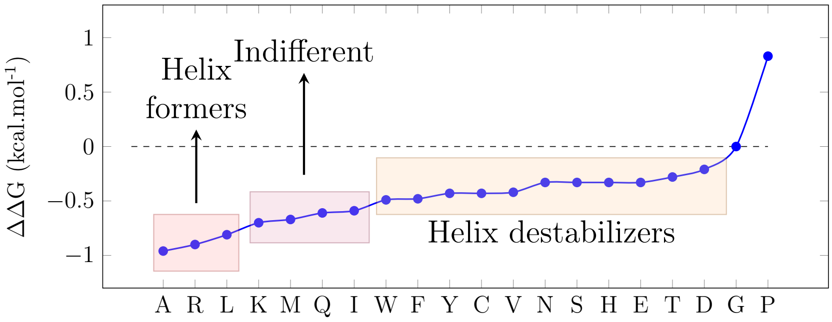

Figure 3.10: α-Helical propensities of each amino acid residue expressed as ΔΔG values in kcal.mol^{-1} related to glycine. ΔΔG values taken from (ZHOU et al., 1994).

A parallel can be traced between the smaller helicities of **R1G2-PS-O1** and **R1A2-PS-O1 GtP** when compared to **PS-2**, and the fact that **PS-2** bears a Phe residue at its N-terminus while the synthesized analogues carry an Arg at the N-terminus.

This residue difference is important since electrostatic interactions between side chains and the backbone at peptide termini contribute to α-helix stabilization. At the negatively-charged C-terminus of carboxylated peptides, for example, chemical modifications such as amidation tend to increase helicity, since the negative charge of the helix dipole is partially neutralized, and this phenomenon has been observed for many natural AMPs (WANG, 2012; ZHANG et al., 2021; TEIXEIRA et al., 2012). Additionally, N-terminal acetylation is a common post-translational modification that occurs naturally in some eukaryotic organisms and is used in synthetic approaches (WANG, 2012; REE et al., 2018; FUSCALDI et al., 2021; REIS et al., 2018), also being responsible for partially neutralizing the helix dipole and increasing helix stability.

Therefore, since both **R1G2-PS-O1** and **R1A2-PS-O1 GtP** carry an Arg residue adjacent to the positively-charged N-terminus, an electrostatic repulsion is likely established, as the guanidine moiety will also be protonated — $pK_a = 13.8$ (FITCH et al., 2015), leading to structural destabilization, evidenced by a smaller H than **PS-2**. This behavior is critical since Arg, like His, enhances helix formation when placed closer to the C-terminus due to the resulting π-cation and H-bonding interactions (ARMSTRONG; BALDWIN, 1993).

SDS and DPC micelles were also used as biomimetic media to assess the conformational preferences of the products (**Figure 3.11**).

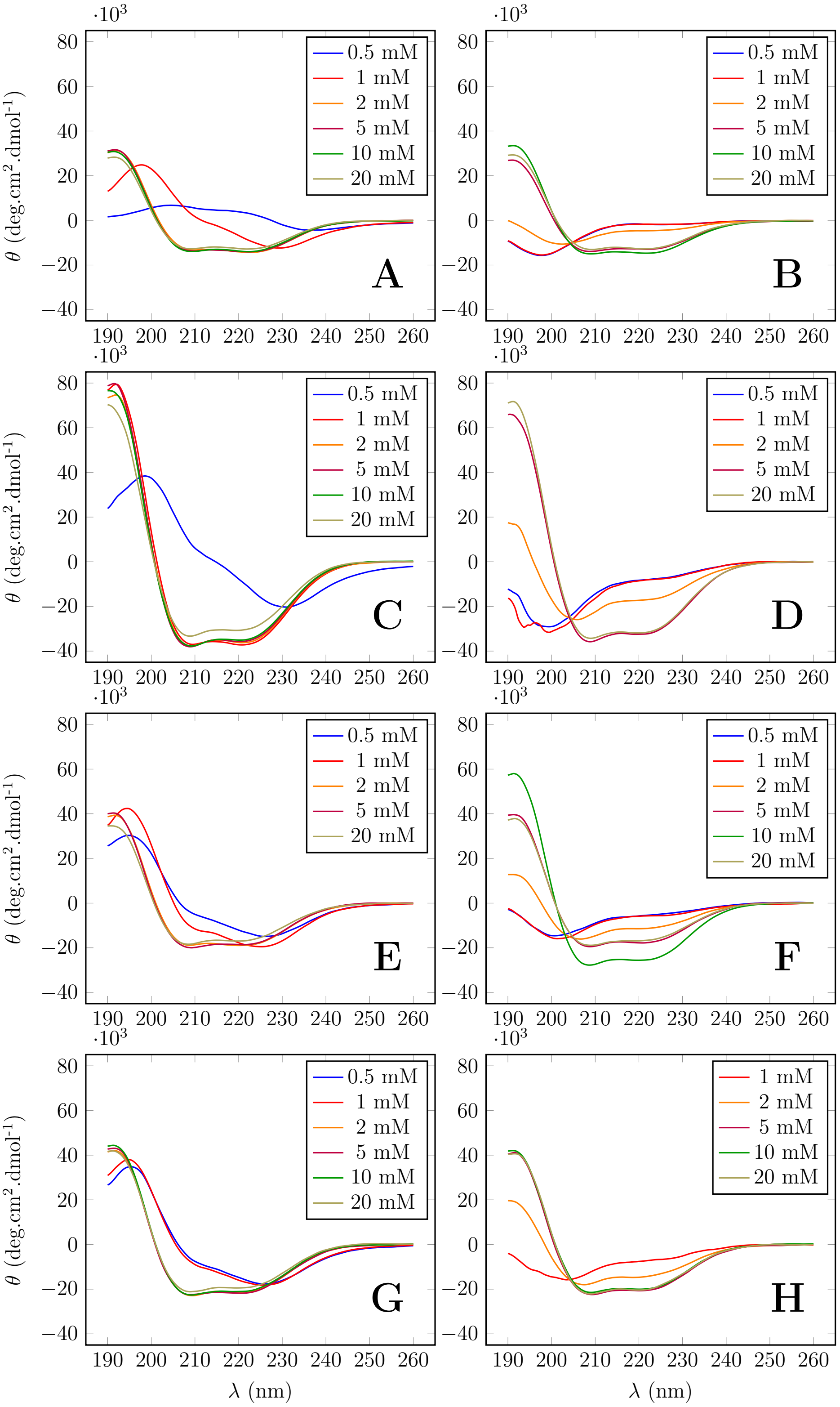

Figure 3.11: CD spectra of (**A**, **B**) **PS-O1**, (**C**, **D**) **PS-O1 GtP**, (**E**, **F**) **R1G2-PS-O1**, and (**G**, **H**) **R1A2-PS-O1 GtP** acquired in the presence of (**A**, **C**, **E**, **G**) SDS and (**B**, **D**, **F**, **H**) DPC micelles.

Three major features are visible in the spectra: (*i*) the minimum threshold for the adoption of helical structures for each micellar composition, (*ii*) the curve profiles at lower concentrations (0.5 and 1 mmol.L^{-1}), and (*iii*) the apparent H trend by comparing minimum θ_{208} values.

First, **PS-O1** and its derivatives adopt an α-helical conformation in the presence of smaller concentrations of SDS when compared to DPC (*e.g.*, **PS-O1** CD spectra show α-helical profiles at 2 mM SDS and 5 mM DPC; **PS-O1 GtP** at 1 mM SDS and 5 mM DPC; **R1G2-PS-O1** at 2 mM SDS and 5 mM DPC; **R1A2-PS-O1 GtP** at 2 mM SDS and 5 mM DPC), indicating a selectivity between them at low detergent concentrations. This can be explained by the process of α-helix folding, comprised of (*i*) an electrostatic attraction between the peptide and the membrane, followed by a (*ii*) binding of the random coil peptide, and subsequent (*iii*) transition from random coil to α-helix (SEELIG, 2004). Therefore, the negative net charge of SDS contributes to the first step of the folding process, since the peptide has a positive net charge, increasing helix formation when compared to the zwitterionic DPC.

Second, the spectral profiles of the peptides in the presence of both detergents at 0.5 and 1.0 mmol.L^{-1} differ significantly, since minimum θ_{198} values are observed in the presence of DPC but not of SDS. In the presence of SDS, α-helix profiles are observed for concentrations as low as 0.5 mmol.L^{-1}. Also, for SDS, the λ values of the curves' inflection points go through a hypsochromic shift as micellar concentration increases and the conformation changes from random coil to α-helix. Furthermore, all SDS concentrations yield curves with similar shapes, as opposed to what is observed for the peptide in the presence of DPC, in which the separation between both structural arrangements is more apparent.

Third, θ_{208} in the presence of SDS or DPC does not establish a linear correlation with concentration, since the smallest θ_{208} values are observed at concentrations lower than 20 mM for both. By analyzing the spectral profiles at micellar concentration of 5.0, 10 and 20 mmol.L^{-1}, the lowest θ_{208} values are observed for 5.0 mmol.L^{-1} SDS and 10 mmol.L^{-1} DPC. This can be explained by the fact that high micellar concentrations can eventually lead to an increase in the concentration of peptide-bound detergent monomers, promoting an overall structure disruption (CATOIRE et al., 2014).

H values obtained from CDPro® for both SDS and DPC are shown in **Figure 3.12**[5]. According to the data, **PS-O1** exhibits a slightly higher maximum helical content in the presence of DPC (10 mmol.L^{-1}, 38.3%), when compared to SDS (2.0 mmol.L^{-1}, 30.8%). Curiously, **R1G2-PS-O1** also displays this behavior (*e.g.*, maximum H in the presence of 1 mmol.L^{-1} SDS, 67.5%, and of 10 mmol.L^{-1} DPC, 80.1%) while **PS-O1 GtP** and

---

[5] **Table A.2, Page 170.** contains the numerical values obtained for each peptide.

R1A2-PS-O1 GtP have shown an opposite trend (*e.g.*, maximum H in the presence of 5 mmol.L^{-1} SDS, 89.1%, and of 5 mmol.L^{-1} DPC, 83.8% for the former and of 10 mmol.L^{-1} SDS, 66.2% and of 5 mmol.L^{-1} DPC, 62.3% for the latter). In summary, while all peptide analogues attain defined helical structures at lower concentrations of SDS than DPC, maximum H values in the presence of DPC are higher for the peptides in comparison to their glucotriazole analogues.

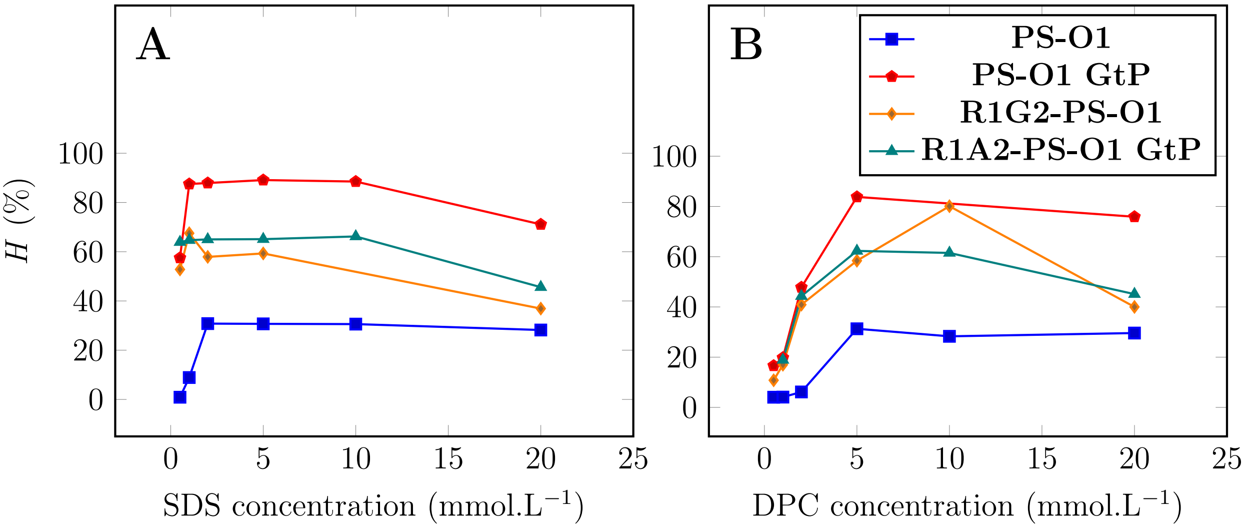

Figure 3.12: Helicity H values for **PS-O1**, **PS-O1 GtP**, **R1G2-PS-O1** and **R1A2-PS-O1 GtP** in the presence of 0.5, 1.0, 2.0, 5.0, 10, and 20 mmol.L^{-1} (**A**) SDS and (**B**) DPC, as calculated by CDPro®.

Finally, conformational preferences of the synthesized analogues were studied in the presence POPC and POPC:POPG 3:1 LUVs. Results from these experiments are more robust due to the high similarity between vesicles and cell membrane bilayers. Furthermore, the POPC:POPG pair is a good probe for biological activity, since different helicity patterns for each can indicate if the AMP is more active towards prokaryotic or eukaryotic cell membranes. POPC and POPC:POPG 3:1 CD spectra obtained for the peptide analogues are shown in **Figure 3.13, Page 78**.

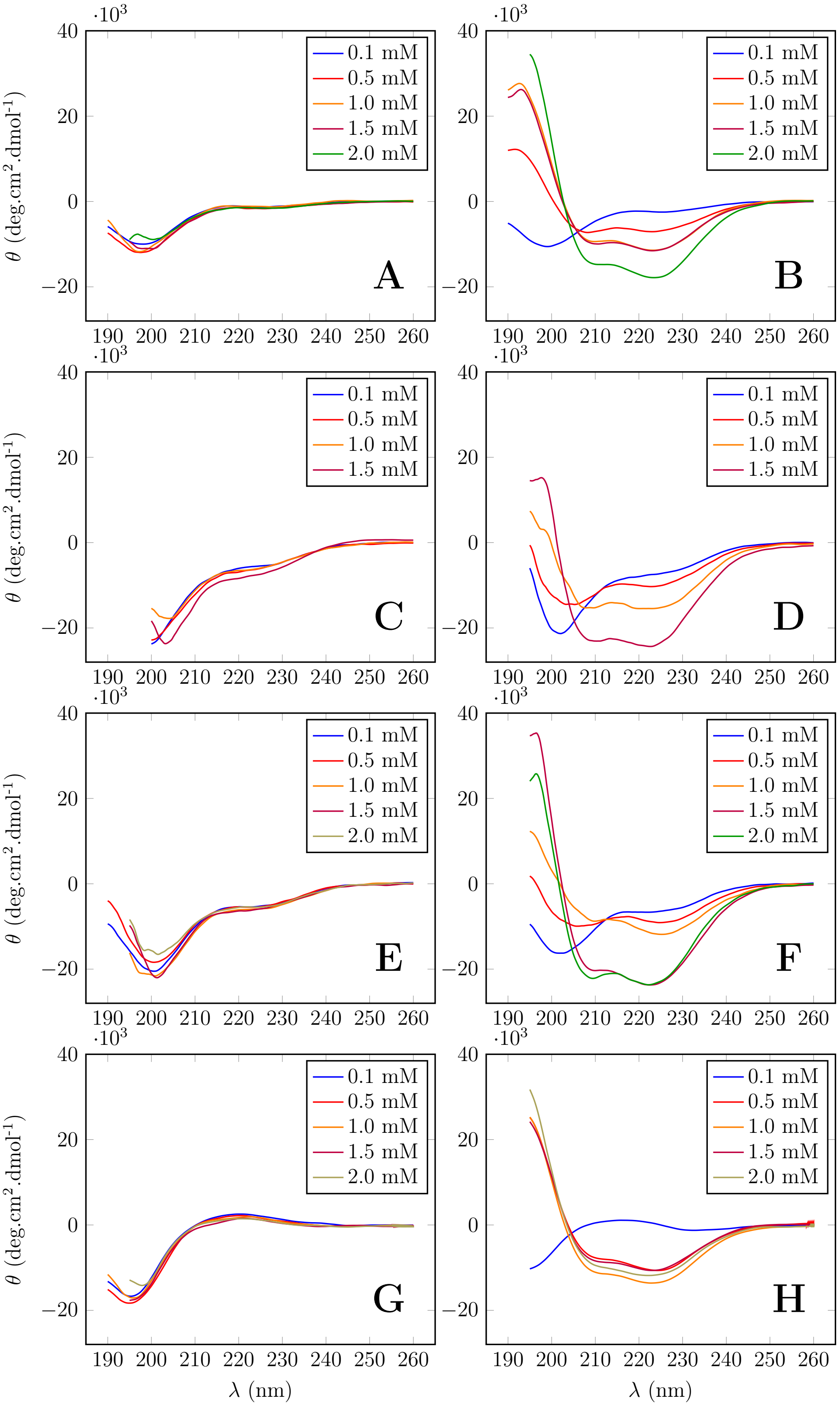

Figure 3.13: CD spectra of (**A**, **B**) **PS-O1**, (**C**, **D**) **PS-O1 GtP**, (**E**, **F**) **R1G2-PS-O1**, and (**G**, **H**) **R1A2-PS-O1 GtP** acquired in the presence of (**A**, **C**, **E**, **F**) POPC and (**B**, **D**, **F**, **H**) POPC:POPG 3:1 LUVs.

At first glance, the absence of α-helical conformations can be observed for all investigated POPC concentrations. On the other hand, spectra acquired in the presence of POPC:POPG 3:1 reveal typical patterns of α-helical conformations after a LUV concentration threshold. These results indicate that the peptide will likely adopt an active α-helical structure when bound to bacterial cell membranes, which is thermodynamically favoured due to electrostatic interactions between the positively charged peptides and the anionic membranes. The absence of helical structures in the presence of zwitterionic vesicles indicate that the peptides do not interact significantly with mammalian cells, which is a desired characteristic for AMPs. The respective helical contents H obtained by CDPro® are displayed in **Figure 3.14**.

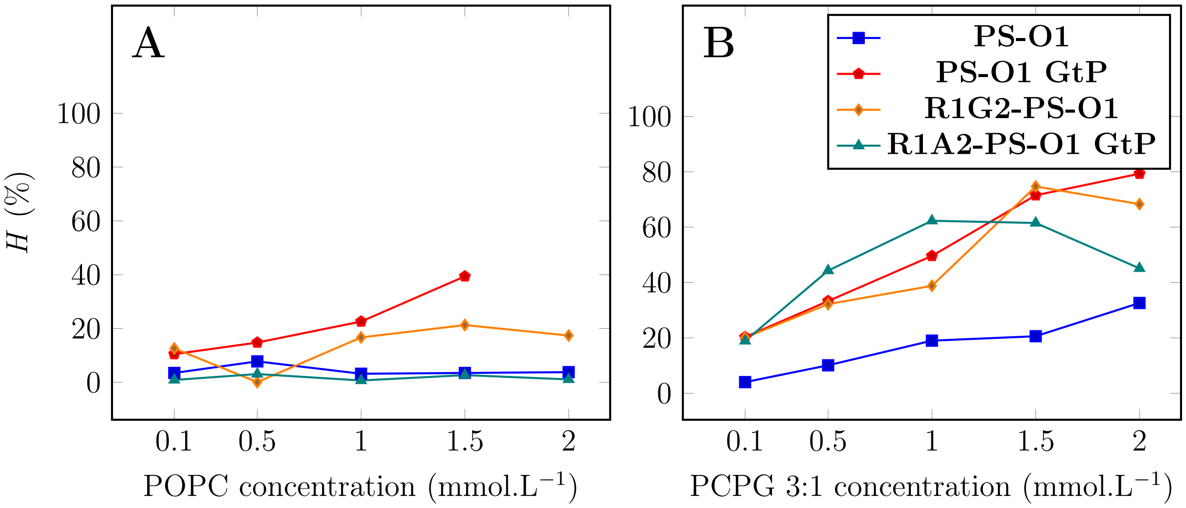

Figure 3.14: Helicity H values for **PS-O1**, **PS-O1 GtP**, **R1G2-PS-O1** and **R1A2-PS-O1 GtP** in the presence 0.1, 0.5, 1.0, 1.5, and 2.0 mmol.L^{-1} (**A**) POPC and (**B**) POPC:POPG 3:1 LUVs, calculated by CDPro®.

As expected, H values for the synthesized analogues in the presence of POPC LUVs are low and do not follow a particular trend, since all curves are characteristic of a random coil conformation. On the other hand, values obtained in the presence of POPC:POPG 3:1 LUVs indicate α-helical conformations at different concentrations among the synthesized compounds, with some displaying α-helical patterns at concentrations as low as 0.5 mmol.L^{-1} POPC:POPG 3:1. Furthermore, glucosylation increased H for **PS-O1 GtP** for all LUVs concentrations compared to **PS-O1**, as did the introduction of Arg for **R1G2-PS-O1**, while the helicity of **R1A2-PS-O1** increased until 1 mmol.L^{-1} POPC:POPG 3:1 compared to **R1G2-PS-O1**, decreasing at higher concentrations.

Comparing the spectral profiles and helix percentages of **PS-O1** derivatives with the ones obtained for **PS-1**, **-2**, **-3**, and their Glucotriazole-peptide (GtP) derivatives in the presence of POPC:POPG 3:1 LUVs (GUIMARÃES, 2017), the values of θ_{208} for the **PS-O1**-derived compounds are considerably more negative, being as negative as $\sim -25,000$

deg.cm^2.dmol^{-1}, while the glucotriazole-peptide of **PS-1** ([pOAcGlc-trz-A^{19}]PS-1) showed $\theta_{208} \sim -10,000$, being the most negative of the group studied by Guimarães. The less pronounced helicity of **PS-1**, **-2**, **-3**, and their GtPs was explained by a partitioning between their unbound random coil forms and bound α-helical forms, which was observed by Isothermal Titration Calorimetry (ITC) experiments.

As a semi-quantitative approach to compare both groups of peptides, CD helical contents obtained by spectra deconvolution can be translated into approximate helix formation enthalpies, $\Delta H^0_{\text{helix}}$. This was first introduced by Wieprecht, by comparing calorimetry and CD data for the AMP magainin 2 amide (GIGKF LHSAK KFGKA FVGEI MSN−NH$_2$) (WIEPRECHT et al., 1999; WIEPRECHT et al., 2000; WIEPRECHT et al., 2002) in the presence of POPC:POPG 3:1 LUVs. In these studies, a $\Delta H^0 \times$ helicity plot (kcal.mol$^{-1} \times$ %) yielded the expression

$$\Delta H^0 = -0.80 \cdot n_{\text{helix}} + 10.5, \tag{3.9}$$

where n_{helix} is the number of amino acid residues that comprise the helix. Also, **Equation 3.9** shows that $\Delta H^0_{\text{helix, r}}$ — the mean enthalpy of helix formation per residue — is equal to −0.80 kcal.mol^{-1}. However, considering all studies done by Wieprecht *et al.*, $\Delta H^0_{\text{helix, r}}$ actually ranges from 0.6 to 0.8. Using **Equation 3.9** as basis, a second expression can be derived, correlating $\Delta H^0_{\text{helix, r}}$ values to helicity, yielding

$$\Delta H^0_{\text{helix}} = n_{\text{helix}} \cdot \Delta\vartheta_{\text{helix}} \cdot \Delta H^0_{\text{helix, r}}, \tag{3.10}$$

where $\Delta\vartheta_{\text{helix}}$ is the difference between the helicity at the smallest and highest LUV concentration. Applying this reasoning to the compounds synthesised in this thesis and juxtaposing them to the results obtained by Guimarães, the comparison between helicities and helix formation thermodynamics becomes clearer (**Table 3.5, Page 81**).

As can be seen, $\Delta H^0_{\text{helix}}$ adequately reflects the differences in H for the compounds. An important aspect is that glucosylation of **PS-O1** promotes a stronger binding to anionic vesicles, while the glucosylation of **R1G2-PS-O1** furnishes an opposite result. Furthermore, the introduction of Arg residues increased interaction enthalpies substantially, which indicate that the membrane partitioning observed for **PS-1**, **-2**, **-3**, and their glucoforms likely does not happen for the arginine-containing derivatives of **PS-O1**.

Table 3.5: $\Delta H^0_{\text{helix}}$ (kcal.mol^{-1}) data calculated by Guimarães (GUIMARÃES, 2017) for **PS-1**, **-2**, **-3**, and their glucoforms, and calculated for **PS-O1**, **PS-O1 GtP**, **R1G2-PS-O1**, and **R1A2-PS-O1 GtP**, based on the number of residues that comprise the helix (n_{helix}) and the difference between the helicity at the smallest and highest LUV concentration ($\Delta\vartheta_{\text{helix}}$) for each peptide.

Peptide	n_{helix}[a]	$\Delta\vartheta_{\text{helix}}$	$\Delta H^0_{\text{helix}}$ (kcal.mol^{-1})
PS-1	15	22.0	-2.64
[pOAcGlc-trz-A^{19}]PS-1	15	27.3	-2.87
PS-2	15	34.6	-3.63
[pOAcGlc-trz-A^{14}]PS-2	15	27.4	-2.88
PS-3	11	19.4	-1.50
[pOAcGlc-trz-A^{19}]PS-3	15	16.8	-1.29
PS-O1	14	28.6	-2.80
PS-O1 GtP	17	59.0	-7.02
R1G2-PS-O1	19	54.6	-7.26
R1A2-PS-O1 GtP	17	52.6	-6.26

[a] n_{helix} for **PS-O1**, **PS-O1 GtP**, **R1G2-PS-O1**, and **R1A2-PS-O1 GtP** are obtained by NMR calculations and better discussed in **Chapter 4.**

Chapter 4 | NMR Studies

4.1 Introduction

NMR is one of the most powerful current spectroscopic tools. Its use over the years since its discovery in 1938 by Rabi (RABI et al., 1938) and initial applications in 1946 by Bloch and Purcell (BLOCH et al., 1946; PURCELL et al., 1946) became widespread to the point of ubiquity across many fields of science. Among the importance of NMR in areas such as metabolomics (EMWAS et al., 2019; WISHART, 2019) and drug discovery (PELLECCHIA et al., 2002), its use in structural biochemistry and biophysics is one of its bigger contributions. Following the works on 2D NMR by Jeener and Ernst (AUE et al., 1976), the investigation of Basic Pancreatic Trypsin Inhibitor (BPTI) by Wüthrich, and his subsequent book about protein and nucleic acid NMR (WÜTHRICH; WANGER, 1975; WÜTHRICH, 1986), NMR-enabled structure calculations of proteins and peptides became an important facet of biophysical and biochemical structural studies. In this section, some detail will be given pertaining the experiments and the assignment methodology, as well as a background on peptide structure calculation protocols.

4.1.1 Experiments

Throughout the years, NMR spectrometer components and experiments were continuously upgraded to yield better results. Biomolecular NMR experiments, in particular to determine the three-dimensional structure of peptides, can be narrowed down to TOtal Correlation SpectroscopY (TOCSY), Nuclear Overhauser Effect SpectroscopY (NOESY), $^{1}H-^{13}C$ Heteronuclear Single Quantum Correlation ($^{1}H-^{13}C$-HSQC), and $^{1}H-^{15}N$ Heteronuclear Single Quantum Correlation ($^{1}H-^{15}N$-HSQC).

TOCSY - TOtal Correlation SpectroscopY

TOCSY experimental results provide chemical shift information on the many spin systems of each amino acid residue. This is done by coherence transfer between all ^{1}H atoms belonging to a single spin system through the spin locking mechanism. To better illustrate this, **Figure 4.1** shows the typical pulse sequence of a TOCSY experiment.

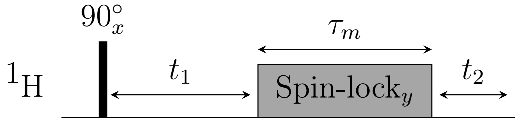

Figure 4.1: General graphic pulse sequence of the 2D-TOCSY experiment. t_1 represents the increments to be performed in the indirect dimension, τ_m is the mixing time, t_2 is the acquisition time in the direct dimension and 90°_x represents a 90° pulse along the x axis.

The pulse sequence begins with a 90°_x pulse, which excites the ^{1}H nuclear spins and nutates them to the $+y$ axis in the rotating frame, acquiring a single-quantum coherence. After t_1, during which the magnetization will evolve, the spin-lock radiofrequency (rf) field is applied along the $+y$ axis, *i.e.*, parallel to the magnetization vector $\vec{M}_y$, during the mixing time τ_m. Data is then acquired during t_2.

The spin-lock rf field can be understood as a sequence of closely-spaced $\tau - 180^\circ_y - \tau$ intervals that promote continuous spin-echoes, essentially locking $\vec{M}_y$ and preventing evolution in the chemical shift. The J-couplings between ^{1}H nuclei, however, continue to evolve during τ_m. The condition of strong coupling is maintained for the J-coupled spins by conferring virtually the same chemical shift to them — *i.e.*, similar coupling constants, J, and chemical shift, δ, values.

The strong coupling condition is the crux of this experiment since, for a strongly coupled AB spin pair, the interactions of spin A cannot be treated independently from the interactions of spin B, and vice-versa. Then, when a spin C is J-coupled to spin B, the establishment of the spin-lock rf field, or the Hartmann-Hahn match, for those spins enables the transfer of single-quantum coherence from spin A to B, and from B to C.

The spin-lock used in this thesis uses the DIPSI-2 pulse sequence (**Figure 4.2**), which employs an isotropic mixing scheme (SHAKA et al., 1988; CAVANAGH; RANCE, 1992), where the effective Hamiltonian contains only bilinear operators — *i.e.*, related to scalar coupling, J.

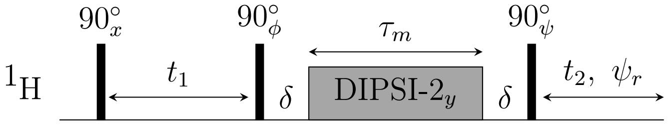

Figure 4.2: General graphic pulse sequence of the 2D-TOCSY experiment applying the DIPSI-2 mixing scheme. t_1 represents the increments in the indirect dimension, δ is the power switching period, τ_m is the mixing time, t_2 is the acquisition time in the direct dimension, $90^\circ_{i=x,\phi,\psi}$ represents a 90° pulse phased along the i axis, and ψ_r is the receiver phase.

For a TOCSY experiment that uses DIPSI-2, $\vec{M}_y$ is nutated to the z-axis by a 90° pulse after t_1. The spin-lock rf field is then applied and z-magnetization is transferred between the spins while the isotropic mixing scheme is maintained. A second 90° pulse restores single-quantum coherence and precludes acquisition during t_2. Pulse phases ϕ and ψ and receiver phase ψ_r represent the phase cycling required to filter z-magnetization, being $\phi = x, -x, x, -x$, $\psi = x, x, -x, -x$ and $\psi_r = x, -x, -x, x$.

Considering that spins of a given spin system will experience the Hartmann-Hahn match and will transfer coherences among them, each amino acid residue will reveal a type of spectral profile, as shown in **Figure 4.3** for a hypothetical Valine (Val)-Alanine (Ala) segment of a peptide structure.

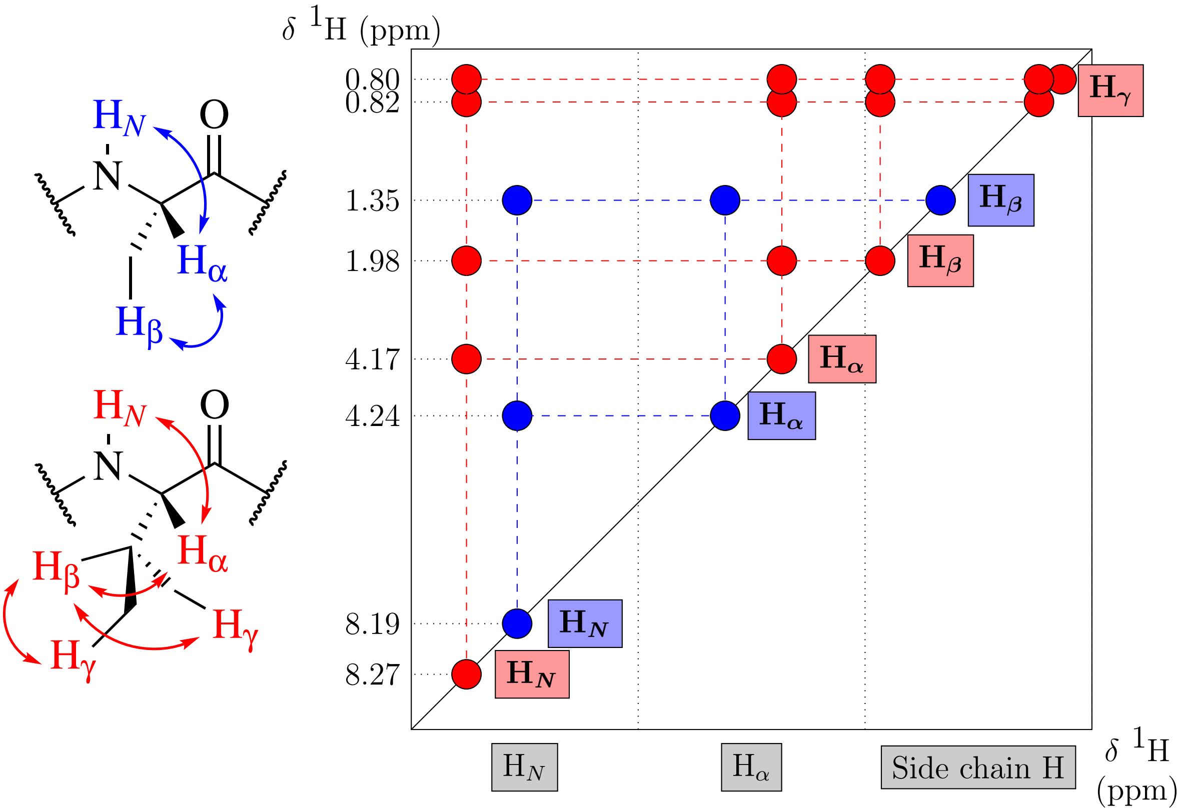

Figure 4.3: Theoretical TOCSY correlation pattern for a Val-Ala segment of a peptide structure, showing correlations between amide hydrogens (H_N), H_α, H_β and H_γ contained in each spin system. Val correlations are shown in red and Ala, in blue. Side-chain structures (left) show the relevant J-coupled spins that give rise to the correlations.

Notable aspects of the pulse sequence used in this thesis (`dipsi2esgpph`, **Figure 4.4, Page 85**) include the use of an excitation sculpting step before acquisition during t_2 for water suppression and the use of gradient pulses (G_z) to select coherence pathways while also improving water suppression — mostly enabled by the presaturation period (`presat`).

NOESY - Nuclear Overhauser Effect SpetroscopY

The NOESY is based on the dipolar coupling between spins—*i.e.*, those that possess spatial proximity—as opposed to J-coupled in the TOCSY. The detection of dipolar-coupled spins enables the analysis of cross-peaks intensities and their conversion into internuclear distance restraints, used in structural calculations. The Nuclear Overhauser Effect (NOE), or the dipolar longitudinal cross-relaxation between spins, is the phenomenon that enables a correlation map to be formed, and it can be explained by discussing four aspects: the NOE phenomenon itself,

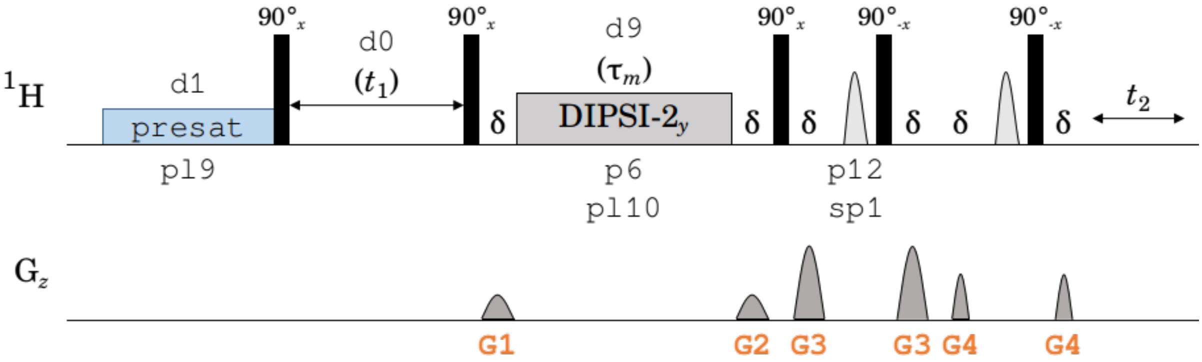

Figure 4.4: Graphical pulse sequence of the `dipsi2esgpph` experiment. `d1`, `d0`, and `d9` represent the relaxation delay, concomitant to the presaturation (`presat`) time, increments in the indirect dimension (t_1), and the TOCSY mixing time (τ_m), respectively. δ represents time interval between pulses. `pl9` and `pl10` are the presaturation and DIPSI-2 power levels (in dB), respectively. `p6` and `p12` represent the pulse lengths of DIPSI-2 and of the shaped pulses, respectively. `sp1` is the shaped pulse parameter 1. `G1`-`G4` represent the gradient pulses of different intensities along the sequence. t_2 is the acquisition time in the direct dimension.

how it can be detected, how it can be translated to distance parameters, and the typical pulse sequence characteristics.

When a given spin S has the population difference of its transitions altered via saturation or inversion by an rf pulse, a dipolar-coupled spin I will have the population difference of its transitions altered as a consequence. **Figure 4.5** shows, on the left, the energy diagram of a dipolar-coupled and J-decoupled, I, S spin pair under isotropic conditions.

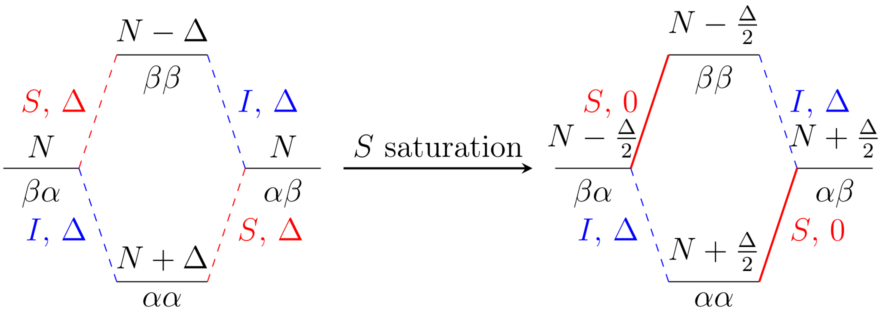

Figure 4.5: Representation of an I,S spin system under isotropic conditions, J-decoupled and dipolar-coupled. The first diagram (left) represents the energy transitions, with relative population differences shown as Δ. The second diagram (right) represents the spin system after saturation of the S transitions, equalizing the population differences of this spin whilst maintaining the same for I.

The population difference of their single-quantum spin transitions are dictated by Boltzmann equilibrium statistics. Saturation of the S spin transitions disturbs the population equilibrium and, therefore, the system will attempt to restore it by longitudinal relaxation processes, R_1, particularly by the dipolar mechanism. The diagram in **Figure 4.5** shows four single-quantum transitions that can occur in this system and can be observed in NMR spectra. There are, however, two more transitions that can contribute to restoring population differences; zero- and double-quantum. Each transition has a particular probability, W, as seen in **Figure 4.6**.

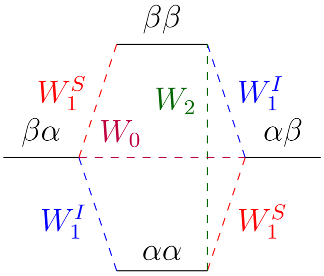

Figure 4.6: Representation of the transition probabilities, W, associated with each energy transition in an I,S spin pair. W_1^i is the single-quantum transition probability ($i = I$ or S) while W_2 and W_0 are the double- and zero-quantum transitions, respectively.

The W_2 and W_0 transitions, although not directly observed in the NMR spectra, are the main contributors for NOE to develop between the spins. When $W_2 > W_0$, a positive NOE is observed, since the population exchange increases the difference for the I transitions. If $W_0 > W_2$, however, a negative NOE is produced as the population difference for I decreases. It is known that W_2 is prevalent in small molecules and/or systems with fast motion, while W_0 dominates for larger molecules and/or environments with slower dynamics. Therefore, negative NOE enhancements are expected in biomolecules like proteins.

Accordingly, the focus of the NOESY experiment is to translate cross-peak intensities to internuclear distance restraints, enabling peptide structure calculations. This is possible due to the nature of NOE enhancement and how it relates to transition probabilities and internuclear distance. **Equation 4.1**, the Solomons equation, shows the dependence of the NOE enhancement from spin S to spin I ($\eta_I\{S\}$) as a function of transition probabilities.

$$\eta_I\{S\} = \frac{\gamma_S}{\gamma_I}\left[\frac{W_2 - W_0}{W_0 + 2W_1^I + W_2}\right] = \frac{\gamma_S}{\gamma_I}\left[\frac{\sigma_{IS}}{\rho_{IS}}\right]. \tag{4.1}$$

The cross-relaxation rate, σ_{IS}, will yield the NOE signal. Furthermore, the dipolar longitudinal relaxation rate of I, ρ_{IS}, shows how W_1^I influences the NOE magnitude. The gyromagnetic ratios, γ_I and γ_S, reflect the different equilibrium populations for each spin. The transitions probabilities, W, are related to internuclear distance by **Equations 4.2-4.4**.

$$W_1^I \propto \gamma_I^2 \gamma_S^2 \left[\frac{3\tau_c}{r^6 \left(1 + \omega_I \tau_c^2\right)} \right], \tag{4.2}$$

$$W_0 \propto \gamma_I^2 \gamma_S^2 \left[\frac{2\tau_c}{r^6 \left(1 + \left(\omega_I - \omega_S\right)^2 \tau_c^2\right)} \right], \tag{4.3}$$

$$W_2 \propto \gamma_I^2 \gamma_S^2 \left[\frac{12\tau_c}{r^6 \left(1 + \left(\omega_I + \omega_S\right)^2 \tau_c^2\right)} \right]. \tag{4.4}$$

Transition probabilities, W, depend on gyromagnetic ratios, γ, transition frequencies, ω, and internuclear distance, r. Therefore, it can be assumed that the NOE build-up rate will also be dependent upon r. This fact is the basis for transient NOE experiment, in which a population inversion, as opposed to saturation, of spin S promotes an NOE build-up during a mixing time τ_m, after which a 90° pulse produces the coherence detected during the acquisition time. As can be seen in **Figure 4.7**, the general pulse sequence involves the nutation of the magnetization vector $\vec{M}_z$ onto the xy-plane ($\vec{M}_{-y}$) by a 90° pulse and, during t_1, chemical shift information is labelled. A second 90° pulse is then applied, nutating $\vec{M}_{-y}$ to the $-z$ axis. During the mixing time τ_m, $\vec{M}_{-z}$ will experience NOE build-up. After τ_m, a final 90° pulse generates a single-quantum coherence along y that is acquired during t_2, yielding a 2D spectrum.

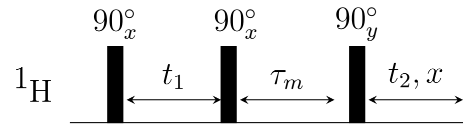

Figure 4.7: General graphic pulse sequence for the NOESY experiment.

The `noesyesgpphzs` experiment (**Figure 4.8, Page 88**), used in this thesis, differs from the general experiment since it includes the use of gradient pulses (G_z) to select coherence pathways, improving water suppression together with an excitation sculpting routine before t_2, and suppressing zero-quantum coherences with a shaped pulse applied during τ_m (THRIPPLETON; KEELER, 2003).

As mentioned previously, the internuclear distance, r, is the variable of interest. Also, what is truly evaluated during a NOESY experiment is the kinetics of NOE build-up, which can be visualized as

$$\frac{dI_z}{dt} = 2\sigma_{IS} S_z^0, \tag{4.5}$$

where the rate of magnetization build-up, dI_z/dt, is a function of the initial S magnetization, S_z^0, and the cross-relaxation term, σ_{IS}. For a homonuclear NOE, this can be expressed as

$$\sigma_{I,I} = W_2 - W_0 = \frac{2\gamma^4 \tau_c}{r^6} \left(\frac{6}{1 + 4\omega_I^2 \tau_c^2} - 1 \right). \tag{4.6}$$

Therefore, r^{-6} is directly obtained from the NOE build-up rate. Instead of relying on ki-

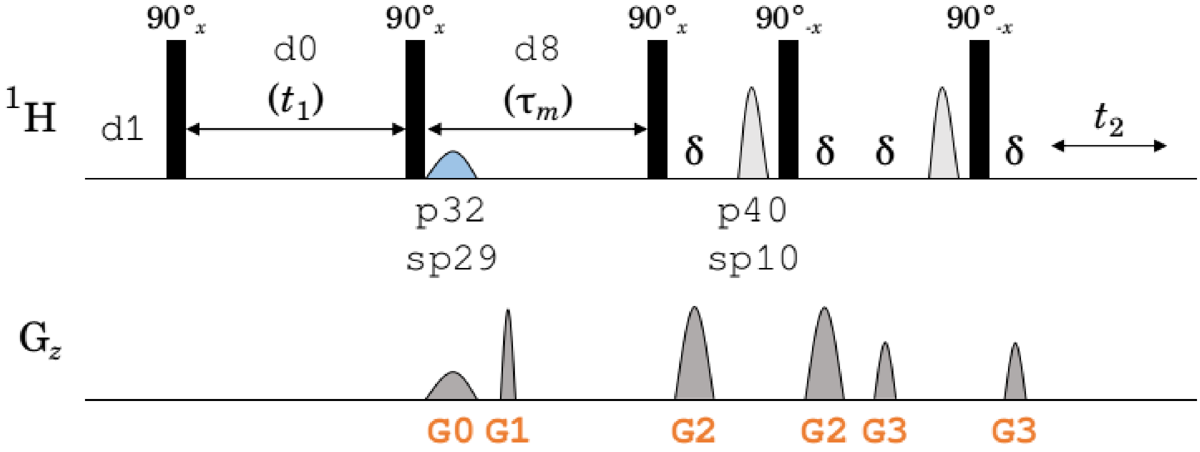

Figure 4.8: Graphical pulse sequence of the `noesyesgpphzs` experiment. `d1`, `d0`, and `d8` represent the relaxation delay, increments in the indirect dimension (t_1), and the NOESY mixing time (τ_m), respectively. δ represents time interval between pulses. `p32` and `p40` represent the pulse lengths of the shaped pulses, and `sp29` and `sp10` are their respective parameters. `G0`-`G3` represent the gradient pulses of different intensities along the sequence. t_2 is the acquisition time in the direct dimension.

netics, NOESY experiments use τ_m values to ensure an initial rate approximation, during which low values of τ_m ensure that NOE is exclusively dependent on r^{-6}. This allows for the NOE enhancement η to be used as the main observable, such that

$$\eta_I\{S\} = k\sigma_{IS}\tau_m = k' r_{IS}^{-6}\tau_m. \tag{4.7}$$

Considering that correlation time (τ_c) values are accessible for the analyzed system, internuclear distances can be easily obtained. In contrast, experimental $\eta_I\{S\}$ values are compared with known intensities $\eta_X\{Y\}$ related to known distances r_{XY}^{-6}, since

$$\frac{\eta_I\{S\}}{\eta_X\{Y\}} = \frac{r_{IS}^{-6}}{r_{XY}^{-6}}, \tag{4.8}$$

allowing the straightforward calculation of r_{IS}^{-6}. Finally, considering that molecular tumbling in solution NMR is isotropic, the more appropriate representation of the internuclear distance term is $\langle r^{-6}\rangle$, since structural averaging eventually ensues.

HSQC - Heteronuclear Single-Quantum Correlation

The ^{1}H$-^{13}$C-HSQC and ^{1}H$-^{15}$N-HSQC experiments identify directly bound (*i.e.*, ^1J-coupled) ^{1}H$-^{13}$C and ^{1}H$-^{15}$N pairs, which are useful for peptide resonance assignments. Besides offering information on ^{15}N and ^{13}C chemical shifts, which may be useful to obtain geometrical restraints, the contour maps are important controls for the assignments of resonances in the TOCSY and NOESY experiments, mainly in cases of correlation superposition.

Notably, since ^{1}H−^{15}N-HSQC yields ^{1}H−^{15}N correlations, using as little D_2O as possible in NMR samples is paramount since ^{2}H atoms can exchange with H_N atoms in the peptide, eliminating a substantial amount of cross peaks. Nevertheless, the acquisition of extra experiments in the presence of D_2O may allow the characterization of well defined structural arrangements in peptide, due to the relatively slower ^{2}H/^{1}H exchange ratio (GOMES et al., 2018).

The typical pulse sequence for a Heteronuclear Single Quantum Correlation (HSQC) experiment is presented in **Figure 4.9**.

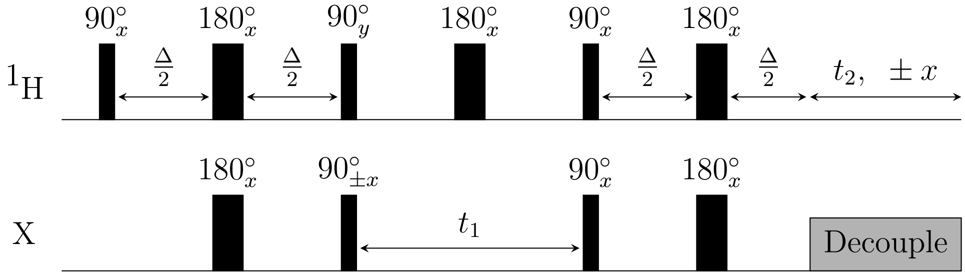

Figure 4.9: General graphic pulse sequence for an HSQC experiment. X represents a heteronucleus, t_1 represents the increments performed in the indirect dimension, and t_2 is the acquisition time in the direct dimension.

Although this pulse sequence is better explained using the product operator formalism[1], some central aspects of the HSQC can be discussed without it. The initial pulse block of the sequence, before t_1, is called an Insensitive Nuclei Enhancement by Polarization Transfer (INEPT) and it represents the transference of single-quantum coherence (*i.e.*, polarization) from the ^{1}H spin system to X. δ information from both nuclei is then labelled into X during t_1 and the 180° pulse refocuses the ^{1}H−X J-coupling evolution, effectively decoupling them. After this period, a reverse-INEPT is applied, in order to transfer coherence back to the more sensitive nucleus, increasing the sensitivity of the experiment. The final coherence transfer characterizes an inverse detection scheme. Finally, during the acquisition time t_2, a decoupling pulse is applied in X.

The ^{1}H−^{13}C-HSQC experiment used in this thesis (`hsqcedetgpsp.3`, **Figure 4.10, Page 90**) has some differences compared to the general pulse sequence, like the use of shaped pulses at the ^{13}C frequency during the INEPT steps. Also, the experiment is multiplicity edited, accomplished by a pulse scheme prior to the final INEPT, gradient pulses (G_z) are employed to select coherence pathways and eliminate artifacts, and the decoupling is done using the Globally-optimized, Alternating-phase, Rectangular Pulses (GARP) routine.

The ^{1}H−^{15}N-HSQC experiment used in this work (`hsqcetgpsi`, **Figure 4.11, Page 90**) has two core differences from the general pulse sequence. First, gradient pulses (G_z) are employed to select coherence pathways and eliminate artifacts. Second, the Preservation of Equivalent Pathways (PEP) technique is used to enchance sensitivity (LEE et al., 2014; CAVANAGH; RANCE, 1993), performed by pulse sequences before and after the final INEPT.

---

[1] A full description of this sequence using the product operator formalism in **Appendix A**.

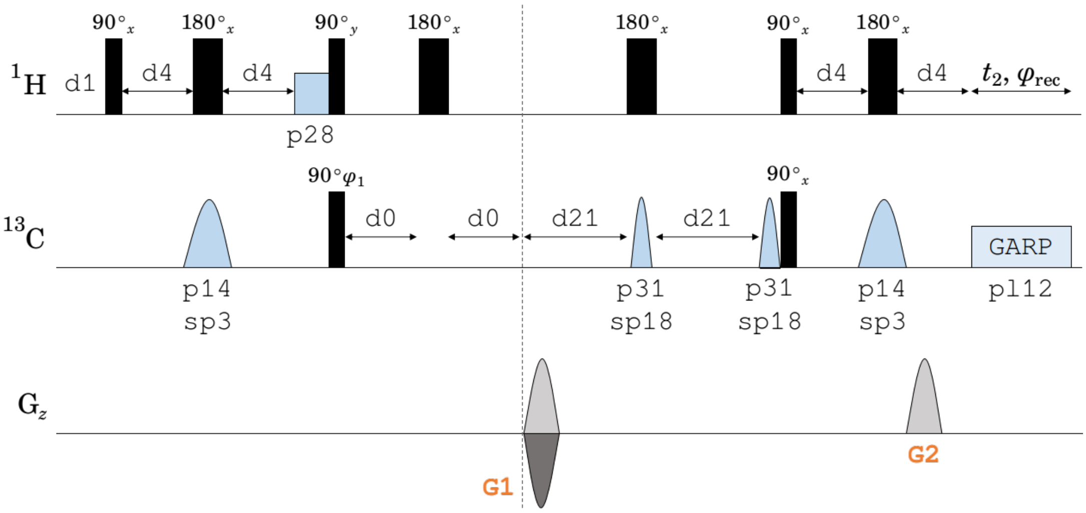

Figure 4.10: Graphical pulse sequence of the `hsqcedetgpsp.3` experiment. `d1`, `d4`, `d0`, and `d21` represent the relaxation delay, $\Delta/2$ increments of INEPT, $t_1/2$ increments in the indirect dimension, and multiplicity edition delays, respectively. `p28`, `p14`, and `p31` represent the pulse lengths of the squared pulse, of the shaped pulse during the INEPT steps, and of the shaped adiabatic pulses. `sp3` and `sp18` are the parameters of the shaped pulses. `pl12` is the power level of the `GARP` decoupling pulses. `G1` and `G2` represent the gradient pulses of different intensities along the sequence. t_2 is the acquisition time in the direct dimension, and ϕ_1 and ϕ_{rec} are the phases of the pulse and receiver in the Echo/Antiecho-TPPI detection, respectively.

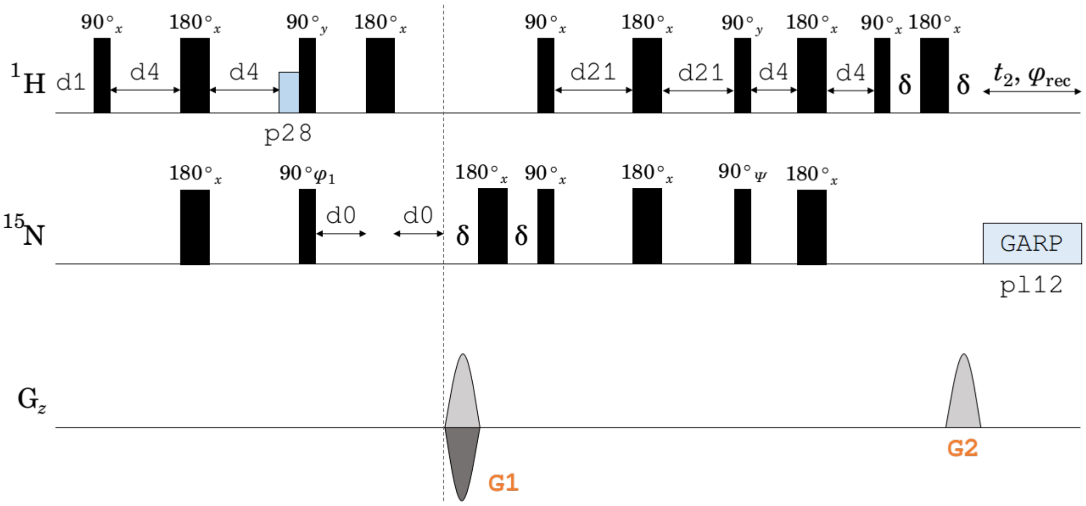

Figure 4.11: Graphical pulse sequence of the `hsqcetgpsi` experiment. `d1`, `d4`, `d0`, and `d21` represent the relaxation delay, $\Delta/2$ increments of INEPT, $t_1/2$ increments in the indirect dimension, and PEP delays, respectively. `p28` represents the pulse length of the squared pulse. δ represents time interval between pulses. `pl12` is the power level of the `GARP` decoupling pulses. `G1` and `G2` represent the gradient pulses of different intensities along the sequence. t_2 is the acquisition time in the direct dimension, and ψ_1 and ψ_{rec} are the phases of the pulse and receiver in the Echo/Antiecho-TPPI detection, respectively.

Information from HSQC spectra is relevant in structural studies since, along with internuclear distance restraints from NOESY data, chemical shifts, especially of H_α, C_α, and H_N, are known secondary structure probes, differing significantly between random coil and α-helical/β-conformations. Furthermore, they can be correlated to dihedral angles ϕ and ψ using programs such as `TALOS+` and `TALOS-N` (CORNILESCU et al., 1999; SHEN et al., 2009; SHEN; BAX, 2013), providing additional structural information for calculations.

4.1.2 Strucuture calculation from NMR data

Each experiment previously described serve a particular purpose in the workflow of NMR structural elucidation. Internuclear distance restraints and chemical shift values are often used in structural calculation, with some related factors and characteristics that will be further discussed. First, analysis of peptide bonds in protein structures indicates that those biopolymers will often adopt a secondary structure, such as α-helices and β-conformations, due to intramolecular hydrogen bonds between amide and carbonyl groups. To adopt a secondary structure, however, the primary structure must fold and adjust the relative position of its backbone atoms to attain a higher structural degree. This folding can be described by the different values of two important dihedral angles, ϕ and ψ, formed between certain atoms along the backbone (**Figure 4.12**).

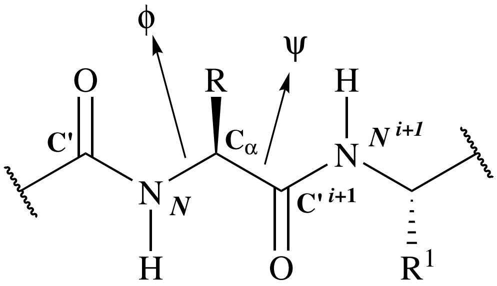

Figure 4.12: Representation of two dihedral angles in a peptide structure, ϕ and ψ. ϕ is the torsion angle of the $N-C_\alpha$ bond, encompassing C', N, C_α, and $C'^{\,i+1}$. ψ is the torsion angle of the $C_\alpha-C'$ bond and encompasses N, C_α, $C'^{\,i+1}$, and N^{i+1}.

Both ϕ and ψ are the two degrees of freedom that lead to the folding of the peptide chain and, by knowing all values for both, accessing the three-dimensional structure of the peptide backbone is straightforward. The Ramachandran diagram is a good example of this structural dependence on both dihedral angles, showing the typical (ϕ, ψ) regions for secondary structures, like α-helices and β-conformations (RAMACHANDRAN et al., 1963). Intermolecular forces are also important and facilitate structural elucidation. Although there are many types of interaction, like hydrogen bonds and Coulomb interactions, van der Waals forces that are established under short distances ($r < 5\,\text{Å}$) are the most preponderant due to their abundance (ALMEIDA et al., 2013).

NMR structural calculations involve Molecular Dynamics (MD) simulations, which aim to find the most stable structures along a conformational space determined by NMR experimental parameters. This can be done by using Newtonian mechanics — *i.e.*, by solving Newton's equations of motion for different integration times — or by using Laplacian mechanics, which produces similar results but avoids some vectorial formalisms and facilitates calculations. Briefly, MD simulations using Newtonian mechanics compute the atoms' trajectory at each time step dt and correlate position $\boldsymbol{r}$ to force $\boldsymbol{F}$ by Newton's second law

$$\boldsymbol{F} = m\boldsymbol{a} = -\nabla V, \tag{4.9}$$

where

$$\nabla V(x, y, z) = \frac{\partial V}{\partial x}\boldsymbol{e_x} + \frac{\partial V}{\partial y}\boldsymbol{e_y} + \frac{\partial V}{\partial z}\boldsymbol{e_z}. \tag{4.10}$$

In **Equations 4.9** and **4.10**, the forces that act upon the system are calculated by the gradient of the potential energy ∇V. Furthermore, $\boldsymbol{e_x}$, $\boldsymbol{e_y}$ and $\boldsymbol{e_z}$ are unit vectors. Alternatively, the potential energy gradient can be written as

$$\nabla V = -m\frac{d^2\boldsymbol{r}}{dt}, \tag{4.11}$$

correlating the forces that act upon the atoms, described by the force parameters that comprise V (also known as the force field), with their position $\boldsymbol{r}$ at a time step dt. Although V has many components related to bond lengths, bond angles, proper and improper dihedral angles, and nonbonding interactions potentials, experimental data is better represented by distance and dihedral angle restraints pseudopotentials for peptide and protein structural studies.

As explained in **Section 4.1.1, Page 84**, average distance values can be obtained from NOE cross-peak intensities by comparing with known values. This is done by calibrating the obtained NOE intensities to certain distances that roughly characterize the interaction strength. ^{1}H–^{1}H distances are often binned to 2.8 Å for strong interactions, 3.4 Å for medium, and 5.0 Å for weak interactions. Therefore, each atom will have a lower distance boundary L_{ij}, typically set at 1.8 Å — the shortest distance between two ^{1}H, according to their van der Waals radii — and an upper distance boundary U_{ij}, equal to the calibrated restraint. A typical quadratic pseudopotential for NOE distance restraints is described as

$$V_{ij} = \begin{cases} C_1\left(r - L_{ij}\right)^2, & \text{if } r < L_{ij} \\ 0, & \text{if } L_{ij} < r < U_{ij} \\ C_2\left(r - U_{ij}\right)^2, & \text{if } r > U_{ij} \end{cases}, \tag{4.12}$$

where an interatomic distance r is evaluated against U_{ij} and L_{ij}, increasing V_{ij} quadratically in case it stays outside the interval, while modulated by the steepness-controlling force constants C_1 and C_2 (ALMEIDA et al., 2013).

The pseudopotential related to dihedral angles ϕ and ψ can be described by a target angle θ_{target} and an allowed variation $\Delta\theta$. They are obtained from the `TALOS` package and will be explained further. The pseudopotential associated to dihedral restraints V_{dihe} is defined by

$$V_{\text{dihe}} = \begin{cases} C_3\left(\theta - \theta_{\text{target}}\right)^2, & \text{if } \theta < \theta_{\text{target}} - \Delta\theta \\ 0, & \text{if } \theta_{\text{target}} - \Delta\theta < \theta < \theta_{\text{target}} + \Delta\theta \\ C_4\left(\theta - \theta_{\text{target}}\right)^2, & \text{if } \theta > \theta_{\text{target}} + \Delta\theta \end{cases}, \tag{4.13}$$

where an angle θ is evaluated against the experimental input data, also increasing V_{dihe} quadratically if outside the defined boundaries, modulated by force constants C_3 and C_4.

Although Newtonian mechanics is used for MD structure calculations in programs such as `XPLOR`, others such as `Xplor-NIH` and `DYANA` use Lagrangian mechanics, using

$$L = T - V, \tag{4.14}$$

where L in the Lagrangian function, T is the kinetic energy and V, the potential, and

$$\frac{d}{dt}\left(\frac{\partial L}{\partial \dot{\theta}_i}\right) - \frac{\partial L}{\partial \theta_i} = 0, \tag{4.15}$$

where θ_i is the dihedral angle and $\dot{\theta}_i$, its time-derivative, *i.e.*, the velocity. Importantly, no term in **Equations 4.14** and **4.15** are vectorial, simplifying the coordinate system and, therefore, the calculations. Furthermore, the structure can be characterized by all torsion angles θ_i that define the parameter $\theta_i = (\theta_1, \theta_2, \ldots, \theta_n)$, where n is the number of rigid bodies of the system. By analysing Newtonian mechanics, *i.e.*, cartesian space MD, and Lagrangian mechanics, or torsion angle space MD, the former has $3N$ cartesian coordinates as degrees of freedom and the latter has n torsion angles, significantly reducing computation complexity (GÜNTERT, 1998).

Different from cartesian MD, torsion angle space MD uses a single potential V, defined by

$$V = \begin{cases} 0, & \text{if distance and angle restraints are met with no steric overlap} \\ V_{\text{target}}, & \text{otherwise} \end{cases}, \tag{4.16}$$

where V_{target} is defined by

$$V_{\text{target}} = \sum_{c=u,\ l,\ v} w_c \sum_{(\alpha,\beta)\in I_c} f_c\left(d_{\alpha\beta}, b_{\alpha\beta}\right) + w_a \sum_{i\in I_a}\left(1 - \frac{1}{2}\left(\frac{\Delta_i}{\Gamma_i}\right)^2\right)\Delta_1^2. \tag{4.17}$$

w_c, where $c = u,\ l,\ v$ represents upper, lower distance bound, and van der Waals interactions, are distance restraint weighing factors and a contribution of a distance restraint violation to the distance restraint function, given by $f_c\left(d_{\alpha\beta}, b_{\alpha\beta}\right)$. The last term represents torsion angle restraints, is weighted by the factor w_a, and has the terms Δ_i, which is the size of an angle violation for a rigid body i, and $\Gamma_i = \pi - \left(\theta_i^{\max} - \theta_i^{\min}\right)/2$, the half-width of the forbidden range of torsion angle values for it (GÜNTERT, 1998).

Finally, perhaps the most widely used algorithm for MD simulations is the simulated annealing (SA), an optimization method based on statistical mechanics and a metallurgic process of heating a given metal to very high temperatures and then slowly cooling it. This process is reproduced in the algorithm, so that the biomolecular structure undergoes a temperature variation simulation in this regime, facilitating the determination of the global energy minimum, instead of stopping on local minima. SA is a variation of the hill-climbing method, using a probabilistic approach in order to comb through neighbouring states based on a given temperature T and an energy difference ΔE between a given state s and its neighbour s^*, where

$$p = 1 - e^{(\Delta E/kT)}. \tag{4.18}$$

p is the probability of accepting the move to a neighbour state and k is a constant that relates the temperature T to energy E (*i.e.*, Boltzmann's constant for physical systems). As can be seen, although p is always higher than zero except at the final point, where the function is optimized and $\Delta E = 0$, it is much closer to 1 at higher T and gradually decreases as the system cools down (GUILMEAU et al., 2021).

For NMR structure calculations, this optimization routine is used to minimize the potential energy function, and some differences can be perceived between cartesian and torsion angle dynamics. For the former, SA is lengthy since much of the computational time is spent on calculating geometrical parameters that do not change significantly (*i.e.*, bong lengths) from the parameterized values. However, the degrees of freedom for torsion angle MD are torsion angle values and, therefore, extensive calculations are skipped and the overall efficiency of the process is increased (ALMEIDA et al., 2013).

4.2 Methodology

4.2.1 Nuclear Magnetic Resonance Experiments

Samples of each compound at 2.0 mmol.L^{-1} were prepared in 600 µL of a pH 7.0 phosphate buffer (20 mmol.L^{-1}) TFE-d_2:H_2O (60:40, v:v) solution. Sodium 3-(trimethylsilyl)propane-1-sulfonate (DSS), 1 mmol.L^{-1}, was used as the internal chemical shift standard for ^{1}H and ^{13}C resonances. TFE-d_2 from Cambridge Isotope Labs (CIL) and ultrapure water were used for the preparation of the solution.

TOCSY, NOESY, ^{1}H−^{13}C-HSQC, and ^{1}H−^{15}N-HSQC experiments were performed at 20 °C, at Laboratório de Ressonância Magnética de Alta Resolução (LAREMAR), UFMG, using a Bruker Avance Neo 600 equipped with a 5 mm BroadBand Observe (BBO) SmartProbe with coils suited for pulsed field gradients. Water resonances in TOCSY and NOESY experiments were suppressed by presaturation. The spectrometer magnetic field was homogenized (shimmed), the probe channels were tuned and matched with respect to each nucleus. Initially, 1D ^{1}H experiments with water presaturation (`zgpr`) were performed to optimize experimental conditions.

TOCSY experiments (`dipsi2esgpph`) were acquired using the Decoupling In the Presence of Scalar Interactions-2 (DIPSI-2) scheme (RUCKER; SHAKA, 1989). The parameters used for the experiments were spectral widths of 6578.947 Hz (10.96 ppm) in both dimensions and 512 increments in the indirect dimension with 16 transients of 4096 total points collected for each Free-Induction Decay (FID).

NOESY experiments (KUMAR et al., 1980) (`noesyesgpphzs`) were acquired with mixing times of 100, 150, 200 and 250 ms with the intent of checking whether or not spin diffusion would ensue. The experiments parameters included a spectral width of 6578.947 Hz (10.96 ppm) in both dimensions and 512 increments in the indirect dimension with 32 transients of 4096 total points collected for each FID.

Two different $^1H-^{13}C$-HSQC experiments (`hsqcedetgpsp.3`) were acquired focusing on the aromatic or aliphatic carbon chemical shift regions of the entire contour map. Their acquisition parameters were:

1. For the aliphatic chemical shift region $^1H-^{13}C$-HSQC, a spectral width of 6578.947 Hz (10.96 ppm) for the ^1H dimension and 12820.513 Hz (85.47 ppm) for the ^{13}C dimension was used, with 512 increments in the indirect dimension with 32 transients of 2048 total points acquired for each FID and offset (O1) equal to 5659.043 Hz (37.72 ppm);

2. For the aromatic chemical shift region, a spectral width of 6578.947 Hz (10.96 ppm) for the ^1H dimension and 9363.296 Hz (62.42 ppm) for the ^{13}C dimension was used, with 256 increments in the indirect dimension with 24 transients of 2048 total points acquired for each FID and offset (O1) equal to 19618.019 Hz (130.79 ppm).

$^1H-^{13}C$-HSQC experiments were acquired with phase sensitivity in such a way that correlations involving CH or CH_3 groups would present positive phase, whereas correlations involving CH_2 groups would present negative phase (WILLKER et al., 1993). $^1H-^{15}N$-HSQC experiments (SCHLEUCHER et al., 1994; FAIRBROTHER et al., 1991) (`hsqcetgpsi`) were acquired with a spectral width of 6578.947 Hz (10.96 ppm) for the ^1H dimension and 2554.93 Hz (42.01 ppm) for the ^{15}N, with 130 increments in the indirect dimension with 400 transients of 1024 total points acquired for each FID and offset (O1) equal to 6993.457 Hz (60.82 ppm).

TOCSY and NOESY experiments were acquired with a States-Time Proportional Phase Increments (States-TPPI) method (MARION et al., 1989) for quadrature detection in the indirect dimension and the Echo-AntiEcho selection method (DAVIS et al., 1992) was used in the heteronuclear experiments.

4.2.2 NMR data processing and analysis

Spectra were processed using `NMRPipe` (DELAGLIO et al., 1995). Linear prediction FID reconstruction algorithms and other features such as zero-filling, appropriate apodization functions, and necessary zeroth- and first-order phase corrections were used for data processing.

The interpretation and assignment of the obtained contour maps were performed using the `NMRViewJ` (JOHNSON; BLEVINS, 1994) program, as part of the NMRFx integrated software for NMR analysis, developed by One Moon Scientific, Inc. following the general workflow of simultaneous analysis described by Wüthrich (WÜTHRICH, 1986).

Correlations observed in the NOESY contour maps were converted into semiquantitative internuclear distance restraints which were then calibrated using algorithms proposed by Hyberts *et al.* (HYBERTS et al., 1992). Distance restraints were associated with NOE correlation intensities such that strong correlations were attributed to a 2.8 Å internuclear distance, medium ones to 3.4 Å and weak ones to 5.0 Å.

4.2.3 Structure calculation by molecular dynamics

Determination of distance restraints related to NOE correlation intensities allowed the calculation of the three-dimensional structures for the four peptide derivatives. Additional calculation input based on restraints of dihedral angles ϕ and ψ was given by the `TALOS-N` and `TALOS+` program suites, and Artificial Neural Network (ANN)-predicted helical fraction and S^2 values for each residue were also determined (SHEN; BAX, 2013; SHEN et al., 2009). From the extended structure, generated as a template with the peptide sequence as reference, 200 structures were calculated using a simulated annealing optimization algorithm (NILGES et al., 1988) as part of `Xplor-NIH` 2.17 (SCHWIETERS et al., 2003; SCHWIETERS et al., 2006).

The optimized calculation used a given number of heating steps up to a temperature of 1000 K and subsequent cooling steps. From the 200 generated structures, the ten most stable ones were used to compose the peptide ensemble in the TFE-d_2:H_2O 60:40 solution. The stereochemical quality of each ensemble was verified using `PROCHECK-NMR` (LASKOWSKI et al., 1996). Manipulation and visualization of the structures were done using `PyMOL` (Schrödinger, LLC, 2015).

Notably, calculations were initially done using only distance restraint data obtained from NOESY; `TALOS-N` or `TALOS+` data is then used as additional dihedral restraints and as a refinement for the calculation. Furthermore, subsequent calculated structures using `TALOS` were compared with the ones obtained exclusively by NOESY data to check whether the obtained results are appropriate. This method of using `TALOS` data as additional refinement to calculations prevents eventual unrealistic structural changes.

4.3 Results and Discussion

4.3.1 NMR signal assignments

The NMR contour maps' correlations were assigned in order to obtain chemical shift and NOE correlation intensity values for the peptides. This was done, as previously stated, using the simultaneous analysis methodology described by Wüthrich (WÜTHRICH, 1986). Importantly, although CD results indicate that all peptides attain a higher degree of helicity in the presence of TFE-d_2:H_2O 50:50 solutions (**Chapter 3, Section 3.2.2, Page 70**), the medium utilized was 60:40 in order to have a better basis of comparison between the results obtained previously for phylloseptin-1, -2 and -3 (**PS-1**, **PS-2** and **PS-3**, respectively) (RESENDE et al., 2008). In the following discussion, an overview of the simultaneous analysis methodology will be described and all presented figures will be of spectra obtained for **PS-O1**, unless the spectra of other peptides are relevant to a given section.

The TOCSY contour map has a crucial role in the assignment (**Section 4.1.1, Page 82**), displaying correlations between two J-coupled spins along a given spin system (**Figure 4.13**). Since magnetization is transferred between hydrogen nuclei in the same spin system during the TOCSY pulse sequence, a proper assignment of this spectrum can yield the precise microenvironment (*i.e.*, chemical shift value) of a substantial amount of ^{1}H atoms of the peptide.

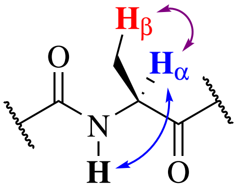

Figure 4.13: Possible (H_N, H_α) and (H_N, H_β) correlations of Ala in a TOCSY spectrum.

Figure 4.14 shows a section of the TOCSY contour map, displaying how the amide hydrogen nuclei of residues Ser-13, Ala-11 and Ala-8 (**PS-O1**), represented by 13.H, 11.H and 8.H, respectively, correlate to their respective side chain ^{1}H atoms.

PS-O1
FLSLI PHAIN AVSTL VHHSG-NH_2
8 11 13

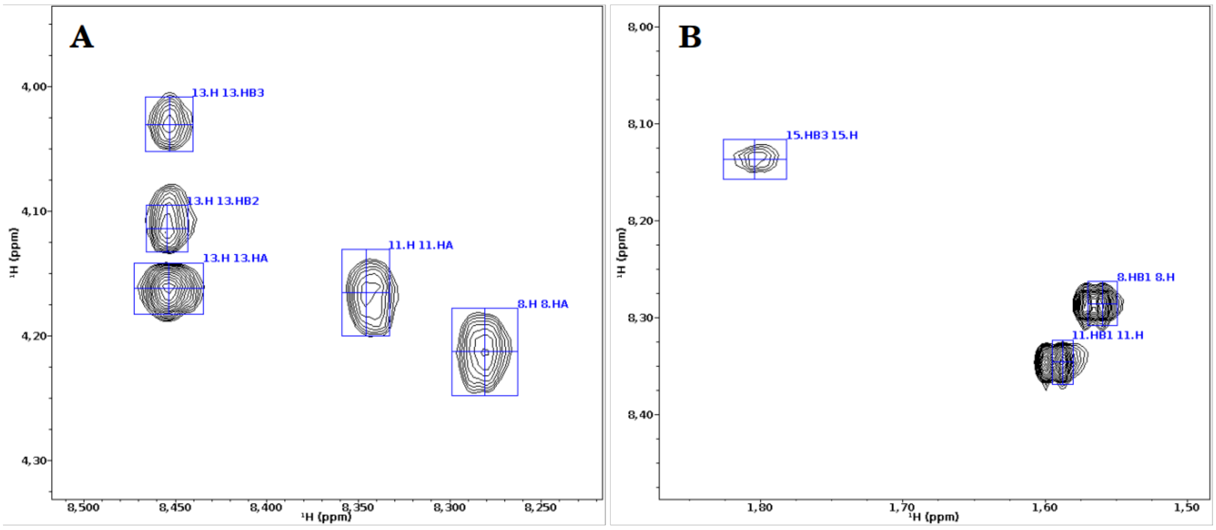

Figure 4.14: Sections of the TOCSY contour map of **PS-O1** (600 MHz) at 2.0 mmol.L^{-1}, in TFE-d_2:H2O 60:40 (v:v), and at pH 7.0 (phosphate buffer at 20 mmol.L^{-1}). Amide hydrogen (H_N) nuclei correlations with side chain ^{1}H atoms in residues Ser-13, Ala-11 and Ala-8 are shown. (**A**) H_α atoms are represented as HA, (**B**) H_β as HB, and H_N as H. Cross-peak nomenclature follows the $AH_i.BH_j$ type, denoting the coupling of residue A's hydrogen H_i with residue B's hydrogen H_j.

Alanine residues, as a matter of fact, are good starting points for resonance assignment, since they possess a simple spin system with only α and β side-chain hydrogens that are sufficiently far apart chemical shift-wise. Furthermore, Ala H_β usually display an average chemical shift of $\bar{\delta} \sim 1.35$ ppm and the spectral region involving correlations between these Ala H_β and H_N is sufficiently devoid of other correlations in the TOCSY contour map, providing great clarity in their observation.

Although superposition may take place due to coincidence of chemical shift values, each amino acid residue's hydrogen atoms are expected to have distinct chemical shift values related to their microenvironments and to follow estimated values[2].

The leftmost section of the TOCSY contour map, especially the amide hydrogen (F1) × α-hydrogen (F2) chemical shift region, has signals with enough resolution and dispersion so as to yield few ambiguities, even though the section containing the side chain hydrogen atom correlations were notably crowded. Both regions, nevertheless, had their correlations properly assigned, as shown in **Figure 4.15, Page 98**.

PS-O1
FLSLI PHAIN AVSTL VHHSG-NH_2

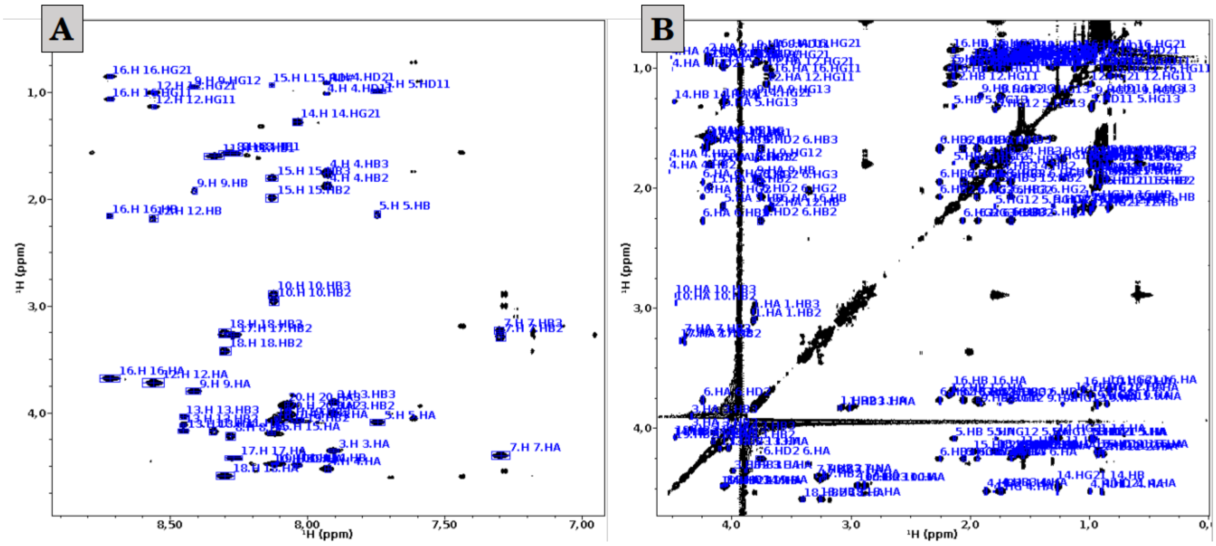

Figure 4.15: Sections of the TOCSY contour map of **PS-O1** (600 MHz) at 2.0 mmol.L^{-1}, in TFE-d_2:H_2O 60:40 (v:v), and at pH 7.0 (phosphate buffer at 20 mmol.L^{-1}). Correlations are shown between (**A**) amide hydrogen atoms (F1) and side chain ones (F2), and (**B**) between side chain hydrogen nuclei with all relevant atoms properly assigned.

By analysing the superposition of the TOCSY contour maps of all four peptides (**Figure 4.16**), the differences in chemical shifts for some (H_N, H_α) cross-peaks give insights into some of their structural features. First, analysis of the H_N chemical shift values for (H_N, H_α) cross-peaks circled in black reveals that, in the middle regions of the peptides (*i.e.*, encompassing

---

[2] ^{1}H, ^{13}C and ^{15}N reference chemical shift values were obtained in the Biological Magnetic Resonance Data Bank, `https://bmrb.io/ref_info/stats.php?restype=aa&set=full`.

residues 7, 9, 12, 13, 15 and 16 for **PS-O1**), δ values for H_N atoms differ and follow a pattern where $\delta_{\textbf{PS-O1 GtP}} > \delta_{\textbf{PS-O1}} \sim \delta_{\textbf{R1G2-PS-O1}} > \delta_{\textbf{R1A2-PS-O1 GtP}}$. This indicates that, along this helical segment, the dihedral angles ϕ and ψ will be similar for **PS-O1** and **R1G2-PS-O1** while being different from **PS-O1 GtP** and **R1A2-PS-O1 GtP**, alluding to possible differences in structural stabilities among these two groups.

PS-O1	FLSLI PHAIN AVSTL VHHSG-NH_2
PS-O1 GtP	(GtP)FLSLI PHAIN AVSTL VHHSG-NH_2
R1G2-PS-O1	RGFLSLI PHAIN AVSTL VHHSG-NH_2
R1A2-PS-O1 GtP	R(GtP)FLSLI PHAIN AVSTL VHHSG-NH_2

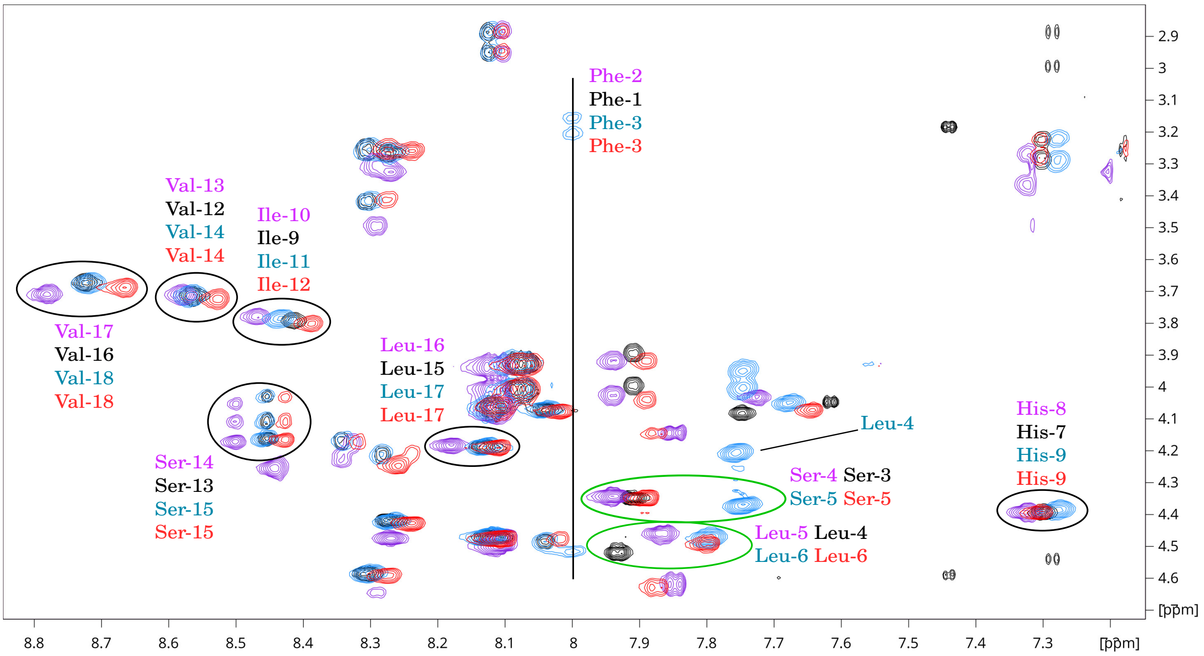

Figure 4.16: Superposition of TOCSY contour maps showing (H_N, H_α) cross-peaks for **PS-O1** (black), **PS-O1 GtP** (purple), **R1G2-PS-O1** (blue) and **R1A2-PS-O1 GtP** (red). Relevant correlations are labeled with their respective amino acid residues for each peptide sequence, displayed above the spectra superposition and color-coded accordingly, with the central region highlighted in brown. Spectra were superposed in `CcpNmr` (SKINNER et al., 2016).

Second, residues near the *N*-terminus (like residues 1, 3 and 4 for **PS-O1**), contrary to what was observed for the more intermediate sections of the peptide, display varied chemical shift values for (H_N, H_α) cross-peaks (green circles and black straight line in **Figure 4.16**). This indicates a smaller degree of structural similarity between the structures, as expected for this region, which is typically less structured than the rest of the peptide. Finally, as an extreme case, **R1G2-PS-O1** was the only peptide to display an (H_N, H_α) cross-peak for Leu-4[3]. This indicates that this peptide might display more helical content near the *N*-terminus. It is worth

---

[3] Due to the insertion of an Arg-Gly residue pair at position 1 of **PS-O1**, this position corresponds to residue Leu-2 in **PS-O1**.

noting that NOESY contour maps for these peptides displayed similar patterns and trends (δ-wise) as observed for the TOCSY.

Once the chemical shift of some hydrogen nuclei was determined, the $^{1}H-^{13}C$-HSQC contour map was used as a control to differentiate C_β atoms of His and Phe residues, for instance. This contour map is used thusly due to the direct correlations between hydrogen chemical shifts along the indirect dimension and ^{13}C chemical shifts along the direct dimension for ^{1}J-coupled (^{1}H, ^{13}C) pairs. Additionally, the heteronuclear spectrum is cleaner than the homonuclear given the greater chemical shift window of carbon-13 when compared to hydrogen, and because only ^{1}J-coupled ^{1}H, ^{13}C pairs are visible in the $^{1}H-^{13}C$-HSQC, reducing cluttering and superposition. Furthermore, $^{1}H-^{13}C$-HSQC data is collected in a phase-sensitive fashion, yielding positive-phase correlations for CH and CH_3 groups, and negative ones for CH_2 groups, providing unambiguous assignments. As an example, Pro-6 H_α and H_δ atoms, once identified in the TOCSY spectrum, can have their respective carbon chemical shift values obtained unequivocally by the correlations present in the heteronuclear contour map (**Figure 4.17**).

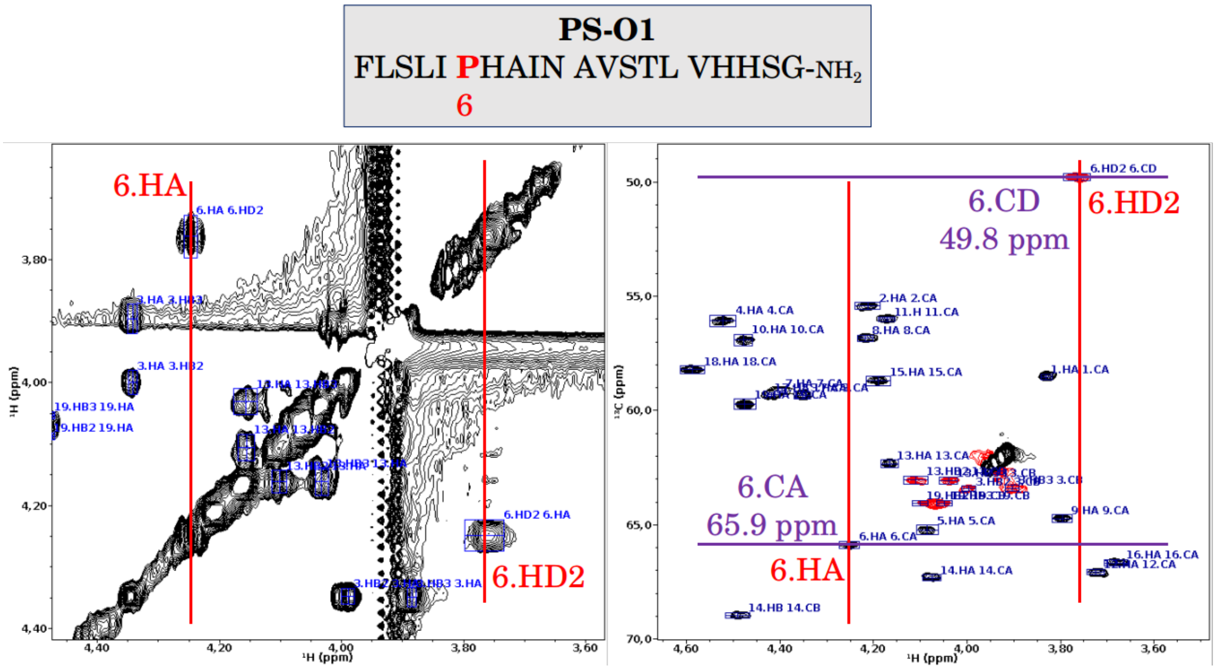

Figure 4.17: Representation of how a carbon-13 nucleus resonance can be properly assigned in a $^{1}H-^{13}C$-HSQC spectrum by knowing the chemical shift of its ^{1}J-coupled hydrogen atom in the TOCSY spectrum. In this case, Pro-6 H_α and H_δ atoms (6.HA and 6.HD2, respectively) of **PS-O1** are directly correlated to their respective carbon atoms, 6.CA and 6.CD, respectively, in the heteronuclear spectrum.

Two spectra were collected for the $^{1}H-^{13}C$-HSQC, one with emphasis on aliphatic carbons and another on aromatics (**Section 4.2.1, Page 94**), which was fruitful, since the acquisition of a single spectrum can hinder data processing, generating problematic phase artifacts. **Figure 4.18** shows both spectra with relevant carbon resonances assigned and, though they present all expected carbon signals, only those within the spectral width are properly digitized.

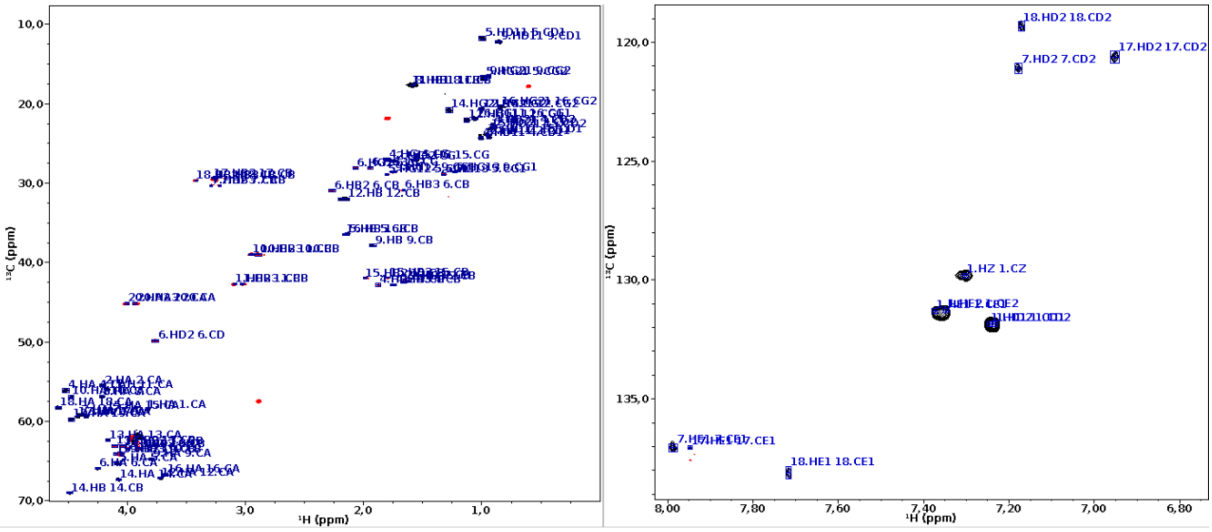

Figure 4.18: Assigned ^{1}H–^{13}C-HSQC spectra of **PS-O1** (600 MHz) at 2.0 mmol.L^{-1}, in TFE-d_2:H$_2$O 60:40 (v:v), and at pH 7.0 (phosphate buffer at 20 mmol.L^{-1}). On the left, the offset was set to the region of aliphatic ^{13}C atoms (37.7 ppm) and, on the right, for aromatic ones (130.8 ppm).

Similar to the analysis of the TOCSY contour maps, the superposition of the respective ^{1}H–^{13}C-HSQC spectra (**Figure 4.19**) provides important insights. Residues in the central regions of the peptides (*i.e.*, residues 8, 11, 13, 15, 18 and 19 for **PS-O1**) display similar H$_\alpha$ chemical shift values (black ellipses in **Figure 4.19**), whereas residues near the *N*-terminus (*i.e.*, residues 2, 3 and 4 for **PS-O1**) yield more spaced correlations (green ellipses in **Figure 4.19**). This indicates an apparent lack of structural similarity, which is expected since peptides rarely have defined secondary structures at the *N*-terminus. Notably, for His-18 (**PS-O1**), its (C$_\alpha$, H$_\alpha$) correlation in **PS-O1 GtP** is distant, chemical shift-wise, from the others, which form a group with lower δ (**Figure 4.19**) and this is also noticed for His-17 (not shown), indicating that **PS-O1 GtP** may present distinct structural properties near the *C*-terminus compared to the other three peptides.

PS-O1	FLSLI P**HAIN AVSTL V**HHSG-NH_2
PS-O1 GtP	(GtP)FLSLI P**HAIN AVSTL V**HHSG-NH_2
R1G2-PS-O1	RGFLSLI P**HAIN AVSTL V**HHSG-NH_2
R1A2-PS-O1 GtP	R(GtP)FLSLI P**HAIN AVSTL V**HHSG-NH_2

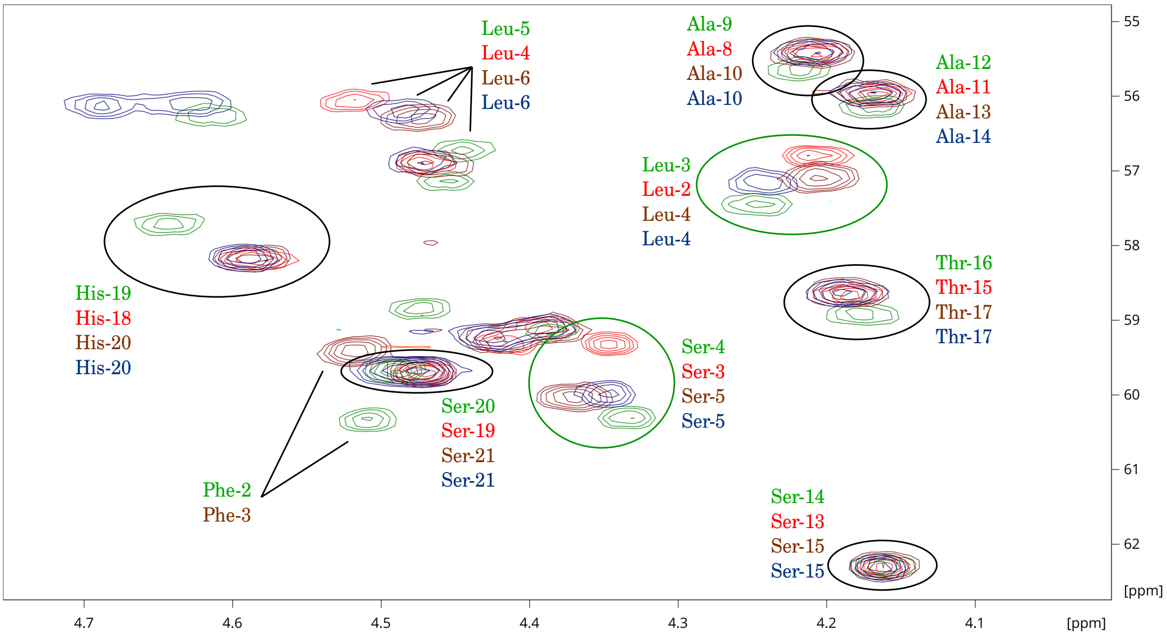

Figure 4.19: Superposition of ^{1}H$-^{13}$C-HSQC contour maps showing (C$_\alpha$, H$_\alpha$) cross-peaks for **PS-O1** (red), **PS-O1 GtP** (green), **R1G2-PS-O1** (brown) and **R1A2-PS-O1 GtP** (blue). Relevant correlations are labeled with their respective amino acid residues for each peptide sequence. Spectra were superposed using `CcpNmr`.

Although a ^{1}H$-^{15}$N-HSQC spectrum was not used in the resonance assignments for **PS-O1**, the other three peptides were assigned using this contour map. The ^{1}H$-^{15}$N-HSQC aids resonance assignment since H$_N$ δ values assing on TOCSY and NOESY contour maps can be correlated to amide N chemical shifts on the heteronuclear spectrum. Additionally, since the chemical shift window for ^{15}N is larger than for ^{1}H, the cross-peaks are more spaced out along the heteronuclear dimension and can be trivially identified and checked using the BMRB database. As an example, **Figure 4.20, Page 103** shows how TOCSY (H$_N$, H$_\alpha$) correlations can be directly associated with (H$_N$, N) cross-peaks in the ^{1}H$-^{15}$N-HSQC contour map for **R1G2-PS-O1** (**Figure 4.21, Page 103**).

The full ^{1}H$-^{15}$N-HSQC contour map displays some other interesting characteristics regarding the peptides, since side-chain amide hydrogens of Asn residues yield cross-peaks similar to C-terminal amide hydrogens of amidated peptides. Additionally, these pairs of amide hydrogens are easily distinguishable from other H$_N$ since the contour map yields the same N chemical shift for two ^{1}H resonances.

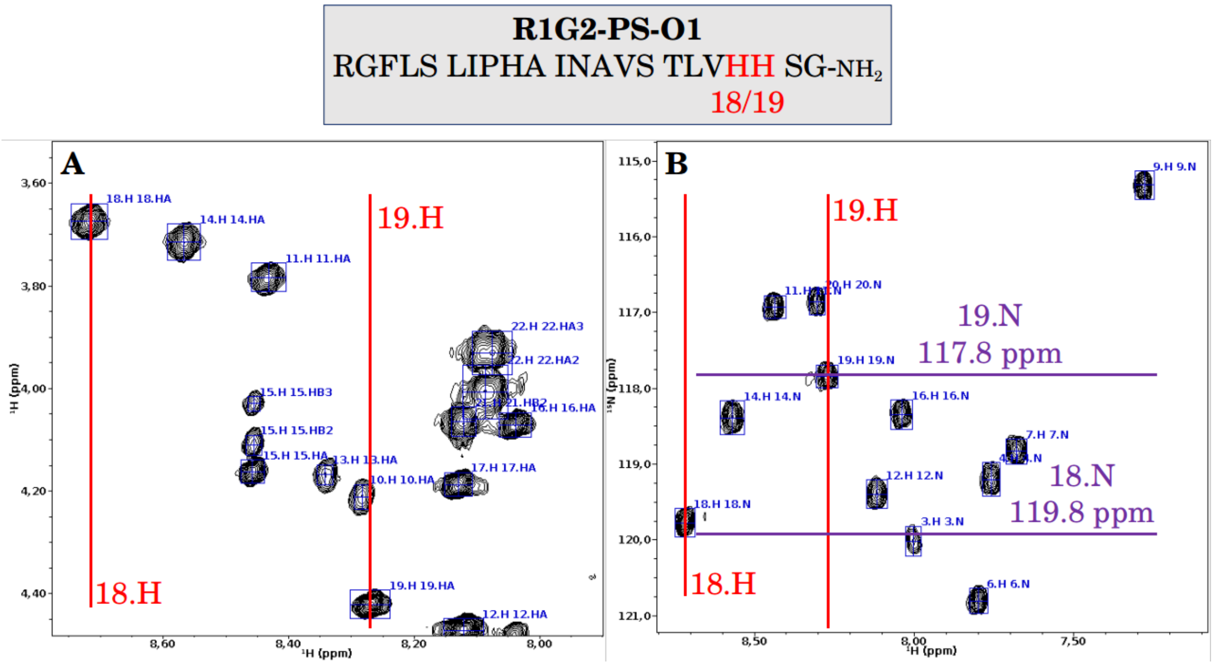

Figure 4.20: Representation of a direct correspondence between (**A**) an (H_N, H_α) correlation observed in a TOCSY contour map and (**B**) an (H_N, N) cross-peak in an $^1H-^{15}N$-HSQC spectrum. In this case, the δ value for the (H_N, H_α) cross-peak of Val-18 for **R1G2-PS-O1** (TOCSY) is directly correlated to the (H_N, H_α) cross-peak with same H_N ($^1H-^{15}N$-HSQC). The same is applied to His-19.

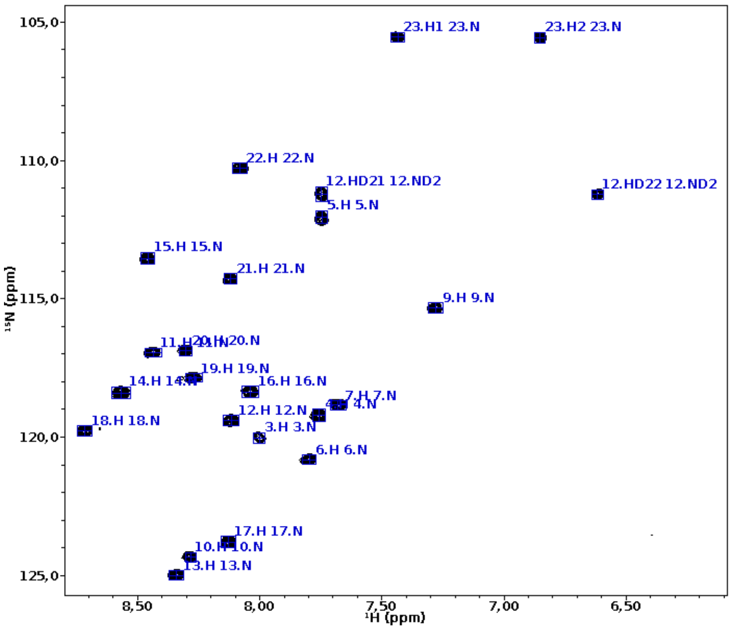

Figure 4.21: Assigned $^1H-^{15}N$-HSQC spectra of **R1G2-PS-O1** (600 MHz) at 2.0 mmol.L^{-1}, in TFE-d_2:H_2O 60:40 (v:v), and at pH 7.0 (phosphate buffer at 20 mmol.L^{-1}).

The NOESY contour map provides important information about close, medium, and long-distance spatial neighbourhoods between hydrogens. Also, cross-peaks are generated by the dipolar coupling between two sufficiently close ^{1}H, as discussed in **Section 4.1.1, Page 84**. The analysis of the NOESY was performed in tandem with the TOCSY since ^{1}H spins of α-helices show characteristic correlations in the first (**Figure 4.22**) and, by knowing the ^{1}H chemical shifts from the TOCSY spectrum, the identification of cross-peaks in the NOESY is facilitated. An amide hydrogen in a residue i, for instance, can interact with the one present in an $i+1$ residue, labeled as an N,N$_{(i,i+1)}$ correlation. Likewise, α,N$_{(i,i+j\ 1\leq j\leq 4)}$, β,N$_{(i,i+1)}$, and $\alpha,\beta_{(i,i+3)}$ correlations are typical for α-helices (WÜTHRICH, 1986).

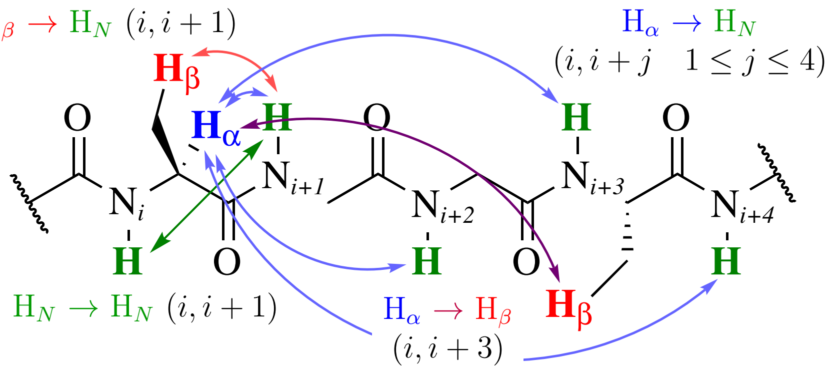

Figure 4.22: Usual ^{1}H spin correlations in the NOESY spectra of α-helical peptides, namely N,N$_{(i,i+1)}$ (green), α,N$_{(i,i+j\ 1\leq j\leq 4)}$ (blue), β,N$_{(i,i+1)}$ (red), and $\alpha,\beta_{(i,i+3)}$ (purple).

As an example of assignment, **Figure 4.23, Page 105** shows how the NOESY spectrum can indicate neighbouring residues and confirm the TOCSY assignment. Additionally, their simultaneous analysis enables the identification of intra- and inter-residual dipolar couplings by checking which correlations are present in both contour maps — when a correlation is seen in both spectra, an intra-residual dipolar coupling is observed, and an inter-residual one is usually present otherwise. This may lead to signal superposition, which can be circumvented by analysing them along both dimensions, since they have different resolutions. Moreover, a close inspection of the NOESY contour map (**Figure 4.24, Page 105**) for **PS-O1** shows many sufficiently dispersed N,N$_{(i,i+1)}$ correlations, indicating the presence of a defined secondary structure.

Additionally, N,N$_{(i,i+1)}$ correlations for **PS-O1** are observed in the spectrum starting from Leu-4, indicating that an α-helix could start from this residue. Likewise, the C-terminal amide hydrogens, represented by NH.TERM, are only correlated to each other and not to sequential H$_N$ atoms, indicating that the helix might not extend to the C-terminus. Finally, significant spin diffusion was observed for longer mixing times such as 200 and 250 ms and a substantial amount of unusual NOE correlations were observed in this case, such as α,N$_{(i,i+5)}$. Therefore, 150 ms was used for the acquisition of all NOESY spectra, whereas 100 ms or less did not yield adequate correlations.

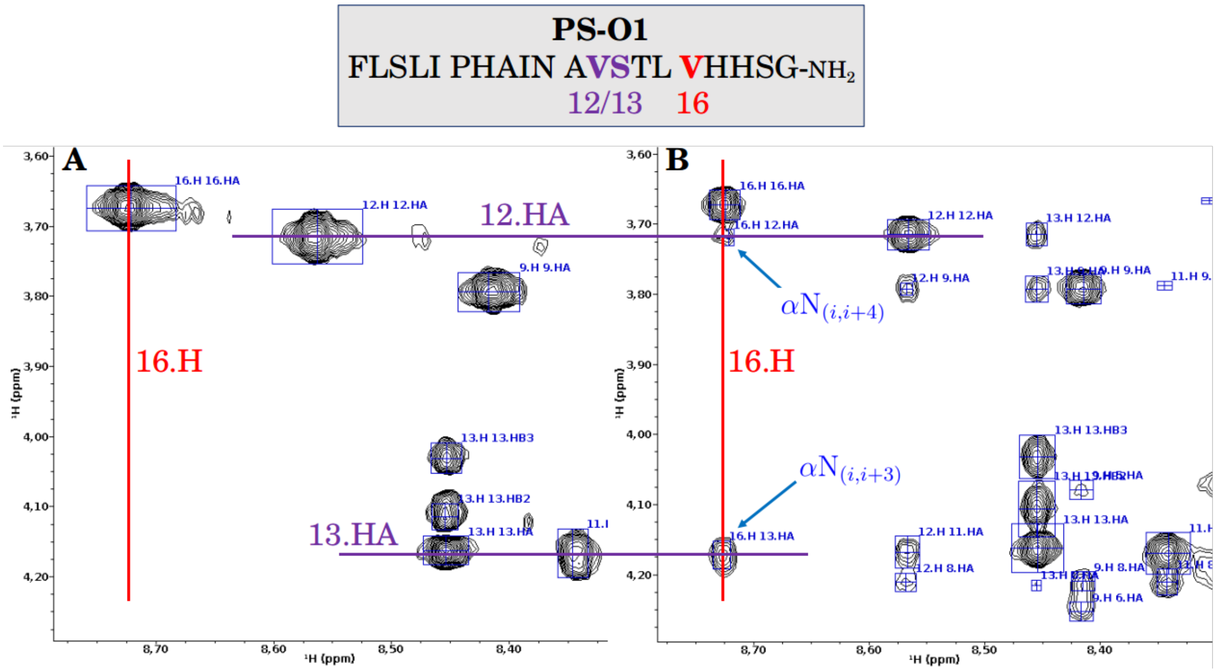

Figure 4.23: Representation of the simultaneous analysis of the (**A**) TOCSY and the (**B**) NOESY spectra. For **PS-O1**, a vertical line of the amide hydrogen of Val-16 (red) corresponds to two cross-peaks in the NOESY, belonging to α-hydrogens of Val-12 and Ser-13 (green lines) and representing $\alpha N_{(i,i+4)}$ and $\alpha N_{(i,i+3)}$ correlations, respectively.

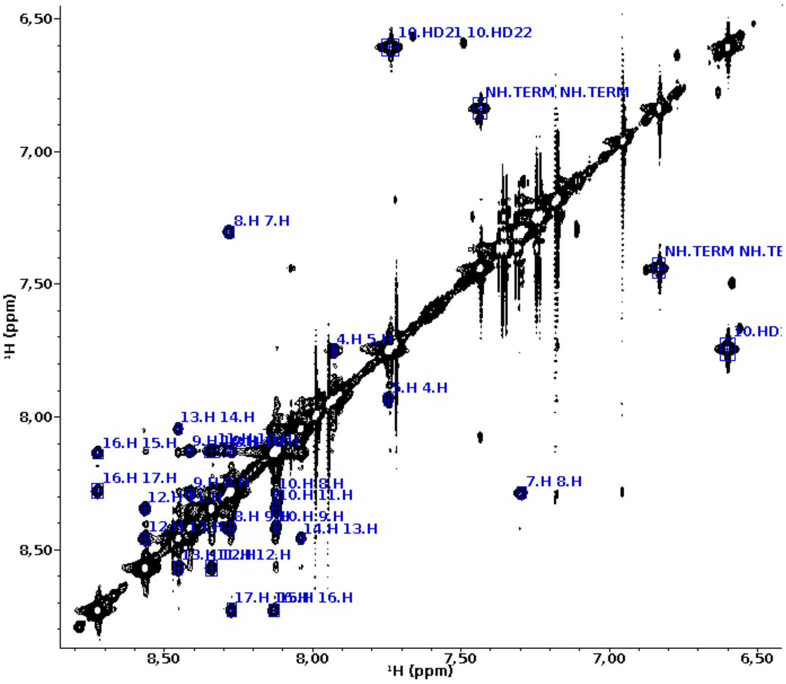

Figure 4.24: NOESY spectrum section of **PS-O1** (600 MHz), at 2.0 mmol.L^{-1}, in TFE-d_2:H$_2$O 60:40 (v:v), and at pH 7.0 (phosphate buffer at 20 mmol.L^{-1}), showing amide hydrogen N,N$_{(i,i+1)}$ correlations. Mixing time was equal to 150 ms.

4.3.2 Three-dimensional structure calculation from NMR data

As mentioned in **Subsubection 4.1.1, Page 84**, since the dipolar coupling between two nuclei depends on internuclear distance, NOESY cross-peak intensities can be converted into interatomic distance restrictions used in structural calculations. Using calibration and conversion algorithms in the `NMRView` program (JOHNSON; BLEVINS, 1994), a distance restraint list can be generated which furnishes characteristic NOEs for helical secondary structures (**Figure 4.25**).

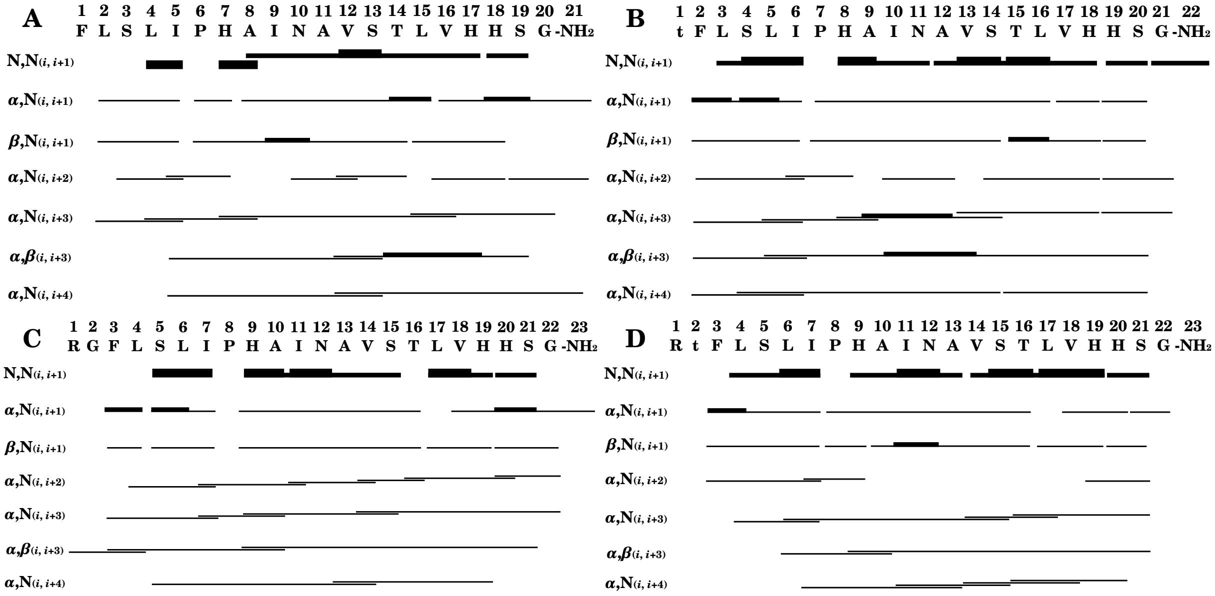

Figure 4.25: Characteristic nOe correlations of an α-helical secondary structure for (**A**) **PS-O1**, (**B**) **PS-O1 GtP**, (**C**) **R1G2-PS-O1**, and (**D**) **R1A2-PS-O1 GtP**. The thickest lines represent strong nOe correlations (2.8 Å), medium thickness ones represent medium range correlations (3.4 Å), and the thinnest lines are related to weak correlations (5.0 Å).

It can be seen that the displayed correlations are thickness-coded and medium/strong (medium and thicker lines, respectively) correlations are predominant between amide hydrogen atoms (N,$N_{(i,i+1)}$) while the rest are, mainly, weak (thinner lines) interactions. Additionally, a considerable degree of secondary structure can be verified for the products, since they show a large quantity of NOE correlations across their primary structure.

Comparison between **Figure 4.25** (**A**) and **Figure 4.25** (**B**) shows that **PS-O1** has correlations predominantly located in the central region, whereas these tend to spread out for **PS-O1 GtP**. $\alpha, \beta_{(i,i+3)}$, $\alpha, N_{(i,i+3)}$, and $\alpha, N_{(i,i+4)}$ correlations, for instance, encompass residues 4-19 for **PS-O1** and 3-20 for **PS-O1 GtP**. As these correlations are characteristic of α-helices (WÜTHRICH, 1986), the introduction of the glucosyl group likely increased the helical content. On the other hand, **Figure 4.25** (**C** and **D**) shows that, for **R1G2-PS-O1**, $(i, i+3)$ and $(i, i+4)$ interactions range from residues 3 to 21, while **R1A2-PS-O1 GtP** does not show such correlations near the N-terminus, encompassing residues 6-20, indicating that the glucotriazole moiety likely hinders interactions important to α-helix stability. Furthermore, by comparing the density of internuclear correlations for each product, **R1G2-PS-O1** probably has the largest helical content, since it has a greater interaction density in the central region and its characteristic NOEs encompass the largest residue interval among the four.

Due to the absence of amide hydrogens in Pro residues, no correlations involving them were observed in **Figure 4.25**. In this case, correlations between H_δ and H_α are essential to characterize its spin system. Also, some medium-strength $(i, i+3)$-type interactions can be seen and, although they usually involve distant atoms, helical bends and turns can shorten distances between them. Finally, NOE distance restraints are naturally underestimated, due to a greater transient NOE generated for shorter distances. Therefore, the greater restraint of a cross-peak pair was selected for calculations.

To further improve the argument for the extent of α-helical structures of each derivative, their chemical shifts were analyzed by the `TALOS-N` program (**Figure 4.26**).

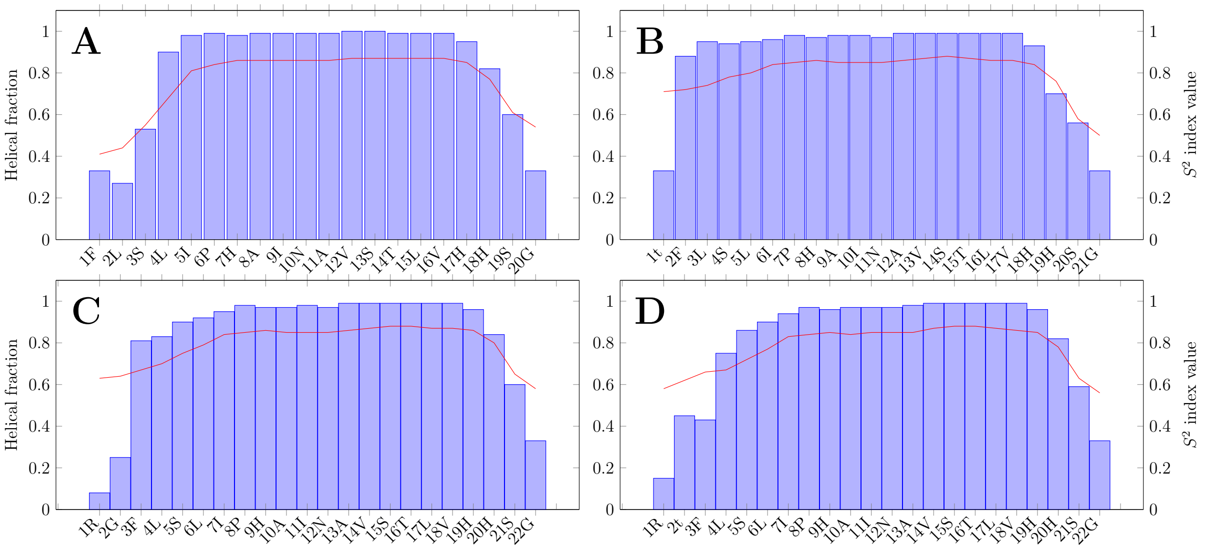

Figure 4.26: Bar charts representing the helical fraction of (**A**) **PS-O1**, (**B**) **PS-O1 GtP**, (**C**) **R1G2-PS-O1**, and (**D**) **R1A2-PS-O1 GtP** as predicted by the `TALOS-N` program's ANN (blue bars) and S^2 values for each residue (red line), also determined by `TALOS-N` with basis on the RCI method. Residues with helical fractions and S^2 values above 0.5 tend to have chemical shift values typical of α-helical structures.

The predicted degree of helical structure by the program's ANN and the calculated S^2 index for each residue (BERJANSKII; WISHART, 2005). Furthermore, for **PS-O1** (**Figure 4.26, A**), residues with typical chemical shifts of α-helices range from residue 4 to 19, representing a predicted 80% helical content. **PS-O1 GtP** (**Figure 4.26, B**), however, has a helix ranging from 2 to 20, corresponding to 90.5%, suggesting that the introduction of the glucotriazole moiety in **PS-O1** at the N-terminus increased helix-stabilizing-interactions. Alternatively, while **R1G2-PS-O1** (**Figure 4.26, C**) shows typical helix δ values for residues 3-21, glucosylation (**Figure 4.26, D**) likely dampened helix-stabilizing interactions near the N-terminus, since Phe-3 lost a substantial amount of helicity, reducing the segment to residues 4-21, corresponding to a reduction from 91% to 86%. Finally, post-translational glucosylation did not influence the helical segment at the C-terminus, since their helical fraction and S^2 remained approximately the same for all products.

Although `TALOS` data is a good probe for verifying the helicity at each residue, the helix-coil equilibrium is better represented by chemical shift analysis. This approach to secondary structure study was initially proposed in the works of Wishart *et al.*, by subtracting experimental δ values from reference random coil data, yielding secondary chemical shifts ($\Delta\delta$), assigning a possible score from -1, 0 or $+1$ to them, and then verifying strings of uninterrupted equal scores along the primary structure, which were indicatives of a given secondary structure (WISHART et al., 1992; WISHART; SYKES, 1994b). This Random Coil Index (RCI) was calculated primarily for H_α, C_α, as they are better indicators of residual secondary structure than H_β, H_N, C_β, and amide ^{15}N (SCHWARZINGER et al., 2001).

Instead of assigning indexes for given nuclei of individual residues, the sole analysis of $\Delta\delta$ values has been used to provide a structural landscape of proteins (YAO et al., 2001; ARAI et al., 2015), since α-helical motifs typically furnish positive $\Delta\delta$ values for C_α and negative $\Delta\delta$ values for H_α and H_N (WISHART; SYKES, 1994a). To this end, the appropriate choice for reference random coil chemical shift values is paramount, and the approaches and reported values have changed considerably over the years (SCHWARZINGER et al., 2000; SCHWARZINGER et al., 2001; WISHARD et al., 1995). The reference values used in this thesis were determined for H_α and C_α using model Ac-QQXQQ-NH_2 peptides, where X is any of the 20 proteinogenic amino acids, and corrected for sequence-, temperature-, and pH-based dependencies (KJAERGAARD; POULSEN, 2011; KJAERGAARD et al., 2011), and they were calculated using the Javascript "*Random coil chemical shifts for intrinsically disordered proteins*", developed by Alex Maltsev of the NIH, and maintained by the University of Copenhagen[4].

The histograms of **Figures 4.27** and **4.28** show $\Delta\delta$ values for H_α and C_α for the synthesized peptides. Although some chemical shift data could not be accurately obtained — *e.g.*, for the glucosylated residues of **PS-O1 GtP** and **R1A2-PS-O1 GtP** and for the N-terminal residue in some cases — the simultaneous analysis of both bar plots reveals that a helical structure extends throughout most of the primary structure of the peptides. For H_α $\Delta\delta$ values (**Figure 4.27**), specifically, the main difference can be seen in the string of residues with negative secondary shifts, which is slightly longer for **R1G2-PS-O1** and **R1A2-PS-O1 GtP** than for the derivatives without Arg, which might indicate a higher percentage of helix in the N-terminal region for them. When the C_α secondary shift profile is also taken into consideration, the comparison between **Figure 4.28, A** and **C** reveals a greater percentage of α-helix at the N-terminus for **R1G2-PS-O1** than for **PS-O1**, while the comparison between **Figure 4.28, A** and **B** shows the substantial structural contribution at the N-terminus provided by the glucosylation.

---

[4] Calculated chemical shift reference values and $\Delta(\delta)$ values for individual residues of each peptide sequence are displayed in **Appendix A, Tables A.4-A.7**. The Javascript is available at `www1.bio.ku.dk/english/research/bms/sbinlab/randomchemicalshifts1/`.

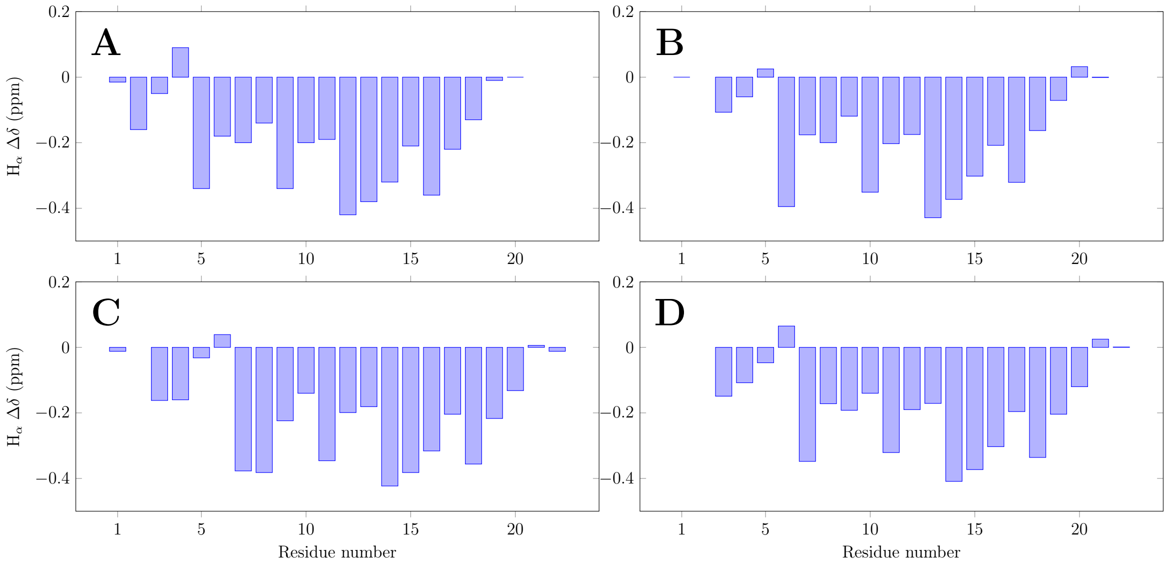

Figure 4.27: H_α secondary chemical shifts ($\Delta\delta$) versus residue number bar plots, corrected for sequence-, temperature-, and pH-contributions for (**A**) **PS-O1**, (**B**) **PS-O1 GtP**, (**C**) **R1G2-PS-O1**, and (**D**) **R1A2-PS-O1 GtP**. Reference random coil shifts and corrections were used according to (KJAERGAARD; POULSEN, 2011; KJAERGAARD et al., 2011). Values of $\Delta(\delta) = 0$ represent amino acid residues for which accurate chemical shift data was not obtained.

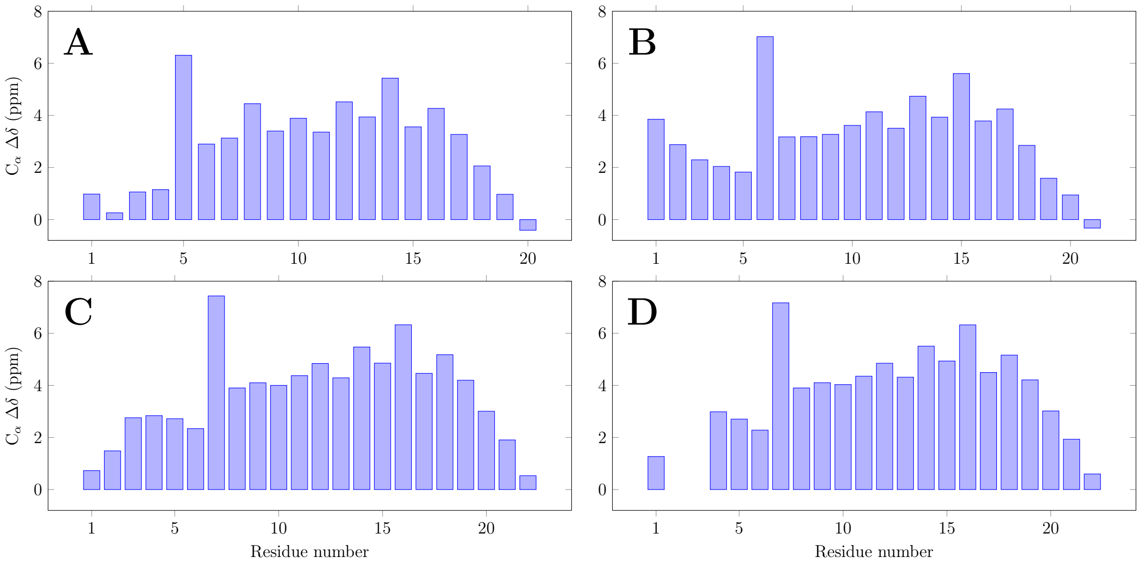

Figure 4.28: C_α secondary chemical shifts ($\Delta\delta$) versus residue number bar plots, corrected for sequence-, temperature-, and pH-contributions for (**A**) **PS-O1**, (**B**) **PS-O1 GtP**, (**C**) **R1G2-PS-O1**, and (**D**) **R1A2-PS-O1 GtP**. Reference random coil shifts and corrections were used according to (KJAERGAARD; POULSEN, 2011; KJAERGAARD et al., 2011). Values of $\Delta(\delta) = 0$ represent amino acid residues for which accurate chemical shift data was not obtained.

As discussed in **Section 4.2.3, Page 96**, `Xplor-NIH` was used to calculate the structures of **PS-O1**, **PS-O1 GtP**, **R1G2-PS-O1**, and **R1A2-PS-O1 GtP** in TFE:H_2O 60:40 (**Figure 4.29**). It is clear that glucosylation introduced a bend to the amphipathic α-helical structure of **PS-O1 GtP** and **R1A2-PS-O1 GtP**, compared to the regular helices of their base peptides. This was alluded to and, regarding the TOCSY spectra superposition (**Figure 4.16, Page 99**), the H_N δ values for the central region of the compounds (*i.e.*, residues 7 to 16) followed a trend of $\delta_{\textbf{PS-O1 GtP}} > \delta_{\textbf{PS-O1}} \sim \delta_{\textbf{R1G2-PS-O1}} > \delta_{\textbf{R1A2-PS-O1 GtP}}$. This indicated that the structural environment of **PS-O1** was similar to that of **R1G2-PS-O1** and both were dissimilar to **PS-O1 GtP** and **R1A2-PS-O1 GtP**, which can attributed to a helix bend post-glucosylation. Furthermore, **PS-O1 GtP** has its bend near the *C*-terminus and, for **R1A2-PS-O1 GtP**, it extends throughout the entire structure, which is likely the cause for the distinct δ of (C_α, H_α) correlations of His-18 and -19 seen in the $^1H-^{13}C$-HSQC (**Figure 4.19, Page 102**).

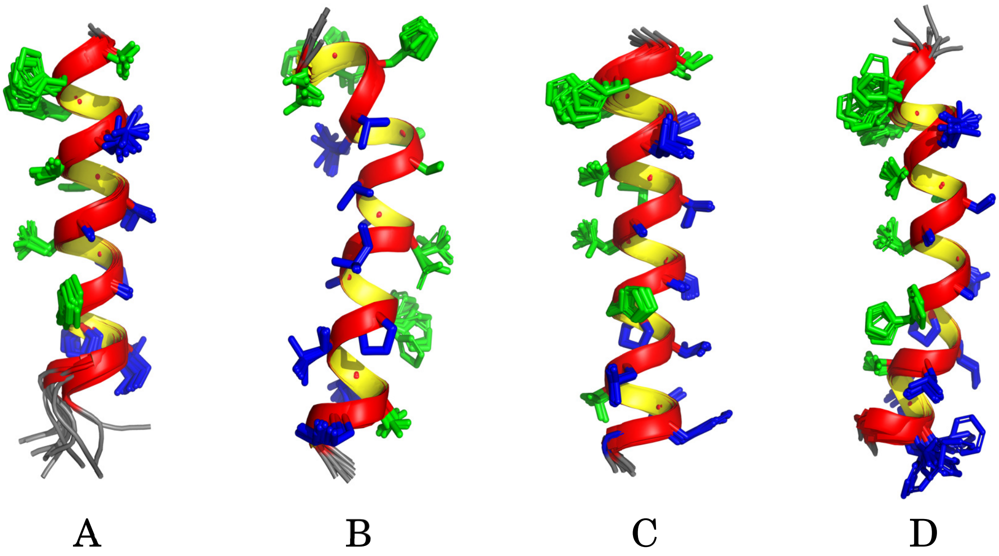

Figure 4.29: Ensembles composed by the ten structures with lowest energy among the 200 calculated with a simulated annealing optimization algorithm using the `Xplor-NIH` program, for a 2.0 mmol.L^{-1} solution of (**A**) **PS-O1**, (**B**) **PS-O1 GtP**, (**C**) **R1G2-PS-O1**, and (**D**) **R1A2-PS-O1 GtP** in TFE-d_2:H_2O (60:40, v:v), pH 7.0 phosphate buffer (20 mmol.L^{-1}). Structural rendering and superposition was made using `PyMOL` and ensembles are displayed from *C*- to *N*-terminus, top to bottom. Hydrophobic side chains are colored in blue while the hydrophilic ones are colored in green and helical segments are colored in red/yellow while random coil regions are colored gray.

The high calculated helical content for the compounds during CD analyses (**Section 3.2.2, Page 70**) is confirmed by the structures and, interestingly, helicities (H) obtained from CD were significantly lower than the helical percentage observed by NMR (**Table 4.1**). Furthermore, the peptide with a better CD-NMR correspondence is **R1A2-PS-O1 GtP**. It is worth noting that, for the entire group, the CD condition that yielded the highest helical percentage was TFE:H_2O 50:50, not 60:40, in which H values were as high as 77.4%. However, if NMR analyses were performed in TFE:H_2O 50:50, H values would probably still not be similar to the ones obtained in CD, suggesting an inherent underestimation of helical content involved in CD analyses.

Table 4.1: Helicity H (%) values for **PS-O1**, **PS-O1 GtP**, **R1G2-PS-O1** and **R1A2-PS-O1 GtP** in TFE:H_2O 60:40 as verified by CD and NMR analyses.

Peptide	H (%) (CD)	H (%) (NMR)
PS-O1	43.5	75.0
PS-O1 GtP	46.7	85.7
R1G2-PS-O1	45.2	91.0
R1A2-PS-O1 GtP	71.4	81.8

Figure 4.30 shows the structural ensemble of **PS-O1**, showing an α-helix encompassing residues 5 to 19, alongside the helical wheel projection made by HeliQuest®, based on the primary structure and assuming an α-helix from residues 5 to 20 (GAUTIER et al., 2008).

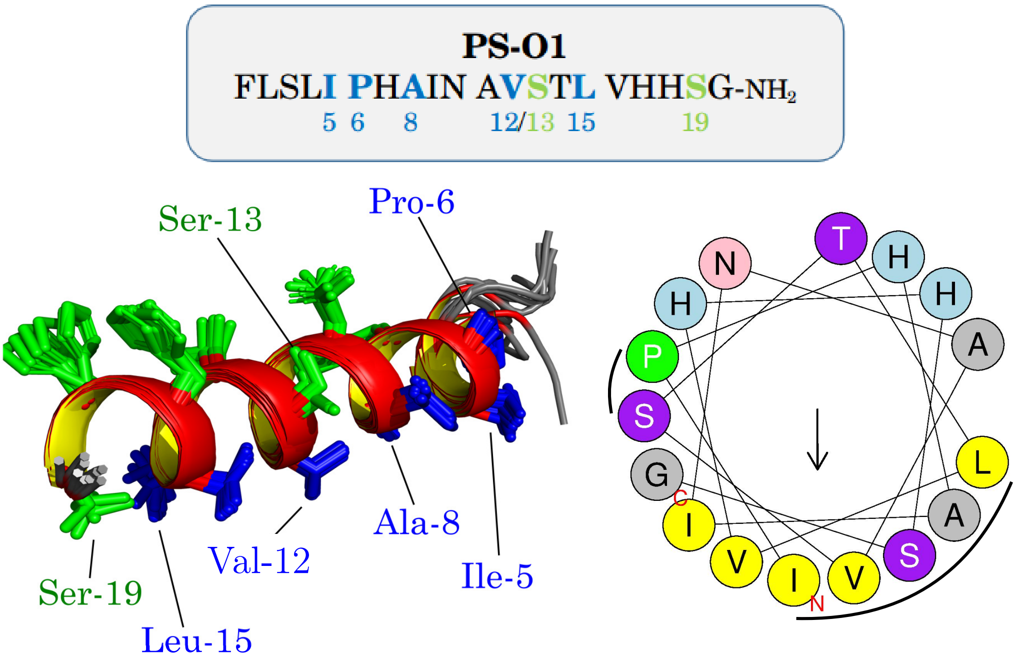

Figure 4.30: Structure ensemble for **PS-O1**, calculated from NMR spectra acquired at 2.0 mmol.L^{-1}, in TFE-d_2:H_2O 60:40 (v:v) and at pH 7.0 (phosphate buffer at 20 mmol.L^{-1}). To the right, a helical wheel projection of **PS-O1** (HeliQuest®) encompassing residues 5-20, is shown, where apolar residues are shown in yellow, Pro in green, Ala and Gly in gray, polar neutral in purple, polar positive in blue, and polar negative in pink. The N- and C-terminus nearmost residues of the peptide are represented by the red letters “N” and “C”, respectively.

Although **PS-O1** displays an extensive hydrophobic face, its continuity is disturbed by residues Ser-13 and Ser-19, the latter dividing an 8-residue-long nonpolar face. As a semi-quantitative parameter, the calculated hydrophobic moment modulus $|\vec{\mu}_H|$, *i.e.*, the measure of the amphipathicity of an α-helix perpendicular its main axis (EISENBERG et al., 1982; SILVERMAN, 2003; PHOENIX; HARRIS, 2002), for **PS-O1** considering residues 5-20, is 0.566.

Figure 4.31 shows the structural ensemble of **PS-O1 GtP** with its wheel projection and, it shows residues at the same relative position of **PS-O1**, the helix bend produces crucial deviations from the regular helix model for the GtP. First, Ser-20, instead of being flanked by Val-14 and Ala-10, as observed for **PS-O1**, stands between Val-14 and Val-18. Ile-7 undergoes similar changes and swaps places with Ser-20 in the helix wheel (**Figure 4.31**). Additionally, His-19 stands between Leu-16 and Leu-5, instead of behaving as an initial residue in the hydrophilic face. This different behavior of His-19 was alluded to in **Section 4.3.1, Page, 96**, where the superposition of the ^{1}H$-^{13}$C-HSQC showed that the H$_\alpha$ chemical shifts for it was very dissimilar from the other His residues, indicating a different structural arrangement. Although the calculated $|\vec{\mu}_H|$ for **PS-O1 GtP** — 0.689 — is larger than for **PS-O1**, the helix bend changes the topology of the peptide and introduces an extra partition in the hydrophobic face, potentially lowering the real value.

PS-O1 GtP
(GtP)FLSLI PHAIN AVSTL VHHSG-NH$_2$
5 13 16 17 19/20

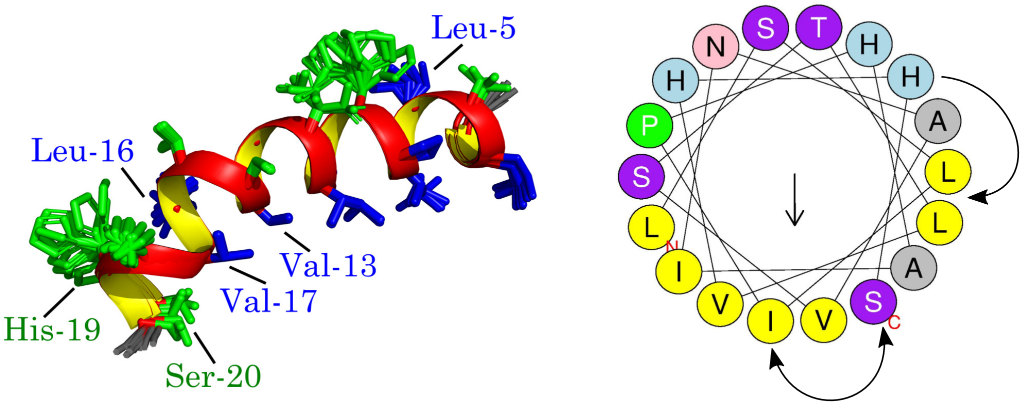

Figure 4.31: Structure ensemble for **PS-O1 GtP**, calculated from NMR spectra acquired at 2.0 mmol.L^{-1}, in TFE-d_2:H$_2$O 60:40 (v:v) and at pH 7.0 (phosphate buffer at 20 mmol.L^{-1}). To the right, a helical wheel projection of **PS-O1 GtP** (HeliQuest®), encompassing residues 3-20, is shown, where apolar residues are shown in yellow, Pro in green, Ala in gray, polar neutral in purple, polar positive in blue and polar negative in pink. The *N*- and *C*-terminus nearmost residues of the peptide are represented by the red letters “N” and “C”, respectively.

Figure 4.32 shows the structural ensemble of **R1G2-PS-O1**. The helical segment of this product is longer than the other compounds, leading to eventual residue superposition, represented by the adjacent circles not connected by straight lines in the calculated helix wheel projection. Comparing **PS-O1** and **R1G2-PS-O1**, there is greater degree of amphipathicity for the latter, since the same amount of uninterrupted apolar residues opposes a smaller amount of uninterrupted polar ones (*i.e.*, for **PS-O1**, the polar face was comprised of six residues while encompassing five in **R1G2-PS-O1**, since Gly-2 and His-19 are superposed). This amphipathicity difference is reflected in $|\vec{\mu}_H| = 0.71$ for **R1G2-PS-O1**.

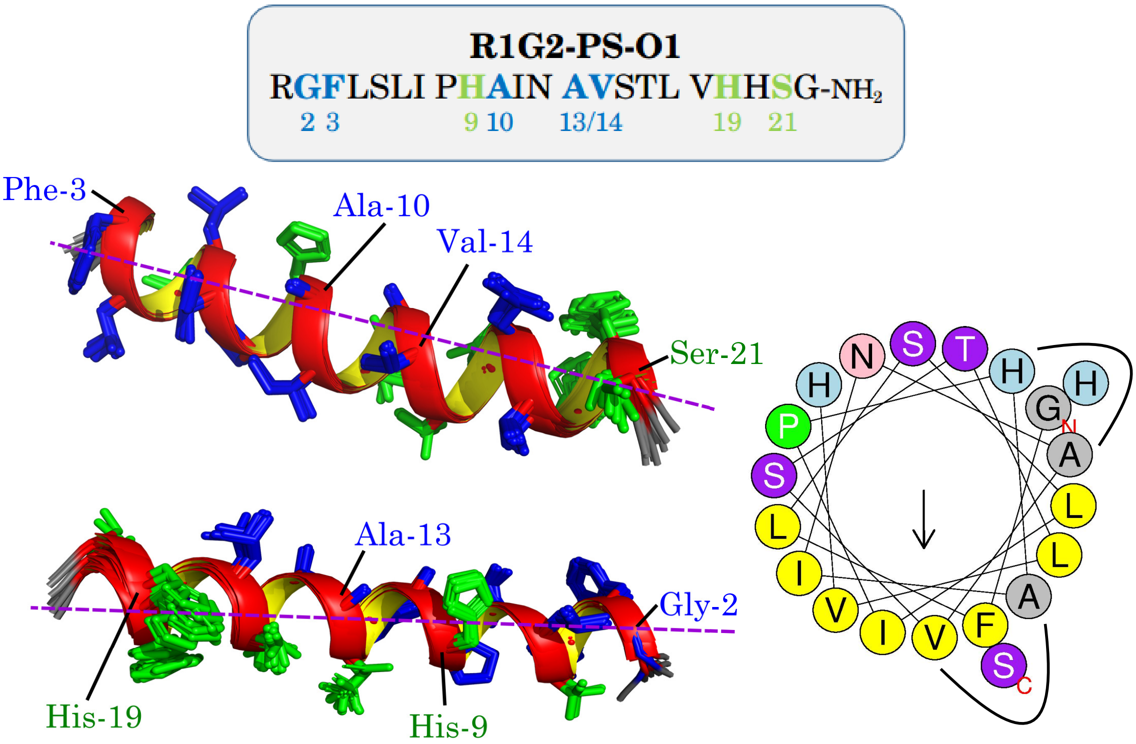

Figure 4.32: Structure ensembles for **R1G2-PS-O1**, calculated from NMR spectra acquired at 2.0 mmol.L^{-1}, in TFE-d_2:H$_2$O 60:40 (v:v) and at pH 7.0 (phosphate buffer at 20 mmol.L^{-1}). To the right, a helical wheel projection of **R1G2-PS-O1** (HeliQuest®), encompassing residues 2-21, is shown, where apolar residues are shown in yellow, Pro in green, Ala in gray, polar neutral in purple, polar positive in blue and polar negative in pink. Residues that are side by side but not connected by straight lines are spatially superposed. The *N*- and *C*-terminus nearmost residues of the peptide are represented by the red letters "N" and "C", respectively.

The structural ensemble of **R1A2-PS-O1 GtP** and its helix wheel are shown in **Figure 4.33**. An extensive hydrophobic face is observed between residues 3 and 20, reflected in $|\vec{\mu}_H| = 0.791$. Nevertheless, some structures of the ensemble reveal an even greater helical segment encompassing residues 2-21. The choice to consider a smaller interval was due to lack of consensus for all structures, supported by a small confidence factor for residues 2 and 21 given by `TALOS-N` (0.03 and 0.18, respectively), indicating that a helix might not be present at them. Moreover, comparing the structures of **PS-O1 GtP** and **R1A2-PS-O1 GtP**, the apparent loss of helical content improved the separation between the faces with different polarity, alluding to stronger anionic membrane interactions and a greater biological potential for **R1A2-PS-O1 GtP**.

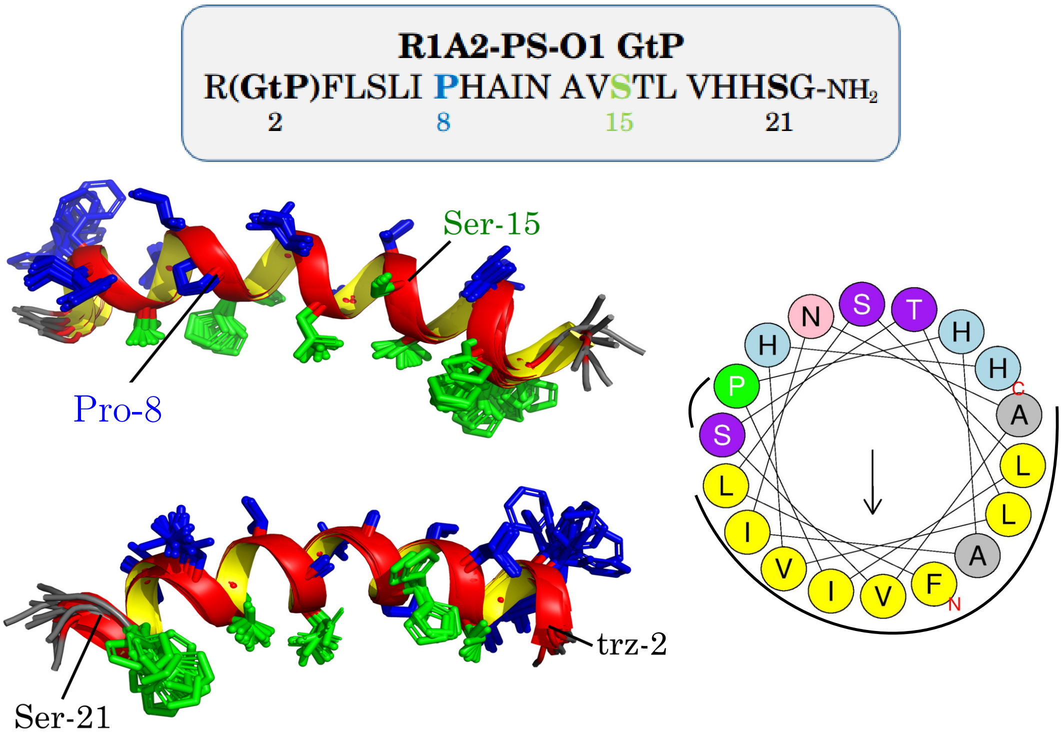

Figure 4.33: Structure ensemble for **R1A2-PS-O1 GtP**, calculated from NMR spectra acquired at 2.0 mmol.L^{-1}, in TFE-d_2:H$_2$O 60:40 (v:v) and at pH 7.0 (phosphate buffer at 20 mmol.L^{-1}). To the right, a helical wheel projection of **R1A2-PS-O1 GtP** (HeliQuest®), encompassing residues 3-20, is shown, where apolar residues are shown in yellow, Pro in green, Ala in gray, polar neutral in purple, polar positive in blue and polar negative in pink. Residues that are side by side but not connected by straight lines are spatially superposed. The N- and C-terminus nearmost residues of the peptide are represented by the red letters "N" and "C", respectively.

The helix bend resulted in an exacerbation of the amphipathicity, since the polar residues are mainly in the concave section of the structure, whereas the apolar are concentrated in the convex region. This result was not evidenced experimentally in the NOESY, for instance, and can be attributed to the interaction between large amino acid residues or other contact interactions. For instance, NOESY data attributed to bends of helix was reported for the AMP LyeTx I and LyeTx I-b, which showed an expressive number of $N, N_{(i,i+2)}$ correlations (SANTOS et al., 2010; REIS et al., 2018). Also, structural calculations can undergo parametrization biases toward these large residues, furnishing helix bends as artifacts of the calculation.

The secondary chemical shift of amide protons is also an important indicator of amphipathicity in α-helical structures (WISHART; SYKES, 1994a). The variation between shorter and longer hydrogen bonds results in negative and positive $\Delta\delta$ values, respectively, and helix curvatures can result in shorter hydrogen bonds on the hydrophobic face and longer bonds on the hydrophilic face (ZHOU et al., 1992). The secondary chemical shift data of amide protons for the synthesized peptides is displayed in **Figure 4.34**.

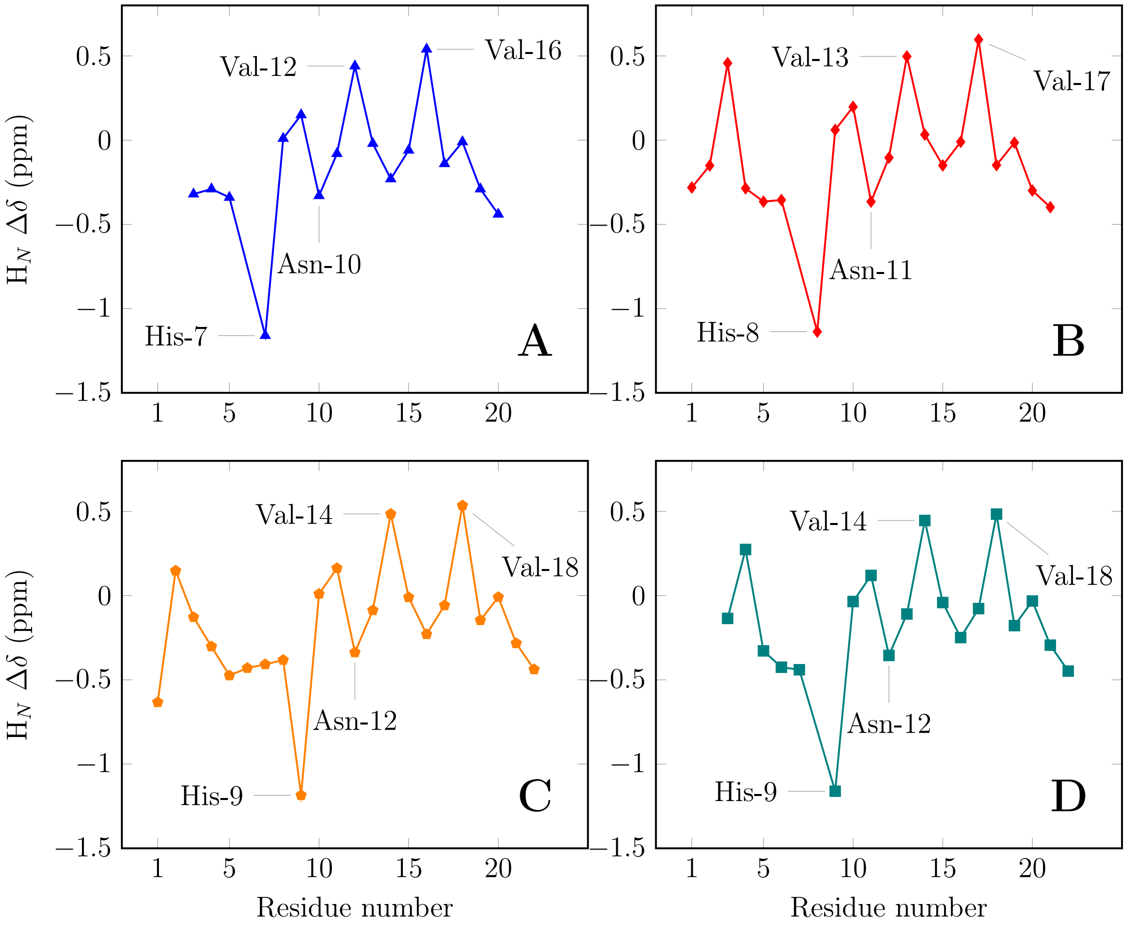

Figure 4.34: Plot of H_N $\Delta\delta$ values versus residue number for (**A**) **PS-O1**, (**B**) **PS-O1 GtP**, (**C**) **R1G2-PS-O1**, and (**D**) **R1A2-PS-O1 GtP**.

The periodic nature of H_N $\Delta\delta$ values is apparent from the four plots, alluding to the overall high amphipaticity of the products and, since their periodic behavior is mostly similar after the global H_N $\Delta\delta$ minima, the residue distribution on their hydrophobic and hydrophilic faces is also be similar, which is expected given their high homology. However, the values obtained for **PS-O1** clearly show a lack of periodicity close to its *N*-terminus, which can be explained by the smaller helical content in this region, whereas a more uniform variation of $\Delta\delta$ values is noticed for the other products. Furthermore, previous publications show that amino acid residues with more negative H_N $\Delta\delta$ values are usually located in the center of the hydrophilic face, whereas residues with more positive values are at the center of the hydrophobic face (ZHOU et al., 1992). This behavior was verified for all four peptides since, when comparing the obtained plots with **Figures 4.30-4.33**, both the helix wheel projections and the three dimensional structures show that His-7 and Asn-10 are at the center of the hydrophilic face of **PS-O1** while Val-12 and Val-16 are at the center of its hydrophobic face. Additionally, the same is true for the respective residues of the other three peptides, as shown in **Figure 4.34**.

The observations and analyses of H_N $\Delta\delta$ values for the four products is complementary to the structural analysis itself since it shows, experimentally, the amphipathic nature of the helical structures and can indicate which residues will comprise each face of the helix. Furthermore, the periodicity of the secondary shift data suggests that all four peptides might have a curved disposition of their α-helix. Further still, since the $\Delta\delta$ amplitude for all products is similar, as evidenced by the superposition of the H_N $\Delta\delta$ plots shown in **Figure 4.35**, it can be assumed that their degrees of amphipaticity and curvature are also similar (ZHOU et al., 1992; WISHART; SYKES, 1994a), even though the calculated structures suggest otherwise.

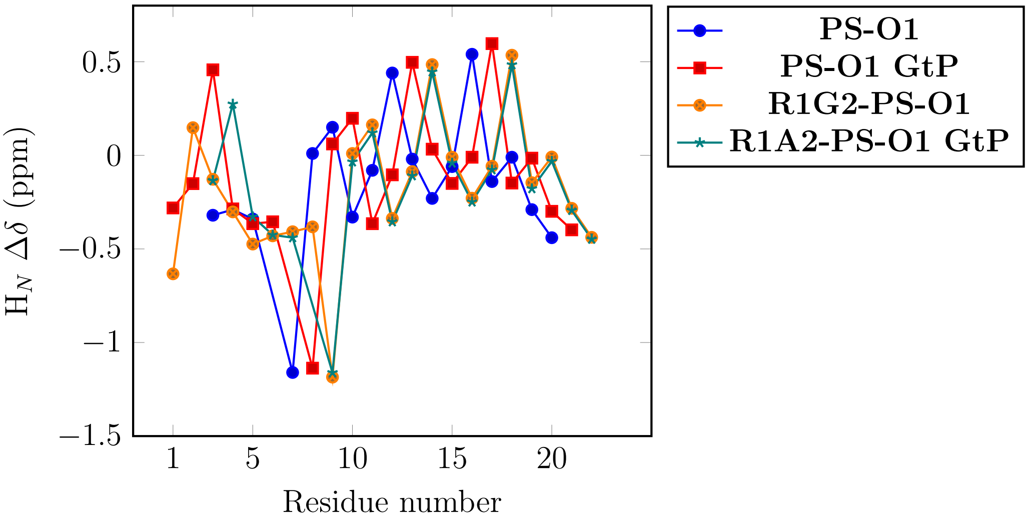

Figure 4.35: Superposition of the plots of H_N $\Delta\delta$ values versus residue number for **PS-O1**, **PS-O1 GtP**, **R1G2-PS-O1**, and **R1A2-PS-O1 GtP**.

Regarding the stereochemical quality of the calculated structures, `PROCHECK-NMR` was used to verify to which regions of the Ramachandran diagram the residues' ϕ and ψ dihedral angles better fit based on known angle values for structures in its database. The resulting diagrams for each peptide derivative are displayed in **Figure 4.36** (RAMACHANDRAN et al., 1963; LASKOWSKI et al., 1996). Most residues have their respective ϕ, ψ pairs located in the most favourable regions for α-helices of the Ramachandran plot (Region "A", **Figure 4.36**). Nevertheless, **PS-O1** (**Figure 4.36, A**) has three residues placed in additional favoured regions. By analysing the Ramachandran plots generated for each residue (data not shown), the three residues are Leu-2, Ser-3 and Leu-4, neither of which are part of the helical structure. Additionally, **R1G2-PS-O1** (**Figure 4.36, C**) has one Gly residue (Gly-2) that falls outside "A", which is explained by its flexibility, even though it belongs to the helical structure. Finally, Ser-21 of **R1A2-PS-O1 GtP** (**Figure 4.36, D**) is observed in a "b" region, providing further evidence that it is not part of the helical segment.

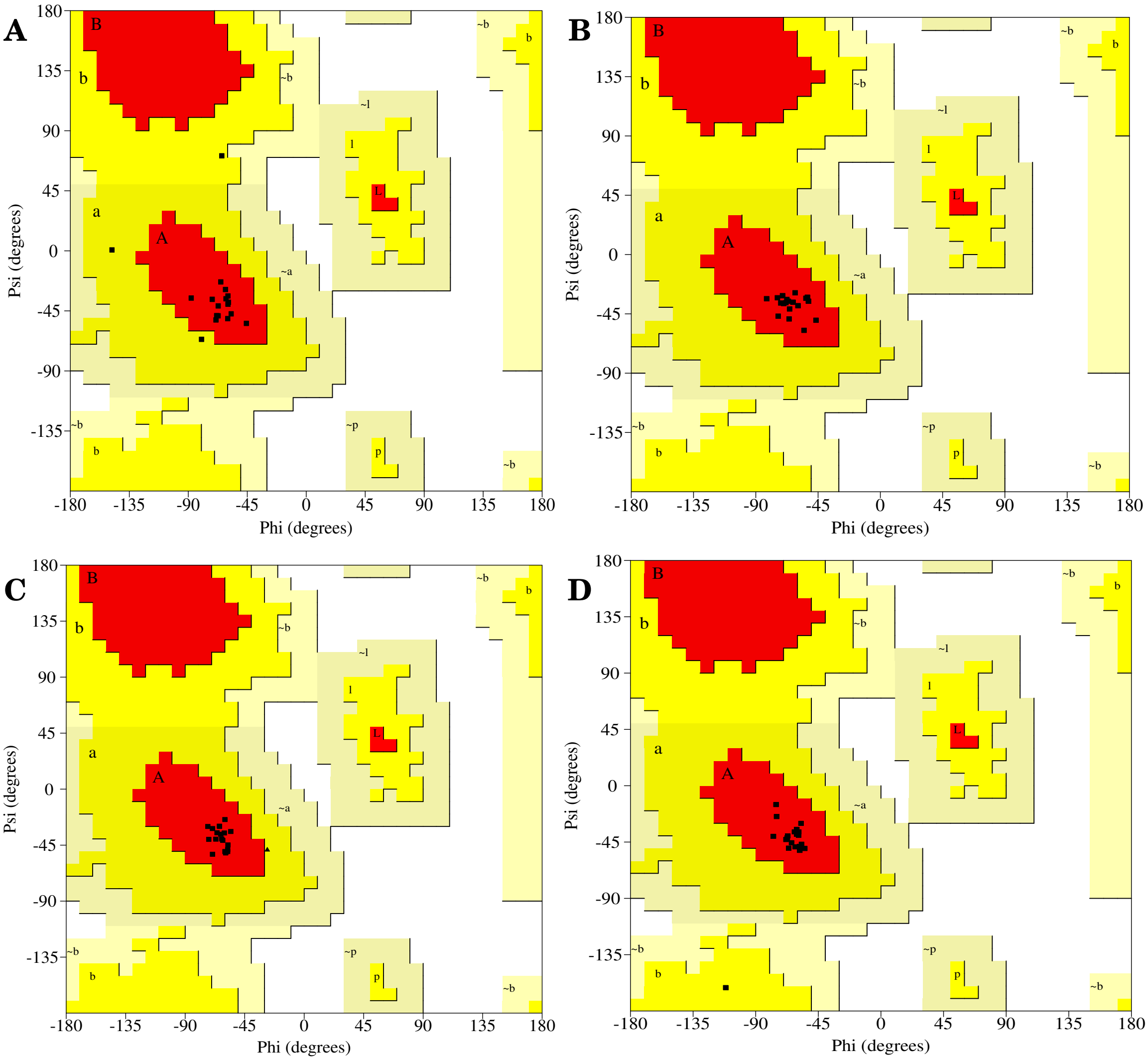

Figure 4.36: Ramachandran diagrams of (**A**) **PS-O1**, (**B**) **PS-O1 GtP**, (**C**) **R1G2-PS-O1**, and (**D**) **R1A2-PS-O1 GtP** in TFE-d_2:H2O (60:40) where non-Gly amino acid residues are shown as black squares and Gly, as black triangles. Different residues are placed in favoured regions (A, B, L), additional favored regions (a, b, l, p), or generously allowed regions (∼a, ∼b, ∼l, ∼p), according to their ϕ and ψ dihedral angles.

The summary of the structural statistics for the four synthesized peptides is displayed in **Table 4.2**. Accordingly, the NOESY spectra of the four molecules yielded a large amount of distance restraints, including a significant percentage of medium distance restraints, ranging from 13 to 19%. This supports the high helical content for these molecules and, interestingly, the two peptides with the highest helix percentage — **PS-O1 GtP** and **R1G2-PS-O1** — have the highest proportion of medium range distance restraints (18 and 19%, respectively). Furthermore, the RMSD for the ensembles ranged from 1.29 to 1.90 Å, indicating a high degree of similarity between them, and glucosylation increased the RMSD values of the respective base peptides, indicating an increase in structural flexibility. Finally, the Ramachandran plot analysis confirms the stereochemical quality of all generated structural ensembles, as discussed.

Table 4.2: Summary of structural statistics for **PS-O1**, **PS-O1 GtP**, **R1G2-PS-O1** and **R1A2-PS-O1 GtP** in TFE-d_2:H_2O (60:40). Distance restraints were obtained from the NOESY spectra and each one is accompanied by its percentage with respect to the total, RMSD data was obtained in `PyMOL`, the percentage of residues in each Ramachandran plot region was obtained by `PROCHECK-NMR` and helix percentage is the relation between the number of residues in the helical segment and the total number of residues.

	PS-O1	**PS-O1 GtP**	**R1G2-PS-O1**	**R1A2-PS-O1 GtP**
Distance Restraints				
Total distance restraints	479	505	556	426
Intraresidual restraints	312 (65%)	298 (59%)	337 (60%)	274 (64%)
Sequential restraints $(i, i+1)$	99 (21%)	117 (23%)	116 (21%)	97 (23%)
Medium distance restraints $(i, i+j)_{j=2,3,4}$	68 (14%)	90 (18%)	103 (19%)	55 (13%)
RMSD (Å) - All residues	1.657	1.846	1.291	1.896
Ramachandran plot analysis				
Residues in most favoured regions (%)	82.4	100	100	94.7
Residues in additional favoured regions (%)	17.6	0	0	5.3
Residues in generously allowed regions (%)	0	0	0	0
Residues in disallowed regions (%)	0	0	0	0
Helix percentage (%)	75	85.7	91	81.8

Some final remarks about the calculated structures regard the biological potential of the peptide derivatives. Considering only helix percentages, **R1G2-PS-O1** should display the highest antimicrobial potential, even more so than the glucotriazole peptides. As a matter of fact, it is expected that the glucosylation of this peptide will reduce its activity. In case this is observed, it will be an important outcome since previously reported results showed an increase in fungicidal and antimicrobial activities for GtPs when compared to their parental sequences (JUNIOR et al., 2017). Additionally, when amphipathicity is considered, **Table 4.3** concisely shows ($|\vec{\mu}_H|$) values, relating them to the helix percentage of each peptide derivative.

Table 4.3: Hydrophobic moment moduli ($|\vec{\mu}_H|$) and helix percentages (%) of **PS-O1**, **PS-O1 GtP**, **R1G2-PS-O1** and **R1A2-PS-O1 GtP** in TFE-d_2:H_2O (60:40).

Peptide	$\lvert\vec{\mu}_H\rvert$	Helix percentage (%)
PS-O1	0.566	75.0
PS-O1 GtP	0.689	85.7
R1G2-PS-O1	0.710	91.0
R1A2-PS-O1 GtP	0.791	81.8

Although the argument for **R1G2-PS-O1** having a higher biological activity than **PS-O1** still stands by analyzing both quantities, the same cannot be said for the GtPs, since **PS-O1 GtP**, for example, has the highest helix percentage of the pair but the lowest $|\vec{\mu}_H|$. Furthermore, **PS-O1** should not display significant activity compared to the rest, since it displays H and $|\vec{\mu}_H|$ values much lower than the other three. Finally, since $|\vec{\mu}_H|$ is a measure of the amphipathicity of the α-helix perpendicularly to its main axis, both values for the GtPs, displaying a bend in their secondary structure, must be used with caution, since they might not reflect their behaviour as accurately as for **PS-O1** and **R1G2-PS-O1**.

Chapter 5 | Biological Tests

5.1 Introduction

Over the years, bacterial and fungal infections as well as resulting clinical complications have been a major health issue worldwide. Also, bacterial resistance is worrysome due to the misuse of antibiotics combined to the natural resistance mechanisms of these microorganisms. However, it spurs the need for the discovery of novel antimicrobial agents that are either more potent or act on alternative biological pathways (SCHRADER et al., 2020; NATHAN, 2020; GUO et al., 2020).

Additionally, the COVID-19 pandemic poses a great risk in this aspect as well, since hospitalization of critically ill patients exposes them to potential nosocomial bacterial infections from pathogens like *Staphylococcus aureus* and *Pseudomonas aeruginosa* when intubations, for example, are performed. As the symptoms from the viral and bacterial infections are similar, the approach taken by hospitals involves the unfocused and indiscriminate prescription of antibiotics, potentially worsening the resistance problem due to bad drug administration (WESTBLADE et al., 2021; RAWSON et al., 2021; LANGFORD et al., 2020; SHAFRAN et al., 2021).

Furthermore, fungal infections were responsible for approximately 1.5 to 2 million deaths worldwide over the past few decades and some opportunistic fungi species — *Candida*, *Aspergillus*, and *Cryptococcus* — pose a serious health risk after they enter the blood stream, being potentially fatal if the subsequent infection is not treated (TADA et al., 2013; SANT et al., 2016). Also, they can be a constant danger to immunocompromised patients, such as those with HIV, cancer or at post-transplantation stages (SANT et al., 2016; WANG et al., 2020).

The need for novel treatment alternatives, therefore, increases daily and, to know possible avenues of pathogen suppression or elimination, a basic understanding of some characteristics of the bacterial and fungal cell is required. Specifically, greater attention will be given to membrane- and cell-wall-constituents, since this thesis focuses on novel drug candidates that target these elements.

Bacterial cells have two main external regions — the cell membrane and cell wall. Morphology and chemical composition for them vary between species but some similarities can be identified. Regarding the cell wall, their composition vary whether the bacteria is Gram-positive or negative. Furthermore, Gram-positive cells have a component disposition as presented in **Figure 5.1**.

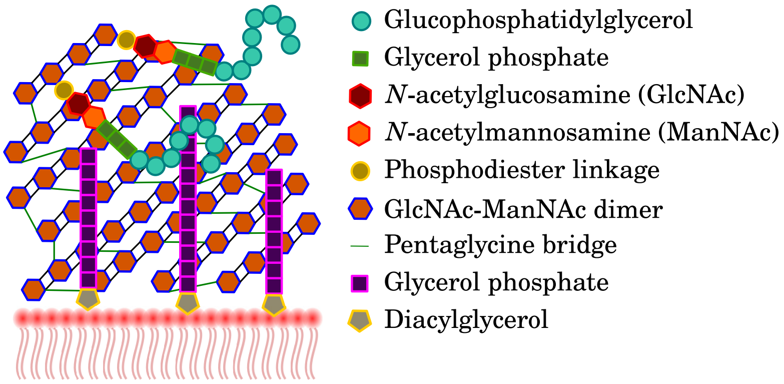

Figure 5.1: Schematic representation of a Gram-positive bacterial cell wall. Above the cell membrane, the anionic lipoteichoic acid (LPA) is anchored to it by a diacylglycerol unit, followed by a glycerol phosphate polymer. The main component of the cell wall is the peptiglucan (PGlu), comprised of GlcNAc-ManNAc dimers linked together and decorated with pentaglycine-bridged pentapeptide units. The PGlu net is linked to the wall teichoic acid (WTA) units by a phosphodiester linkage and it is made of a GlcNAc-ManNAc pair bound to one to three glycerol phosphate units and 20 to 40 glucophosphatidylglycerol units.

Gram-positive bacterial cell wall are complex structures formed by peptidoglucan (PGlu) units; *N*-acetylglucosamine (GlcNAc)-*N*-acetylmannosamine (ManNAc) dimers linked together and decorated with $(Gly)_5$-bridged pentapeptide stems (NYGAARD et al., 2015). Bound to these PGlu chains through phosphodiester linkages, Wall Teichoic Acid (WTA) units are made of an GlcNAc-ManNAc pair linked to glycerol phosphate and glucophosphatidylglycerol units (SWOBODA et al., 2010). Anchored to the cell membrane by diacylglycerol residues, lipoteichoic acid (LPA) units extend throughout the cell wall (ROHDE, 2019). This negatively-charged external structure serves as an initial barrier and also to hold the internal pressure of the cytoplasm.

Gram-negative bacterial cell walls (**Figure 5.2**) are considerably different. The inner cell membrane is succeeded by a periplasm and a thin layer of PGlu (SWOBODA et al., 2010). Above this central portion, there is another heterogenous and negatively-charged membrane, carrying phosphate heads along its inner face and lipopolisaccharide (LPS) chains along the outer (ZHANG et al., 2013). These chains are three-unit components comprised of lipid A, a core oligosaccharide and an *O*-antigen, also known as *O*-polysaccharide (LI et al., 2016; BERTANI; RUIZ, 2018). Lipid A is a GlcNAc dissacharide with fatty acid residues bound to *O* and *N* atoms and with phosphate groups in positions 1 and 4' (BERTANI; RUIZ, 2018). The core oligosaccharide is a union of heptoses, hexoses and 3-deoxy-D-*manno*-oct-2-ulosonic acid (Kdo), is similar across all bacteria (ZHANG et al., 2013), and can be modified with phosphate or Phosphatidylethanolamine (PE) groups (ERRIDGE et al., 2002). The *O*-antigen section is composed of an extended, two-to-eight-residue-long polysaccharide chain that varies considerably among different bacteria (ERRIDGE et al., 2002; BERTANI; RUIZ, 2018). Cell wall biological components of Gram-negative bacteria are also negatively charged.

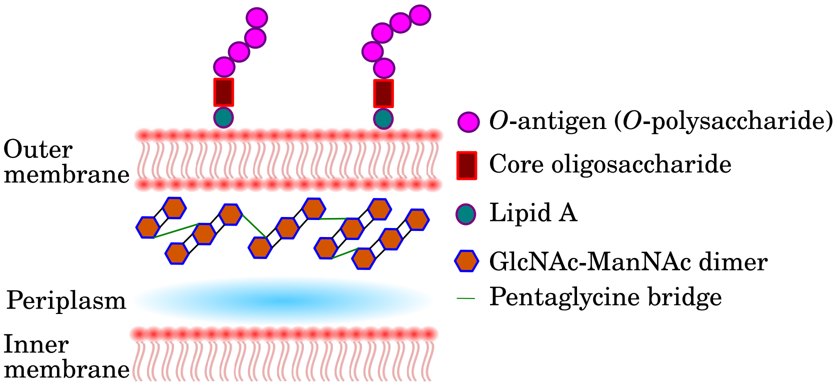

Figure 5.2: Schematic representation of a Gram-negative cell wall component distribution. Above the inner membrane, a thin PGlu layer stand between the periplasm and a second, outer membrane that is heterogenous in nature, having an inner, phospholipid layer and an outer LPS layer.

Bacterial membranes have a lateral microheterogeneity, with function microdomains with variable fluidity and order of constituent lipids (WILLDIGG; HELMANN, 2021). Nevertheless, their lipid composition remains similar across different species. Negative phospholipids like PG, CL, and PS are the major constituents alongside some zwitterionic ones like PE, yielding an overall negative character to the membrane (SOHLENKAMP; GEIGER, 2016).

Regarding targets for antimicrobial drug action, some act on cell wall integrity, like fosfomycin and penicillin, inhibiting the formation of PGlu disaccharide units inside the cell and extracellular polypeptide crosslink formation, respectively (NYGAARD et al., 2015). On the other hand, AMPs usually target membrane integrity due to their charge difference, although some of them may interact with internal targets after transposition (SUGAWARA et al., 2010; HALE; HANCOCK, 2007; BROGDEN, 2005). Regarding membrane disruption mechanisms, while many different models have been studied, the barrel stave, toroidal, disordered toroidal pore, carpet, charged lipid clustering, and electroporation will be further discussed. Also, although the terms “pore” and “ion channel” are often used, small defects are usually caused by AMPs along the membrane and they seldom form defined cavities (MALMSTEN, 2016).

In the barrel stave model (**Figure 5.3, A-C**), peptides acquire an α-helical conformation as they approach the membrane surface and, upon binding, the hydrophobic face separates the bilayer polar phosphate heads, introducing a local membrane thinning. After a threshold concentration, the monomers aggregate and insertion/pore formation occurs, followed by cytoplasm leakage and peptide translocation (REDDY et al., 2004).

The toroidal pore model (**Figure 5.4, A**) expands upon the barrel stave assuming that the transmembrane channels formed are supramolecular complexes of peptide monomers interspersed by phospholipid molecules (YEAMAN; YOUNT, 2003). Furthermore, a disordered toroidal pore model (**Figure 5.4, B**) has been proposed and, although the process is similar and lipid molecules are curved inwards, pore formation is stochastic and only one or two monomers are actually at the center, while the majority is at the mouth of the channel (NGUYEN et al., 2011).

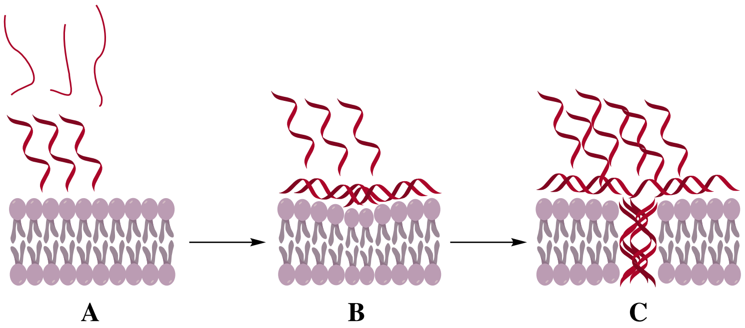

Figure 5.3: Schematic representation of the barrel stave model with three major steps highlighted. **A** represents the initial accumulation of peptide monomers on the bilayer surface. **B** shows the conformational change in order to be parallel to the membrane surface and, subsequently, the membrane thinning that ensues. Finally, peptide aggregation, after a concentration threshold is reached, induces a pore formation (**C**).

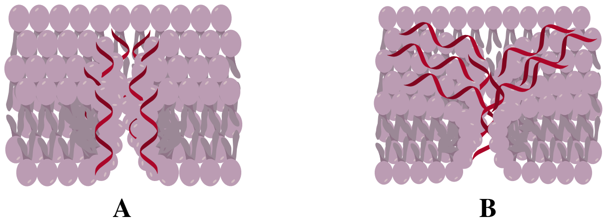

Figure 5.4: Schematic representation of the toroidal pore and disordered toroidal pore models of peptide-membrane interaction. In **A**, the transmembrane channel is formed by a supramolecular complex of peptide monomers and phospholipids, while **B** depicts the disordered version, showing a lesser peptide concentration inside the pore and a considerable amount around the mouth of the pore.

Antimicrobial peptides can act as detergents according to the carpet model (LEI et al., 2019) (**Figure 5.5**), which assumes that a high concentration of membrane-bound peptides promote its disruption, leading to micelle-like structures. This model can be considered as an extension of the disordered toroidal pore model (NGUYEN et al., 2011). In this case, membrane dissolution occurs in a dispersion-like manner and does not involve the formation of transmembrane channels.

Charged lipid clustering and electroporation models are based on electrostatic charge accumulation and contribute to the loss of membrane integrity. The first is described by a gradual lipid segregation where the cationic peptide face attracts negatively-charged bilayer constituents like PG or PS, inducing the formation of channels that lead to cell content leakage (EPAND; EPAND, 2011). Finally, electroporation occurs when peptide-membrane association provokes an increase in the transmembrane potential $\Delta\psi$ up to 0.2 V and, at this stage, bilayer curvature ensues and the movement of water molecules increase the probability of defects to develop, resulting in pores throughout the surface (TIELEMAN, 2004; MITEVA et al., 1999).

Fungal cell wall and membrane anatomies are considerably different from the bacterial cell. While all fungi cell walls have a common core, its outer parts vary for different species. Since

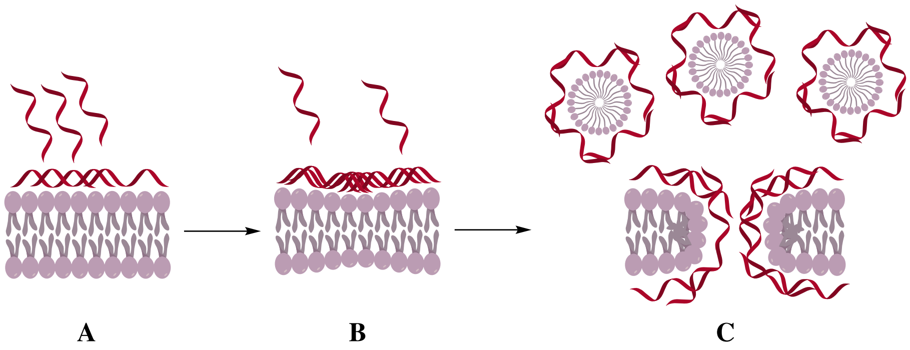

Figure 5.5: Representation of the carpet model. **A** describes the formation of the carpet along the membrane surface by hydrophillic interaction between the peptide and phosphate heads of the lipid bilayer. Afterwards, **B** shows membrane thinning and monomer accumulation, followed by lysis in a micellar fashion in **C**.

Candida yeasts were used in this work, the basic structure of its cell wall is presented in **Figure 5.6**. Its initial part is comprised of a basket-like scaffold made of a β-(1,3) glucan-β-(1,6) glucan-chitin core (GARCIA-RUBIO et al., 2020; GOW et al., 2017). Whereas chitin is a glucopolymer made of a series of N-acetylglucosamine units covalently bound in a β-(1,4) fashion, glucan units are covalent polymers of glucose units bound in a β-(1,3) or (1,6) manner (SONG et al., 2012; FREE, 2013). Both polymers are bound by hydrogen bonds and mannosylated Cell Wall Protein (CWP) units are covalently linked to the β-(1,6) glucan units by glucophosphatidylinositol (GPI) (GARG et al., 2016; PAULICK; BERTOZZI, 2008). It is important to note that, since the mannosylated CWP units are usually phosphorylated in yeasts, a negative net charge is observed for fungi cell wall (LIPKE; OVALLE, 1998; IBEAS et al., 2001; SOWA-JASIłEK et al., 2020).

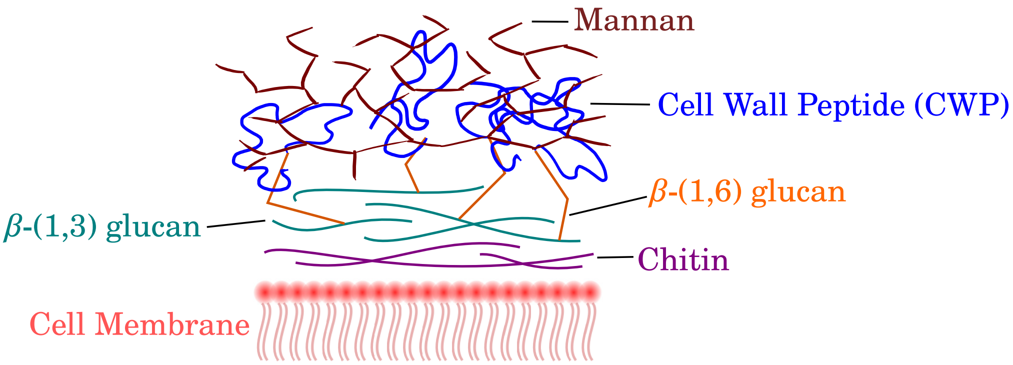

Figure 5.6: Schematic representation of the cell wall components of *Candida* yeasts. In this fungus, the cell wall is composed of an initial scaffold composed of a β-(1,3) glucan-β-(1,6) glucan-chitin core, where the glucan and chitin chains are bound by intermolecular hydrogen bonds. Above this basket-like formation and covalently bound to the β-(1,6) glucan units, chains of mannosylated proteins form the CWP part of the structure.

The membrane is comprised of glycerophospholipids, being a glycerol-3-phosphate moiety containing two fatty acid units with substituents like choline (PC), serine (PS) and ethanolamine

(PE), sphingolipids like ceramide, and ergosterol (SANT et al., 2016). The phospholipid composition of these membranes makes them zwitterionic, similar to mammalian ones. Also, as opposed to cholesterol in mammalian cell membranes, ergosterol is the main sterol component in fungal cell membranes. This results in a unique approach to the design of potential antifungal drugs, since ergosterol and its biosynthetic pathway is the most optimal alternative. Additionally, membrane-exclusive mechanisms of action tend to be disfavored, since mammalian cells would be potentially affected. Therefore, polyenes and azoles, two of the most common membrane agents against fungal infections, unsurprisingly target either the structure or the biosynthesis of ergosterol (TADA et al., 2013). Echinocandins, another widespread antifungal, targets the unique composition of the cell wall, disrupting the biosynthesis of the β-(1,3) glucan units (STRUYFS et al., 2021; GARCIA-RUBIO et al., 2020).

Ergosterol is such an ubiquitous target for antifungal drugs that some of the most commonly prescribed drugs in Brazil are azol derivatives like fluconazole, isavuconazole, itraconazole and posaconazole. As such, the biosynthetic pathway of ergosterol, which involves over 20 steps and is essential to membrane integrity, is an attractive target of scientific development (TADA et al., 2013). In light of this, azole-like modifications were made to peptides by our research group and preliminary biological activity data displayed promising results regarding the antifungal activity of glucotriazole peptides [p-Glc-trz-G^1]HSP1-NH$_2$ and [p-GlcNAc-trz-G^1]HSP1-NH$_2$, showing inhibition effects on ergosterol biosynthesis in *Candida albicans* (JUNIOR et al., 2017).

When discussing antifungal AMPs, since membrane interaction is not so straightforward as for bacteria, they have more complex mechanisms of action. They interact with the membrane and affect intracellular targets, resulting in reactive oxygen species (ROS) production, programmed cell death, and cell cycle impairment (STRUYFS et al., 2021). Additionally, inhibition of β-(1,3) glucan or chitin biosynthesis are employed by some AMPs (ULLIVARRI et al., 2020). Some antifungal peptides of note are produced by amphibians, like magainins and dermaseptins—found in the skin secretions of *Xenopus* and *Phyllomedusa* species, respectively (XU X. LAI, 2015). Interestingly, while dermaseptins enact membrane lysis by a dissipating ion gradient, magainins do so by interacting with the lipid bilayer itself (ULLIVARRI et al., 2020).

Regarding recent advances in AMP application to antifungal treatment, the peptide AKK8 (RWRFKWWKK), a nine-residue-long, tryptophan-rich fragment of Ranacyclin AJ (found in the secretion of Chinese torrent frog *Amolops jingdongensis*) displayed noticeable activity against standard and clinically isolated *C. albicans*, and a positive effect of Arg and Lys residues was observed (WUBULIKASIMU et al., 2020). Additionally, an extensive study was performed on AMP-17 (produced by the household fly *Musca domestica*) against *C. albicans*, and it was found that membrane and cell wall integrities were affected, the latter being lowered to *ca.* 21.7%, alongside increased expression of its synthesis-related gene *FKS2*, indicating more complex modes of action for antifungal AMPs (MA et al., 2020). Finally, CGA-N12 (ALQGAKERAHQQ), a peptide fragment of chromogranin A, showed anti-*Candida* activity by inducing apoptosis even though membrane lysis was not observed and ergosterol levels were unchanged, being another evidence of different mechanistic pathways (LI et al., 2020).

The study of biologically active peptides as antimicrobial and antifungal agents is, therefore, an attractive field of study that still has room to be better understood and to grow in order to combat the continuous and, unfortunately, increasing health problems that are currently faced.

5.2 Methodology

5.2.1 Antifungic activity assays

Fungistatic and fungicidal activity

The fungistatic activity of peptides **PS-O1**, **PS-O1 GtP**, **R1G2-PS-O1**, and **R1A2-PS-O1 GtP** was evaluated by the Minimum Inhibitory Concentration (MIC) values obtained using the broth microdilution assay, according to protocols of the Clinical and Laboratory Standards Institute's norm M27 for yeasts (ALEXANDER, 2017). The compounds were tested at concentrations ranging from 0.5 to 128 $\mu g.mL^{-1}$.

From the streak lines, isolated colonies were collected and transferred to an assay tube containing 10 mL of sterile saline (0.85%). The resulting suspension was homogenized and the optical density was adjusted with a spectrophotometer until an equivalent turbidity of 0.5 in the McFarland scale was achieved, corresponding to a 0.08 - 0.10 absorbance at 530 nm.

The work suspension was produced by transferring 20 µL of the standard suspension to a sterile microtube containing 980 µL of Sabouraud Dextrose Broth (SDB) (1:50 dillution) and then by transferring the microtube contents to a sterile Erlenmeyer flask containing 19 mL of Gibco Roswell Park Memorial Institute (RPMI) medium (1:20 dilution).

For plate assembly, the wells were filled with 100 µL of RPMI medium followed by 20 µL of the studied compound solution and its serial dilution. Additionally, 100 µL of the *Candida* suspensions (1.10^3 Color Formation Units (CFU).mL^{-1}) were distributed in each well. As positive controls, miconazole, fluconazole, amphotericin B, and nystatin (Inlab, São Paulo, SP, Brazil) were used. Growth medium, bacterial growth, evaluated compound and negative controls were also employed. After the 96-well plates were assembled, they were incubated at 28 °C for 48 hours. Tests were performed triplicate-wise and MIC values determined by the smallest concentration where fungal growth was not observed.

The Minimum Fungicidal Concentration (MFC) was determined by the method described by Lyu *et al.* (LYU et al., 2016). A 10 µL sample of all wells that did not show visible growth during the MIC assay was transferred to a Petri dish with 4% Sabouraud Dextrose Agar (SDA) and spread along the agar surface with the aid of a Drigalski spatula. The dish was incubated for 48 hours at 28 °C. The MFC was the smallest concentration that inhibits colony formation on the Petri dish. As positive controls, miconazole, fluconazole, amphotericin B, and nystatin (Inlab, São Paulo, SP, Brazil) were used. Growth control wells were also submitted to this test in order to evaluate the growth stimulation capacity of the medium.

Antifungic drug synergism assays

The effect of the combination of **R1G2-PS-O1** with miconazole, amphotericin B, and nystatin was studied by the checkerboard method. Initially, mirror plates with serial dilutions (31.25 to 0.49 µg.mL^{-1}) of the compounds to be combined in SDB were prepared. The assay was performed in a second microplate using the following procedure:

1. 50 µL of each compound (peptide and antifungic drug) were added from the mirror plates — thusly, the combined volume per well was 100 µL;
2. 100 µL of a *Candida albicans* `ATCC 10231` inoculum, with a density of 106 CFU.mL^{-1} was added; and
3. the plates were incubated at 32 °C for 48 hours.

After incubation, the plates were evaluated regarding the absence of presence of visual cell growth. The result was interpreted as a Fractionary Inhibitory Concentration (FIC), calculated as the FIC index ($\mathrm{FIC_i}$)

$$\mathrm{FIC_i} = \mathrm{FIC_i}\ (\mathrm{A}) + \mathrm{FIC_i}\ (\mathrm{B}), \tag{5.1}$$

where $\mathrm{FIC_i}$ (A) is the quotient between the MIC of **R1G2-PS-O1** in conjunction with an antifungic drug and the MIC of **R1G2-PS-O1** in isolation. Conversely, $\mathrm{FIC_i}$ (B) is the quotient between the MIC of the antifungic drug in conjunction with **R1G2-PS-O1** and the MIC of the antifungic drug in isolation.

$\mathrm{FIC_i}$ values are evaluated as representing a synergistic effect when $\mathrm{FIC_i} \leq 0.5$, an additive effect when $0.5 < \mathrm{FIC_i} \leq 1.0$, an indifferent effect when $1 < \mathrm{FIC_i} \leq 4.0$, and an antagonic effect when $\mathrm{FIC_i} > 4.0$ (LIMA et al., 2018).

5.2.2 Antibacterial activity

The peptides **PS-O1**, **PS-O1 GtP**, **R1G2-PS-O1**, and **R1A2-PS-O1 GtP** were evaluated as antibacterial agents in the presence of two bacteria strains, one Gram-positive (*Staphylococcus aureus*) and one Gram-negative (*Escherichia coli*). To determine MIC values, the broth microdilution method was used, as described by the Clinical and Laboratory Standards Institute (WEINSTEIN, 2018). Employed concentrations ranged from 0.24 to 125 µg.mL^{-1} and results were observed after 24 hours of incubation at 32 °C. In these conditions, MIC values were considered as the smallest concentration of the tested agent capable of halting visible microbial growth. Amoxicilin and gentamicine were used as positive control for Gram-positive and -negative strains, respectively. Sterile Mueller-Hinton Broth (MHB), sample (MHB + compound), bacterial growth (MHB + inoculum), and DMSO (DMSO + inoculum) controls were also used. Experiments were done in triplicate.

After MIC data acquisition, Minimum Bactericidal Concentration (MBC) values were determined by the transference of 50 µL of contents from MIC well and of contents from wells with concentration above the MIC to a new microplate containing 150 µL of MHB in its wells (LYU et al., 2016). Results were observed after 48 hours of incubation at 32 °C. MBC values were considered as the smallest concentration of the agent capable of killing the bacteria and, therefore, stopping visible growth. Experiments were conducted in triplicate.

5.2.3 *In vitro* cytotoxicity evaluation

Cytotoxicity assays were done using VERO cells (`ATCC CCL-81`), as recommended by ISO 10993-5 and following the method described by Momoka *et al* (MOKOKA et al., 2013). Cell cultivation was done in 75 mL flasks containing Dulbecco's Modified Eagle Medium (DMEM) supplanted with 5% Bovine Fetal Serum (BFS), 50 mg.mL^{-1} of L-glutamine and gentamycin, 200 U.mL^{-1} of penicillin, and 2.5 mg.mL of amphotericin B, incubated at 37 °C, in a 5% CO_2 atmosphere. Subcultivations were done three times a week where the cell monolayer was washed with a Phosphate-Buffer Saline (PBS) solution (NaCl 137 mM, KCl 2.7 mM, Na_2HPO_4 1.4 mM, at pH 7.2) and treated with a tripsin:EDTA solution (NaCl 136 mM, KCl 5 mM, glucose 55 mM, $NaHCO_3$ 69 mM, 0.5 g tripsin 1:250 (m:v), EDTA 0.5 mM), for cell release.

Cells were distributed in microplates of 96 CC_{50} well (5.10^4 cells per well) with DMEM (5%) and incubated at 37 °C for 24 hours. The medium was then removed and 100 µL.well^{-1} DMEM (without BFS) was added along with 100 µL.well^{-1} of different concentrations of the peptides (3.12 to 200 µg.mL^{-1}) dilluted in DMEM, in triplicate. Plates were incubated at 37 °C for 48 hours and, after removal of the culture medium, 30 µL of a 2 mg.mL^{-1} MTT solution in PBS was added, and the plates were then incubated at 37 °C for 3 hours. To ensure formazan crystal formation by MTT metabolization, 100 µL.well^{-1} of DMSO was added. Values of CC_{50} were calculated by non-linear regression using the `GraphPad Prism 7.0` software (GraphPad Software Inc., La Jolla, CA). Experiments were done in triplicate and repeated three times.

5.3 Results

5.3.1 Antifungic activity

The fungicidal and fungistatic activity of **PS-O1**, **PS-O1 GtP**, **R1G2-PS-O1** and **R1A2-PS-O1 GtP** were evaluated against *C. albicans* (`ATCC18804`, `SC 5314 ATCC MYA-2876`, and `ATCC10231`), *C. glabrata* (`ATCC2001`), *C. tropicalis* (`ATCC28707`), and *C. krusei* (`ATCC34135`), and the results are displayed in **Table 5.1**. Also, the four compounds were evaluated against ten clinical isolates of *Candida albicans*, and the results are displayed in **Table 5.2** and **5.3**.

Table 5.1: MIC and MFC values (µg.mL^{-1}) for **PS-O1**, **PS-O1 GtP**, **R1G2-PS-O1** and **R1A2-PS-O1 GtP** evaluated against *C. albicans* (`ATCC18804`, `SC 5314 ATCC MYA-2876`, and `ATCC10231`), *C. glabrata* (`ATCC2001`), *C. tropicalis* (`ATCC28707`), and *C. krusei* (`ATCC34135`). Concentrations above 125 µg.mL^{-1} indicate that the compound was inactive at the tested concentrations. Amphotericin B was used as control.

	C. albicans `ATCC 18804`		***C. glabrata*** `ATCC 2001`		***C. tropicalis*** `ATCC 28707`		***C. krusei*** `ATCC 34135`		***C. albicans*** `SC 5314` `ATCC MYA-2876`		***C. albicans*** `ATCC 10231`	
	MIC	**CFM**	**MIC**	**CFM**	**MIC**	**CFM**	**MIC**	**CFM**	**MIC**	**CFM**	**MIC**	**CFM**
PS-O1	125	125	125	125	125	125	125	>125	>125	-	>125	-
PS-O1 GtP	>125	-	31.25	62.5	125	125	125	125	>125	-	>125	-
R1G2-PS-O1	15.62	15.62	7.81	7.81	62.5	62.5	15.62	31.25	15.62	15.62	31.25	31.25
R1A2-PS-O1 GtP	62.5	62.5	15.62	31.25	>125	-	31.25	62.5	62.5	62.5	>125	-
Amphotericin B	0.98	1.96	0.25	0.98	1.96	3.92	1.95	15.62	1.95	1.95	0.49	0.98

Table 5.2: MIC and MFC values (µg.mL^{-1}) for **PS-O1**, **PS-O1 GtP**, **R1G2-PS-O1** and **R1A2-PS-O1 GtP** evaluated against clinical isolates (S1, S2, S3, S4, and S5) of *C. albicans* obtained from candidiasis. Concentrations above 125 µg.mL^{-1} indicate that the compound was inactive at the tested concentrations. Amphotericin B was used as control.

	C. albicans **S1**		***C. albicans*** **S2**		***C. albicans*** **S3**		***C. albicans*** **S4**		***C. albicans*** **S5**	
	MIC	**CFM**	**MIC**	**CFM**	**MIC**	**CFM**	**MIC**	**CFM**	**MIC**	**CFM**
PS-O1	125	125	125	125	62.5	62.5	62.5	125	125	125
PS-O1 GtP	125	125	>125	-	>125	-	>125	-	125	125
R1G2-PS-O1	31.25	31.25	31.25	31.25	15.62	15.62	31.25	31.25	31.25	31.25
R1A2-PS-O1 GtP	125	125	62.5	62.5	62.5	125	125	125	62.5	62.5
Amphotericin B	0.49	0.49	0.98	0.98	0.98	0.98	15.62	15.62	0.98	0.98

Table 5.3: MIC and MFC values (µg.mL^{-1}) for **PS-O1**, **PS-O1 GtP**, **R1G2-PS-O1** and **R1A2-PS-O1 GtP** evaluated against clinical isolates (S6, S7, S8 and S9) of *C. albicans* obtained from candidiasis. Concentrations above 125 µg.mL^{-1} indicate that the compound was inactive at the tested concentrations. Amphotericin B was used as control.

	C. albicans S6		*C. albicans* S7		*C. albicans* S8		*C. albicans* S9	
	MIC	**CFM**	**MIC**	**CFM**	**MIC**	**CFM**	**MIC**	**CFM**
PS-O1	>125	-	62.5	62.5	>125	-	62.5	62.5
PS-O1 GtP	>125	-	62.5	62.5	>125	-	125	125
R1G2-PS-O1	7.81	7.81	7.81	7.81	62.5	62.5	15.62	15.62
R1A2-PS-O1 GtP	62.5	62.5	31.25	31.25	125	125	62.5	62.5
Amphotericin B	1.95	1.95	0.98	0.98	0.98	0.98	0.49	0.49

MIC data is displayed as graphs in **Figure 5.7**, in order to facilitate visualization.

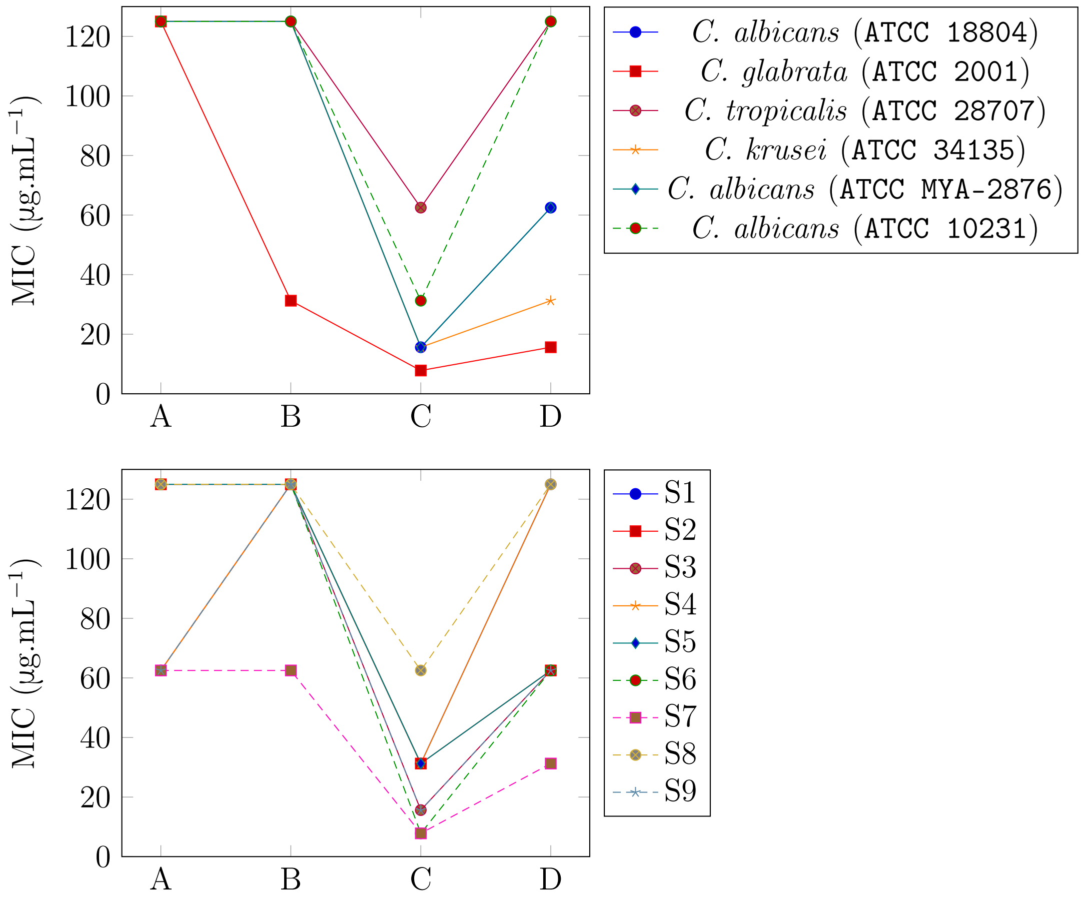

Figure 5.7: MIC values for (A) **PS-O1**, (B) **PS-O1 GtP**, (C) **R1G2-PS-O1** and (D) **R1A2-PS-O1 GtP** evaluated against (top) *C. albicans* (`ATCC18804`, `SC 5314 ATCC MYA-2876`, and `ATCC10231`), *C. glabrata* (`ATCC2001`), *C. tropicalis* (`ATCC28707`), and *C. krusei* (`ATCC34135`), and (bottom) ten clinical isolates (S1 to S9) of *Candida albicans* obtained from patients with candidiasis.

The four peptides showed moderate activity against `ATCC` lineages of *Candida sp.* and clinical isolates of *Candida albicans* when compared to amphotericin B. Furthermore, while **PS-O1** and **PS-O1 GtP** were not active against the yeasts, Arg-containing derivatives **R1G2-PS-O1** and **R1A2-PS-O1 GtP** displayed higher activity, especially the first, indicating that ergosterol biosynthetic steps were probably not the target for these compounds. In contrast, *C. glabrata* was much more susceptible to the influence of the Arg-compounds while still being unaffected by **PS-O1** and **PS-O1 GtP**, further indicating that some other biological property was the main target. Furthermore, since MIC and MFC values were the approximatelly the same for all compounds, they likely show fungicidal potential.

Although further studies are necessary in order to ascertain by which specific mechanisms these compounds act, it can be assumed that the **PS-O1** backbone was not adequate for antinfungal activity to the point that glucosylation did not enhance its activity. Likewise, Arg-containing **R1G2-PS-O1** had its biological potential worsened by the introduction of the glucotriazole unit. This evidence points to two main possibilities:

1. First, while ergosterol biosynthesis probably was not the main target, some form of membrane interaction should take place since **R1G2-PS-O1** has the highest helical content and a large hydrophobic moment modulus $|\vec{\mu}_H|$;
2. As mentioned, the introduction of the Arg residue, although not part of the helical structure, was probably of major importance to the biological activity of **R1G2-PS-O1**, as shown by MIC values. Furthermore, some sort of interaction was probably hindered by the introduction of either the triazole ring, the glucose unit, or both.

To better explain these assumptions, an understanding of the typical action mechanism of azole drugs and the eventual disturbance of the ergosterol biosynthetic pathway is needed. Ergosterol (**Figure 5.8**), in order to properly exercise its main function in cell proliferation, needs to have a planar a-face (*i.e.*, without any substituents at C-14) and a double bond between carbon atoms C-5 and C-6 (SHAFIEI et al., 2020).

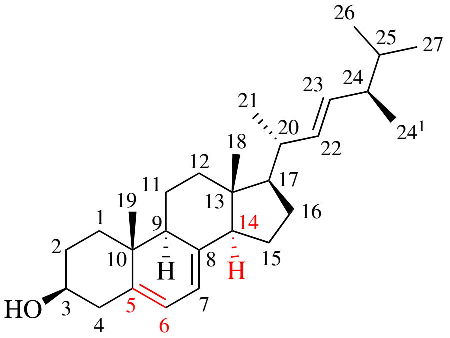

Figure 5.8: Ergosterol representation with enumerated carbons, showing emphasis on the demethylated C-14 atom and the double bond between C-5 and C-6 (MOSS, 1989).

During ergosterol biosynthesis, a lanosterol molecule is demethylated by the CYP51 enzyme, also known as lanosterol-14α-demethylase and belonging to the cytochrome superfamily. It catalyzes the oxidative removal of the methyl group in C-14 and introduces a double bond between C-14 and C-15 (**Figure 5.9**) (SHAFIEI et al., 2020; LAMB et al., 1999).

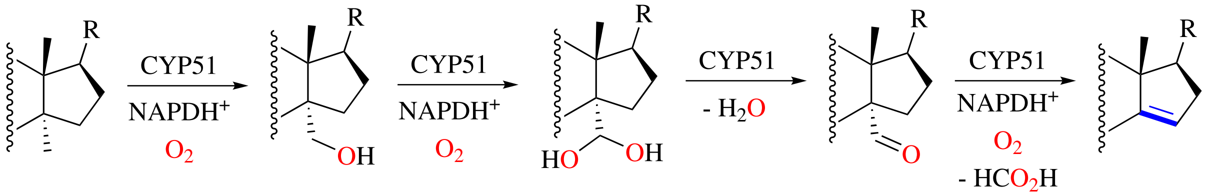

Figure 5.9: Representation of the lanosterol demethylation reaction, showing two oxygenation process followed by formic acid elimination, all catalyzed by the CYP51 (lanosterol-14α-demethylase) enzyme.

The presence of an heme group in CYP51 is crucial, being an iron-containing porphirine unit that provides molecular oxygen to the monooxygenation steps of this process (ZHANG et al., 2019). Azoles act on the demethylation step as reversible, non-competitive inhibitors of the heme group and preventing proton access to the active site of CYP51 (SHAFIEI et al., 2020; MAKVANDI et al., 2021), behaving as axial ligands (**Figure 5.10**).

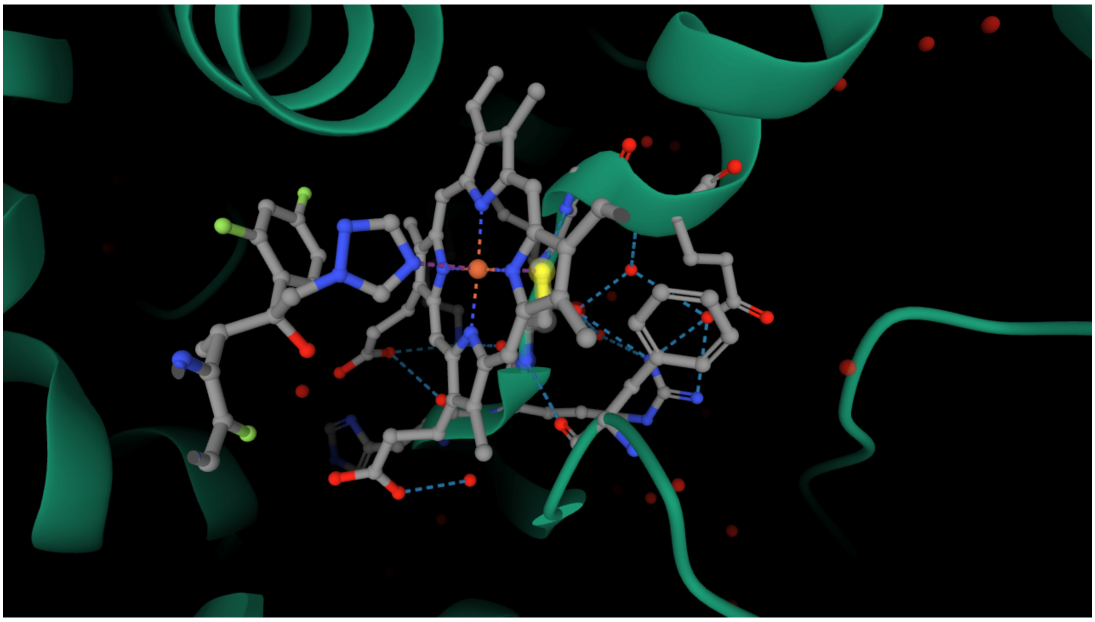

Figure 5.10: Representation of the CYP51 iron-contaning heme group of *Saccharomyces cerevisiae* complexed with Voriconazole (PDB 5HS1), showing the interaction between the N-4 atom of the 1,2,4-triazole moiety, the iron atom of the porphyrinic unit and the sulfur-containing side-chain of Cys-464, producing the inhibition effect (SAGATOVA et al., 2016). Nitrogens are represented in blue, the iron, in orange, and the sulfur, in yellow. Coordinations to the iron are represented as a dashed purple line.

Low levels of ergosterol have many consequences to fungal cells, like compromised membrane stability, nutrient transport, and chitine synthesis, ultimately interfering in cellular proliferation and increasing host-defense mechanisms susceptibility. Finally, the buildup of toxic ergosterol precursors also damages the cell, resulting in an initial inhibitory character of the drug that can, eventually, become fungicidal (HOF, 2006).

Regarding the heterocyclic unit in these drugs, the pyridine-type *N*-3 in 1,2,3-triazoles positions itself vertically to the porphirine plane. While basicity is not a direct indicator of activity, it can be used when it is directly correlated to iron affinity (*i.e.*, tetrazole being the less basic also displays the smallest inhibitory effect of CYP51) (SHAFIEI et al., 2020). Furthermore, triazoles display the greater selectivity for fungal cytochrome P450, as opposed to mammalian, indicating a better selectivity (HOF, 2006).

With these aspects properly established, an interaction between glucotriazole derivatives **PS-O1 GtP** and **R1A2-PS-O1 GtP** and the iron-containing porphirine group would be established by coordination of ttriazole moiety. Additionally, for this interaction to occur, the peptide would have to interact with the fungal cell membrane first and, as shown in **Table 4.3, Page 118**, the hydrophobic moment modulus $|\vec{\mu}_H|$ is greater for **R1A2-PS-O1 GtP** than the one calculated for **PS-O1 GtP**, even though the helix percentage of the second was higher. This indicates that, since the Arg-containing GtP was significantly more active than **PS-O1 GtP**, the higher membrane affinity of **R1A2-PS-O1 GtP** was the main factor, facilitating membrane insertion and eventual triazole-heme interactions in the fungus. However, ergosterol-related interference is probably not the main target of these compounds since the most active of the four peptide derivatives does not have a glucotriazole unit and had its activity hindered by its introduction.

Regarding this last point, although more complex structural studies are required, the correlation between basicity and iron affinity can be used to infer the reason for the negative effect of glucotriazole insertion in **R1A2-PS-O1 GtP**. Assuming that the guanidinium moiety of the Arg side chain is dynamic, the possible interaction between this positively-charged group and the 1,2,3-triazole ring can be considered. This consideration is important since cation-π-type interactions between the heterocycle and the cation (TSOU et al., 2002; SHI et al., 2002) would result in an overall lowering of the molecular orbital energies of 1,2,3-triazole, eventually reducing nucleophilicity, basicity and coordination capabilities, hindering CYP51 inhibition.

Still regarding antifungic activity, drug synergism assays were performed for **R1G2-PS-O1** with miconazole, nystatin, and amphotericin B against *Candida albicans* `ATCC 10231`, and the obtained FIC values are shown in **Table 5.4, Page 134**. As can be seen, although the peptide displayed additive effects with amphotericin B and nystatin, the synergic effect observed with miconazole represents a novel treatment alternative to be explored when combating fungal infections.

5.3.2 Antibacterial activity

The bactericidal and bacteriostatic activity of **PS-O1**, **PS-O1 GtP**, **R1G2-PS-O1** and **R1A2-PS-O1 GtP** were evaluated against *Escherichia coli* and *Staphylococcus aureus*, and the

Table 5.4: Fractionary Inhibitory Concentration (FIC) values and indexes for (FIC_i) **R1G2-PS-O1** with miconazole, nystatin and amphotericin B evaluated against *Candida albicans* `ATCC 10231`.

Drug	FIC		FIC_i	Effect
	R1G2-PS-O1	Drug		
Miconazole	0.12	0.25	0.37	*Synergic*
Nystatin	0.5	0.5	1.0	*Additive*
Amphotericin B	0.06	0.5	0.56	*Additive*

results are displayed in **Table 5.5**.

Table 5.5: MIC and MBC values (µg.mL^{-1}) for **PS-O1**, **PS-O1 GtP**, **R1G2-PS-O1** and **R1A2-PS-O1 GtP** evaluated against *Escherichia coli* and *Staphylococcus aureus*. Concentrations above 125 µg.mL^{-1} indicate that the compound was inactive at the tested concentrations. Gramicidin was used as control.

Compounds	***E. coli***		***S. aureus***	
	MIC	MBC	MIC	MBC
PS-O1	>125	-	>125	-
PS-O1 GtP	>125	-	>125	-
R1G2-PS-O1	>125	-	62.5	125
R1A2-PS-O1 GtP	>125	-	>125	-
Gramicidin	0.49	0.98	0.24	0.49

As can be seen, although the diversity of bacterial strains used to evaluate the antibacterial potential was low, only **R1G2-PS-O1** displayed any activity, and the Gram-positive *Staphylococcus aureus* was more sensitive to it, indicating a potential selectivity that could be linked to cell wall composition. Furthermore, similar conclusions can be made regarding the glucosylation of **R1G2-PS-O1** and how it potentially lowered its antibacterial activity. Finally, comparison between MIC and MBC values point to a bacteriostatic character of the peptide, as opposed to the apparent fungicidal character discussed previously.

5.3.3 *In vitro* cytotoxicity evaluation

The *in vitro* cytotoxicity of **PS-O1**, **PS-O1 GtP**, **R1G2-PS-O1** and **R1A2-PS-O1 GtP** were evaluated in the presence of VERO cells (`ATCC CCL-81`), and the results are displayed in **Figure 5.11**[1]. As can be seen, all peptide display virtually no cytotoxicity, even at high concentrations, like 200 µg.mL^{-1}, which is an excellent result, since membrane-active AMPs display mechanisms of action against bacteria and fungi that could be problematic for mammalian cells

---

[1] Cell viability and their respective average and standard deviation values are displayed in **Appendix A, Table A.8**.

at high concentrations, such as the carpet model. Furthermore, although the membrane surface of bacterial cells and the cell wall of fungi display a negative net charge (LIPKE; OVALLE, 1998; SOWA-JASIłEK et al., 2020; SOHLENKAMP; GEIGER, 2016), the positive net charge of common AMPs is responsible for a selectivity for negative membranes, not a specificity. As a matter of fact, all cationic AMPs have presented some level of cytotoxicity against mammalian cells (BACALUM; RADU, 2015), where pore-formation mechanisms are prevalent (YEAMAN; YOUNT, 2003), and haemolytic activity is one of the current points of contention against the use of peptide therapeutics, alongside poor bioavailability (GRECO et al., 2020).

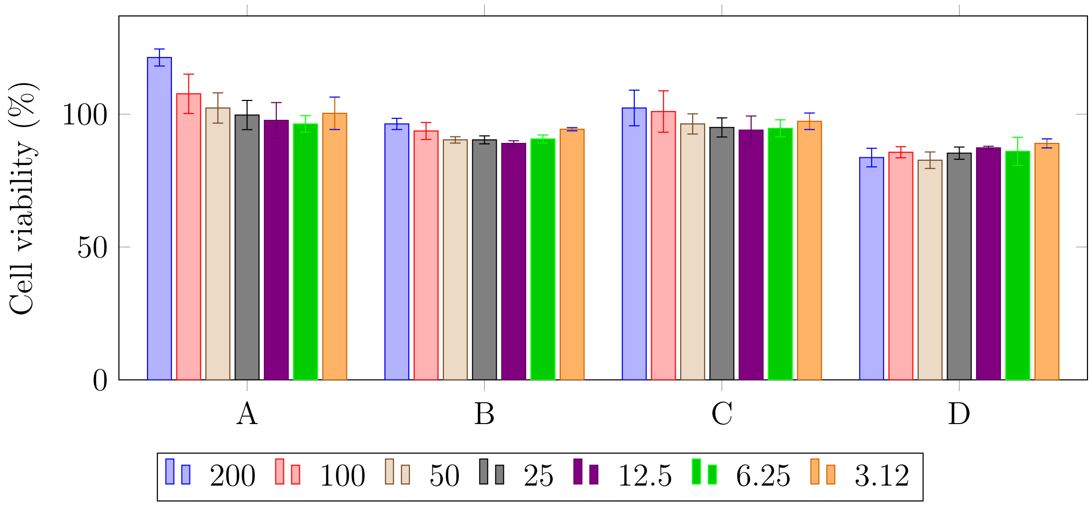

Figure 5.11: *In vitro* cytotoxicity of (A) **PS-O1**, (B) **PS-O1 GtP**, (C) **R1G2-PS-O1**, and (D) **R1A2-PS-O1 GtP** evaluated in the presence of VERO cells (`ATCC CCL-81`). VERO cells were treated with different concentrations of peptides (200 to 3.12 μg.mL^{-1}, indicated by the colors of the legend) for 48 hours. Results are expressed as the average ± one standard deviation (indicated by the error bar) of three independent experiments.

As such, even though the antifungic and antibacterial character of the synthesized products were moderate compared to the controls (amphotericin B and gramicidin), the low cytotoxicity provides an important justification for their use as therapeutics, especially considering that **R1G2-PS-O1** showed synergic effects with miconazole against *C. albicans*, providing an important avenue to treat infections caused by this species with a substantially low toxicity when compared to, for instante, amphotericin B (LANIADO-LABORÍN; CABRALES-VARGAS, 2009).

Chapter 6 | Structural studies of LyeTx I-b$_{\mathbf{cys}}$ and LyeTx I-bPEG

6.1 Introduction

Among the varied sources of AMPs, spider and scorpion venom are important sources of novel potential drugs (JÚNIOR et al., 2019; KUHN-NENTWIG, 2003; WANG; WANG, 2016). In particular, the venom of the spider species *Lycosa erythrognata* is the source of LyeTx I (**Table 6.1**), a *C*-terminus-amidated peptide. This peptide displays activity against *S. aureus*, *E. coli*, *Candida krusei* and *Cryptococcus neoformans* with low hemolytic character, and NMR results revealed an α-helical conformation in the presence of detergent micelles (SANTOS et al., 2010). A subsequent publication in 2018 (REIS et al., 2018) showed studies of the analogue LyeTx I-b (**Table 6.1**); designed by the removal of His-16 from the wild-type sequence, and by *N*-terminal acetylation. These modifications resulted in increased structural amphipathicity and biological activity against Gram-positive and Gram-negative bacteria compared to LyeTx I—it is 10-fold more active against *E. coli.* Finally, in 2021 (BRITO et al., 2021), the PEGylated analogue of LyeTx I-b, LyeTx I-bPEG (**Table 6.1**) was synthesized by the Methoxy polyethyleneGlycol-maleimide (mPEG-MAL) conjugation (**Figure 6.1**) of a Cys-modified LyeTx I-b (LyeTx I-b$_{\text{cys}}$ **Table 6.1**). Whereas MIC values determined for the base peptide and for its PEGylated analogue were the same, PEGylation reduced *ca.* 10 times induced hemolysis, representing an attractive pharmaceutical prospect for the peptide-PEG conjugate. As a whole, PEGylation is an interesting peptide modification since it prolongs the residence time of drugs in the body, decreases degradation rates, toxicity and immunogenicity (BRITO et al., 2021).

Table 6.1: Primary structures of LyeTx I, LyeTx I-b, LyeTx I-b$_{cys}$ and LyeTx I-bPEG, with relevant residues and positions shown in bold. **Ac** refers to the *N*-terminus acyl group and **C-PEG** refers to the PEGylated cysteine residue.

Peptide	Primary structure
LyeTx I	IWLTA LKFLG KNLGK **H**LAKQ Q**L**AKL-NH_2
LyeTx I-b	**Ac**IWLTA LKFLG KNLGK LAKQQ **L**AKL-NH_2
LeyTx I-b$_{cys}$	**Ac**IWLTA LKFLG KNLGK LAKQQ **C**AKL-NH_2
LyeTx I-bPEG	**Ac**IWLTA LKFLG KNLGK LAKQQ **(C-PEG)**AKL-NH_2

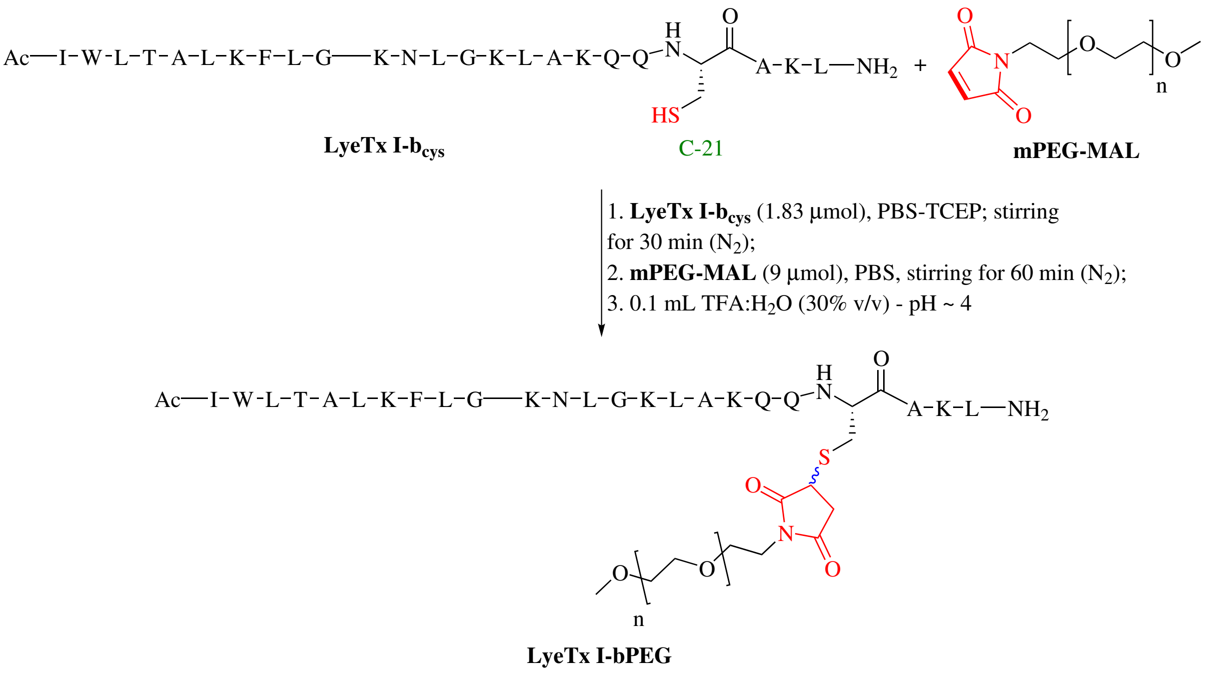

Figure 6.1: Representation of the Michael addition between LyeTx I-b$_{cys}$ and mPEG-MAL, yielding LyeTx I-bPEG.

To enrich the discussion regarding the biological activity of LyeTx I-bPEG, NMR analyses and structural calculations for LyeTx I-b$_{cys}$ and LyeTx I-bPEG were performed and the results were compared to the three-dimensional structures of the peptides LyeTx I and LyeTx I-b, which have been previously determined (SANTOS et al., 2010; REIS et al., 2018).

6.2 Methodology

LyeTx I-b$_{cys}$ (**Table 6.1**) was synthesized using the Fmoc-SPPS strategy, described in **Chapter 2, Section 2.2.1, Page 51**. mPEG-MAL conjugation was performed by collaborator Júlio César Moreira Brito (BRITO et al., 2021) at Fundação Ezequiel Dias (FUNED, Brazil). NMR spectra were collected similarly to as described in **Chapter 4, Section 4.2.1, Page 94** with some modifications.

Two-dimensional NMR experiments were carried out for LyeTx I-b$_{\mathrm{cys}}$ at 2.0 mM and for LyeTx I-bPEG at 1.5 mM in TFE-d_2:H_2O (60:40, v:v) solutions (600 µL) adjusted to pH 7.0 using phosphate buffer at 20 mM. DSS at 1.0 mM was used as the internal reference for LyeTx I-bcys and at 2.0 mM for LyeTx I-bPEG. TOCSY, NOESY and HSQC data was acquired at 20 °C on a Bruker Avance Neo 600 equipped with a 5 mm BBO SmartProbe with coils suited for pulsed field gradients. ^{1}H NMR data was acquired for LyeTx I-b$_{\mathrm{cys}}$ using a spectral width of 6578 Hz and for LyeTx I-bPEG with a spectral width of 6849 Hz. Water suppression was achieved by pre-saturation.

TOCSY experiments were acquired using the DIPSI-2 scheme (RUCKER; SHAKA, 1989). The parameters used for the experiments were spectral width of 6578 Hz, 512 t_1 increments with 16 transients of 4096 points for LyeTx I-b$_{\mathrm{cys}}$ and spectral width of 6849 Hz, 512 t_1 increments with 16 transients of 4096 points for LyeTx I-bPEG. A spin-lock time of 80 ms was used in the TOCSY experiments.

NOESY spectra (KUMAR et al., 1980) were acquired with mixing times of 100, 150, 200 and 250 ms for LyeTx I-b$_{\mathrm{cys}}$ and of 100, 120, 150 and 250 ms for LyeTx I-bPEG to check for spin diffusion. The parameters used for NOESY experiments were: spectral width of 6578 Hz, 512 t_1 increments with 24 transients of 4096 points for LyeTx I-b$_{\mathrm{cys}}$ and spectral width of 6849 Hz, 512 t_1 increments with 40 transients of 4096 points for LyeTx I-bPEG.

^{1}H−^{13}C-HSQC spectral data were acquired in phase-sensitive fashion such that correlations involving CH and CH_3 groups would present positive phase, whereas those involving CH_2, negative (WILLKER et al., 1993). Regarding the acquisition parameters for the LyeTx I-b$_{\mathrm{cys}}$ sample, F1 and F2 spectral widths of 15,822 and 6578 Hz were used, respectively; 512 t_1 increments with 24 transients of 2048 points. In the case of the LyeTx I-bPEG samples, F1 and F2 spectral widths of 15,822 and 6849 Hz, 416 t_1 increments with 24 transients of 2048 points were used.

^{1}H−^{15}N-HSQC data (FAIRBROTHER et al., 1991; SCHLEUCHER et al., 1994) were acquired using F1 and F2 spectral widths of 2311 and 6578 Hz, respectively, 88 t_1 increments with 400 transients of 1024 points for LyeTx I-b$_{\mathrm{cys}}$ and using F1 and F2 spectral widths of 2554 and 6849 Hz, respectively, 80 t_1 increments with 464 transients of 1024 points for LyeTx I-bPEG.

Bruker Topspin® software was used for data acquisition and initial processing. Further processing, data conversion, spectra analysis, data extraction and structural calculation was done according to **Chapter 4, Section 4.2.2, Page 95** and **Section 4.2.3, Page 96**, using 19,000 simulated annealing steps at 1000 K and 11,000 cooling steps. It is worth noting that, since the PEG section of LyeTx I-bPEG has a high degree of structural flexibility, it was not included in its structural calculations. Structural ensembles were comprised of the ten lowest energy structures among the 200 calculated and manipulation of the structures was done using PyMOL (Schrödinger, LLC, 2015).

6.3 Results

The synthesis, analysis and purification of both LyeTx I-b$_{\mathrm{cys}}$ and LyeTx I-bPEG are thoroughly described in a previous publication (BRITO et al., 2021). Briefly, purification was done by RP-HPLC and initial analysis was done by MALDI-ToF-MS while NMR analysis revealed some important points regarding the Michael addition that will be expanded upon here, along with the entire structural discussion and comparison between the two peptides and LyeTx I and LyeTx I-b.

NMR spectra of LyeTx I-b$_{\mathrm{cys}}$ and LyeTx I-bPEG are characterized by a high number of sufficiently dispersed correlations, suggesting well-folded conformations for both. Furthermore, they revealed important changes regarding the spectra profile and chemical shift values for some nuclei, confirming reaction completion. As an example, the absence of olefinic signals in the ^{1}H spectrum of the PEGylated peptide and the presence of signals typical of succinimidyl moieties in its $^{1}\mathrm{H}-^{13}\mathrm{C}$-HSQC spectrum (BRITO et al., 2021) indicate a successful PEGylation. Broadening or even duplication of some resonances related to Cys-21 and nearby residues, such as Glutamine (Gln)-20 and Ala-22 were observed, which are expected due to the formation of epimers—given the lack of stereoselective elements in the reaction (NAIR et al., 2014).

Analysing the TOCSY contour maps of LyeTx I-b$_{\mathrm{cys}}$ and LyeTx I-bPEG (**Figure 6.2, Page 140**), H_{α}-H_{N} correlations for residues Ala-17 up to Ala-22 of the PEGylated derivative are either broadened or explicitly duplicated, as is the case for Gln-20, Cys-21 and Ala-22, proving the formation of epimers. One important aspect of **Figure 6.2** is a signal broadening up to residue Ala-17; four residues apart from Cys-21, indicating that a helical segment encompasses these two residues, since chemical shift changes due to epimer formation at Cys-21 will likely impact nearby residues, like Ala-17 in the case of a helical structure due to $(i, i+4)$ interactions. Furthermore, the helix should extend until Ala-22 or, at most, to Lys-23, otherwise additional broadening or splitting would be observed for residues after Ala-22.

Similarly, the $^{1}\mathrm{H}-^{15}\mathrm{N}$-HSQC spectra (**Figure 6.3**) serve as further evidence for effective mPEG-MAL conjugation; additionally, chemical shift differences for it are more noticeable due to the larger spectral window of the ^{15}N nucleus.

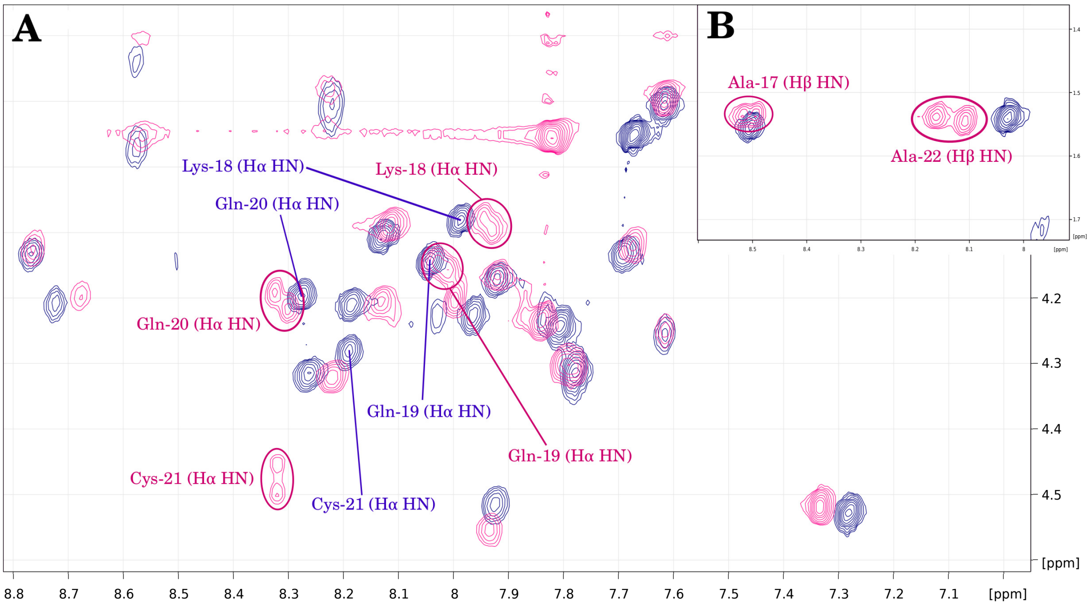

Figure 6.2: (**A**) Overlay of LyeTx I-b$_{cys}$ (dark blue) and LyeTx I-bPEG (pink) TOCSY contour maps. The highlighted correlations (**B**) range from Ala-17 to Ala-22 and show that mPEG-MAL conjugation resulted in signal broadening or splitting for Hα.HN and, for alanine residues, Hβ.HN correlations in LyeTx I-bPEG, while this was not observed for LyeTx I-b$_{cys}$.

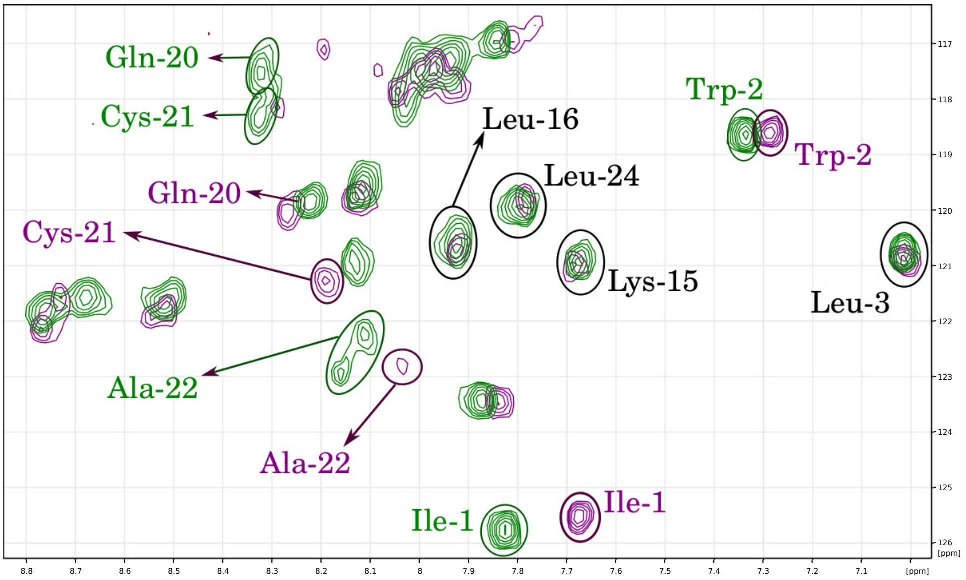

Figure 6.3: Superposition of LyeTx I-b$_{cys}$ (bordeaux) and LyeTx I-bPEG (green) ^{1}H-^{15}N-HSQC contour maps. Correlations highlighted from residues Gln-20 up to Ala-22 show substantial chemical shift difference between LyeTx I-b$_{cys}$ and LyeTx I-bPEG, while residues that are far from the mPEG-MAL conjugation site, such as Leu-16, Leu-24, Lys-15 and Leu-3 (highlighted in black) have a similar chemical shift value between both polypeptide structures.

The H_N-H_N region of the NOESY and $^1\mathrm{H}-^{15}\mathrm{N}$-HSQC contour maps of LyeTx I-b$_{\mathrm{cys}}$ and LyeTx I-bPEG (**Figure 6.4**) shows a great deal of correlations, further supporting the presence of well-defined α-helices. The H_N-H_N region of the NOESY spectrum of LyeTx I-bPEG is more crowded in the region between 7.9 and 8.6 ppm when compared to the respective spectrum of LyeTx I-b$_{\mathrm{cys}}$. This regions comprises the majority of the signals related to residues close to the conjugation site, serving as additional evidence to epimer formation.

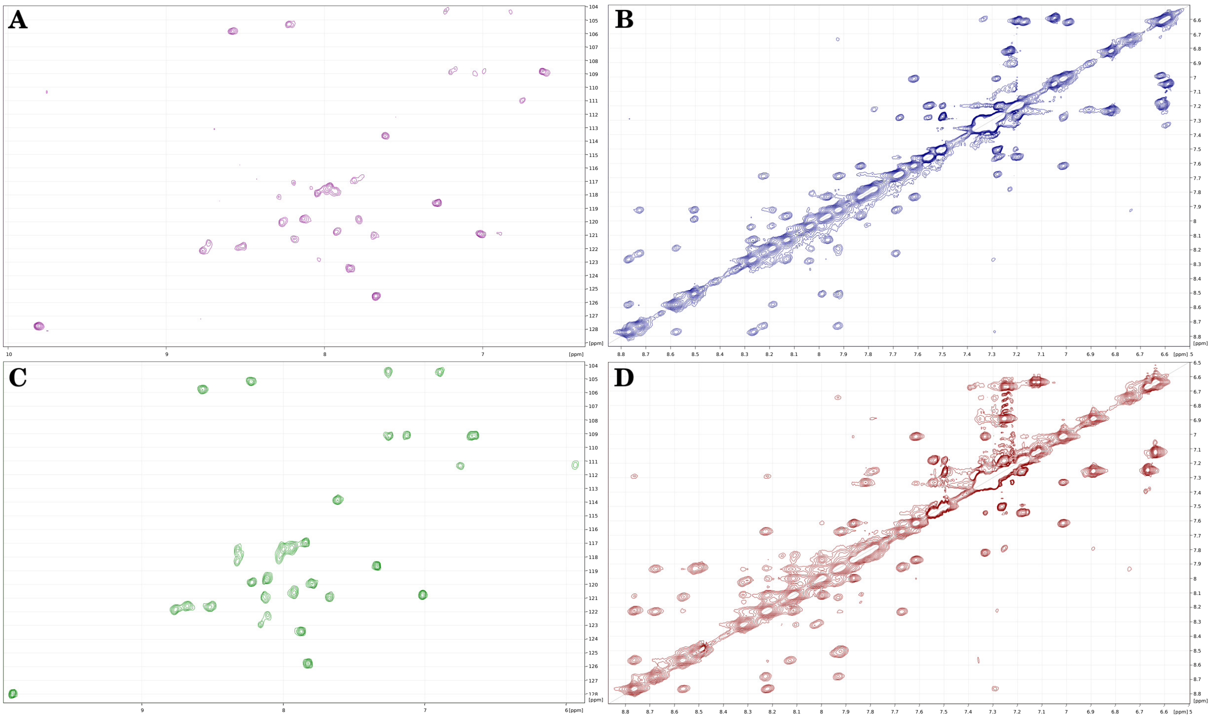

Figure 6.4: (**A**, **C**) $^1\mathrm{H}-^{15}\mathrm{N}-\mathrm{HSQC}$ spectra and (**B**, **D**) amide-amide region of the NOESY spectra of (**A**, **B**) LyeTx I-b$_{\mathrm{cys}}$ at 1.5 mM in TFE-d_2:$\mathrm{H_2O}$ - pH 7.0 (phosphate buffer), 20 °C and of (**C**, **D**) LyeTx I-bPEG at 2.0 mM in TFE-d_2:$\mathrm{H_2O}$ - pH 7.0 (phosphate buffer), 20 °C.

The summary of internuclear NOE correlations for both peptides (**Figure 6.5, Page 142**) better displays helix-associated correlations. First, the large number of $(i, i+1)$ cross-peaks extend throughout the entire primary structure in both cases. Moreover, many medium-range NOE interactions are also seen for LyeTx I-b$_{\mathrm{cys}}$ and LyeTx I-bPEG, including $(i, i+3)$ and $(i, i+4)$ extending from the acylated N-terminus to Ala-17.

Additionally, considerable resonance superposition from Ala-17 up to the C-terminus hampered the assignment of medium-range correlations—α, β $(i, i+3)$, α, N $(i, i+3)$ and α, N $(i, i+4)$—for both structures, even though an α, β $(i, i+3)$ correlation involving Gln-20 and Lys-23 indicates a structured segment encompassing residues 20 to 23 for LyeTx I-b$_{\mathrm{cys}}$ and LyeTx I-bPEG. Previous publications by Santos and collaborators and Reis and collaborators (SANTOS et al., 2010; REIS et al., 2018) showed many H_N, H_N $(i, i+2)$ correlations in the NOESY spectra of LyeTx I and LyeTx I-b, respectively, used to justify a slight helix bend for the peptides.

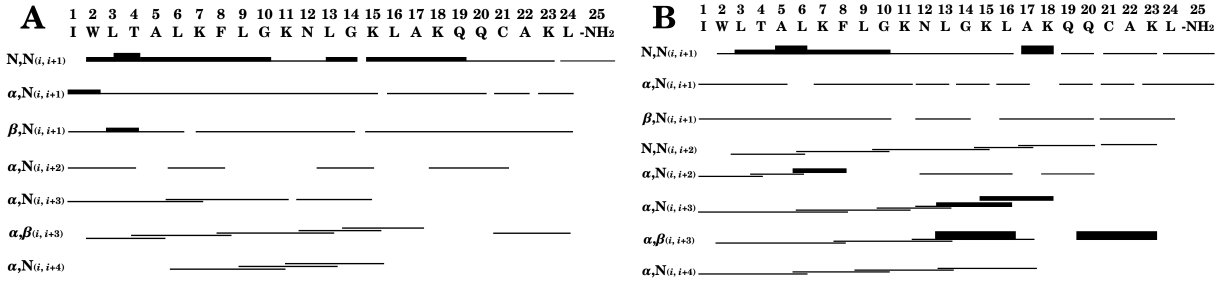

Figure 6.5: Graphical summary of nOe correlations characteristic of α-helical structures observed in NOESY contour maps of (**A**) LyeTx I-b$_{\text{cys}}$ and (**B**) LyeTx I-bPEG. Thin, medium and thick bars represent weak, medium and strong nOe correlations, respectively. NH_2 represents the carboxamide terminus.

Although these correlations were not observed in the NOESY spectrum of LyeTx I-b$_{\text{cys}}$, a few were for LyeTx I-bPEG, suggesting similar structural attributes between the PEGylated form and LyeTx I and LyeTx I-b.

As a side note, comparing **Figure 6.5** and the characteristic NOE correlations of the **PS-O1** derivatives (**Figure 4.25, Page 106**) reveals interesting differences. Since neither derivative has *N*-terminal acylations, the positive charge of the nitrogen atom lowers helical stability is this region and the amount of internuclear correlations for them. **PS-O1 GtP**, nevertheless, does not follow this trend since the Gt unit likely offers some stabilization to furnish the observed correlations at the *N*-terminus, as discussed. However, *N*-terminal acylation proved to be a simple yet very effective way of guaranteeing the helical stability for the peptides.

To gain additional structural information, specifically regarding if the *C*-terminus presents a defined helix for both peptides, dihedral angle values and restraints based on δ were calculated by `TALOS+` (SHEN et al., 2009). **Figure 6.6** shows the results of these calculations, indicating that α-helices extend from Trp-2 to Lys-23 for both peptides. This is in line with the results obtained for LyeTx I-b (REIS et al., 2018), for which the *C*-terminus carboxamide and the *N*-terminus acylation seem to ensure structural stability at these termini.

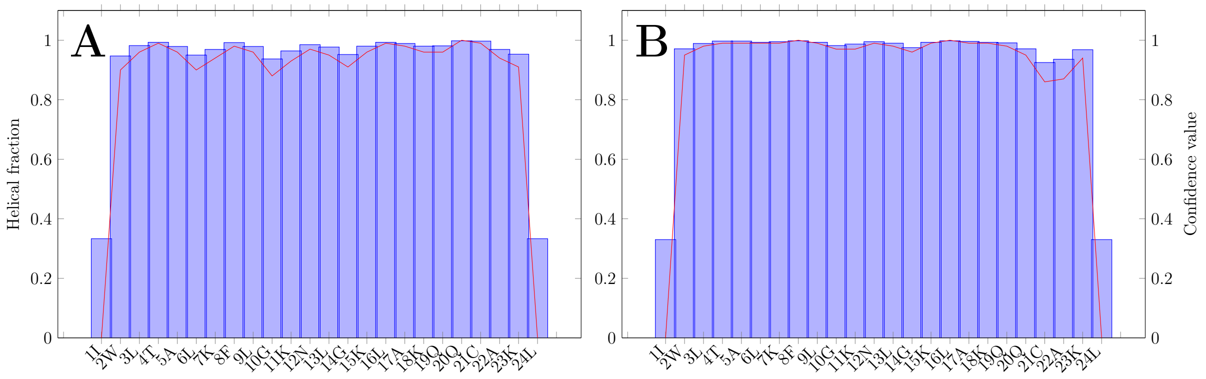

Figure 6.6: Neural-network-predicted helical content of each amino acid residue (blue bars) and their respective confidence values (red line) for (**A**) LyeTx I-b$_{\text{cys}}$ and (**B**) LyeTx I-bPEG, as calculated by `TALOS+` (SHEN et al., 2009).

With the internuclear distance restraints, derived from the NOESY spectra correlations, and dihedral angle restraints, derived from chemical shift data, the 3D structures of LyeTx I-b$_{\mathrm{cys}}$ and LyeTx I-bPEG were calculated using an SA optimization algorithm. The ensembles formed by the ten most stable structures for the cysteine-containing and PEGylated peptides, alongside the ensembles of LyeTx I (SANTOS et al., 2010) and LyeTx I-b (REIS et al., 2018) for comparison, are shown in **Figure 6.7**.

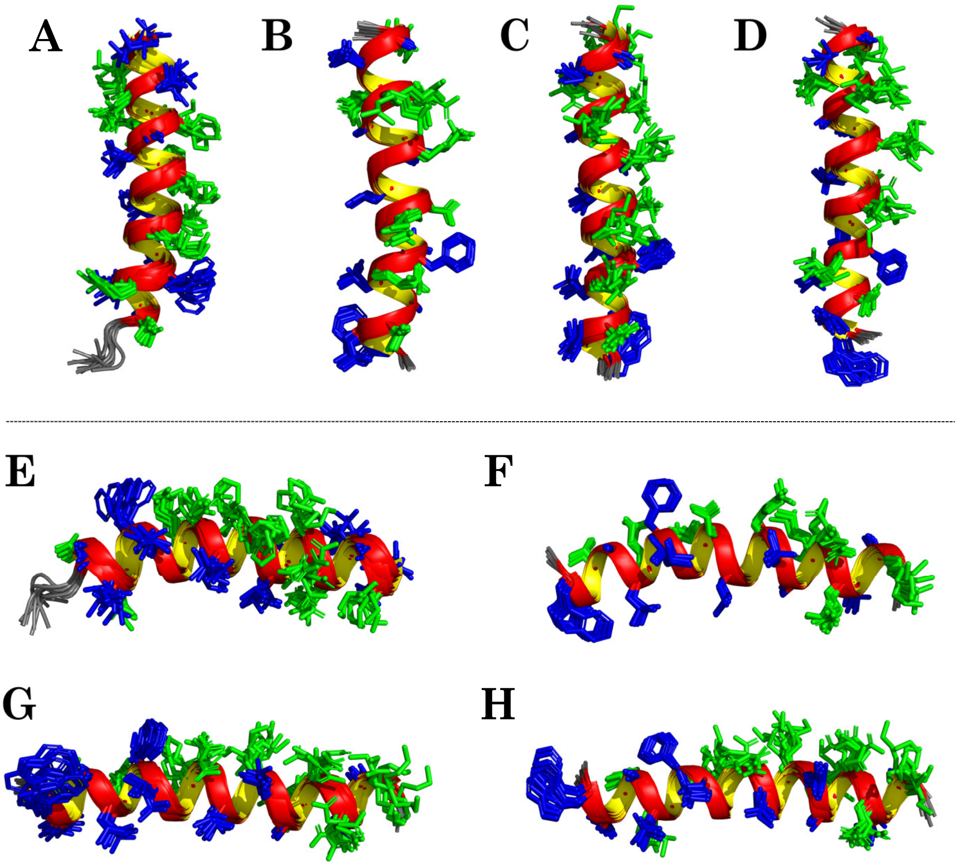

Figure 6.7: Ensembles comprised of the 10 most stable structures of (**A**, **E**) LyeTx I (SANTOS et al., 2010), (**B**, **F**) LyeTx I-b (REIS et al., 2018), (**C**, **G**) LyeTx I-b$_{\mathrm{cys}}$ and (**D**, **H**) LyeTx I-bPEG. Panels **A-D** represent vertical perspective of each helical structure while panels **E-H** represent horizontal points for them. Hydrophobic residues are displayed in dark blue and hydrophilic residues in green. Due to the high flexibility of the PEG segment, it was not included in the structural calculations of LyeTx I-bPEG.

Both calculated ensembles are characterized by well-defined helical segments covering, basically, the entire peptide sequence, as observed for LyeTx I-b (REIS et al., 2018), making it clear that both the N-terminus acyl and the C-terminus acetamide moieties provide important structural elements such as stabilization of the positive end of the helix dipole and extra hydrogen bonds interactions near the peptide termini, so that the helices encompass a large extension of yeTx I-b$_{\mathrm{cys}}$ and LyeTx I-bPEG.

As suggested by the number of H_N, H_N $(i, i+2)$ correlations in LyeTx I-bPEG, a slight bend of helix is observed in the ensembles. When compared to LyeTx I-b, the number of these correlations is smaller (REIS et al., 2018), justifying the subtler curvature observed for the PEGylated analogue. Also, from the visual inspection of the four structural ensembles (**Figure 6.7**), it can be seen that LyeTx I and LyeTx I-b$_{\text{cys}}$ have a substantially larger conformational flexibility in comparison to LyeTx I-b and LyeTx I-bPEG, as seen by the cohesion or lack thereof between the structures that compose each ensemble. The structural flexibility is confirmed by the respective RMSD values for the superposition of either all heavy or only the backbone atoms for each ensemble (**Table 6.2**).

Table 6.2: Comparison of RMSD values for all residues and helical segments of LyeTx I (SANTOS et al., 2010), LyeTx I-b (REIS et al., 2018), LyeTx I-b$_{\text{cys}}$ and LyeTx I-bPEG. Data was obtained by structural manipulation and visualization in MOLMOL (KORADI et al., 1996). Helical segments for LyeTx I comprised residues Thr-4 up to Leu-25 while for LyeTx I-b, LyeTx I-b$_{\text{cys}}$ and LyeTx I-bPEG comprised residues Trp-2 up to Lys-23.

	LyeTx I	**LyeTx I-b**	**LyeTx I-b$_{\text{cys}}$**	**LyeTx I-bPEG**
RMSD (Å) - all residues				
Backbone	0.99 ± 0.30	0.46 ± 0.18	0.85 ± 0.25	0.71 ± 0.22
Backbone and heavy atoms	1.97 ± 0.41	0.98 ± 0.21	1.62 ± 0.30	1.45 ± 0.25
RMSD (Å) - helical segment				
Backbone	0.72 ± 0.18	0.37 ± 0.16	0.72 ± 0.22	0.59 ± 0.19
Backbone and heavy atoms	1.47 ± 0.26	0.89 ± 0.21	1.49 ± 0.28	1.29 ± 0.24

RMSD values overall decrease from LyeTx I to LyeTx I-b. An increase is then noticed comparing LyeTx I-b to LyeTx I-b$_{\text{cys}}$ and a second decrease between LyeTx I-b$_{\text{cys}}$ to LyeTx I-bPEG. Although LyeTx I-bPEG has a higher degree of conformational freedom than LyeTx I-b, indicated by the higher RMSD values of the latter, the introduction of the PEG unit did not furnish a large enough structural flexibility compared to LyeTx I, remaining similar to LyeTx I-b. The maintenance of three-dimensional characteristics after a major chemical modification like mPEG-MAL conjugation could indicate that the biological activity of LyeTx I-bPEG will remain similar to LyeTx I-b. This is a positive feature, since AMPs have a drug potential tied to their structural attributes.

Regarding the calculated structures of LyeTx I-b$_{\text{cys}}$ and LyeTx I-bPEG, all (ϕ, ψ) dihedral angle pairs are located in the most favorable regions of the Ramachandran plot (**Figure 6.8**), indicating a high stereochemical quality of the calculated structures and the summary of structural statistics for both ensembles is presented in **Table 6.3**.

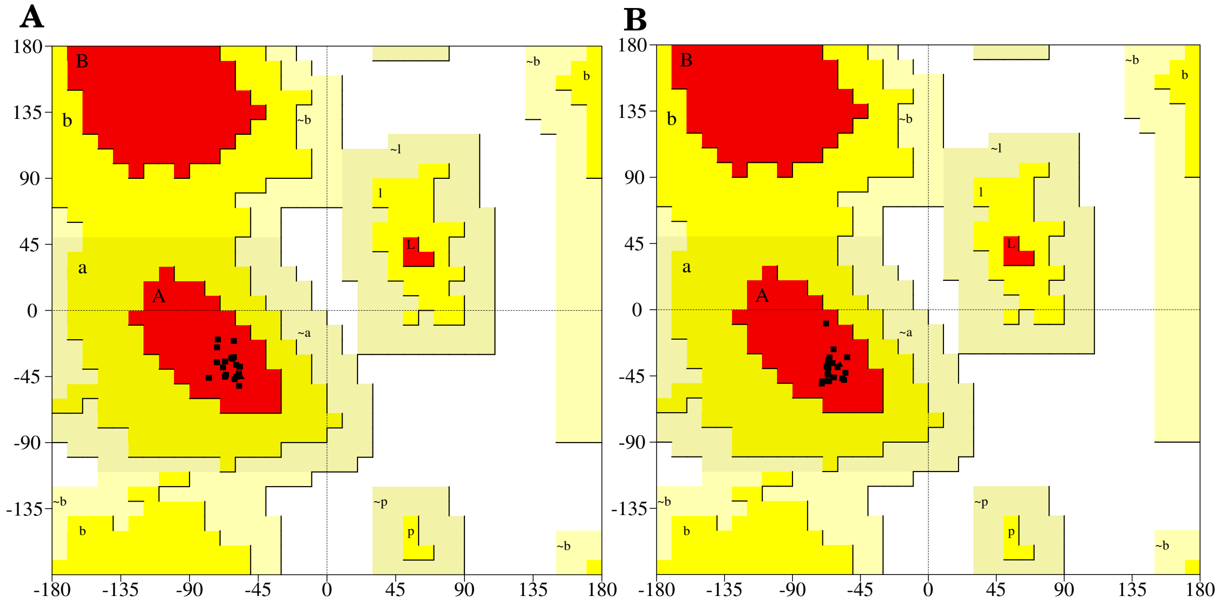

Figure 6.8: Ramachandran plots for the most stable calculated structure of (**A**) LyeTx I-b$_{\text{cys}}$ and (**B**) LyeTx I-bPEG.

Table 6.3: Summary of structural statistics of LyeTx I-b$_{\text{cys}}$ at 2.0 mM and LyeTx I-bPEG at 1.5 mM in TFE-d_2:H$_2$O (60:40) at 20 °C, pH 7.0 (phosphate buffer at 20.0 mM). Data was obtained by structural manipulation and visualization in `MOLMOL` (KORADI et al., 1996). The helical segments for both peptides ranges from Trp-2 to Lys-23.

	LyeTx I-b$_{\text{cys}}$	**LyeTx I-bPEG**
Total number of restraints	490	530
Number of intraresidue restraints	323	330
Number of sequential restraints $(i, i+1)$	123	124
Number of medium range restraints $(i, i+j)_{j=2,3,4}$	44	76
RMSD (Å) - all residues		
Backbone	0.85 ± 0.25	0.71 ± 0.22
Backbone and heavy atoms	1.62 ± 0.30	1.45 ± 0.25
RMSD (Å) - helical segment		
Backbone	0.72 ± 0.22	0.59 ± 0.19
Backbone and heavy atoms	1.49 ± 0.28	1.29 ± 0.24
Ramachandran plot analysis		
Residues in most favoured regions	100	100
Residues in additional allowed regions	0	0
Residues in generously allowed regions	0	0
Residues in disallowed regions	0	0

Comparing the amphipathicity of LyeTx I, LyeTx I-b, LyeTx I-b$_{\text{cys}}$, and LyeTx I-bPEG (**Figure 6.9, Page 146**), LyeTx I does not show a clear partition between hydrophobic and hydrophilic faces, having a stochastic distribution of residues, as previously reported by Santos and coworkers (SANTOS et al., 2010).

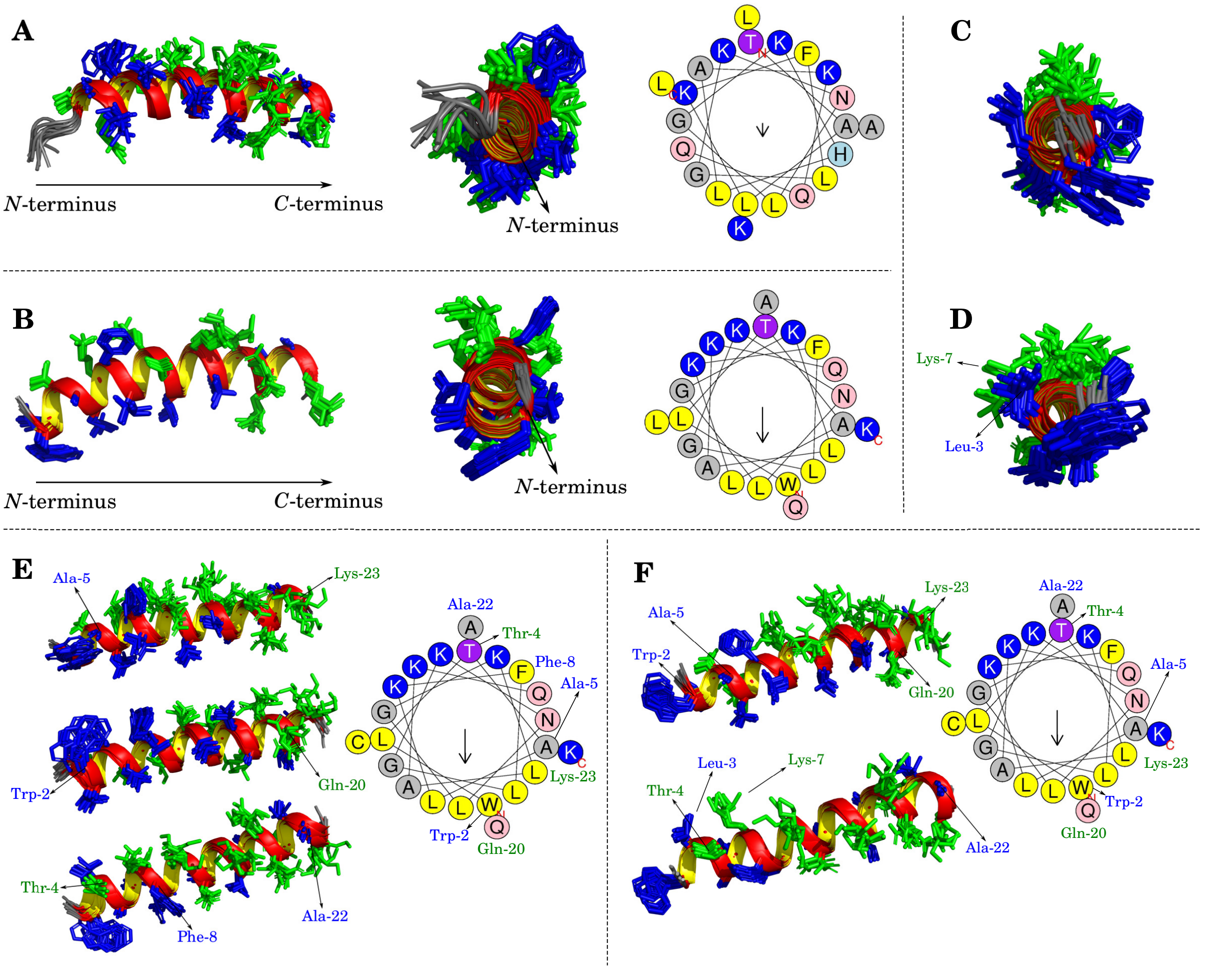

Figure 6.9: Lateral and frontal views of (**A**) LyeTx I (SANTOS et al., 2010) and (**B**) LyeTx I-b (REIS et al., 2018) helix structures with their respective Schiffer-Edmundson projections from HelixQuest. Frontal views of (**C**) LyeTx I-b$_{\text{cys}}$ and (**D**) LyeTx I-bPEG helices are shown and panels (**E**) and (**F**) explicitly show the residues involved in disrupting the hydrophobic and hydrophilic faces of LyeTx I-b$_{\text{cys}}$ and LyeTx I-bPEG, respectively, as verified by their respective Schiffer-Edmundson projections. In all helix plots, the hydrophobic residues are shown in dark blue and the hydrophilic ones in green.

On the other hand, LyeTx I-b shows a more distinct separation between them, although still having their hydrophobic continuities disrupted by Gln-20 and hydrophilic by Ala-22. Comparatively, LyeTx I-b$_{\text{cys}}$ did not show a substantial change in amphipathic character, which was expected considering the replacement of a hydrophobic Leu residue by a hydrophobic Cys residue. However, the introduction of the PEG moiety resulted in some structural features such as the apparent eclipsed arrangement of Leu-3 and Lys-7; not observed for LyeTx I-b$_{\text{cys}}$, disrupting the continuity of the hydrophilic face of LyeTx I-bPEG. Furthermore, the Michael addition shifted the position of some residues away from the ones calculated in its Schiffer-Edmundson projection, like Trp-2 and Ala-5, which overlap with Lys-23.

These findings indicate that the PEGylation apparently reduced the amphipathic character of the peptide analogue, although direct correlation between amphipathicity and biological activity is not straightforward, since there are reports of AMPs like ocellatins (GOMES et al., 2018), which are not highly amphipathic but show pronounced membrane affinity. Brito and coworkers (BRITO et al., 2021) have performed biological assays with LyeTx I-bPEG and, interestingly, a similar activity and much smaller hemolytic potential (ten-fold) was observed for LyeTx I-bPEG when compared to LyeTx I-b. Therefore, it can be understood that other factors like net charge, number of charged residues, helical content, and the presence of chemically active moieties can impact on the activity of AMPs against microorganisms.

The results described in this chapter were used to corroborate other data obtained by the research group and the final work was published in the journal Frontiers in Molecular Biosciences (October 13, 2022) by Brito, J. C. M., Carvalho, L. R. *et al* (BRITO et al., 2022). In this work, further biophysical assays were performed for LyeTx I-b and LyeTx I-bPEG, namely Surface Plasmon Resonance (SPR) experiments, Dynamic Light Scattering (DLS) experiments, zeta potential (ζ-potential) assays, calcein leakage assays, and proteolytic degradation experiments. The biophysical results regarding the membrane interactions of LyeTx I-b and LyeTx I-bPEG showed that PEGylation resulted in a decrease in affinity for negatively charged — POPC:POPG 3:1 — membranes.

The lower affinity coefficient (K) observed in the SPR experiments for LyeTx I-bPEG (3500 M^{-1}) compared with LyeTx I-b (6800 M^{-1}) suggests that the PEG chain may hinder the interaction with the phospholipid bilayer. Furthermore, LyeTx I-b displayed higher calcein release percentages (15 and 94% for POPC and POPC:POPG 3:1 vesicles, respectively) compared to LyeTx I-bPEG (8 and 68%, respectively), indicating a smaller lytic activity. Conversely, the mode of interaction with anionic membranes is likely maintained after PEGylation, since the PEGylated form exhibited higher changes in the ζ-potential of LUVs at lower concentrations ($<$ 40 mM), while both peptides resulted in a similar increase ($\Delta\zeta \sim 60$ mV) at higher concentrations ($>$ 40 mM). Finally, PEGylation significantly increased proteolytic degradation resistance, since LyeTx I-bPEG showed great stability in the presence of trypsin or proteinase K even after 24 hours of exposure, whereas LyeTx I-b was completely degraded after 6 hours in the presence of either enzyme. These results might explain the substantially lower haemolytic activity of the PEGylated form evidenced earlier and might occur due to the size of the polymer, which can hinder the proper adsorption into the active site of these enzymes.

Chapter 7 | Conclusions

The rapid rise of antimicrobial resistant bacteria is a major public health problem. The number of deaths related to this problem continues to increase yearly. To combat this, the discovery of novel antimicrobial agents is a good avenue of research, especially novel AMPs, since they possess particular action mechanisms that do not result in antimicrobial resistance as often as others, primarily causing membrane disruption.

Chapter 2 showed the synthesis of six peptide analogues, namely **PS-O1**, **R1G2-PS-O1**, **[Pra^1]PS-O1**, **R[Pra]PS-O1**, **PS-O1 GtP**, and **R1A2-PS-O1 GtP**. They are derived from the phylloseptins present in the skin secretion of *Phyllomedusa hypochondrialis* and two of them, **PS-O1 GtP** and **R1A2-PS-O1 GtP**, have a glucotriazole unit anchored to the polypeptide structure by a 1,4-triazole bridge. The polypeptide structures were synthesized by Fmoc-SPPS and the Gt unit was anchored by CuAAC, with final yields ranging from 8.7 to 26.5%. All derivatives were purified by RP-HPLC (73.4 to 91.5%), furnishing products with purities ranging from 91.6 to 98.4%. MALDI-ToF-MS was used to confirm the presence of the intended compounds. The only synthesis that furnished a by-product with considerable yield was of **R1A2-PS-O1 GtP**, where an RP-HPLC band was analyzed by MALDI-ToF-MS and showed an $[M+H]^+$ $m/z = 2849.79$, corresponding to an extra Leu residue.

Chapter 3 described the analysis of **PS-O1**, **R1G2-PS-O1**, **PS-O1 GtP**, and **R1A2-PS-O1 GtP** by CD in the presence of different biomimetic media. In TFE-d_2:H$_2$O, all peptides attained α-helical structures starting from TFE-d_2:H$_2$O 30:70 and achieved the highest helix percentage at 50:50. Furthermore, glucosylation increased the maximum helicity of GtPs. This is likely the result of a $\pi - \pi$-type interaction between the triazole ring and the phenyl group of the neighbouring Phe. Moreover, the possibility of a cation-π-type interaction was discarded due to the low percentage of protonated structures. The analysis of the peptides in the presence of SDS and DPC micelles showed that they folded in smaller concentrations of SDS than DPC. Also, DPC micelles furnished higher maximum helical contents for **PS-O1** and **R1G2-PS-O1**, while the same behavior was noticed for the glucotriazole-peptides in the presence of SDS. Finally, spectra acquired in the presence of POPC and POPC:POPG 3:1 LUVs showed a more pronounced distinction between random and folded structures, since no concentration of POPC resulted in α-helical character for any peptide, while it was clearly observed for varied concentrations of POPC:POPG 3:1, showing a desirable interaction bias.

Chapter 4 showed the NMR analyses of **PS-O1**, **R1G2-PS-O1**, **PS-O1 GtP**, and **R1A2-**

PS-O1 GtP in the presence of TFE-d_2:H_2O 60:40. Overall, all spectra showed an appropriate signal dispersion, characteristic of well-resolved secondary structures. Furthermore, they showed a high amount of inter-residue NOE correlations typical of α-helices. δ and secondary chemical shift analysis revealed that, while the presence of the Gt moiety in **PS-O1 GtP** increased helical content at the N-terminus compared to **PS-O1**, the opposite was true when **R1A2-PS-O1 GtP** was compared to **R1G2-PS-O1**. All structural ensembles displayed a large helicity, encompassing 75 to 91% of the sequences, a high amount of residues in most favoured regions of the Ramachandran plot (82.4 to 100%) and low RMSD values considering all residues (from 1.291 to 1.896). Furthermore, glucosylation resulted in a bend of helix for **PS-O1 GtP** and **R1A2-PS-O1 GtP**. Finally, while amphipathicity was increased post glucosylation, the same was not observed for helix percentages since, while **PS-O1 GtP** has a higher H and $|\vec{\mu}_H|$ than **PS-O1**, **R1A2-PS-O1 GtP** has a higher $|\vec{\mu}_H|$ and smaller H than **R1G2-PS-O1**. Moreover, amide proton secondary shifts analyses confirm the amphipaticity of the α-helices and suggest a consistent curvature for the obtained helices, which was only reflected in the glucotriazole derivatives.

Chapter 5 showed antifungic tests of the synthesized derivatives against *Candida* yeasts (`ATCC` and clinical isolates), antifungic drug synergism assays of **R1G2-PS-O1**, antibacterial testes agains *E. coli* and *S. aureus*, and *in vitro* cytotoxicity assays in the presence of VERO cells. While all peptides showed moderate activity, **R1G2-PS-O1** was the most active of the four compounds, being more active than both GtPs. This was thought to happen due to a possible preference for membrane interaction mechanisms over ergosterol biosynthesis pathways and to a possible interaction between the triazole and the guanidine moiety in **R1A2-PS-O1 GtP**, lowering the energy of the triazole and hindering its coordination capabilities.

Chapter 6 discussed the structural studies of LyeTx I-b$_{\text{cys}}$ and LyeTx I-bPEG, derived from LyeTx I, present in the venom of *Lycosa erythrognata*. Both peptides showed similar characteristics as discussed for the **PS** derivatives, besides a superior helicity. Furthermore, different chemical shift values were observed at the residues near the conjugation site (Cys-21) in the TOCSY and ^{1}H$-$^{15}N-HSQC spectra. Moreover, while LyeTx I-b$_{\text{cys}}$ showed no H_N, H_N $(i, i+2)$ correlations in the NOESY spectra, the PEGylated derivative did. This type of correlation was associated with a bend of helix observed previously for LyeTx I and LyeTx I-b. Analysing the NMR structural ensembles for both, PEGylation did not alter any major structural aspects of LyeTx I-b, except for an increase in structural flexibility; attributed to the PEG unit itself. This is an important result since the maintenance of structural aspects even after a major modification like PEGylation could indicate biological applications. Finally, some published results suggest that PEGylation decreased membrane affinity and lytic capabilities, maintained the mode of interaction of LyeTx I-b and increased proteolytic degradation resistance substantially.

Bibliography

ACHARYA, Y.; DHANDA, G.; SARKAR, P.; HALDAR, J. Pursuit of next-generation glycopeptides:a journey with vancomycin. **Chemical Communications**, v. 58, p. 1881–1898, 2022.

ALEXANDER, B. D. **Reference method for broth dilution antifungal susceptibility testing for yeasts**. 4. ed. United States, PA: Clinical and Laboratory Standards Institute, 2017. ISBN 1562388274.

ALLOLIO, C. et al. Arginine-rich cell-penetrating peptides induce membrane multilamellarity and subsequently enter via formation of a fusion pore. **PNAS**, v. 115, p. 11923–11928, 2018.

ALMEIDA, F. C. L.; MORAES, A. H.; GOMES-NETO, F. An overview on protein structure determination by NMR: Historical and future perspectives of the use of distance geometry methods. In: _____. **Distance Geometry: Theory, Methods, and Applications**. New York, NY: Springer New York, 2013. p. 377–412.

ALVES, N. J. et al. Functionalized liposome purification *via* Liposome Extruder Purification (LEP). **Analyst**, v. 138, p. 4746–4751, 2013.

AMBLARD, F.; CHO, J. H.; SCHINAZI, R. F. Cu(I)-catalyzed Huisgen azide-alkyne 1,3-dipolar cucloaddition reaction in nucleoside, nucleotide, and oligonucleotide chemistry. **Chemical Reviews**, v. 109, p. 4207–4220, 2009.

AMBLARD, M.; FEHRENTZ, J.; MARTINEZ, J.; GILLES, S. Methods and protocols of modern solid phase peptide synthesis. **Molecular Biotechnology**, v. 33, p. 239–254, 2006.

ANTONOVICS, I.; YOUNG, G. T. Amino-acids and peptides. Part XXV. The mechanism of the base-catalyzed racemisation of the *p*-nitrophenyl esters of acylpeptides. **Journal of the Chemical Society C: Organic**, p. 595–601, 1967.

ARAI, M.; SUGASE K. DYSON, H. J.; WRIGHT, P. E. Conformational propensities of intrinsically disordered proteins influence the mechanism of binding and folding. **PNAS**, v. 112, p. 9614–9619, 2015.

ARMSTRONG, K. M.; BALDWIN, R. L. Charged histidine affects α-helix stability at all positions in the helix by interacting with the backbone charges. **PNAS**, v. 90, p. 11337–11340, 1993.

AUE, W. P.; BARTHOLDI, E.; ERNST, R. R. Two-dimensional spectroscopy. application to nuclear magnetic resonance. **The Journal of Chemical Physics**, v. 64, p. 2229, 1976.

BACALUM, M.; RADU, M. Cationic antimicrobial peptides cytotoxicity on mammalian cells: An analysis using therapeutic index integrative concept. **International Journal of Peptide Research and Therapeutics**, v. 21, p. 47–55, 2015.

BAE, I.; HAN, H.; CHANG, S. Highly efficient one-pot synthesis of N-sulfonylamidines by Cu-catalyzed three-component coupling of sulfonyl azide, alkyne, and amine. **Journal of the American Chemical Society**, v. 127, p. 2038–2039, 2005.

BAHAR, A. A.; REN, D. Antimicrobial peptides. **Pharmaceuticals**, v. 6, p. 1543–1575, 2013.

BAKSHI, K.; LIYANAGE, M. R.; VOLKIN, D. B.; MIDDAUGH, C. R. Circular dichroism of peptides. In: NIXON, A. E. (Ed.). **Therapeutic Peptides. Methods in Molecular Biology (Methods and Protocols)**. Totowa, New Jersey: Humana Press, 2014. v. 1088, cap. 17, p. 247–253. ISBN 9781627036733.

BEDNARSKA, N. G.; WREN, B. W.; WILLCOCKS, S. J. The importance of the glycosylation of antimicrobial peptides: natural and synthetic approaches. **Drug Discovery Today**, v. 22, p. 919–926, 2017.

BEHRENDT, R.; WHITE, P.; OFFER, J. Advances in Fmoc solid-phase peptide synthesis. **Journal of Peptide Science**, v. 22, p. 4–27, 2016.

BERG, R.; STRAUB, B. F. Advancements in the mechanistic understanding of the copper-catalyzed azide-alkyne cycloaddition. **Beilstein Journal of Organic Chemistry**, v. 9, p. 2715–2750, 2013.

BERJANSKII, M. V.; WISHART, D. S. A simple method to predict protein flexibility using secondary chemical shifts. **Journal of the American Chemical Society**, v. 127, p. 14970–14971, 2005.

BERTANI, B.; RUIZ, N. Function and biogenesis of lipopolysaccharides. **EcoSalPlus**, v. 2018, p. 1–19, 2018.

BILJE, M. N. A.; EKAMBARAM, M.; LO, E. C. M.; YIU, C. K. Y. The combined antimicrobial effect of arginine and fluoride toothpaste. **Scientific Reports**, v. 9, p. 8405–8015, 2019.

BINDA, E.; MARINELLI, F.; MARCONE, G. L. Old and new glycopeptide antibiotics: Action and resistance. **Antibiotics**, v. 3, p. 572–594, 2014.

BLABER, M.; ZHANG, X.; MATTHEWS, B. W. Structural basis of amino acid α helix propensity. **Science**, v. 260, p. 1637–1640, 1993.

BLOCH, F.; HANSEN, W. W.; PACKARD, M. Nuclear induction. **Physical Review**, v. 69, p. 127, 1946.

BOTTOM, C. B.; HANNA, S. S.; SIEHR, D. J. Mechanism of the ninhydrin reaction. **Biochemical Education**, v. 6, p. 4–5, 1978.

BRAND, G. D. et al. The skin secretion of the amphibian *phyllomedusa nordestina*: A source of antimicrobial and antiprotozoal peptides. **Molecules**, v. 18, p. 7058–7070, 2013.

BRITO, J. C. M. et al. PEGylation of the antimicrobial peptide LyeTx I-b maintains structure-related biological properties and improves selectivity. **Frontiers in Molecular Biosciences**, v. 9, 2022.

BRITO, J. C. M. et al. Pegylated LyeTx I-b peptide is effective against carbapenem-resistant *acinetobacter baumannii* in an *in vivo* model of pneumonia and shows reduced toxicity. **International Journal of Pharmaceutics**, v. 609, p. 12156, 2021.

BROGDEN, K. A. Antimicrobial peptides: pore formers or metabolic inhibitors in bacteria? **Nature Reviews in Microbiology**, v. 3, p. 238–250, 2005.

BULHELLER, B. M.; RODGER, A.; HIRST, J. D. Circular and linear dichroism of proteins. **Physical Chemistry Chemical Physics**, v. 9, p. 2020–2035, 2007.

BUTLER, M. S. et al. Glycopeptide antibiotics: Back to the future. **The Journal of Antibiotics**, p. 1–14, 2014.

BUTTERFIELD, S. M.; PATEL, P. R.; WATERS, M. L. Contribution of aromatic interactions to α-helix stability. **Journal of the American Chemical Society**, v. 124, p. 9751–9755, 2002.

CALDERON, L. d. A.; SILVA, A. d. A. E.; CIANCAGLINI, P.; STÁBELI, R. G. Antimicrobial peptides from *Phyllomedusa* frogs: from biomolecular diversity to potential nanotechnologic medical applications. **Amino Acids**, v. 40, p. 29–49, 2011.

CARPINO, L. A. Methyl ester nonequivalence in the ^{1}H NMR spectra of diastereomeric dipeptide esters incorporating N-terminal α-phenylglycine units. **Journal of Organic Chemistry**, v. 53, p. 875–878, 1988.

CARPINO, L. A.; HAN, G. Y. The 9-fluoromethoxycarbonyl function, a new base-sensitive amino-protecting group. **Journal of the American Chemical Society**, v. 92, p. 5748–5749, 1970.

CARPINO, L. A.; HAN, G. Y. The 9-fluoromethoxycarbonyl amino-protecting group. **Journal of Organic Chemistry**, v. 22, p. 3404–3409, 1972.

CARPINO, L. A. et al. The 2,2,4,6,7-pentamethyldiydrobenzofuran-5-sulfonyl group (Pbf) as arginine side chain protectant. **Tetrahedron Letters**, v. 34, p. 7829–7832, 1993.

CATOIRE, L. J.; WARNET XAVIER, L.; WARCHAWSKI, D. E. Micelles, bicelles, amphpols, nanodiscs, liposomes, or intact cells: the hitchhiker's guide to the study of membrane proteins by nmr. In: MUS-VETEAU, I. (Ed.). **Membrane proteins production for structural analysis**. New York: Springer-Verlag, 2014. cap. 12, p. 315–345. ISBN 9781493906628.

CAVANAGH, J.; RANCE, M. Suppression of cross-relaxation effects in tocsy spectra via a modified DIPSI-2 mixing sequence. **Journal of Magnetic Resonance**, v. 96, p. 670–678, 1992.

CAVANAGH, J.; RANCE, M. Sensitivity-enhanced NMR techniques for the study of biomolecules. In: . [S.l.]: Academic Press, 1993, (Annual Reports on NMR Spectroscopy, v. 27). p. 1–58.

CDC. **Antibiotic Resistance Threats in the United States**. 2019. 118 p.

CHAN, D. I.; PRENNER, E. J.; VOGEL, H. J. Tryptophan- and arginine-rich antimicrobial peptides: Structures and mechanism of action. **Biochimica et Biophysica Acta**, v. 1758, p. 1184–1202, 2006.

CHAN, W. C.; WHITE, P. D. **Fmoc solid phase peptide synthesis: A practical approach**. 1. ed. New York, United States of America: Oxford Univesity Press, 2000. 346 p. ISBN 0199637253.

CHEN, C. H.; LU, T. K. Development and challenges of antimicrobial peptides for therapeutic applications. **Antibiotics**, v. 9, p. 24, 2020.

CHENG, K. et al. The interactions between the antimicrobial peptide P-113 and living *candida albicans* cells shed light on mechanisms of antifungal activity and resistance. **International Journal of Molecular Sciences**, v. 21, p. 2654, 2020.

CHOW, H. Y.; ZHANG, Y.; MATHESON, E.; LI, X. Ligation technologies for the synthesis of cyclic peptides. **Chemical Reviews**, v. 119, p. 9971–10001, 2019.

CLARK, S. et al. The lexicon of antimicrobial peptides: a complete set of arginine and tryptophan sequences. **Communications Biology**, v. 4, p. 605–619, 2021.

CORNILESCU, G.; DELAGLIO, F.; BAX, A. Protein backbone angle restraints from searching a database for chemical shift and sequence homology. **Journal of Biomolecular NMR**, v. 13, p. 289–302, 1999.

CRUCIANI, O. et al. An improved nmr study of liposomes using 1-palmitoyl-2-oleoyl-sn-glycero-3-phosphatidylcholine as model. **Molecules**, v. 11, p. 334–344, 2006.

CUTRONA, K. J.; KAUFMAN, B. A.; FIGUEROA, D. M.; ELMORE, D. E. Role of arginine and lysine in the antimicrobial mechanism of histone-derived antimicrobial peptides. **FEBS Letters**, v. 589, p. 3915–3920, 2015.

DAVIS, A. L.; KEELER, J.; LAUE, E. D.; MOSKAU, D. Experiments for recording pure-absorption heteronuclear correlation spectra using pulsed field gradients. **Journal of Magnetic Resonance**, v. 98, p. 207–216, 1992.

DELAGLIO, F. et al. NMRPipe: a multidimensional spectral processing system based on UNIX pipes. **Journal of Biomolecular NMR**, v. 6, p. 277–293, 1995.

DIJKSTEEL, G. S.; ULRICH, M. M. W.; MIDDELKOOP, E.; BOEKEMA, B. K. H. L. Review: Lessons learned from clinical trials using antimicrobial peptides (AMPs). **Frontiers in Microbiology**, v. 12, p. 616979, 2021.

DUPLÂTRE, G.; MARQUES, M. F. F.; MIGUEL, M. d. G. Size of sodium dodecyl sulfate micelles in aqueous solutions as studied by positron annihilation lifetime spectroscopy. **Journal of Physical Chemistry**, v. 100, p. 16608–16612, 1996.

EISENBERG, D.; WEISS, R. M.; TERWILLIGER, T. C. The helical hydrophobic moment, a measure of the amphiphilicity of a helix. **Nature**, v. 299, p. 371–374, 1982.

EL AYOUCHIA, H. B. et al. Understanding the mechanism and regioselectivity of the copper(I) catalyzed [3+2] cycloaddition reaction between azide and alkyne: a systematic DFT study. **RSC Advances**, v. 8, p. 7670–7678, 2018.

EL-FAHAM, A.; ALBERICIO, F. Peptide coupling reagents, more than a letter soup. **Chemical Reviews**, v. 111, p. 6557–6602, 2011.

EMWAS, A. et al. NMR spectroscopy for metabolomics research. **Metabolites**, v. 9, p. 123–162, 2019.

EPAND, R. M.; EPAND, R. F. Bacterial membrane lipids in the action of antimicrobial peptides. **Journal of Peptide Science**, v. 17, p. 298–305, 2011.

ERRIDGE, C.; BENNETT-GUERRERO, E.; POXTON, I. R. Structure and function of lipopolysaccharides. **Microbes and Infection**, v. 4, p. 837–851, 2002.

FAIRBROTHER, W. J. et al. Polypeptide backbone resonance assignments and secondary structure of *bacillus subtilis* enzyme $\mathrm{III}^{\mathrm{glc}}$ determined by two-dimensional and three-dimensional heteronuclear NMR spectroscopy. **Biochemistry**, v. 30, p. 6896–6907, 1991.

FAUSTINO, C.; PINHEIRO, L. Lipid systems for the delivery of amphotericin B in antifungal therapy. **Pharmaceutics**, v. 12, p. 29–76, 2020.

FELÍCIO, M. R. et al. Peptides with dual antimicrobial and anticancer activities. **Chemical Society Reviews**, v. 45, p. 4859–4872, 2016.

FIELDS, G. B. Methods for removing the Fmoc group. In: _____. **Peptide Synthesis Protocols**. Totowa, NJ, USA: Humana Press, 1995. p. 17–27.

FIELDS, G. B.; NOBLE, R. L. Solid phase peptide synthesis utilizing 9-fluorenylmethoxycarbonyl amino acids. **International Journal of Peptide and Protein Research**, v. 35, p. 161–214, 1990.

FITCH, C. A. et al. Arginine: Its pk_a value revisited. **Protein Science**, v. 24, p. 752–761, 2015.

FRANCO, L. L. **Síntese de *N*-glicosilssulfonamidas, de Aza-açúcares Derivados de *N*-Acetilglicosamina e D-Glicose e Tentativa de Síntese de Inibidores Potenciais de Quitinases.** Tese (Doutorado) — Universidade Federal de Minas Gerais, 2015.

FREE, S. J. Chapter two - fungal cell wall organization and biosynthesis. In: FRIEDMANN, T.; DUNLAP, J. C.; GOODWIN, S. F. (Ed.). [S.l.]: Academic Press, 2013, (Advances in Genetics, v. 81). p. 33–82.

FRIEDMAN, M. Applications of the ninhydrin reaction for analysis of amino acids, peptides, and proteins to agricultural and biomedical sciences. **Journal of Agricultural and Food Chemistry**, v. 52, p. 385–406, 2004.

FUSCALDI, L. L. et al. Shortened derivatives from native antimicrobial peptide LyeTx I: *In vitro* and *in vivo* biological activity assessment. **Experimental Biology and Medicine**, v. 246, p. 414–425, 2021.

FUTAKI, S. et al. Aginine-rich peptides: An abundant source of membrane-permeable peptides having potential as carriers for intracellular protein delivery. **The Journal of Biological Chemistry**, v. 276, p. 5836–5840, 2001.

GAO, Y. et al. Identification and characterisation of the antimicrobial peptide, Phylloseptin-PT, from the skin secretion of *phyllomedusa tarsius*, and comparison of activity with designed, cationicity-enhanced analogues and diastereomers. **Molecules**, v. 21, p. 1667–1681, 2016.

GARCIA-RUBIO, R.; OLIVEIRA, H. C. de; RIVERA, J.; TREVIJANO-CONTADOR, N. The fungal cell wall: *Candida*, *cryptococcus*, and *aspergillus* species. **Frontiers in Microbiology**, v. 10, p. 1–13, 2020.

GARG, M.; SEEBERGER, P. H.; SILVA, D. V. Glycosylphosphatidylinositols: Occurrence, synthesis, and properties. In: **Reference Module in Chemistry, Molecular Sciences and Chemical Engineering**. [S.l.]: Elsevier, 2016. v. 81, p. 33–82. ISBN 978-0-12-409547-2.

GAUTIER, R.; DOUGUET, D.; ANTONNY, B.; DRIN, G. HELIQUEST: a web server to screen sequences with specific α-helical properties. **Bioinformatics**, v. 24, p. 2101–2102, 2008.

GHOSH, S.; PANJA, P.; DALAL, C.; JANA, N. R. Arginine-terminated, chemically designed nanoparticle for direct cell translocation. **ACS Applied Bio Materials**, v. 2, p. 339–348, 2019.

GOMES, B. et al. Designing improved active peptides for therapeutic approaches against infectious diseases. **Biotechnology Advances**, v. 36, p. 415–429, 2018.

GOODMAN, M.; STUEBEN, K. C. Amino acid active esters. III. Base-catalyzed racemization of peptide active esters. **Journal of Organic Chemistry**, v. 27, p. 3409–3416, 1962.

GOW, N. A. R.; LATGE, J.; MUNRO, C. A. The fungal cell wal: stucture, biosynthesis, and function. **Microbiology Spectrum**, v. 5, p. 1–25, 2017.

GRECO, I. et al. Correlation between hemolytic activity, cytotoxicity and systemic in vivo toxicity of synthetic antimicrobial peptides. **Scientific Reports**, v. 10, n. 13206, 2020.

GREENFIELD, N. J. Using circular dichroism spectra to estimate protein secondary structure. **Nature Protocols**, v. 1, p. 2876–2890, 2006.

GRIMSEY, E.; COLLINS, D. W. P.; MIKUT, R.; HILPERT, K. The effect of lipidation and glycosylation on short cationic antimicrobial peptides. **BBA - Biomembranes**, v. 1862, p. 183195–183205, 2020.

GUILMEAU, T.; CHOUZENOUX, E.; ELVIRA, V. **Simulated annealing: a review and a new scheme**. 2021. SSP 2021 - IEEE Statistical Signal Processing Workshop, Jul 2021, Rio de Janeiro, Brazil. Hal-03275401f.

GUIMARÃES, C. F. R. C. **Síntese de peptídeos: cinética de dimerização via formação de ligação de dissulfeto, obtenção e estudos biofísicos de glicotriazol-peptídeos**. Tese (Doutorado) — Universidade Federal de Minas Gerais, July 2017.

GÜNTERT, P. Structure calculation of biological macromolecules from NMR data. **Quarterly Reviews of Biophysics**, v. 2, p. 145–237, 1998.

GUO, Y. et al. Prevalence and therapies of antibiotic-resistance in *Staphylococcus aureus*. **Frontiers in Cellular and Infection Microbiology**, v. 10, 2020.

GUSMÃO, K. A. G. et al. Ocellatin peptides from the skin secretion of the South American from *Leptodactylus labyrinthicus* (Leptodactylidae): characterization, antimicrobial activities and membrane interactions. **Journal of Venomous Animals and Toxins including Tropical Diseases**, v. 23, p. 1–14, 2017.

HALDÓN, E.; NICASIO, M. C.; PÉREZ, P. J. Copper-catalyzed azide-alkyne cycloadditions (CuAAC): an update. **Organic & Biomolecular Chemistry**, v. 13, p. 9528–9550, 2015.

HALE, J. D.; HANCOCK, R. E. Alternative mechanisms of action of cationic antimicrobial peptides on bacteria. **Expert Review of Anti-infective Therapy**, v. 5, p. 951–959, 2007.

HANCOCK, R. E. W.; SAHL, H. Antimicrobial and host-defence peptides as new anti-infective therapeutic strategies. **Nature Biotechnology**, v. 24, p. 1551–1557, 2006.

HEARD, K. L.; HUGHES, S.; MUGHAL, N.; MOORE, L. S. P. COVID-19 and fungal superinfection. **Lancet Microbe**, v. 1, p. e107, 2020.

HEDHLI, J. et al. Synthesis, chemical characterization and multiscale biological evaluation of a dimeric-cRGD peptide for targeted imaging of $\alpha_V\beta_3$ integrin activity. **Scientific Reports**, v. 7, p. 1–15, 2017.

HEIN, J. E.; FOKIN, V. V. Copper-catalyzed azide-alkyne cycloaddition (CuAAC) and beyond: new reactivity of copper(I) acetylides. **Chemical Society Reviews**, v. 39, p. 1302–1315, 2010.

HENDAUS, M. A.; JOMHA, F. A. Covid-19 induced superimposed bacterial infection. **Journal of Biomolecular Structure and Dynamics**, 2020.

HIMO, F. et al. Copper(I)-catalyzed synthesis of azoles. DFT study predicts unprecedented reactivity and intermediates. **Journal of the American Chemical Society**, v. 127, p. 210–216, 2005.

HOF, H. A new, broad-spectrum azole antifungal: posaconazole - mechanisms of action and resistance, spectrum of activity. **Mycoses**, v. 49, p. 2–6, 2006.

HOLT, A.; KILLIAN, J. A. Orientation and dynamics of transmembrane peptides: the power of simple models. **European Biophysics Journal**, v. 39, p. 609–621, 2010.

HUISGEN, R. 1,3-dipolar cycloadditions: Past and future. **Angewandte Chemie International Edition**, v. 2, p. 565–632, 1963.

HYBERTS, S. G.; GOLDBERG, M. S.; HAVEL, T. F.; WAGNER, C. The solution structure of eglin c based on measurements of many NOEs and coupling constants and its comparison with X-ray structures. **Protein Science**, v. 1, p. 736–751, 1992.

IACOBUCCI, C.; REALE, S.; GAL, J.; DE ANGELIS, F. Dinuclear copper intermediate in copper(I)-catalyzed azide-alkyne cycloaddition directly observed by electrospray ionization mass spectrometry. **Angewandte Chemie International Edition**, v. 54, p. 3065–3068, 2015.

IBEAS, J. I. et al. Fungal cell wall phosphomannans facilitate the toxic activity of a plant pr-5 protein. **The Plant Journal**, v. 23, p. 375–383, 2001.

ISIDRO-LLOBET, A.; ÁLVAREZ, M.; ALBERICIO, F. Amino acid-protecting groups. **Chemical Reviews**, v. 109, p. 2455–2504, 2009.

IZDEBSKI, J.; PACHULSKA, M.; ORŁOWSKA, A. *N*-Cyclohexyl-*N*'-isopropylcarbodiimide: a hybrid that combines the structural features of DCC and DIC. **International Journal of Peptide & Protein Research**, v. 44, p. 414–419, 1999.

JIN, L.; TOLENTINO, D. R.; MELAIMI, M.; BERTRAND, G. Isolation of bis(copper) key intermediates in Cu-catalyzed azide-alkyne “click reaction”. **Science Advances**, v. 1, p. e1500304–e1500309, 2015.

JOHNSON, B. A.; BLEVINS, R. A. NMR View: A computer program for the visualization and analysis of NMR data. **Journal of Biomolecular NMR**, v. 4, p. 603–614, 1994.

JOHNSON, W. C. Secondary structures of proteins through circular dichroism spectroscopy. **Annual Reviews of Biophysics and Biophysical Chemistry**, v. 17, p. 145–166, 1988.

JUNIOR, E. F. C. et al. Glycotriazole-peptides derived from the peptide HSP1: synergistic effect of triazole and saccharide rings on the antifungal activity. **Amino Acids**, v. 49, p. 1389–1400, 2017.

JÚNIOR, E. F. S.; MENEZES, L. F. S.; ARAÚJO, I. F. S.; SCHWARTZ, E. F. Natural occurrence in venomous arthropods of antimicrobial peptides active against protozoan parasites. **Toxins**, v. 11, p. 563–590, 2019.

KAISER, E.; COLESCOTT, R. L.; BOSSINGER, C. D.; COOK, P. I. Color test for detection of free terminal amino groups in the solid-phase peptide synthesis. **Analytical Biochemistry**, v. 34, p. 595–598, 1970.

KASHA, M.; RAWLS, H. R.; EL-BAYOUMI, M. A. The exciton model in molecular spectroscopy. **Pure and Applied Chemistry**, v. 11, p. 371–392, 1965.

KELLY, S. M.; JESS, T. J.; PRICE, N. C. How to study proteins by circular dichroism. **Biochimica et Biophysica Acta**, v. 1751, p. 119–139, 2005.

KING, D. S.; FIELDS, C. G.; FIELDS, G. B. A cleavage method which minimizes side reactions following Fmoc solid phase peptide synthesis. **International Journal of Peptide and Proteins Research**, v. 36, p. 255–266, 1990.

KJAERGAARD, M.; BRANDER, S.; POULSEN, F. M. Random coil chemical shifts for intrinsically disordered proteins: Effects of temperature and ph. **Journal of Biomolecular NMR**, v. 49, p. 139–149, 2011.

KJAERGAARD, M.; POULSEN, F. M. Sequence correction of random coil chemical shifts: correlation between neighbor correction factors and changes in the Ramachandran distribution. **Journal of Biomolecular NMR**, v. 50, p. 157–165, 2011.

KNOBLOCH, J. et al. Membrane-drug interactions studied using model membrane systems. **Saudi Journal of Biolocal Sciences**, v. 22, p. 714–718, 2015.

KORADI, R.; BILLETER, M.; WÜTHRICH, K. MOLMOL: A program for display and analysis of macromolecular structures. **Journal of Molecular Graphics**, v. 14, p. 51–55, 1996.

KUHN-NENTWIG, L. Antimicrobial and cytolytic peptides of venomous arthropods. **Cellular and MOlecular Life Sciences**, v. 60, p. 2651–2668, 2003.

KUMAR, A.; ERNST, R. R.; WÜTHRICH, K. A two-dimensional Nuclear Overhauser Enhancement (2D NOE) experiment for the elucidation of complete proton-proton cross-relaxation networks in biological macromolecules. **Biochemical and Biophysical Research Communications**, v. 95, p. 1–6, 1980.

L'ABBÉ, G. Are azidocumulenes accessible? **Bulletin des Sociétés Chimiques Belges**, v. 93, p. 579–583, 1984.

LADKHIN, A. S.; FERNÁNDEZ-VIDAL, M.; WHITE, S. H. Cd spectroscopy of peptides and proteins bound to large unilamellar vesicles. **Journal of Membrane Biology**, v. 236, p. 247–253, 2010.

LAMB, D.; KELLY, D.; KELLY, S. Molecular aspects of azole antifungal action and resistance. **Drug Resistance Updates**, v. 2, p. 390–402, 1999.

LAMOTHE, P. J.; MCCORMICK, P. G. Role of hydrindantin in the determination of amino acids using ninhydrin. **Analytical Chemistry**, v. 45, p. 1906–1911, 1973.

LANGFORD, B. J. et al. Bacterial co-infection and secondary infection in patients with COVID-19: a living rapid review and meta-analysis. **Clinical Microbiology and Infection**, v. 26, p. 1622–1629, 2020.

LANIADO-LABORÍN, R.; CABRALES-VARGAS, M. N. Amphotericin B: side effects and toxicity. **Revista Iberoamericana de Micología**, v. 26, p. 223–227, 2009.

LASKOWSKI, R. A. et al. AQUA and PROCHECK-NMR: programs for checking the quality of protein structures solved by NMR. **Journal of Biomolecular NMR**, v. 8, p. 477–486, 1996.

LEE, J. H.; OKUNO, Y.; CAVAGNERO, S. Sensitivity enhancement in solution NMR: Emerging ideas and new frontiers. **Journal of Magnetic Resonance**, v. 241, p. 18–31, 2014.

LEI, J. et al. The antimicrobial peptides and their potential clinical applications. **American Journal of Translational Research**, v. 11, p. 3919–3931, 2019.

LEITE, J. R. S. A. et al. Phylloseptins: a novel class of anti-bacterial and anti-protozoan peptides from the *Phyllomedusa* genus. **Peptides**, v. 26, p. 565–573, 2005.

LI, B. et al. Aqueous phosphoric acid as a mild reagent for deprotection of *tert*-butyl carbamates, esters, and ethers. **Journal of Organic Chemistry**, v. 71, p. 9045–9050, 2006.

LI, H. et al. Lipopolysaccharide structure and biosynthesis in *helicobacter pylori*. **Helicobacter**, v. 21, p. 445–461, 2016.

LI, R. et al. Effects of CGA-N12 on the membrane structure of *candida tropicalis* cells. **Biochemical Journal**, v. 477, p. 1813–1825, 2020.

LI, W.; SEPAROVIC, F.; O'BRIEN-SIMPSON, N. M.; WADE, J. D. Chemically modified and conjugated antimicrobial peptides against superbugs. **Chemical Society Reviews**, v. 50, p. 4932–4975, 2021.

LIANG, L.; ASTRUC, D. The copper (I)-catalyzed alkyne-azide cycloaddition (CuAAC) "click" reaction and its applications. an overview. **Coordination Chemistry Reviews**, v. 255, p. 2933–2945, 2011.

LIBÉRIO, M. d. S. et al. The crude skin secretion of the pepper frog *Leptodactylus labyrinthicus* is rich in metallo and serine peptidases. **PLOS One**, v. 9, p. 1–9, 2014.

LIMA, W. G. et al. Absence of antibacterial, anti-candida, and anti-dengue activities of a surfactin isolated from *bacillus subtilis*. **Journal of Pharmaceutical Negative Results**, v. 9, p. 27–32, 2018.

LIPKE, P. N.; OVALLE, R. Cell wall architecture in yeast: New structure and new challenges. **Journal of Bacteriology**, v. 180, p. 3735–3740, 1998.

LIU, B. et al. Design of novel antimicrobial peptide dimer analogues with enhanced antimicrobial activity *in vitro* and *in vivo* by intermolecular triazole bridge strategy. **Peptides**, v. 88, p. 115–125, 2017.

LIU, Y. et al. Structure–activity relationship of an antimicrobial peptide, Phylloseptin-PHa: balance of hydrophobicity and charge determines the selectivity of bioactivities. **Drug Design, Development and Therapy**, v. 13, p. 447–458, 2019.

LIU, Y. et al. A novel amphibian antimicrobial peptide, Phylloseptin-PV1, exhibits effective anti-*staphylococcal* activity without inducing either hepatic or renal toxicity in mice. **Frontiers in Microbiology**, v. 11, p. 1–14, 2020.

LUNA, O. F. et al. Deprotection reagents in Fmoc solid phase peptide synthesis: Moving away from piperidine? **Molecules**, v. 21, p. 1542–1554, 2016.

LUNDT, B. F.; JOHANSEN, N. L.; VØLUND, A.; MARKUSSEN, J. Removal of *t*-butyl and *t*-butoxycarbonyl protecting groups with trifluoroacetic acid. **International Journal of Peptide and Protein Research**, v. 12, p. 258–268, 1978.

LYU, Y. et al. Antimicrobial activity, improved cell selectivity and mode of action of short PMAP-36-derived peptides against bacteria and Candida. **Scientific Reports**, v. 6, p. 27258–27270, 2016.

MA, H. et al. Antimicrobial peptide AMP-17 affects *candida albicans* by disrupting its cell wall and cell membrane integrity. **Infection and Drug Resistance**, v. 13, p. 2509–2520, 2020.

MACFAYDEN, D. A. On the mechanism of the reaction of ninhydrin with α-amino acids: I. Absorption spectra of ninhydrin and certain derivatives. **The Journal of Biological Chemistry**, v. 186, p. 1–12, 1950.

MACFAYDEN, D. A.; FOWLER, N. On the mechanism of the reaction of ninhydrin with α-amino acids: II. A spectrophotometric study of hydridantin reactions. **The Journal of Biological Chemistry**, v. 186, p. 13–22, 1950.

MAKVANDI, P. et al. Drug delivery (nano)platforms for oral and dental applications: Tissue regeneration, infection control, and cancer management. **Advanced Science**, v. 8, p. 2004014, 2021.

MALIK, M. S.; AHMED, S. A.; KAMAL, A. Application of triazoles as bioisosteres and linkers in the development of microtubule targeting agents. **RSC Medicinal Chemistry**, v. 11, p. 327–348, 2020.

MALMSTEN, M. Interaction of antimicrobial peptides with bacterial membranes and membrane components. **Current Topics in Medicinal Chemistry**, v. 16, p. 16–24, 2016.

MARION, D.; IKURA, M.; TSCHUDIN, R.; BAX, A. Rapid recording of 2D NMR spectra without phase cycling. Application to the study of hydrogen exchange in proteins. **Journal of Magnetic Resonance**, v. 85, p. 393–399, 1989.

MARSTON, H. D. et al. Antimicrobial resistance. **Journal of the American Medical Association**, v. 316, p. 1193–1204, 2016.

MAYER, L. D.; HOPE, M. J.; CULLIS, P. R. Vesicles of variable sizes produced by a rapid extrusion procedure. **Biochimica et Biophysica Acta**, v. 858, p. 161–168, 1986.

MCCALDIN, D. J. The chemistry of ninhydrin. **Chemical Reviews**, v. 60, p. 39–51, 1960.

MERGLER, M.; DICK, F. The aspartimide problem in Fmoc-based SPPS. Part III. **Journal of Peptide Science**, v. 11, p. 650–657, 2005.

MERGLER, M. et al. The aspartimide problem in Fmoc-based SPPS. Part I. **Journal of Peptide Science**, v. 9, p. 36–46, 2003.

MERGLER, M. et al. The aspartimide problem in Fmoc-based SPPS. Part II. **Journal of Peptide Science**, v. 9, p. 518–526, 2003.

MERRIFIELD, R. B. Solid phase peptide synthesis. I. The synthesis of a tetrapeptide. **Journal of the American Chemical Society**, v. 85, p. 2149–2154, 1963.

MERRIFIELD, R. B. Solid phase peptide synthesis. II. the synthesis of bradykinin. **Journal of the American Chemical Society**, v. 86, p. 304–305, 1964.

MICHAEL, A. Ueber die einwirkung von diazobenzolimid auf acetylenedicarbonsäuremethylester. **Journal fur Praktische Chemie**, v. 48, p. 94–95, 1893.

MILES, A. J.; WALLACE, B. A. Circular dichroism spectroscopy of membrane proteins. **Chemical Society Reviews**, v. 45, p. 4859–4872, 2016.

MITCHELL, A. R. Bruce Merrifield and solid-phase peptide synthesis: A historical assessment. **Biopolymers**, v. 90, p. 175–184, 2008.

MITEVA, M.; ANDERSSON, M.; KARSHIKOFF, A.; OTTING, G. Molecular electroporation: a unifying concept for the description of membrane pore formation by antibacterial peptides, exemplified with NK-lysin. **FEBS Letters**, v. 462, p. 155–158, 1999.

MOELBERT, S.; NORMAND, B.; DE LOS RIOS, P. Kosmotropes and chaotropes: modelling preferential exclusion, binding and aggregate stability. **Biophysical Chemistry**, v. 112, p. 45–57, 2004.

MOFFITT, W. Optical rotatory dispersion of helical polymers. **Journal of Chemical Physics**, v. 25, p. 467–478, 1956.

MOKOKA, T. A. et al. Antimicrobial activity and cytotoxicity of triterpenes isolated from leaves of *maytenus undata* (celastraceae). **BMC Complementary and Alternative Medicine**, v. 13, 2013.

MONTALBETTI, C. A. G. N.; FALQUE, V. Amide bond formation and peptide coupling. **Tetrahedron**, v. 61, p. 10827–10852, 2005.

MOORE, S.; STEIN, W. H. Photometric ninhydrin method for use in the chromatography of amino acids. **Journal of Biological Chemistry**, v. 176, p. 367–388, 1948.

MORADY, S. V. et al. Glycosylation, an effective synthetic strategy to improve the bioavailability of therapeutic peptides. **Chemical Science**, v. 7, p. 2492–2500, 2016.

MORTISHIRE-SMITH, R. J.; DRAKE, A. F.; NUTKINS, J. C.; WILLIAM, D. H. Left handed α-helix formation by a bacterial peptide. **FEBS Letters**, v. 278, p. 244–246, 1991.

MOSS, G. P. Nomenclature of sterols. **Pure & Applied Chemistry**, v. 61, p. 1783–1822, 1989.

NAIR, D. P. et al. The thiol-Michael addition click reaction: A powerful and widely used tool in materials chemistry. **Chemistry of Materials**, v. 26, p. 724–744, 2014.

NATHAN, C. Resisting antimicrobial resistance. **Nature Reviews Microbiology**, v. 18, 2020.

NGUYEN, L. T.; HANEY, E. F.; VOGEL, H. J. The expanding scope of antimicrobial peptide structures and their modes of action. **Trends in Biotechnology**, v. 29, p. 464–472, 2011.

NILGES, M.; CLORE, G. M.; GRONENBORN, A. M. Determination of three-dimensional structures of proteins from interproton distance data by dynamical simulated annealing from a random array of atoms. **FEBS Letters**, v. 239, p. 129–136, 1988.

NYGAARD, R.; ROMANIUK, J. A. H.; RICE, D. M.; CEGELSKI, L. Spectral snapshots of bacterial cell-wall composition and the influence of antibiotics by whole-cell NMR. **Biophysical Journal**, v. 108, p. 1380–1389, 2015.

OWSLEY, D. C.; CASTRO, C. E. Substitution of aryl halides with copper(i) acetylides: 2-phenylfuro[3,2-*b*]pyridine. **Organic Synthesis**, v. 52, p. 128–130, 1972.

ÖZKILIÇ, Y.; TÜZÜN, N. Ş. A DFT study on the binuclear CuAAC reaction: Mechanism in light of new experiments. **Organometallics**, v. 35, p. 2589–2599, 2016.

PACE, C. N.; SCHOLTZ, J. M. A helix propensity scale based on experimental studies of peptides and proteins. **Biophysical Journal**, v. 75, p. 422–427, 1998.

PALLADINO, P.; STETSENKO, D. A. New TFA-free cleavage and final deprotection in Fmoc solid phase peptide synthesis: Dilute HCl in fluoro alcohol. **Organic Letters**, v. 14, p. 6346–6349, 2012.

PARADÍS-BAS, M.; TULLA-PUCHE, J.; ALBERICIO, F. The road to the synthesis of "difficult peptides". **Chemical Society Reviews**, v. 45, p. 631–654, 2016.

PAULICK, M. G.; BERTOZZI, C. R. The glycosylphosphatidylinositol anchor: A complex membrane-anchoring structure for proteins. **Biochemistry**, v. 47, p. 6991–7000, 2008.

PEARSON, D. A.; BLANCHETTE, M.; BAKER, M. L.; GUINDON, C. A. Trialkylsilanes as scavengers for the trifluoroacetic acid deblocking of protecting groups in peptide synthesis. **Tetrahedron Letters**, v. 30, p. 2739–2742, 1989.

PELLECCHIA, M.; SEM, D. S.; WÜTHRICH, K. NMR in drug discovery. **Nature Reviews**, v. 1, p. 211–219, 2002.

PHOENIX, D. A.; HARRIS, F. The hydrophobic moment and its use in the classification of amphiphilic structures (Review). **Molecular Membrane Biology**, v. 19, p. 1–10, 2002.

PIRES, D. A. T.; BEMQUERER, M. P.; DO NASCIMENTO, C. J. Some mechanistic aspects on Fmoc solid phase peptide syntehsis. **International Journal of Peptide Research and Therapeutics**, v. 20, p. 53–69, 2014.

PROTA, G.; PONSIGLIONE, E. On the reaction of ninhydrin with cysteine and its analogues: A revision. **Tetrahedron**, v. 29, p. 4271–4274, 1973.

PURCELL, E. M.; TORREY, H. C.; POUND, R. V. Resonance absorption by nuclear magnetic moments in a solid. **Physical Review**, v. 69, p. 37–38, 1946.

RABI, I. I.; ZACHARIAS, J. R.; MILLMAN, S.; KUSCH, P. A new method of measuring nuclear magnetic moment. **Physical Review**, v. 53, p. 318, 1938.

RAHMAN, F. I. Mucormycosis or black fungus infection is a new scare in south asian countries during the COVID-19 pandemic: Associated risk factors and preventive measures. **Journal of Medical Virology**, v. 93, p. 6447–6448, 2021.

RAMACHANDRAN, G. N.; RAMAKRISHNAN, C.; SASISEKHARAN, V. Stereochemistry of polypeptide chain configurations. **Journal of Molecular Biology**, v. 7, p. 95–99, 1963.

RAMAGE, R.; GREEN, J.; BLAKE, A. J. An acid labile arginine derivative for peptide synthesis: N^G-2,2,5,7,8-pentamethylchroman-6-sulphonyl-L-arginine. **Tetrahedron**, v. 47, p. 6353–6370, 1991.

RAMASAMY, S. et al. Synergistic effect of copper and ruthenium on regioselectivity in the alkyne–azide click reaction of internal alkynes. **Organic Process Research & Development**, v. 22, p. 880–887, 2018.

RANJBAR, B.; GILL, P. Circular dichroism techniques: Biomolecular and nanostructural analyses - A review. **Chemical Biology & Drug Design**, v. 74, p. 101–120, 2009.

RAWSON, T. M.; WILSON, R. C.; HOLMES, A. Understanding the role of bacterial and fungal infection in COVID-19. **Clinical Microbiology and Infection**, v. 27, p. 9–11, 2021.

REDDY, K. V. R.; YEDERY, R. D.; ARANHA, C. Antimicrobial peptides: premises and promises. **International Journal of Antimicrobial Agents**, v. 24, p. 536–547, 2004.

REE, R.; VARLAND, S.; ARNESEN, T. Spotlight on protein N-terminal acetylation. **Experimental & Molecular Medicine**, v. 50, p. 90–103, 2018.

REIS, P. V. M. et al. LyeTxI-b, a synthetic peptide derived from *lycosa erythrognata* spider venom, shows potent antibiotic activity *in vitro* and *in vivo*. **Frontiers in Microbiology**, v. 9, p. 1–12, 2018.

RESENDE, J. M. et al. Solution NMR structures of the antimicrobial peptides phylloseptin-1, -2, and -3 and biological activity: The role of charges and hydrogen bonding interactions in stabilizing helix conformations. **Peptides**, v. 29, p. 1633–1644, 2008.

RESENDE, J. M. et al. Membrane interactions of Phylloseptin-1, -2, and -3 peptides by oriented solid-state NMR spectroscopy. **Biophysical Journal**, v. 107, p. 901–911, 2014.

REZENDE, S. B. et al. Advances on chemically modified antimicrobial peptides for generating peptide antibiotics. **Chemical Communications**, v. 57, p. 11578–11591, 2021.

RICE, A.; WERESZCZYNSKI, J. Probing the disparate effects of arginine and lysine residues on antimicrobial peptide/bilayer association. **Biochimica et Biophysica Acta**, v. 1859, p. 1941–1950, 2017.

RICHARDSON, J. S. The anatomy and taxonomy of protein structure. **Advances in Protein Chemistry**, v. 34, p. 167–339, 1981.

RODIONOV, V. O.; FOKIN, V. V.; FINN, M. G. Mechanism of the ligan-free cu$^{\mathrm{I}}$-catalyzed azide-alkyne cycloaddition reaction. **Angewandte Chemie International Edition**, v. 44, p. 2210–2215, 2005.

RODRÍGUEZ, V. et al. Synthesis of glucosyl amino acid derivatives for obtaining N-glucopeptides via SPPS: Optimization of the synthetic route. **ChemistrySelect**, v. 6, p. 4083–4088, 2021.

ROHDE, M. The Gram-positive bacterial cell wall. **Microbiology Spectrum**, v. 7, p. 1–21, 2019.

ROSTOVTSEV, V. V.; GREEN, L. G.; FOKIN, V. V.; SHARPLESS, K. B. A stepwise Huisgen cycloaddition process: copper(I)-catalyzed regioselective "ligation" of azides and terminal alkynes. **Angewandte Chemie Interantional Edition**, v. 41, p. 2596–2599, 2002.

RUBEK, J.; FEITLER, D. Improved method for the study of reaction intermediates. Mechanism of peptide synthesis mediated by carbodiimides. **Journal of the American Chemical Society**, v. 95, p. 4052–4053, 1973.

RUCKER, S. P.; SHAKA, A. J. Broadband homonuclear cross polarization in 2D N.M.R. using DIPSI-2. **Molecular Physics**, v. 68, p. 509–517, 1989.

RUHEMANN, S. CCXII. - triketohydrindene hydrate. **Journal of the Chemical Society, Transactions**, v. 97, p. 2025–2031, 1910.

RUMBLE, J. R. **CRC Handbook of Chemistry and Physics**. 102. ed. [S.l.]: CRC Press, 2021. 1624 p. ISBN 9780367712600.

SAGATOVA, A. A. et al. Triazole resistance mediated by mutations of a conserved active site tyrosine in fungal lanosterol 14α-demethylase. **Scientific Reports**, v. 6, p. 1–11, 2016.

SALVI, G.; DE LOS RIOS, P.; VENDRUSCOLO, M. Effective interactions between chaotropic agents and proteins. **Proteins: Structure, Function, and Bioinformatics**, v. 61, p. 492–499, 2005.

SAM, Q. H. et al. Immunomodulation as therapy for fungal infection: Are we closer? **Frontiers in Microbiology**, v. 9, p. 1–16, 2018.

SANT, D. G.; TUPE, S. G.; RAMANA, C. V.; DESHPANDE, M. V. Fungal cell membrane - promising drug target for antifungal therapy. **Journal of Applied Microbiology**, v. 121, p. 1498–1510, 2016.

SANTOS, D. M. et al. LyeTx I, a potent antimicrobial peptide from the venom of the spider *lycosa erythrognata*. **Amino Acids**, v. 39, p. 135–144, 2010.

SARIN, V. K.; KENT, S. B. H.; TAM, J. P.; MERRIFIELD, R. B. Quantitative monitoring of solid-phase peptide synthesis by the ninhydrin reaction. **Analytical Biochemistry**, v. 117, p. 147–157, 1981.

SCHLEUCHER, J. et al. A general enchancement scheme in heteronuclear multidimensional NMR employing pulsed field gradients. **Journal of Biomolecular NMR**, v. 4, p. 301–306, 1994.

SCHRADER, S. M.; VAUBOURGEIX, J.; NATHAN, C. Biology of antimicrobial resistance and approaches to combat it. **Science Translational Medicine**, v. 12, p. 1–14, 2020.

Schrödinger, LLC. The PyMOL molecular graphics system, version 1.8. 2015.

SCHWARZINGER, S. et al. Random coil chemical shifts in acidic 8 M urea: Implementation of random coil shift data in NMRview. **Journal of Biomolecular NMR**, v. 18, p. 43–48, 2000.

SCHWARZINGER, S. et al. Sequence-dependent correction of random coil NMR chemical shifts. **Journal of the American Chemical Society**, v. 123, p. 2970–2978, 2001.

SCHWIETERS, C. D.; KUSZEWSKI, J. J.; CLORE, G. M. Using Xplor-NIH for NMR molecular structure determination. **Progress in Nuclear Magnetic Resonance Spectroscopy**, v. 48, p. 47–62, 2006.

SCHWIETERS, C. D.; KUSZEWSKI, J. J.; TJANDRA, N.; CLORE, G. M. The Xplor-NIH NMR molecular structure determination package. **Journal of Magnetic Resonance**, v. 160, p. 66–74, 2003.

SEDDON, A. M.; CURNOW, P.; BOOTH, P. J. Membrane proteins, lipids and detergents: not just a soap opera. **Biochimica et Biophysica Acta**, v. 1666, p. 105–117, 2004.

SEELIG, J. Thermodynamics of lipid–peptide interactions. **Biochimica et Biophysica Acta (BBA) - Biomembranes**, v. 1666, p. 40–50, 2004.

SEMENOV, S. N. et al. Autocatalytic cycles in a copper-catalyzed azide-alkyne cycloaddition reaction. **Journal of the American Chemical Society**, v. 140, p. 10221–10232, 2018.

SHAER, D. A.; MUSAIMI, O. A.; ALBERICIO, F.; TORRE, B. G. de la. 2021 FDA TIDES (peptides and oligonucleotides) harvest. **Pharmaceuticals**, v. 15, p. 222, 2022.

SHAFIEI, M.; PEYTON, L.; HASHEMZADEH, M.; FOROUMADI, A. History of the development of antifungal azoles: A review on structures, SAR, and mechanism of action. **Bioorganic Chemistry**, v. 104, p. 104240, 2020.

SHAFRAN, N. et al. Secondary bacterial infection in COVID-19 patients is a stronger predictor for death compared to influenza patients. **Scientific Reports**, v. 11, p. 12703–12711, 2021.

SHAKA, A. J.; LEE, C. J.; PINES, A. Iterative schemes for bilinear opeartors; applications to spin decoupling. **Journal of Magnetic Resonance**, v. 77, p. 274–293, 1988.

SHEEHAN, J. C.; CRUICKSHANK, P. A.; BOSHART, G. L. Notes- a convenient synthesis of water-soluble carbodiimides. **Journal of Organic Chemistry**, v. 26, p. 2525–2528, 1961.

SHEEHAN, J. C.; HESS, G. P. A new method of forming peptide bonds. **Journal of the American Chemical Society**, v. 77, p. 1067–1068, 1955.

SHELTON, P. T.; JENSEN, K. J. Linkers, resins, and general procedures for solid-phase peptide synthesis. In: _____. **Peptide Synthesis and Applications**. Totowa, New Jersey: Humana Press, 2013. p. 23–41.

SHEN, Y.; BAX, A. Protein backbone and sidechain torsion angles predicted from NMR chemical shifts using artificial neural networks. **Journal of Biomolecular NMR**, v. 56, p. 227–241, 2013.

SHEN, Y.; DELAGLIO, F.; CORNILESCU, G.; BAX, A. TALOS+: a hybrid method for predicting protein backbone torsion angles from NMR chemical shifts. **Journal of Biomolecular NMR**, v. 44, p. 213–223, 2009.

SHENG, S.; KRAFT, J. J.; SCHUSTER, S. M. A specific quantitative colorimetric assay for L-asparagine. **Analytical Biochemistry**, v. 211, p. 242–249, 1993.

SHI, Z.; OLSON, C. A.; KALLENBACH, N. R. Cation-π interaction in model α-helical peptides. **Journal of the American Chemical Society**, v. 124, p. 3284–3291, 2002.

SILVERMAN, B. D. Hydrophobic moments of tertiary protein structures. **PROTEINS: Structure, Function, and Genetics**, v. 53, p. 580–588, 2003.

SINHA, S. et al. Structure and interactions of a host defense antimicrobial peptide Thanatin in lipopolysaccharide micelles reveal mechanism of bacterial cell agglutination. **Scientific Reports**, v. 7, p. 17795–17807, 2017.

SKINNER, S. P. et al. CcpNmr AnalysisAssign: a flexible platform for integrated NMR analysis. **Journal of Biomolecular NMR**, v. 66, p. 111–124, 2016.

SOHLENKAMP, C.; GEIGER, O. Bacterial membrane lipids: diversity in structures and pathways. **FEMS Microbiology Reviews**, v. 40, p. 133–159, 2016.

SONG, E.-H.; SHANG, J.; RATNER, D. M. 9.08 - polysaccharides. In: MATYJASZEWSKI, K.; MÖLLER, M. (Ed.). **Polymer Science: A Comprehensive Reference**. Amsterdam: Elsevier, 2012. p. 137–155. ISBN 978-0-08-087862-1.

SOWA-JASIłEK, A. et al. Antifungal activity of anionic defense peptides: Insight into the action of galleria mellonella anionic peptide 2. **International Journal of Molecular Sciences**, v. 21, 2020.

SREERAMA, N.; WOODY, R. W. Estimation of protein secondary structure from circular dichroism spectra: Comparison of CONTIN, SELCON, and CDSSTR methods with an expanded reference set. **Analytical Biochemistry**, v. 287, p. 252–260, 2000.

STILLWELL, W. **An introduction to biological membranes**. 2. ed. California, United States: Academic Press, 2016. 565 p. ISBN 9780444637727.

STONE, N.; GUPTA, N.; SCHWARTZ, I. Mucormycosis: time to address this deadly fungal infection. **Lancet Microbe**, v. 2, p. e343–e344, 2021.

STROHALM, M.; HASSMAN, M.; KOŠATA, B.; KODÍČEK, M. mMass data miner: An open source alternative for mass spectrometric data analysis. **Rapid Communications in Mass Spectrometry**, v. 22, n. 6, p. 905–908, 2008.

STRUYFS, C.; CAMMUE, B. P. A.; THEVISSEN, K. Membrane-interacting antifungal peptides. **Frontiers in Cell and Developmental Biology**, v. 9, p. 1–17, 2021.

SUGAWARA, M. et al. Membrane structure and interaction of human catestatin by multidimensional solution and solid-state NMR. **The FASEB Journal**, v. 24, p. 1737–1746, 2010.

SWOBODA, J. G.; CAMPBELL, J.; MEREDITH, T. C.; WALKER, S. Wall teichoic acid function, biosynthesis, and inhibition. **ChemBioChem**, v. 11, p. 35–45, 2010.

SZOKA, F.; PAPAHADJOPOULOS, D. Comparative properties and methods of preparation of lipid vesicles (liposomes). **Annual Reviews of Biophysics and Bioengeneering**, v. 9, p. 467–508, 1980.

TADA, R.; LATGÉ, J.; AIMANIANDA, V. Undressing the fungal cell wall/cell membrane - the antifungal drug targets. **Current Pharmaceutical Design**, v. 19, p. 3738–3747, 2013.

TEIXEIRA, V.; FEIO, M. J.; BASTOS, M. Role of lipids in the interaction of antimicrobial peptides with membranes. **Progress in Lipid Research**, v. 51, p. 149–177, 2012.

THRIPPLETON, M. J.; KEELER, J. Elimination of zero-quantum interference in two-dimensional NMR spectra. **Angewandte Chemie International Edition**, v. 42, p. 3938–3941, 2003.

TIELEMAN, D. P.; SPOEL, D. van der; BERENDSEN, H. J. C. Molecular dynamics simulations of dodecylphosphocholine micelles at three different aggregate sizes: micellar structures and chain relaxation. **Journal of Physical Chemistry B**, v. 104, p. 6380–6388, 2000.

TIELEMAN, P. D. The molecular basis of electroporation. **BMC Biochemistry**, v. 5, p. 1–12, 2004.

TORNØE, C. W.; CHRISTENSEN, C.; MELDAL, M. Peptidotriazoles on solid phase: [1,2,3]-Triazoles by regiospecific copper(I)-catalyzed 1,3-dipolar cycloadditions of terminal alkynes to azides. **Journal of Organic Chemistry**, v. 67, p. 3057–3064, 2002.

TORRES, L. et al. Antimicrobial alumina nanobiostructures of disulfide- and triazole-linked peptides: Synthesis, characterization, membrane interactions and biological activity. **Colloids and Surfaces B: Biointerfaces**, v. 177, p. 94 – 104, 2019.

TROLL, W.; CANNAN, K. A modified photometric ninhydrin method for the analysis of amino and imino acids. **Journal of Biological Chemistry**, v. 200, p. 803–811, 1952.

TSOU, L. K.; TATKO, C. D.; WATERS, M. L. Simple cation-π interaction between a phenyl ring and a protonated amine stabilizes an α-helix in water. **Journal of the American Chemical Society**, v. 124, p. 14917–14921, 2002.

ULLIVARRI, M. F. de; ARBULU, S.; GARCIA-GUTIERREZ, E.; COTTER, P. D. Antifungal peptides as therapeutic agents. **Frontiers in Cellular and Infection Microbiology**, v. 10, p. 1–22, 2020.

USMANI, S. S. et al. THPdb: Database of FDA-approved peptide and protein therapeutics. **PLoS One**, v. 12, p. e0181748, 2017.

VAZDAR, M. et al. Arginine "magic": Guanidinium like-charge ion pairing from aqueous salts to cell penetrating peptides. **Accounts of Chemical Research**, v. 51, p. 1455–1464, 2018.

VENTOLA, C. L. The antibiotic resistance crisis. **Pharmacy & Therapeutics**, v. 40, p. 277–283, 2015.

WANG, C.; SHIH, L.; CHANG, K. Y. Large-scale analysis of antimicrobial activities in relation to amphipaticity and charge reveals novel characterization of antimicrobial peptides. **Molecules**, v. 22, p. 2037–2044, 2017.

WANG, F.; ZHANG, X.; CHEN, G.; ZHAO, Y. Living bacterial microneedles for fungal infection treatment. **Research**, v. 2020, p. 1–9, 2020.

WANG, G. Post-translational modifications of natural antimicrobial peptides and strategies for peptide engineering. **Current Biotechonology**, v. 1, p. 72–79, 2012.

WANG, G.; LI, X.; WANG, Z. Apd3: the antimicrobial peptide database as a tool for research and education. **Nucleid Acids Research**, v. 44, p. D1087–D1093, 2016.

WANG, J.; LI, H.; ZOU, G.; WANG, L. Novel template-assembled oligosaccharide clusters as epitope mimics for HIV-neutralizing antibody 2G12. design, synthesis, and antibody binding study. **Organic & Biomolecular Chemistry**, v. 5, p. 1529–1540, 2007.

WANG, X.; WANG, G. Insights into antimicrobial peptides from spiders and scorpions. **Protein & Peptide Letters**, v. 23, p. 707–721, 2016.

WARCHAWSKI, D. E. et al. Choosing membrane mimetics for nmr structural studies of transmembrane proteins. **Biochimica et Biophysica Acta**, v. 1808, p. 1957–1974, 2011.

WARD, D. E.; LAZNY, R.; PEDRAS, M. S. C. Synthesis of the host-selective phytotoxin Destruxin B. Avoiding diketopiperazine formation from an N-methyl amino acid dipeptide by use of the Boc-hydrazine derivative. **Tetrahedron Letters**, v. 38, p. 339–342, 1997.

WEINSTEIN, M. P. **Performance Standards for Antimicrobial Susceptibility Testing**. 28. ed. United States, Wayne, PA: Clinical and Laboratory Standards Institute, 2018. ISBN 1562388398.

WEST, R. Siegfried Ruhemann and the discovery of ninhydrin. **Journal of Chemical Education**, v. 42, p. 386–387, 1965.

WESTBLADE, L. F.; SIMON, M. S.; SATLIN, M. J. Bacterial coinfections in coronavirus disease 2019. **Trends in Microbiology**, v. 29, p. 930–941, 2021.

WHITAKER, J. R. Ninhydrin assay in the presence of thiol compounds. **Nature**, v. 189, p. 662–663, 1961.

WHO. **WHO Report on Surveillance of Antibiotic Consumption**. 2018. 128 p.

WIEPRECHT, T.; APOSTOLOV, O.; BEYERMANN, M.; SEELIG, J. Thermodynamics of the α-helix-coil transition of amphipathic peptides in a membrane environment: Implications for the peptide-membrane binding equilibrium. **Journal of Molecular Biology**, v. 294, p. 785–794, 1999.

WIEPRECHT, T.; APOSTOLOV, O.; BEYERMANN, M.; SEELIG, J. Interaction of a mitochondrial presequence with lipid membranes: Role of helix formation for membrane binding and perturbation. **Biochemistry**, v. 39, p. 15297–15305, 2000.

WIEPRECHT, T.; BEYERMANN, M.; SEELIG, J. Thermodynamics of the coil–α-helix transition of amphipathic peptides in a membrane environment: the role of vesicle curvature. **Biophysical Chemistry**, v. 96, p. 191–201, 2002.

WILLDIGG, J. R.; HELMANN, J. D. Mini review: Bacterial membrane composition and its modulation in response to stress. **Frontiers in Moleculer Biosciences**, v. 8, p. 1–11, 2021.

WILLKER, W.; LEIBFRITZ, D.; KERSSEBAUM, R.; BERMEL, W. Gradient selection in inverse heteronuclear correlation spectroscopy. **Magnetic Resonance in Chemistry**, v. 31, p. 287–292, 1993.

WISHARD, D. S. et al. ^{1}h, ^{13}c and ^{15}n random coil NMR chemical shifts of the common amino acids. I. investigations of nearest-neighbor effects. **Journal of Biomolecular NMR**, v. 5, p. 67–81, 1995.

WISHART, D. S. NMR metabolomics: a look ahead. **Journal of Magnetic Resonance**, v. 306, p. 155–161, 2019.

WISHART, D. S.; SYKES, B. D. [12] chemical shifts as a tool for structure determination. In: **Nuclear Magnetic Resonance, Part C**. [S.l.]: Academic Press, 1994, (Methods in Enzymology, v. 239). p. 363–392.

WISHART, D. S.; SYKES, B. D. The ^{13}C chemical-shift index: A simple method for the identification of protein secondary structure using ^{13}C chemical-shift data. **Journal of Biomolecular NMR**, v. 4, p. 171–180, 1994.

WISHART, D. S.; SYKES, B. D.; RICHARDS, F. M. The chemical shift index: a fast and simple method for the assignment of protein secondary structure through NMR spectroscopy. **Biochemistry**, v. 31, p. 1647–1651, 1992.

WOHLFARTH, C. **Static dielectric constant of 2,2,2-trifluoroethanol: Datasheet from Landolt-Börnstein - Group IV Physical Chemistry · Volume 27: "Static Dielectric Constants of Pure Liquids and Binary Liquid Mixtures"**. [S.l.]: Springer-Verlag Berlin Heidelberg, 2015.

WOHLFARTH, C. **Static dielectric constant of water: Datasheet from Landolt-Börnstein - Group IV Physical Chemistry · Volume 27: "Static Dielectric Constants of Pure Liquids and Binary Liquid Mixtures"**. [S.l.]: Springer-Verlag Berlin Heidelberg, 2015.

WOODY, R. W. [4] Circular dichroism. **Methods in Enzymology**, v. 246, p. 34–71, 1995.

WORELL, B. T.; MALIK, J. A.; FOKIN, V. V. Direct evidence of a dinuclear copper intermediate in Cu(I)-catalyzed azide-alkyne cycloadditions. **Science**, v. 340, p. 457–460, 2013.

WU, M. et al. Effects of glycosylation and D-amino acid substitution on the antitumor and antibacterial activities of bee venom peptide HYL. **Bioconjugate Chemistry**, v. 31, p. 2293–2302, 2020.

WUBULIKASIMU, A. et al. A designed antifungal peptide with therapeutic potential for clinical drug-resistant *candida albicans*. **Biochemical and Biophysical Research Communications**, v. 533, p. 404–409, 2020.

WÜTHRICH, K. **NMR of Proteins and Nucleic Acids**. 1. ed. New Jersey, United States: Wiley Interscience, 1986. 320 p. ISBN 0471828939.

WÜTHRICH, K.; WANGER, G. NMR investigations of the dynamics of the aromatic amino acid residues in the basic pancreatic trypsin inhibitor. **FEBS Letters**, v. 50, p. 265–268, 1975.

XU X. LAI, R. The chemistry and biological activities of peptides from amphibian skin secretions. **Chemical Reviews**, v. 115, p. 1760–1846, 2015.

YANG, C. et al. An engineered arginine-rich α-helical antimicrobial peptide exhibits broad-spectrum bactericidal activity against pathogenic bacteria and reduces bacterial infections in mice. **Scientific Reports**, v. 8, p. 14602–14616, 2018.

YANG, C. et al. An engineered arginine-rich α-helical antimicrobial peptide exhibits broad-spectrum bactericidal activity against pathogenic bacteria and reduces bacterial infections in mice. **Scientific Reports**, v. 8, p. 14602–14605, 2018.

YAO, J. et al. NMR structural and dynamic characterization of the acid-unfolded state of apomyoglobin provides insights into the early events in protein folding. **Biochemistry**, v. 40, p. 3561–3571, 2001.

YEAMAN, M. R.; YOUNT, N. Y. Mechanisms of antimicrobial peptide action and resistance. **Pharmacological Reviews**, v. 55, p. 27–55, 2003.

ZANDSALIMI, F. et al. Antimicrobial peptides: a promising strategy for lung cancer drug discovery? **Expert Opinion of Drug Discovery**, v. 15, p. 1343–1354, 2020.

ZHANG, G.; MEREDITH, T. C.; KAHNE, D. On the essentiality of lipopolysaccharide to gram-negative bacteria. **Current Opinion in Microbiology**, v. 16, p. 779–785, 2013.

ZHANG, J. et al. The fungal CYP51s: Their functions, structures, related drug resistance, and inhibitors. **Frontiers in Microbiology**, v. 10, p. 1–17, 2019.

ZHANG, Q. et al. Antimicrobial peptides: mechanism of action, activity and clinical potential. **Military Medical Research**, v. 8, p. 48–73, 2021.

ZHANG, Y.; KNAPP, S. Simplified beta-glycosylation of peptides. **Tetrahedron**, v. 74, p. 2891–2903, 2018.

ZHOU, N. E.; MONERA, O. D.; KAY, C. M.; HODGES, R. S. α-helical propensities of amino acids in the hydrophobic face of an amphipathic α-helix. **Protein and Peptide Letters**, v. 1, p. 114–119, 1994.

ZHOU, N. E.; ZHU, B. Y.; SYKES, B. D.; HODGES, R. S. Relationship between amide proton chemical shifts and hydrogen bonding in amphipathic α-helical peptides. **Journal of the American Chemical Society**, v. 114, p. 4320–4326, 1992.

ZHU, L. et al. On the mechanism of copper(I)-catalyzed azide-alkyne cycloaddition. **The Chemical Record**, v. 16, p. 1501–1517, 2016.

ZIARIANI, G. M. et al. Ninhydrin in synthesis of heterocyclic compounds. **ARKIVOC**, v. 2015 (vi), p. 1–139, 2015.

Chapter A | Appendix A

A.1 Helicity (*H*) values for obtained by CD

Table A.1: Helicity (*H*) values for **PS-O1**, **PS-O1 GtP**, **R1G2-PS-O1** and **R1A2-PS-O1 GtP** in 0:100, 10:90, 30:70, 50:50, and 60:40 TFE:H_2O proportions.

PS-O1		**PS-O1 GtP**		**R1G2-PS-O1**		**R1A2-PS-O1 GtP**	
TFE:H_2O	***H* (%)**	**TFE:H_2O**	***H* (%)**	**TFE:H_2O**	***H* (%)**	**TFE:H_2O**	***H* (%)**
0:100	8.23	0:100	15.4	0:100	8.2	0:100	19.7
10:90	5.5	10:90	25.2	10:90	16.7	10:90	18.2
30:70	45.9	30:70	49.5	30:70	44.5	30:70	65.3
50:50	-	50:50	64.1	50:50	71.9	50:50	77.4
60:40	43.45	60:40	46.7	60:40	45.2	60:40	71.4

Table A.2: Helicity (*H*) values for **PS-O1**, **PS-O1 GtP**, **R1G2-PS-O1** and **R1A2-PS-O1 GtP** using 0.5, 1.0, 2.0, 5.0, 10, and 20 mmol.L^{-1} SDS and DPC concentrations.

PS-O1		**PS-O1 GtP**		**R1G2-PS-O1**		**R1A2-PS-O1 GtP**	
SDS (mmol.L^{-1})	***H* (%)**	**SDS (mmol.L^{-1})**	***H* (%)**	**SDS (mmol.L^{-1})**	***H* (%)**	**SDS (mmol.L^{-1})**	***H* (%)**
0.5	0.9	0.5	57.5	0.5	52.8	0.5	63.9
1.0	8.9	1.0	87.5	1.0	67.5	1.0	64.7
2.0	30.8	2.0	87.9	2.0	57.9	2.0	65.0
5.0	30.7	5.0	89.1	5.0	59.3	5.0	65.1
10.0	30.6	10.0	88.5	10.0		10.0	66.2
20.0	28.2	20.0	71.1	20.0	36.9	20.0	45.6
DPC (mmol.L^{-1})	***H* (%)**	**DPC (mmol.L^{-1})**	***H* (%)**	**DPC (mmol.L^{-1})**	***H* (%)**	**DPC (mmol.L^{-1})**	***H* (%)**
0.5	4.05	0.5	16.6	0.5	10.8	0.5	
1.0	4.10	1.0	19.8	1.0	17.0	1.0	18.9
2.0	6.15	2.0	47.8	2.0	40.9	2.0	44.3
5.0	31.3	5.0		5.0	58.4	5.0	62.3
10.0	28.3	10.0	83.8	10.0	80.1	10.0	61.5
20.0	29.6	20.0	75.9	20.0	40.0	20.0	45.1

Table A.3: Helicity (H) values for **PS-O1**, **PS-O1 GtP**, **R1G2-PS-O1** and **R1A2-PS-O1 GtP** using 0.1, 0.5, 1.0, 1.5, and 2.0 mmol.L^{-1} POPC and POPC:POPG 3:1 concentrations.

PS-O1		**PS-O1 GtP**		**R1G2-PS-O1**		**R1A2-PS-O1 GtP**	
POPC (mmol.L^{-1})	***H* (%)**	**POPC (mmol.L^{-1})**	***H* (%)**	**POPC (mmol.L^{-1})**	***H* (%)**	**POPC (mmol.L^{-1})**	***H* (%)**
0.1	3.5	0.1	10.5	0.1	12.6	0.1	0.9
0.5	7.8	0.5	14.8	0.5	0.10	0.5	3.1
1.0	3.2	1.0	22.6	1.0	16.7	1.0	0.7
1.5	3.5	1.5	39.4	1.5	21.3	1.5	2.7
2.0	3.8	2.0		2.0	17.4	2.0	1.1
PCPG 3:1 (mmol.L^{-1})	***H* (%)**	**PCPG 3:1 (mmol.L^{-1})**	***H* (%)**	**PCPG 3:1 (mmol.L^{-1})**	***H* (%)**	**PCPG 3:1 (mmol.L^{-1})**	***H* (%)**
0.1	4.03	0.1	20.3	0.1	20.1	0.1	18.9
0.5	10.1	0.5	33.3	0.5	32.2	0.5	44.3
1.0	19.0	1.0	49.6	1.0	38.8	1.0	62.3
1.5	20.6	1.5	71.5	1.5	74.7	1.5	61.5
2.0	32.6	2.0	79.3	2.0	68.3	2.0	45.1

A.2 Secondary chemical shift data

Table A.4: Reference (δ_{ref}), experimental (δ_{exp}), and secondary ($\Delta\delta$) chemical shift values (ppm) for C_α, H_N, and H_α atoms of individual residues of **PS-O1**. Absent values were not obtainable unambiguously or are not applicable — *e.g.*, amide proton chemical shifts for Pro-6. Reference data was corrected for sequence-, temperature-, and pH-dependencies, considering neighboring residues, a temperature of 25 °C, and a pH of 7.0, according to (KJAERGAARD; POULSEN, 2011; KJAERGAARD et al., 2011).

Residue number	**Residue**	C_α (ppm)			H_N (ppm)			H_α (ppm)		
		δ_{ref}	δ_{exp}	$\Delta\delta$	δ_{ref}	δ_{exp}	$\Delta\delta$	δ_{ref}	δ_{exp}	$\Delta\delta$
1	**F**	57.531	58.506	0.98	8.328			4.672	4.657	-0.01
2	**L**	55.144	55.408	0.26	8.058			4.362	4.204	-0.16
3	**S**	58.264	59.328	1.06	8.222	7.907	-0.32	4.402	4.347	-0.05
4	**L**	54.903	56.049	1.15	8.230	7.938	-0.29	4.432	4.519	0.09
5	**I**	58.898	65.203	6.31	8.083	7.747	-0.34	4.425	4.081	-0.34
6	**P**	62.957	65.853	2.90				4.430	4.247	-0.18
7	**H**	55.979	59.108	3.13	8.463	7.304	-1.16	4.592	4.393	-0.20
8	**A**	52.364	56.816	4.45	8.273	8.281	0.01	4.350	4.211	-0.14
9	**I**	61.303	64.700	3.40	8.269	8.417	0.15	4.129	3.791	-0.34
10	**N**	53.003	56.890	3.89	8.459	8.126	-0.33	4.670	4.470	-0.20
11	**A**	52.629	55.984	3.36	8.429	8.346	-0.08	4.348	4.163	-0.19
12	**V**	62.525	67.042	4.52	8.082	8.526	0.44	4.137	3.712	-0.42
13	**S**	58.371	62.308	3.94	8.468	8.453	-0.02	4.543	4.160	-0.38
14	**T**	61.866	67.294	5.43	8.269	8.041	-0.23	4.386	4.069	-0.32
15	**L**	55.127	58.684	3.56	8.188	8.132	-0.06	4.390	4.185	-0.21
16	**V**	62.366	66.640	4.27	8.183	8.721	0.54	4.029	3.671	-0.36
17	**H**	56.005	59.276	3.27	8.417	8.276	-0.14	4.637	4.416	-0.22
18	**H**	56.127	58.190	2.06	8.310	8.301	-0.01	4.716	4.584	-0.13
19	**S**	58.735	59.707	0.97	8.405	8.115	-0.29	4.464	4.470	0.01
20	**G**	45.505	45.097	-0.41	8.520	8.076	-0.44	4.008	4.008	0.00

Table A.5: Reference (δ_{ref}), experimental (δ_{exp}), and secondary ($\Delta\delta$) chemical shift values (ppm) for C_α, H_N, and H_α atoms of individual residues of **PS-O1 GtP**. Absent values were not obtainable unambiguously or are not applicable — *e.g.*, amide proton chemical shifts for Pro-7. Reference data was corrected for sequence-, temperature-, and pH-dependencies, considering neighboring residues, a temperature of 25 °C, and a pH of 7.0, according to (KJAERGAARD; POULSEN, 2011; KJAERGAARD et al., 2011). Residue 1 (Ala) was used as a placeholder for the glucotriazole moiety in calculations of reference chemical shifts.

Residue number	**Residue**	C_α (ppm)			H_N (ppm)			H_α (ppm)		
		δ_{ref}	δ_{exp}	$\Delta\delta$	δ_{ref}	δ_{exp}	$\Delta\delta$	δ_{ref}	δ_{exp}	$\Delta\delta$
1	**“A”**	52.780	56.632	3.852	8.403	3.948	-0.281	4.229		
2	**F**	57.455	60.333	2.878	8.227	4.508	-0.151	4.659		
3	**L**	55.151	57.445	2.294	7.986	8.443	0.457	4.360	4.253	-0.107
4	**S**	58.264	60.304	2.04	8.222	7.936	-0.286	4.402	4.342	-0.06
5	**L**	54.903	56.727	1.824	8.230	7.865	-0.365	4.432	4.457	0.025
6	**I**	58.898	65.923	7.025	8.083	7.728	-0.355	4.425	4.030	-0.395
7	**P**	62.957	66.132	3.175				4.430	4.254	-0.176
8	**H**	55.979	59.162	3.183	8.463	7.326	-1.137	4.592	4.392	-0.2
9	**A**	52.364	55.636	3.272	8.273	8.334	0.061	4.350	4.231	-0.119
10	**I**	61.303	64.919	3.616	8.269	8.467	0.198	4.129	3.778	-0.351
11	**N**	53.003	57.141	4.138	8.459	8.094	-0.365	4.670	4.467	-0.203
12	**A**	52.629	56.136	3.507	8.429	8.325	-0.104	4.348	4.173	-0.175
13	**V**	62.525	67.262	4.737	8.082	8.579	0.497	4.137	3.708	-0.429
14	**S**	58.371	62.304	3.933	8.468	8.501	0.033	4.543	4.170	-0.373
15	**T**	61.866	67.474	5.608	8.269	8.119	-0.15	4.386	4.084	-0.302
16	**L**	55.127	58.913	3.786	8.188	8.178	-0.01	4.390	4.182	-0.208
17	**V**	62.366	66.612	4.246	8.183	8.780	0.597	4.029	3.708	-0.321
18	**H**	56.005	58.854	2.849	8.417	8.269	-0.148	4.637	4.474	-0.163
19	**H**	56.127	57.713	1.586	8.310	8.295	-0.015	4.716	4.645	-0.071
20	**S**	58.735	59.680	0.945	8.405	8.106	-0.299	4.464	4.496	0.032
21	**G**	45.505	45.179	-0.326	8.520	8.122	-0.398	4.008	4.007	-0.001

Table A.6: Reference (δ_{ref}), experimental (δ_{exp}), and secondary ($\Delta\delta$) chemical shift values (ppm) for C_α, H_N, and H_α atoms of individual residues of **R1G2-PS-O1**. Absent values were not obtainable unambiguously or are not applicable — *e.g.*, amide proton chemical shifts for Pro-8. Reference data was corrected for sequence-, temperature-, and pH-dependencies, considering neighboring residues, a temperature of 25 °C, and a pH of 7.0, according to (KJAERGAARD; POULSEN, 2011; KJAERGAARD et al., 2011).

Residue number	**Residue**	C_α (ppm)			H_N (ppm)			H_α (ppm)		
		δ_{ref}	δ_{exp}	$\Delta\delta$	δ_{ref}	δ_{exp}	$\Delta\delta$	δ_{ref}	δ_{exp}	$\Delta\delta$
1	**R**	56.566	57.295	0.729	8.525			4.289	4.277	-0.012
2	**G**	45.055	46.540	1.485	8.505			3.911		
3	**F**	57.612	60.369	2.757	8.131	8.003	-0.128	4.679	4.517	-0.162
4	**L**	55.205	58.044	2.839	8.059	7.757	-0.302	4.367	4.207	-0.160
5	**S**	58.264	60.984	2.720	8.222	7.748	-0.474	4.402	4.370	-0.032
6	**L**	54.903	57.244	2.341	8.230	7.800	-0.430	4.432	4.471	0.039
7	**I**	58.898	66.332	7.434	8.083	7.675	-0.408	4.425	4.048	-0.377
8	**P**	62.957	66.858	3.901				4.430	4.048	-0.382
9	**H**	55.979	60.079	4.100	8.463	7.278	-1.185	4.592	4.368	-0.224
10	**A**	52.364	56.364	4.000	8.273	8.283	0.010	4.350	4.210	-0.140
11	**I**	61.303	65.678	4.375	8.269	8.432	0.163	4.129	3.783	-0.346
12	**N**	53.003	57.845	4.842	8.459	8.122	-0.337	4.670	4.471	-0.199
13	**A**	52.629	56.918	4.289	8.429	8.342	-0.087	4.348	4.167	-0.181
14	**V**	62.525	67.997	5.472	8.082	8.567	0.485	4.137	3.714	-0.423
15	**S**	58.371	63.224	4.853	8.468	8.458	-0.010	4.543	4.161	-0.382
16	**T**	61.866	68.193	6.327	8.269	8.040	-0.229	4.386	4.070	-0.316
17	**L**	55.127	59.589	4.462	8.188	8.130	-0.058	4.390	4.186	-0.204
18	**V**	62.366	67.545	5.179	8.183	8.718	0.535	4.029	3.673	-0.356
19	**H**	56.005	60.202	4.197	8.417	8.271	-0.146	4.637	4.420	-0.217
20	**H**	56.127	59.134	3.007	8.310	8.301	-0.009	4.716	4.584	-0.132
21	**S**	58.735	60.640	1.905	8.405	8.122	-0.283	4.464	4.470	0.006
22	**G**	45.505	46.037	0.532	8.520	8.082	-0.438	4.008	3.996	-0.012

Table A.7: Reference (δ_{ref}), experimental (δ_{exp}), and secondary ($\Delta\delta$) chemical shift values (ppm) for C_α, H_N, and H_α atoms of individual residues of **R1A2-PS-O1 GtP**. Absent values were not obtainable unambiguously or are not applicable — *e.g.*, amide proton chemical shifts for Pro-8. Reference data was corrected for sequence-, temperature-, and pH-dependencies, considering neighboring residues, a temperature of 25 °C, and a pH of 7.0, according to (KJAERGAARD; POULSEN, 2011; KJAERGAARD et al., 2011). Residue 2 (Ala) was used as a placeholder for the glucotriazole moiety in calculations of reference chemical shifts.

Residue number	**Residue**	C_α (ppm)			H_N (ppm)			H_α (ppm)		
		δ_{ref}	δ_{exp}	$\Delta\delta$	δ_{ref}	δ_{exp}	$\Delta\delta$	δ_{ref}	δ_{exp}	$\Delta\delta$
1	**R**	56.278	57.546	1.268	8.457			4.255		
2	**A**	52.718			8.420			4.237		
3	**F**	57.529			8.236	8.101	-0.135	4.652	4.503	-0.149
4	**L**	55.151	58.137	2.986	7.986	8.260	0.274	4.360	4.252	-0.108
5	**S**	58.264	60.968	2.704	8.222	7.894	-0.328	4.402	4.355	-0.047
6	**L**	54.903	57.184	2.281	8.230	7.805	-0.425	4.432	4.497	0.065
7	**I**	58.898	66.067	7.169	8.083	7.643	-0.440	4.425	4.077	-0.348
8	**P**	62.957	66.858	3.901				4.430	4.258	-0.172
9	**H**	55.979	60.081	4.102	8.463	7.302	-1.161	4.592	4.400	-0.192
10	**A**	52.364	56.395	4.031	8.273	8.238	-0.035	4.350	4.210	-0.140
11	**I**	61.303	65.655	4.352	8.269	8.389	0.120	4.129	3.808	-0.321
12	**N**	53.003	57.852	4.849	8.459	8.104	-0.355	4.670	4.480	-0.190
13	**A**	52.629	56.943	4.314	8.429	8.320	-0.109	4.348	4.177	-0.171
14	**V**	62.525	68.030	5.505	8.082	8.528	0.446	4.137	3.728	-0.409
15	**S**	58.371	63.305	4.934	8.468	8.427	-0.041	4.543	4.170	-0.373
16	**T**	61.866	68.189	6.323	8.269	8.020	-0.249	4.386	4.083	-0.303
17	**L**	55.127	59.622	4.495	8.188	8.111	-0.077	4.390	4.194	-0.196
18	**V**	62.366	67.527	5.161	8.183	8.667	0.484	4.029	3.693	-0.336
19	**H**	56.005	60.215	4.210	8.417	8.239	-0.178	4.637	4.433	-0.204
20	**H**	56.127	59.144	3.017	8.310	8.278	-0.032	4.716	4.596	-0.120
21	**S**	58.735	60.666	1.931	8.405	8.111	-0.294	4.464	4.489	0.025
22	**G**	45.505	46.102	0.597	8.520	8.072	-0.448	4.008	4.009	0.001

A.3 Cytotoxicity values

Table A.8: *In vitro* cytotoxicity values of **PS-O1**, **PS-O1 GtP**, **R1G2-PS-O1**, and **R1A2-PS-O1 GtP** in the presence of VERO cells (`ATCC CCL-81`). Values are displayed for three experiments with their respective mean (μ) and standard deviation (σ) values.

	Cell viability (%)									
	PS-O1					**PS-O1 GtP**				
Concentration (μg.mL^{-1})	Exp. 1	Exp. 2	Exp. 3	μ	σ	Exp. 1	Exp. 2	Exp. 3	μ	σ
200	125	119	120	121.33	3.2	98	94	97	96.33	2.1
100	116	102	105	107.67	7.4	95	96	90	93.67	3.2
50	107	104	96	102.33	5.7	89	91	91	90.33	1.2
25	105	100	94	99.67	5.5	92	90	89	90.33	1.5
12.5	105	96	92	97.67	6.7	90	89	88	89.00	1.0
6.25	99	97	93	96.33	3.1	92	89	91	90.67	1.5
3.12	107	99	95	100.33	6.1	94	95	94	94.33	0.6
	R1G2-PS-O1					**R1A2-PS-O1 GtP**				
Concentration (μg.mL^{-1})	Exp. 1	Exp. 2	Exp. 3	μ	σ	Exp. 1	Exp. 2	Exp. 3	μ	σ
200	104	108	95	102.33	6.7	84	80	87	83.67	3.5
100	106	105	92	101.00	7.8	85	84	88	85.67	2.1
50	99	98	92	96.33	3.8	82	80	86	82.67	3.1
25	99	94	92	95.00	3.6	84	84	88	85.33	2.3
12.5	98	96	88	94.00	5.3	87	87	88	87.33	0.6
6.25	97	96	91	94.67	3.2	84	82	92	86.00	5.3
3.12	100	98	94	97.33	3.1	87	90	90	89.00	1.7

A.4 Product operator formalism for the HSQC

The HSQC, as mentioned in **Chapter 4, Section 4.1.1, Page 82**, is better explained using the product operator formalism, and the mathematical explanation of this pulse sequence is better understood when one divides it in some steps, as shown in **Figure A.1**. For each step (**A** to **K**), the initial spin operator that represents the density matrix $\rho(0)$ at that stage will undergo relevant transformations like pulses and spin evolutions, either in the chemical shift or J-coupling. The Hamiltonian operators $\hat{\mathcal{H}}$ for each of these transformations are:

1. Pulses: $\hat{\mathcal{H}} = \phi \hat{I}_i$, where ϕ is the pulse degree in radians (*i.e.*, $\pi/2$ or π) and $\hat{I}_i$ is the spin operator along the axis of the pulse;
2. Chemical shift evolution: $\hat{\mathcal{H}}_z = -\Omega_i \hat{I}_z \tau$, where $\Omega_i = \gamma_i B_0$, γ_i is the magnetogyric ratio of nucleus i and τ is the time period of the evolution;

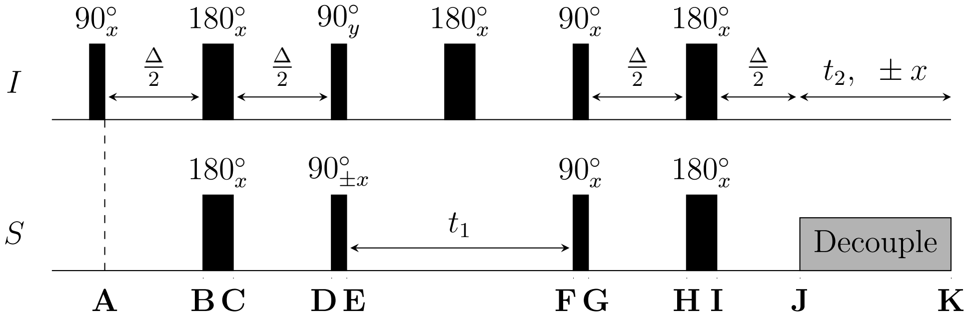

Figure A.1: General HSQC pulse sequence. I and S represent two different nuclei, t_1 represents the increments to be performed in the indirect dimension and t_2 is the acquisition time in the direct dimension. Relevant steps in the pulse sequence are marked with letters **A** to **K**.

3. J-coupling evolution: $\hat{\mathcal{H}} = 2\pi J_{IS}\hat{I}_z\hat{S}_z$, where J_{IS} is the J-coupling operator between spins I and S, $\hat{I}_z$ is the I-spin operator along the z-axis and $\hat{S}_z$ is the S-spin operator along the z-axis.

Considering the Hamiltonian operators $\hat{\mathcal{H}}$ described above, the general operations to be performed with the spin operators assume change in the density matrix $\rho(0)$ during a time t that is described by

$$\frac{d\rho}{dt} = i\hbar\,[H,\rho] \implies \rho(t) = e^{-i\hat{\mathcal{H}}t}\rho(0)\; e^{i\hat{\mathcal{H}}t}. \tag{A.1}$$

Considering that the density matrix $\rho(0)$ will be proportional to one of the main spin operator along a given axis, $\hat{I}_i$, where $i = x$, y or z, one gets

$$\rho(t) = e^{-i\hat{\mathcal{H}}t}\rho(0)\; e^{i\hat{\mathcal{H}}t} = e^{-i\hat{\mathcal{H}}t}\hat{I}_i\; e^{i\hat{\mathcal{H}}t} = \hat{I}_i\cos\theta + \frac{\left[\hat{\mathcal{H}},\hat{I}_i\right]}{i\hbar}\sin\theta, \tag{A.2}$$

where $\left[\hat{\mathcal{H}},\hat{I}_i\right]$ is the commutator of both operators and θ is the angle of the transformation.

At step **A**, the initial magnetization is along the z-axis, therefore

$$\rho(0) \propto \;\hat{I}_z \tag{A.3}$$

$$\hat{I}_z \xrightarrow{\pi/2,\hat{I}_x} \hat{I}_z\cos(\pi/2) + \left[-\hat{I}\sin(\pi/2)\right] = -\hat{I}_y. \quad (\mathbf{A}) \tag{A.4}$$

Afterwards, the magnetization evolves in the chemical shift and the J-coupling. Since the initial pulses in the I channel comprise a sequence similar to $[90^\circ_x - \tau - 180^\circ_x - \tau]$, constituting a spin-echo, the chemical shift evolution is refocused and will, therefore, not be considered and only the J-coupling evolution will be evaluated. At step **B**, the magnetization will take form of

$$\rho(0) \propto -\hat{I}_y \tag{A.5}$$

$$-\hat{I}_y \xrightarrow{2\pi J\hat{I}_z\hat{S}_z\Delta/2} -\hat{I}_y\cos(2\pi J\Delta/2) + 2\hat{I}_x\hat{S}_z\sin(2\pi J\Delta/2)\,. \quad (\mathbf{B}) \tag{A.6}$$

The π pulses on both channels change the magnetization like such:

$$\rho(0) \propto -\hat{I}_y \cos(2\pi J\Delta/2) + 2\hat{I}_x\hat{S}_z \sin(2\pi J\Delta/2) \quad (2\pi J\Delta/2) = a \tag{A.7}$$

$$-\hat{I}_y \cos a + 2\hat{I}_x\hat{S}_z \sin a \xrightarrow{\pi,\hat{I}_x} \hat{I}_y \cos a + 2\hat{I}_x\hat{S}_z \sin a \tag{A.8}$$

$$\hat{I}_y \cos a + 2\hat{I}_x\hat{S}_z \sin a \xrightarrow{\pi,\hat{S}_x} \hat{I}_y \cos a - 2\hat{I}_x\hat{S}_z \sin a. \quad (\mathbf{C}) \tag{A.9}$$

Subsequent J-coupling evolution after **C** during $\Delta/2$ yields

$$\rho(0) \propto \hat{I}_y \cos a - 2\hat{I}_x\hat{S}_z \sin a \tag{A.10}$$

$$\begin{aligned} &\hat{I}_y \cos a - 2\hat{I}_x\hat{S}_z \sin a \xrightarrow{a\hat{I}_z\hat{S}_z} \hat{I}_y \cos a \cos a - 2\hat{I}_x\hat{S}_z \cos a \sin a - 2\hat{I}_x\hat{S}_z \sin a \cos a - \hat{I}_y \sin a \sin a \\ =\ &\hat{I}_y\left[\cos^2 a - \sin^2 a\right] - 2\hat{I}_x\hat{S}_z\left[2\cos a \sin a\right] = \hat{I}_y \cos 2a - 2\hat{I}_x\hat{S}_z \sin 2a \\ =\ &\hat{I}_y \cos(4\pi J\Delta/2) - 2\hat{I}_x\hat{S}_z \sin(4\pi J\Delta/2). \quad (\mathbf{D}) \end{aligned} \tag{A.11}$$

At **E**, two 90° pulses with different phases are applied in both channels, resulting in

$$\rho(0) \propto \hat{I}_y \cos(4\pi J\Delta/2) - 2\hat{I}_x\hat{S}_z \sin(4\pi J\Delta/2) \quad (4\pi J\Delta/2) = 2a \tag{A.12}$$

$$\hat{I}_y \cos 2a - 2\hat{I}_x\hat{S}_z \sin 2a \xrightarrow{\pi/2,\hat{I}_y} \hat{I}_y \cos 2a + 2\hat{I}_z\hat{S}_z \sin 2a, \tag{A.13}$$

$$\hat{I}_y \cos 2a + 2\hat{I}_z\hat{S}_z \sin 2a \xrightarrow{\pi/2,\hat{S}_x} \hat{I}_y \cos 2a - 2\hat{I}_z\hat{S}_y \sin 2a. \quad (\mathbf{E}) \tag{A.14}$$

Only single-quantum coherence was established between spins I and S until **E**, since either spin I had its magnetization vector along the x or y axis ($\hat{I}_x/\hat{I}_y$), or the terms with both I and S spin operators had the former in the transverse plane and the latter in the longitudinal ($\hat{I}_x\hat{S}_z$). The application of the two 90° pulses at the end of the INEPT sequence promoted a multiple-quanta coherence for both spins, represented by $\hat{I}_z\hat{S}_z$, and the second pulse then generated $\hat{I}_z\hat{S}_y$, representing a coherence transference from I to S.

Additionally, since the magnetization of interest is the developed single-quantum coherence for S, $\hat{I}_y \cos(4\pi J\Delta/2)$ can be removed. This can be performed by adjusting the time period $\Delta/2$, cancelling the cos term or by considering

$$\cos\left(\frac{4\pi J\Delta}{2}\right) = \cos(2\pi J\Delta), \tag{A.15}$$

$$\cos(2\pi J\Delta) = 0 \Leftrightarrow 2\pi J\Delta = \pi/2 \therefore \Delta = 1/4J. \tag{A.16}$$

Equation A.16 could be written so that $2\pi J\Delta = (2n+1)\pi/2$, resulting in $\Delta = (2n+1)/4J$ but, since experimental time is an important factor in NMR experiments due to relaxation processes and instrumental cost, the smallest value of $\Delta = 1/4J$ can be considered. Futhermore, this also brings the term $-2\hat{I}_z\hat{S}_y \sin(4\pi J\Delta/2)$ to $-2\hat{I}_z\hat{S}_y$; considered to be $\rho(0)$ in the following step of the pulse sequence.

The next step in the pulse sequence regards the indirect dimension acquisition time t_1. During it, magnetization will evolve in the chemical shift as

$$\rho(0) \propto \; -2\hat{I}_z\hat{S}_y \tag{A.17}$$

$$-2\hat{I}_z\hat{S}_y \xrightarrow{\Omega_S\hat{S}_z t_1} -2\hat{I}_z\hat{S}_y\cos(\Omega_S t_1) + 2\hat{I}_z\hat{S}_x\sin(\Omega_S t_1)\,. \tag{A.18}$$

The term $2\hat{I}_z\hat{S}_x\sin(\Omega_S t_1)$ is canceled after a phase cycling routine, like CYCLOPS. In the case of HSQC, the t_1 acquisition time has an 180°_x pulse in the I channel at the midpoint. This pulse induces another spin-echo for both spins and J-coupling is refocused during a spin-echo. At step **B**, a spin-echo was also established but J-coupling evolution was still considered. However, only one 180°_x pulse is applied during t_1 while, in the first INEPT sequence, two of them were, promoting the differences in evolution. Therefore, the magnetization considered in the following step is relative to the term $-2\hat{I}_z\hat{S}_y\cos(\Omega_S t_1)$, which will be influenced as

$$\rho(0) \propto \; -2\hat{I}_z\hat{S}_y\cos(\Omega_S t_1) \tag{A.19}$$

$$-2\hat{I}_z\hat{S}_y\cos(\Omega_S t_1) \xrightarrow{\pi/2,\hat{I}_x} 2\hat{I}_y\hat{S}_y\cos(\Omega_S t_1)\,, \tag{A.20}$$

$$2\hat{I}_y\hat{S}_y\cos(\Omega_S t_1) \xrightarrow{\pi/2,\hat{S}_x} 2\hat{I}_y\hat{S}_z\cos(\Omega_S t_1)\,. \quad (\mathbf{G}) \tag{A.21}$$

After both 90°_x pulses, the S single-quantum coherence ($-2\hat{I}_z\hat{S}_y$) was transferred back to an I coherence ($2\hat{I}_y\hat{S}_z$) to be detected during t_2. During the next $\Delta/2$, the magnetization evolves in the J-coupling only, since another spin-echo will be established, as

$$\rho(0) \propto 2\hat{I}_y\hat{S}_z\cos(\Omega_S t_1) \tag{A.22}$$

$$2\hat{I}_y\hat{S}_z\cos(\Omega_S t_1) \xrightarrow{2\pi J\hat{I}_z\hat{S}_z\Delta/2} \cos(\Omega_S t_1)\left[2\hat{I}_y\hat{S}_z\cos(2\pi J\Delta/2) - \hat{I}_x\sin(2\pi J\Delta/2)\right]. \quad (\mathbf{H}) \tag{A.23}$$

The two 180°_x pulses provoke the following changes on the magnetization:

$$\rho(0) \propto \cos(\Omega_S t_1)\left[2\hat{I}_y\hat{S}_z\cos(2\pi J\Delta/2) - \hat{I}_x\sin(2\pi J\Delta/2)\right] \quad (2\pi J\Delta/2) = a \tag{A.24}$$

$$\cos(\Omega_S t_1)\left[2\hat{I}_y\hat{S}_z\cos a - \hat{I}_x\sin a\right] \xrightarrow{\pi,\hat{I}_x} \cos(\Omega_S t_1)\left[-2\hat{I}_y\hat{S}_z\cos a + \hat{I}_x\sin a\right] \tag{A.25}$$

$$\cos(\Omega_S t_1)\left[-2\hat{I}_y\hat{S}_z\cos a + \hat{I}_x\sin a\right] \xrightarrow{\pi,\hat{S}_x} \cos(\Omega_S t_1)\left[2\hat{I}_y\hat{S}_z\cos a + \hat{I}_x\sin a\right]. \quad (\mathbf{I}) \tag{A.26}$$

For the final $\Delta/2$ period, the magnetization will evolve as

$$\rho(0) \propto \cos(\Omega_S t_1)\left[2\hat{I}_y\hat{S}_z\cos a + \hat{I}_x\sin a\right] \quad (\Omega_S t_1) = b \tag{A.27}$$

$$\begin{aligned}
&\cos b\left[2\hat{I}_y\hat{S}_z\cos a + \hat{I}_x\sin a\right] \xrightarrow{2\pi J\hat{I}_z\hat{S}_z\Delta/2} 2\hat{I}_y\hat{S}_z\cos a\cos b\cos a - \hat{I}_x\cos a\cos b\sin a \\
&+ \hat{I}_x\sin a\cos b\cos a + \hat{I}_y\sin a\cos b\sin a = 2\hat{I}_y\hat{S}_z\cos^2 a\cos b + \hat{I}_y\sin^2 a\cos b \\
&= 2\hat{I}_y\hat{S}_z\cos^2(2\pi J\Delta/2)\cos(\Omega_S t_1) + \hat{I}_y\sin^2(2\pi J\Delta/2)\cos(\Omega_S t_1)\,. \quad (\mathbf{J})
\end{aligned} \tag{A.28}$$

Similar to **E**, by using the appropriate value for Δ, $\cos^2(2\pi J\Delta/2)$ can be eliminated while maximizing the sin. In this case, when $\Delta = 1/2J$, $2\hat{I}_y\hat{S}_z\cos^2(2\pi J\Delta/2)\cos(\Omega_S t_1)$ goes to to zero while the term $\hat{I}_y\sin^2(2\pi J\Delta/2)\cos(\Omega_S t_1)$ goes to to $\hat{I}_y\cos(\Omega_S t_1)$, evolving during t_2 as

$$\rho(0) \propto \hat{I}_y\cos(\Omega_S t_1) \tag{A.29}$$

$$\hat{I}_y\cos(\Omega_S t_1) \xrightarrow{\Omega_S\hat{I}_z t_2} \cos(\Omega_S t_1)\left[\hat{I}_x\cos(\Omega_I t_2) + \hat{I}_y\sin(\Omega_I t_2)\right]. \quad (\mathbf{K}) \tag{A.30}$$

During t_2, only chemical shift evolution will be present, as a decoupling pulse in the S channel is used. Two I magnetizations will be detected at the end of the pulse sequence (**Equation A.30**) which, when considering I to being of an ^{1}H and S of a ^{13}C, detection will occur through the most sensitive nucleus. Furthermore, both $\hat{I}_x$ and $\hat{I}_y$ are modulated by chemical shift terms, Ω_S and Ω_I, during their respective acquisition times t_1 and t_2. A Fourier transform of the signal

$$S(t_1,t_2) = S_x + iS_y = \cos(\Omega_S t_1)\cos(\Omega_I t_2) + i\cos(\Omega_S t_1)\sin(\Omega_I t_2) \tag{A.31}$$

$$S(t_1,t_2) = \cos(\Omega_S t_1)\left[\cos(\Omega_I t_2) + i\sin(\Omega_I t_2)\right] \tag{A.32}$$

$$S(t_1,t_2) = \cos(\Omega_S t_1)\, e^{i\Omega_I t_2}e^{-R_2 t_2}, \tag{A.33}$$

where $e^{-R_2 t_2}$ is related to the longitudinal relaxation rate (R_2), yields a spectrum that has I and S cross-peaks with chemical shifts encoded; in this case, Ω_S along f_1 and Ω_I along f_2. Additionally, they do not carry J-coupling information, since there is no J term in either signal, furnishing a decoupled heteronuclear spectrum.